

**ATMOSPHERIC VOLUME EMISSION TOMOGRAPHY FROM A
SATELLITE PLATFORM**

A Thesis

**Submitted to the Faculty of Graduate Studies and Research
in Partial Fulfillment of the Requirements
for the Degree of
Doctor of Philosophy
in the Department of Physics and Engineering Physics**

by

Douglas Arthur Degenstein

Saskatoon, Saskatchewan

August, 1999

**The author claims copyright ©. Use shall not be made of the
material contained herein without proper acknowledgment.**



National Library
of Canada

Acquisitions and
Bibliographic Services

395 Wellington Street
Ottawa ON K1A 0N4
Canada

Bibliothèque nationale
du Canada

Acquisitions et
services bibliographiques

395, rue Wellington
Ottawa ON K1A 0N4
Canada

Your file *Votre référence*

Our file *Notre référence*

The author has granted a non-exclusive licence allowing the National Library of Canada to reproduce, loan, distribute or sell copies of this thesis in microform, paper or electronic formats.

The author retains ownership of the copyright in this thesis. Neither the thesis nor substantial extracts from it may be printed or otherwise reproduced without the author's permission.

L'auteur a accordé une licence non exclusive permettant à la Bibliothèque nationale du Canada de reproduire, prêter, distribuer ou vendre des copies de cette thèse sous la forme de microfiche/film, de reproduction sur papier ou sur format électronique.

L'auteur conserve la propriété du droit d'auteur qui protège cette thèse. Ni la thèse ni des extraits substantiels de celle-ci ne doivent être imprimés ou autrement reproduits sans son autorisation.

0-612-43510-5

Canada

UNIVERSITY OF SASKATCHEWAN

College of Graduate Studies and Research

SUMMARY OF DISSERTATION

Submitted in partial fulfillment

of the requirements for the

DEGREE OF DOCTOR OF PHILOSOPHY

by

DOUGLAS ARTHUR DEGENSTEIN

Department of Physics and Engineering Physics
University of Saskatchewan

Fall 1999

Examining Committee:

Dr. B.L.F. Daku

Dean's Designate, Chair
College of Graduate Studies and Research

Dr. T. Steele

Chairman of Advisory Committee, Department of
Physics and Engineering Physics

Dr. E.J. Llewellyn

Supervisor, Department of Physics and Engineering
Physics

Dr. A.H. Manson

Department of Physics and Engineering Physics

Dr. K.V. Paulson

Department of Physics and Engineering Physics

Dr. R.E. Pywell

Department of Physics and Engineering Physics

Dr. G. Sofko

Department of Physics and Engineering Physics

Dr. C.M. Sargent

Department of Mechanical Engineering

External Examiner:

Dr. R.W. Nicholls O.C., F.R.S.C.

Department of Physics and Astronomy

York University

4700 Keele Street

Toronto, Ontario

M3J 1P3



In presenting this thesis in partial fulfillment of the requirements for a Postgraduate degree from the University of Saskatchewan, the author agrees that the Libraries of this University may make it freely available for inspection. The author further agrees that permission for copying of this thesis in any manner, in whole or in part, for scholarly purposes may be granted by the professor who supervised this thesis work or, in his absence, by the Head of the Department or the Dean of the College in which this thesis work was done. It is understood that any copying or publication or use of this thesis or parts thereof for financial gain shall not be allowed without written approval from the author. It is also understood that due recognition shall be given to the author and to the University of Saskatchewan in any scholarly use which may be made of any material in this thesis.

Requests for permission to copy or to make other use of material in this thesis in whole or in part should be addressed to:

Head of the Department of Physics and Engineering Physics
116 Science Place
University of Saskatchewan
Saskatoon, Saskatchewan
Canada S7N 5E2

To Howard T. Katt and B. Jim Korn.

Abstract

It is extremely important for current modeling efforts that the two and three dimensional structure of the atmospheric constituents be known. It is equally important that these constituent profiles be known globally with high temporal resolution. Optical instruments onboard satellite platforms can provide measurements that make this knowledge possible.

This work presents a tomographic technique to use line of sight brightness measurements of the atmosphere made by an orbiting optical instrument to determine the two dimensional volume emission profile that has been remotely sensed. The basic technique was originally developed to deblur Fabry-Perot images and is closely related to the processes used in medical imaging. Although the tomographic technique was originally developed as a statistical analysis it is shown that it is the viewing geometry that is the fundamental characteristic with respect to algorithm performance.

Further, it is shown that the tomographic technique is capable of resolving structures in the atmospheric volume emission profile that are as small as 300 km along the satellite track with 1 km vertical resolution. It is found that this holds for a wide range of realistic operational conditions that include significant observational noise.

The Swedish based Odin spacecraft, scheduled for launch in early 2000, will fly in a sun-synchronous dusk-dawn orbit and will include the Canadian OSIRIS instrument. OSIRIS is able to measure the oxygen infrared atmospheric band simultaneously at multiple tangent altitudes at two separate wavelengths. These measurements are related to the mesospheric ozone profile and are ideal inputs for the tomographic technique. It is shown that there is no degradation in the algorithm performance even though the oxygen infrared atmospheric band emissions are absorbed.

Acknowledgments

I would like to begin my thanks with an acknowledgment of the Canadian Space Agency for their financial support of not only myself but the entire OSIRIS project. In particular I would like to express my gratitude to Mr. Victor Wehrle who was always there to help accommodate my requests. Without the support of the Canadian Space Agency this work as well as many other very worthwhile endeavours would not be possible. I would also like to thank the Natural Sciences and Engineering Research Council, Petro-Canada and the Institute of Space and Atmospheric Studies for other financial support I received throughout my life as a graduate student.

Many other individuals also deserve my thanks and appreciation. I would like to thank everybody at Routes Inc. who built OSIRIS and were available to answer any questions I had. I would also like to express my sincere appreciation to both Dr. Nick Lloyd and Dr. Dick Gattinger as they often provided a very receptive wall against which I was able to bounce ideas. Also I would like to say thank you to anyone else related with the Odin/OSIRIS project, or even those that were not, that helped me learn something along the way; even if that something was only small.

In closing I would like to give a very special thank you to Dr. Ted Llewellyn who provided me with many, many things but most importantly he gave me opportunity. He gave me the opportunity to learn from him and with him. He also provided for me the opportunity to be involved in a project through which I could learn from many other exceptional people. He provided all the resources that were required to complete this work. If I needed it he made it happen. Without these resources this work would not have been possible. Without Ted this work would not have been possible. Thank you very much Ted Llewellyn for all your time, effort and especially your concern.

3.3.2	The Model Satellite Attitude and Position Parameters	29
3.3.3	The Two Dimensional Discrete Volume Emission Grid	33
3.4	The Definition of a Modeled Observation	36
3.4.1	The Observed Brightness Along a Single Line of Sight.....	36
3.4.2	The Complete Modeled Observation	37
CHAPTER IV	SIMULATED OBSERVATION SETS	39
4.1	Introduction	39
4.2	The Model Imager Used for Test Data.....	39
4.3	The Model Spacecraft and Imaging Parameters Used for the Simulated Images. 42	
4.3.1	The Orbit and Orientation of the Spacecraft.....	42
4.3.2	The Duration of an Observation Set	44
4.3.3	The Temporal Resolution of an Observation Set.....	45
4.4	The Input Volume Emission Profiles for Test Purposes	46
4.5	The Resolution Parameters and Grid Cell Size	51
4.6	Sample Observation Sets.....	55
4.7	Observational Noise Values	57
4.8	The Image Set Parameters.....	58
CHAPTER V	THE TWO DIMENSIONAL ATMOSPHERIC TOMOGRAPHY TECHNIQUE	60
5.1	Introduction	60
5.2	The Current Technique.....	60
5.2.1	Background to the Current Technique.....	60
5.2.2	Changes to the Original Equations.....	63
5.2.3	Comparison of McDade and Llewellyn Approach to MLEM Technique.....	65
5.2.4	Algorithm Concept for Atmospheric Emissions Measured from a Satellite Platform.....	66
5.2.5	The Initial Estimate.....	68
5.2.6	Estimate of Retrieval Accuracy	70
5.3	Computational Considerations	71
5.3.1	The Termination Condition.....	71
5.3.2	Observation Estimate Precision	73
5.3.3	The Number of Observations in a Retrieval and Joining Retrievals.....	73
CHAPTER VI	THE SAMPLING GEOMETRY AND ITS EFFECT ON THE INVERSIONS	75
6.1	Introduction	75
6.2	Intersection Geometry	75
6.3	Sampling Density	77
6.4	The Three Regions of Interest.....	78
6.5	The Edge Effect.....	86

6.6 The Number of Images Used in a Single Inversion.....	94
CHAPTER VII THE OBSERVATION WEIGHTING FILTER	97
7.1 Introduction	97
7.2 Path Length Envelopes.....	98
7.2.1 The Shape of the Path Length Envelope.....	98
7.2.2 The Dependence of the Path Length Envelope on the Grid Cell Size	102
7.3 Weighting Function Envelopes	104
7.3.1 The Importance of the Weighting Function Envelope.....	104
7.3.2 The Effect of the Weighting Factor Exponent on the Weighting Function Envelopes	105
7.4 The Region of Influence of a Cell as a Result of the Observation Weighting Filter.....	106
7.4.1 The Basic Shape of the Observation Weighting Filter.....	107
7.4.2 The Averaging Kernel Formed by the Observation Weighting Filter.....	109
7.5 The Averaging Kernels in Each of the Three Central Regions.....	112
7.5.1 Region (C-1)	112
7.5.2 Region (C-2)	114
7.5.3 Region (C-3)	121
7.6 Convergence for Different Filter Shapes.....	128
7.6.1 Reasons for Superior Convergence with Higher Weighting Factor Exponents	129
7.6.2 Convergence Results for Different Weighting Factor Exponents.....	133
7.7 Examples of the Tomographic Recovery for Different Weighting Factor Exponents and Grid Cell Sizes	137
7.8 Concluding Remarks	141
CHAPTER VIII OPERATIONAL MODES	142
8.1 Introduction	142
8.2 Comparison of Observations, Sampling Densities and Results Using Three Different Nod Modes	142
8.3 Comparison of the Results for Three Different Imaging Rates in the Absence of Noise.....	148
8.4 Choice of Imaging Rate in the Presence of Noise.....	151
8.5 Concluding Remarks.....	155
CHAPTER IX SCALE SIZE EXPERIMENT	157
9.1 Introduction	157
9.2 Preliminary Comments on the Test Conditions	157
9.2.1 Noise and Error Types.....	157
9.2.2 Structure Types	158
9.3 The Simulated Observations Used in the Experiment.....	163

9.4 Inversion Results	170
9.4.1 Results With Noise-Free Input Data	170
9.4.2 Results With Absolute and Relative Noise Levels	183
9.4.2.1 Absolute Noise	184
9.4.2.2 Relative Noise	189
9.4.3 Results for Missing Images and Bad Pixels.....	197
9.5 Scale Size Experiment Conclusions	200
CHAPTER X OSIRIS ON ODIN	201
10.1 Introduction	201
10.2 Introduction to OSIRIS.....	202
10.3 Introduction to the Oxygen Infrared Atmospheric Band.....	204
10.4 Changes to the Tomographic Technique that are Required for Odin/OSIRIS..	206
10.4.1 Effects of the Optical Filters and Absorption of the Oxygen Infrared Atmospheric Band	206
10.4.2 Changes Required to the Tomographic Equations.....	209
10.4.3 Effect on the Observation Weighting Filters	210
10.5 The Need for the Absorption Correction.....	214
10.6 Tests for Emission Structure in the Presence of Absorption.....	216
10.6.1 Stare Mode Without Noise.....	216
10.6.1.1 Correct Atmospheric Weighting Parameters.....	217
10.6.1.2 Incorrect Atmospheric Weighting Parameters.....	219
10.6.2 10 to 60 km Nod Mode With Noise	223
10.6.2.1 Correct Atmospheric Weighting Parameters.....	224
10.6.2.2 Incorrect Atmospheric Weighting Parameters	226
10.7 Conclusions for OSIRIS on Odin	228
CHAPTER XI SUMMARY AND CONCLUSIONS	230
11.1 Summary of the Present Work	230
11.2 Recommendations for Future Work.....	232
APPENDIX A THE REQUIREMENT FOR TWO DIMENSIONAL TOMOGRAPHY	234
APPENDIX B CALCULATION OF MODEL OBSERVATION PARAMETERS	239
B.1 Location of Angle and Radial Distance at Points Along a Line of Sight.....	239
B.2 Intersection With Grid Cell Elements.....	241
B.3 Determination of the Parameters	243
APPENDIX C ESTIMATE OF ACCURACY	244

APPENDIX D	COMPUTATIONAL OPTIMIZATION TECHNIQUES	250
	D.1 The Path Length Precision Required to Model Observations	250
	D.2 Joining Inversions to Produce Arbitrarily Large Recovered Profiles.....	254
APPENDIX E	CALCULATION OF THE OXYGEN INFRARED ATMOSPHERIC BAND SPECTRUM	259
	E.1 Energy Levels for the States of the $O_2(a^1\Delta_g - X^3\Sigma_g^-)$ Spectra.....	259
	E.2 Selection Rules for the $O_2(a^1\Delta_g - X^3\Sigma_g^-)$ Spectra	261
	E.3 Intensities of the $O_2(a^1\Delta_g - X^3\Sigma_g^-)$ Emission and Absorption Spectra.....	261
	E.4 Line Shapes of the $O_2(a^1\Delta_g - X^3\Sigma_g^-)$ Spectra	263
	E.5 Algorithm for the $O_2(a^1\Delta_g - X^3\Sigma_g^-)$ Synthetic Spectra.....	265
APPENDIX F	ATTENUATION OF $O_2(a^1\Delta_g \rightarrow X^3\Sigma_g^-)$ THROUGH SELF ABSORPTION	267
	F.1 Calculation of Extinction Coefficients Due to the $O_2(a^1\Delta_g \leftarrow X^3\Sigma_g^-)$ Absorption Spectrum	267
	F.2 The Selection of Coefficients and Comparison With Measured Values.....	271
	F.3 Method Used to Calculate Absorption Correction Coefficients	273
REFERENCES		277

List of Figures

Figure 1.1: Description of the paths along which line integrals can be calculated.....	3
Figure 1.2: The first and last line integrals made from a satellite borne imager that do not intersect the solid earth.	4
Figure 1.3: The change in the angle between the boundary rays for line integrals for altitudes less than 115 km above the surface of the earth.....	5
Figure 2.1: Sample rays for the line integrals in the Abel transform for atmospheric measurements.....	8
Figure 2.2: The geometry for the line integrals in the Cormack transform. For each set of rays (red and black) the angle θ is constant and l is varied.	9
Figure 2.3: Definition of the ray for the line integral in the Radon transform.....	11
Figure 2.4: An incomplete set of line integral rays (6 in total) that characterize a given point (r, ϕ) . The line integrals are taken along the blue rays while the red lines, beginning at the origin, indicate the vectors l	12
Figure 2.5: Geometry used for x-ray transmission (CT) Tomography.....	17
Figure 2.6: Geometry used with PET reconstruction of positron decay inside a human patient.	18
Figure 3.1: The Ascending node coordinate system is defined by the orbit plane and an arbitrary ascending node equator crossing. This coordinate system is used to define the two dimensional volume emission grid.....	25
Figure 3.2: The Satellite coordinate system is defined by the orbit plane and the satellite position. This coordinate system is used to determine those regions of the volume emission grid that are sampled by the instrument.....	26
Figure 3.3: The Instrument coordinate system is defined by the optical axis of the lens and a preferred direction. This coordinate system is used to define the instantaneous field of view of the simple instrument.....	27
Figure 3.4: The Instrument coordinate system and three sample look direction unit vectors that make up the discrete field of view. Each vector can sample a different atmospheric source function.....	29
Figure 3.5: The rotation $-\omega$ about the \hat{z}_{inst} axis that is used to align the \hat{x}_{inst} axis with the local zenith at the tangent point of the optical axis.....	31
Figure 3.6: The rotation θ about the new \hat{y}'_{inst} axis that is used to align the \hat{x}'_{inst} axis with the \hat{x}_{sat} axis.....	32

Figure 3.7: The rotation $-\phi$ about the \hat{x}_{sat} axis that is used to align the \hat{z}'_{inst} axis with the \hat{z}_{sat} axis and the \hat{y}'_{inst} axis with the \hat{y}_{sat} axis.	32
Figure 3.8: The two dimensional volume emission grid geometry in the ascending node coordinate system. A sample line of sight, \underline{P}_{asc} , is shown.	34
Figure 4.1: A schematic representation (not to scale) of the one dimensional vertical imager used throughout this work. The imager consists of multiple single pixel instruments (identical to those discussed in Section 3.3.1) that all share the same coordinate system and objective lens.	40
Figure 4.2: The orbital variation of the attitude angle θ for two operational modes.	44
Figure 4.3: The basis vertical volume emission profile for each angular division in the two dimensional input grid. This is a typical daytime emission profile for the oxygen infrared atmospheric band.	47
Figure 4.4: The two dimensional volume emission grid, with no angular structure. The low frequency oscillation is due to the oblateness of the Earth. The colour scale represents the volume emission rate in kR/km.	47
Figure 4.5: A sample volume emission grid derived using equation 4.5 and a value of λ equal to 30° . This grid which covers only a partial orbit corresponds to 700 images taken once every two seconds.	48
Figure 4.6: A sample two dimensional volume emission grid with 10 km vertical structure and 400 km horizontal structure derived from equation 4.6. The grid covers only a partial orbit and corresponds to 700 images taken once every two seconds.	49
Figure 4.7: An angular cross section taken from the centre of the grid shown in Figure 4.6. This plot clearly illustrates the vertical modulation of the basis vertical profile shown in Figure 4.3.	50
Figure 4.8: A radial shell cross section taken from the centre of the grid shown in Figure 4.6. This plot clearly illustrates the angular modulation imposed by equation 4.6.	50
Figure 4.9: Low and high resolution observation sets constructed using an unstructured volume emission grid similar to that shown in Figure 4.4. The colour scale represents the observed brightness in kR.	52
Figure 4.10: Pixel cross sections for the two dimensional plots seen in Figure 4.9. This plot illustrates the differences between the high and low resolution observations.	53
Figure 4.11: Progression of a line of sight that is tangent at 40.5 km above the surface of the Earth. The central altitude of the geocentric shells is marked on the figure.	54
Figure 4.12: Comparison of the pixel cross section for moderate and high resolution observations.	55

Figure 4.13: Three sample observation sets for different structure types and attitude modes. The top plot was generated using emissions with a four degree wave structure while the lower plots used emissions with thirty degree angular structure.....	57
Figure 4.14: A sample observation set with a uniform 20% probability of having each image missing and Gaussian random noise, standard deviation of 2 MR...	58
Figure 5.1: The distribution of the 391.4 nm emission obtained from a tomographic inversion of observations made in a rocket tomography experiment (McDade et al., 1991).....	62
Figure 5.2: The inputs and outputs of the tomographic algorithm used to retrieve the two dimensional volume emission profiles from the brightness observations made from a satellite platform.	67
Figure 5.3: A block and data flow diagram for the satellite tomography algorithm.....	68
Figure 5.4: An input volume emission profile, the initial estimate of the profile given by equation 5.16, and the final estimate of the profile after 30 iterations.....	70
Figure 5.5: The error distribution histogram widths for both the recovered volume emissions and the estimate of the observations. This plot is typical of all good recoveries where there is effectively no decrease in the histogram width after 30 iterations.....	72
Figure 5.6: An input observation set and the estimate of the observation set based on the recovery grid after 30 iterations.	72
Figure 6.1: The three standard intersection types for lines of sight that sample a grid cell. These are: 1) Angle-Angle, 2) Shell-Shell, tangent before the cell and 3) Shell-Shell, tangent after the cell.	76
Figure 6.2: The five other intersection types for lines of sight that sample a grid cell...	77
Figure 6.3: The number of times that each grid cell, 0.2° by 1.0 km, is sampled by 700 images taken once every two seconds. The superimposed lines of sight are for pixels 10, 50 and 80 for each of the images 0, 349 and 699.....	77
Figure 6.4: A radial shell cross section from the plot shown in Figure 6.3. This cross section illustrates the flat central region, where almost constant sampling occurs, and the left and right regions where there are large changes in the sampling density.....	78
Figure 6.5: Observations that intersect the grid cell at AngleNumber 92 and ShellNumber 49 in the (L-1) region (a) and the other grid cells that these observations sample (b).....	80
Figure 6.6: Observations that intersect the grid cell at AngleNumber 122 and ShellNumber 49 in the (L-2) region (a) and the other grid cells that these observations sample (b).....	81

Figure 6.7: Observations that intersect the grid cell at AngleNumber 336 and ShellNumber 10 in the (C-1) region (a) and the other grid cells that these observations sample (b).....	82
Figure 6.8: Observations that intersect the grid cell at AngleNumber 336 and ShellNumber 49 in the (C-2) region (a) and the other grid cells that these observations sample (b).....	83
Figure 6.9: Observations that intersect the grid cell at AngleNumber 336 and ShellNumber 30 in the (C-3) region (a) and the other grid cells that these observations sample (b).....	84
Figure 6.10: Observations that intersect the grid cell at AngleNumber 540 and ShellNumber 49 in the (R-2) region (a) and the other grid cells that these observations sample (b).....	85
Figure 6.11: Observations that intersect the grid cell at AngleNumber 580 and ShellNumber 49 in the (R-1) region (a) and the other grid cells that these observations sample (b).....	86
Figure 6.12: Input and recovered volume emission profiles that illustrate the edge effect in both the (L) and (R) regions.....	87
Figure 6.13: The cells that are sampled by the first observation that intersects the top leftmost cell (72,97) of the volume emission grid. This observation and the cells that it samples define the left hand envelope of the edge effect.	88
Figure 6.14: The other cells that are sampled by observations that intersect grid cell (81,71) which is along the first line of sight shown in Figure 6.13.	89
Figure 6.15: The other cells that are sampled by observations that intersect grid cell (91,46) which is further along the first line of sight shown in Figure 6.13. These are approximately the same set of cells as those shown Figures 6.13 and 6.14.	89
Figure 6.16: Other cells that are sampled by observations that intersect the cell (141,21) at the tangent point of the first observation. These are approximately the same set of cells as those shown in Figures 6.13, 6.14 and 6.15.....	90
Figure 6.17: A far broader range, compared to those in Figures 6.14, 6.15 and 6.16, of cells are intersected by observations on the far side of the tangent point of the first observation.....	91
Figure 6.18: An even broader range of cells is sampled by observations that intersect a cell further along the first observation path than the cell shown in Figure 6.17.	91
Figure 6.19: A complete range of cells is sampled by observations that intersect a cell near the end of the first observation path.	92
Figure 6.20: The cells sampled by observations that sample a cell (102,49) in the transition region where no intersections occur before the tangent point of any line of sight.....	92

Figure 6.21: Cells intersected by observations that sample cell (132,46) in the transition region where the intersections are of all three types.....	93
Figure 6.22: Five recovered volume emission radial shell cross sections together with the sampling densities at each of the relevant grid cells. The recoveries are for observation sets that include different numbers of images and imaging rates.	96
Figure 7.1: The path length through different grid cells in the absence of angular boundaries. These paths include type 2 and 3 intercepts where the tangent altitude is always below the shell of interest.....	99
Figure 7.2: Intercept path lengths through a 0.2° by 1.0 km cell with minimum and maximum radii of 6429 and 6430 km. All lines of sight that are tangent above 6425 km and intercept the cell do so in an Angle-Angle manner and so are constrained to the maximum length.	100
Figure 7.3: Path length envelope if only Shell-Shell and Angle-Angle intercepts of a grid cell are allowed. All other types of intercept for a line of sight that is tangent at the given altitude are shorter.	101
Figure 7.4: The path length envelopes for cell sizes of 0.1° , 0.2° and 0.6° . The envelopes for cells with larger angular sizes have a smaller range of tangent altitudes with Angle-Angle type intercepts.....	103
Figure 7.5: Observation weighting filter envelopes for different cell sizes and different weighting factor exponents.....	106
Figure 7.6: Three observation weighting filters for lines of sight that sample 1 km by 0.2° grid cells in the (C-1), (C-2) and (C-3) regions.	108
Figure 7.7: The averaging kernels for the observation weighting filters shown in Figure 7.6 for cells in regions (C-1), (C-2) and (C-3).....	111
Figure 7.8: The weighting filter functions for a cell in the (C-1) region, the angular dimension of the grid cell is 0.2° . The filter function is essentially independent of the weighting factor exponent.	113
Figure 7.9: The weighting filter functions for a cell in the (C-2) region that correspond to a grid cell size of 0.1° and $m = 1, 3$ and 5	115
Figure 7.10: The averaging kernels for a grid cell in the (C-2) region, the cell size is 0.1° and $m = 1, 3$ and 5 . These averaging kernels are almost independent of the weighting factor exponent.	116
Figure 7.11: The weighting filter functions, in the (C-2) region, that correspond to a grid cell size of 0.2° and $m = 1, 3$ and 5	117
Figure 7.12: The averaging kernels for a grid cell in the (C-2) region, the cell size is 0.2° and $m = 1, 3$ and 5 . These averaging kernels tighten as the weighting factor exponent is increased.	118

Figure 7.13: The weighting filter functions, in the (C-2) region, that correspond to a grid cell size of 0.6° and $m = 1, 3$ and 5 . There are considerable differences as the weighting factor exponent is increased.	119
Figure 7.14: The averaging kernels for a grid cell in the (C-2) region, the cell size is 0.6° and $m = 1, 3$ and 5 . These averaging kernels tighten significantly as the weighting factor exponent is increased.	120
Figure 7.15: The weighting filter functions, in the (C-3) region, that correspond to a grid cell size of 0.1° and $m = 1, 3$ and 5 . As the weighting factor exponent is increased there is a noticeable change in the weighting filter function.....	122
Figure 7.16: The averaging kernels for a grid cell in the (C-3) region, the cell size is 0.1° and $m = 1, 3$ and 5 . These averaging kernels tighten as the weighting factor exponent is increased.	123
Figure 7.17: The weighting filter functions, in the (C-3) region, that correspond to a grid cell size of 0.2° and $m = 1, 3$ and 5 . As the weighting factor exponent increases there is a significant change in shape.	124
Figure 7.18: The averaging kernels for a grid cell in the (C-3) region, the cell size is 0.2° and $m = 1, 3$ and 5 . These averaging kernels significantly tighten as the weighting factor exponent is increased.	125
Figure 7.19: The weighting filter functions, in the (C-3) region, that correspond to a grid cell size of 0.6° and $m = 1, 3$ and 5 . There are very severe differences between the plots for different values of the weighting factor exponent.	126
Figure 7.20: The averaging kernels for a grid cell in the (C-3) region, the cell size is 0.6° and $m = 1, 3$ and 5 . These averaging kernels severely tighten as the weighting factor exponent increases.	128
Figure 7.21: A typical vertical volume emission profile.	128
Figure 7.22: Typical line of sight brightnesses for observations that sample cells in the three grid regions. The discontinuities are due to discrete sampling.	129
Figure 7.23: The path lengths through the entire grid for observations that sample cells in each of the (C-1), (C-2) and (C-3) regions. Apparent discontinuities in these path lengths are due to the discrete nature of the grid.	131
Figure 7.24: The initial estimate of the volume emission rate contained within cells in the (C-1), (C-2) and (C-3) regions. These initial estimates are based on equation 7.6 and the data in Figures 7.22 and 7.23.....	132
Figure 7.25: Angular cross sections for the calculated volume emission rates (after the first iteration) and the actual input values for six different weighting factor exponents.	134
Figure 7.26: Angular cross sections for the calculated volume emission rates (after the second iteration) and the actual input values for six different weighting factor exponents.	134

Figure 7.27: Angular cross sections for the calculated volume emission rates (after the third iteration) and the actual input values for six different weighting factor exponents.	135
Figure 7.28: Radial shell cross sections for the calculated volume emission rates (after the first iteration) and the actual input values for six different weighting factor exponents.	136
Figure 7.29: Radial shell cross sections for the calculated volume emission rates (after the second iteration) and the actual input values for six different weighting factor exponents.	136
Figure 7.30: Radial shell cross sections for the calculated volume emission rates (after the third iteration) and the actual input values for six different weighting factor exponents.	137
Figure 7.31: The two dimensional volume emission profiles that correspond to the input grid (a) and two recoveries (b and c). These grids were chosen to illustrate the effect of using the optimal parameters as well as an ill-conditioned set.	138
Figure 7.32: The error distribution and quadratic fit for the well recovered profile shown in Figure 7.31. The peak is not offset and the distribution width is 3.61%.	139
Figure 7.33: Radial shell cross sections for optimal and non-optimal choices of the weighting filter functions.	140
Figure 8.1: Three observation sets that correspond to the different nod modes. These are the stare, nod from 10 to 60 km and the nod from 10 to 110 km. The colour scale represents the limb brightness in kR.	144
Figure 8.2: The sampling densities for the observations shown in Figure 8.1. The colour scale represents the number of times that each grid cell is sampled.	145
Figure 8.3: Sample recoveries of the input volume emission profile shown in the top panel (a), for the three different nod modes: stare (b), nod from 10 to 60 km (c) and nod from 10 to 110 km (d). The colour scale is the volume emission rate (kR/km).	147
Figure 8.4: The input and recovered grids for one of the three inversions considered in the imaging rate study. Only a single recovery is shown as the grids are visually identical for all three imaging rates. The colour scale represents the volume emission rate in kR/km	149
Figure 8.5: The error histograms and quadratic fits for the three inversions made for the different imaging rates.	150
Figure 8.6: Two observation sets in the absence and presence of noise. The colour scale is the measured pixel brightness in kR.	152
Figure 8.7: Cross sections of the observation data shown in Figure 8.6.	153

Figure 8.8: The input and the best and worst case retrievals for the different noise values and imaging rates.	154
Figure 8.9: The error histograms for the best (a) and worst (b) case retrievals for the fifteen test conditions.	155
Figure 8.10: Error histogram widths for three imaging rates and five noise levels.....	156
Figure 9.1: Input two dimensional volume emission profiles for various scale size structures. The low frequency modulation is due to the Earth's oblateness.	160
Figure 9.2: Radial and angular cross sections for the two dimensional input volume emission grids shown in Figure 9.1. These plots illustrate the structure imposed on the basic airglow profile.	163
Figure 9.3: Simulated observation sets (with no noise) generated from selected structured input volume emission grids shown in Figure 9.1.	164
Figure 9.4: Cross sections for a single pixel (number 50) taken from the selected observation sets shown in Figure 9.3.	165
Figure 9.5: The same pixel cross sections as those shown in Figure 9.4 but with an absolute random Gaussian noise (standard deviation 2 MR) imposed on the observations.....	166
Figure 9.6: Fourier coefficients for the observations at pixel number 50 for different structures and a 2 MR Gaussian (absolute) random noise level.	167
Figure 9.7: Noise free observation sets generated for the 10 to 60 km nod mode.....	168
Figure 9.8: Observation sets that include 2 MR absolute Gaussian random noise and either missing images (a) or missing pixels (b). The probability of data loss is 0.1 in both cases.	169
Figure 9.9: Recovered volume emission grids for the different structures that were tested. These two dimensional plots include only forty degrees of the grid in order to emphasize the structure retrieval.	175
Figure 9.10: A series of radial shell cross sections for different imaging rates, nod modes and structures.	181
Figure 9.11: A series of angular cross sections for the different scale size structures. The stare mode and a fixed 0.5 Hz imaging rate was used for each of these retrievals.....	183
Figure 9.12: The input and retrieved volume emission grids for the three degree structure with different operational modes. The observations contain random Gaussian noise with a standard deviation of 10 MR.....	185
Figure 9.13: Selected radial shell cross sections from the recovery grids shown in Figure 9.12.	186
Figure 9.14: Selected radial shell cross sections from the recovery grids shown in Figure 9.12 that illustrate the effects of a simple box car filter.	187

Figure 9.15: Error histogram widths for results obtained with different wave structures and different observational modes for different absolute noise levels.	189
Figure 9.16: Retrieval of the three degree structure for different signal to noise levels.	191
Figure 9.17: Selected radial shell cross sections for the recovery grids shown in Figure 9.16.	193
Figure 9.18: The filtered recoveries of the three degree structure for different signal to noise levels.....	194
Figure 9.19: Selected radial shell cross sections from the recovery grids shown in Figure 9.18.	195
Figure 9.20: Error histogram widths for the results obtained with three different wave structures and three observational modes for five different signal to noise levels.	196
Figure 9.21: Selected radial shell cross sections from retrievals made with missing images and pixels.	197
Figure 10.1: A representation of the Odin spacecraft in its sun-synchronous orbit.....	202
Figure 10.2: The OSIRIS instrument. The upper module is the electronics unit while the lower module is the optical unit. The three entrance apertures for the InfraRed Imaging System are in the bottom left corner.....	203
Figure 10.3: The oxygen infrared atmospheric band emission spectrum as emitted at 40 km (a) and the same spectrum as seen by a satellite borne instrument looking along a 40 km tangent altitude line of sight (b).	205
Figure 10.4: The QQ branch line, with $J' = J'' = 3$, for the two oxygen infrared atmospheric band spectra shown in Figure 10.3.	205
Figure 10.5: The unattenuated and the absorbed spectra (Figure 10.3) with the 1.266 μm filter superimposed.	207
Figure 10.6: The band capture fractions for different lines of sight tangent at various radial distances in the two dimensional recovery grid.	209
Figure 10.7: The averaging kernels for absorbed emissions at shell altitudes of 85 km (a), 65 km (b), 45 km (c) and 25 km (d) above the minimum. The weighting factor exponent m is equal to 5.	212
Figure 10.8: The observation weighting filters (for the absorbed emissions) at shell altitudes 85 km (a), 65 km (b), 45 km (c) and 25 km (d) above the minimum shell altitude.	213
Figure 10.9: The effect of absorption on limb images generated with identical volume emission profiles.	215
Figure 10.10: The tomographic retrieval with no absorption correction.....	216

Figure 10.11: Input and recovered volume emission grids for the correct absorption weighting factors.....	217
Figure 10.12: Cross sections of the input and recovered oxygen infrared atmospheric band grids for the correct absorption weighting factors.....	218
Figure 10.13: Error histogram for the recovery with the correct absorption weighting factors.....	219
Figure 10.14: The temperature profiles and the percentage differences between the density profiles used to study the effect of profile knowledge on the tomographic retrieval.	220
Figure 10.15: Input and recovered volume emission grids for incorrect absorption weighting factors.....	221
Figure 10.16: Cross sections of the input and recovered volume emission grids for the incorrect absorption weighting factors.....	222
Figure 10.17: Error histogram for the recovery with incorrect absorption weighting factors.....	223
Figure 10.18: Cross sections of the input and recovered volume emission grids with the correct absorption weighting factors.....	225
Figure 10.19: Error histogram for the recovery with the correct absorption weighting factors.....	226
Figure 10.20: Cross sections of the input and recovered volume emission grids with the incorrect absorption weighting factors for the 10 to 60 km nod mode.	227
Figure 10.21: Error histogram for the recovery with the incorrect absorption weighting factors.....	228
Figure A.1: A line of sight (ray) drawn on a volume emission grid that contains structure in the horizontal, or angular, dimension. The line of sight appears curved due to the rectangular representation of the radial volume emission grid.	235
Figure A.2: The volume emission rate along the line of sight shown in Figure A.1. The volume emission is not symmetric as there is no horizontal homogeneity.....	235
Figure A.3: An input two dimensional volume emission profile and two retrieved profiles. The first retrieval (b) used a series of one dimensional retrievals to form the two dimensional profile while the other retrieval (c) used the tomographic technique.....	237
Figure A.4: Radial cross sections for the two dimensional plots shown in Figure A.3.....	238
Figure C.1: A moderately structured input volume emission profile and two tomographic recoveries for simulated observations that were generated without and with measurement noise.....	245

Figure C.2: Error distribution histograms and quadratic fits for the two recoveries shown in Figure C.1. The distribution for the recovery with noisy data is wider than that for the noiseless data.	247
Figure C.3: A highly structured input volume emission profile and the tomographic recovery in the absence of observational noise.	248
Figure C.4: Radial shell cross sections of the two volume emission grids shown in Figure C.3. This plot illustrates the inability of the tomographic recovery to fully resolve the small scale structures.	249
Figure C.5: Error distribution histogram and quadratic fit for the recovery shown in Figure C.3. The errors are not random and suggest a failure of the technique.	249
Figure D.1: Three error distribution and fit plots that illustrate the percentage errors associated with the recovery of an unstructured volume emission profile. Each plot is for a different path length precision.	252
Figure D.2: Recovery for an entire orbit using 700 images per inversion and joining the individual recoveries.	255
Figure D.3: Three cross sections for different magnitudes of the volume emission that illustrate no discontinuity at 98.1° where the join occurred.	257
Figure E.1: The nine branches allowed in the $O_2(a^1\Delta_g - X^3\Sigma_g^-)$ spectrum.	261
Figure E.2: Emission and absorption spectra for a 300 K rotational temperature. These two spectra are visually identical.	266
Figure F.1: Histogram representation of a line shape. Each bar represents a region of constant emission or absorption.	268
Figure F.2: Comparison between the absorbance values used throughout this thesis with those measured by Lafferty et al. [1998]. The first two plots are models while the third is an actual measurement.	273
Figure F.3: The geometry used to calculate the remaining band signal from any position along any given line of sight.	274
Figure F.4: $O_2(a^1\Delta_g \rightarrow X^3\Sigma_g^-)$ emission spectrum emitted at 40 km and the same spectrum as seen by a satellite borne instrument looking along a 40 km tangent altitude line of sight.	275
Figure F.5: Remaining band signal from the second plot of Figure F.4 with the Odin/OSIRIS 1.266 μm filter superimposed upon it.	276

List of Tables

Table 4.1: The image set parameters used for various test conditions in this thesis.	59
Table 8.1: The error histogram width and peak offset parameters for the three retrievals made for data generated at different imaging rates. The computing time for each retrieval is also listed.....	150
Table 9.1: Error histogram halfwidths for the retrieval of different wave structures with different observational modes and six different missing image probabilities.....	198
Table 9.2: Error histogram halfwidths for the retrieval of different wave structures with different observational modes and seven different bad pixel probabilities.....	199
Table D.1: Error fit widths and offsets together with the calculation times and storage requirements for different path length precisions and different structure scale size.....	253
Table D.2: Inversion times and accuracies for different numbers of images and imaging rates.	258
Table E.1: Line strengths for $a^1\Delta_g - X^3\Sigma_g^-$ transitions.....	262

Glossary of Terms

α	The angle along the satellite orbit from an arbitrary ascending node crossing in the ascending node coordinate system.
α_{ij}	The band capture fraction for an absorbed emission that originates at cell j and measured in observation i .
β	The look direction angle for a line of sight in the instrument coordinate system.
β_{ij}	Observation weighting filter value for observation i that intersects cell j .
$\delta(\beta)$	The sensitivity of the measurement with respect to the look direction β .
ω, ϕ, θ	Look direction rotation angles.
γ	Angle of any point in the volume emission grid. This angle is different for each of the sat and asc coordinate systems.
$\underline{P}_{inst}, \underline{P}_{asc}, \underline{P}_{sat}$	Look direction unit vectors.
$O_{i_{ev}}^{(n-1)}$	The previous estimate of observation i based on the iterative solution in the volume emission recovery grid.
<i>AngleNumber</i>	The index of any angle in the discrete two dimensional volume emission grid.
ART	Algebraic Reconstruction Technique.
asc	An abbreviation for the ascending node coordinate system.
CT	Computed Tomography.
<i>DeltaAngle</i>	Angular grid cell size.
<i>DeltaShell</i>	Radial grid cell size.
ECT	Emission Computed Tomography.
edge effect	The error in the retrieval at the angular edges of the recovery grid.
i	Index of a particular observation.
imager	The instrument that makes the measurements used in the tomographic recovery.
image set	A group of images that are included in an observation set.

imaging rate	The time between images in an image set.
inst	An abbreviation for the instrument coordinate system.
<i>j</i>	Index of a particular cell in the volume emission grid.
<i>k</i>	Index in the instantaneous field of view.
<i>l</i>	Index in the non-stationary field of view.
<i>m</i>	The weighting factor exponent.
MART	Multiplicative Algebraic Reconstruction Technique.
ML	Maximum Likelihood.
MLEM	Maximum Likelihood Expectation Maximization.
MP	Maximum Probability.
noise	Any deviation from a set of measurements made under ideal conditions.
<i>NumFOV</i>	The number of times the instantaneous field of view is subdivided.
<i>NumImages</i>	The number of images that are included in an observation set.
<i>NumObs</i>	The number of measurements in an observation set.
<i>NumPixels</i>	The number of pixels in the imager. This is also the same as the number of simultaneous measurements.
<i>NumTimes</i>	The number of times the non-stationary field of view is subdivided.
observation	A single measurement.
observation set	A group of measurements.
Odin	A Swedish satellite scheduled for launch in early 2000.
OSIRIS	(Optical Spectrograph and InfraRed Imaging System) A Canadian instrument that will fly on Odin.
PET	Positron Emission Tomography.
<i>r</i>	A radial distance in the volume emission grid.
sampling density	The number of times a grid cell is sampled in an observation set.
sat	An abbreviation for the satellite coordinate system.
<i>ShellMax</i>	The maximum radial distance in the volume emission grid.
<i>ShellMin</i>	The minimum radial distance in the volume emission grid.
<i>ShellNumber</i>	The index of any radial distance in the discrete two dimensional volume emission grid.
SPECT	Single Photon Emission Computed Tomography.

CHAPTER I

INTRODUCTION

1.1 The Requirement for Atmospheric Tomography

Before the advent of rocket and satellite investigations of the upper atmosphere it was generally assumed that the constituent profiles depended only on altitude above the surface of the earth, *i.e.* the upper atmosphere was homogenous with respect to altitude. However, it was recognized from both clouds and weather patterns that this homogeneity could not extend to the troposphere. The early rocket observations showed that the radial homogeneity assumption was not applicable to the upper atmosphere, although it was believed that the atmosphere could still be localized with respect to latitude. However, as the atmospheric constituent profiles depend on the solar input there will necessarily be variations with latitude. Thus, even the general background knowledge of the atmosphere requires a full three dimensional measurement capability. Other atmospheric phenomena such as gravity waves, aurora and tidal motions all result in two and three dimensional structures that may have both large and small scale sizes.

Satellites provide the opportunity to make global atmospheric measurements over a total time scale that is short compared to that for a network of ground based observatories. However, satellites cannot fly for an extended period of time at altitudes below 300 km so that even measurements in the lower thermosphere must be made through remote sensing. Passive remote sensing implies that information is collected along paths through the atmosphere. These paths, although confined to a plane, cover a two dimensional space. If two and three dimensional information is to be retrieved from these line of sight measurements then it is necessary to develop analysis techniques that do not assume horizontal homogeneity, *i.e.* the atmosphere has structure in dimensions other than the vertical (see Appendix A). Tomographic methods, where tomography is the representation of a three dimensional object by means of its two dimensional cross sections, are such techniques and have been extensively applied in the field of medical imaging but are still in their infancy for atmospheric investigations. The present work is

an attempt to develop a tomographic technique that is appropriate for studying atmospheric structures that can be measured through natural atmospheric emissions, *i.e.* the airglow, the aurora and the Rayleigh scattered sunlight.

1.2 Tomography from Odin/OSIRIS

The Odin spacecraft, scheduled for launch in early 2000, will provide a unique opportunity to make integrated atmospheric emission rate measurements that can be used as inputs for a two dimensional tomographic recovery of atmospheric structure. The OSIRIS instrument on Odin includes three separate infrared imagers that will make line of sight measurements, simultaneously at multiple tangent altitudes, of the oxygen infrared atmospheric band, Rayleigh scattered sunlight and the Meinel OH bands. The purpose of the work in this thesis is to develop a procedure that can recover two dimensional structure in the measured atmospheric emission.

Each optical measurement made from a satellite platform is essentially an integral of the volume emission rate along the line of sight. Measurements of this type are fundamental inputs to tomographic recovery techniques that determine the two dimensional distribution of a field that is sampled by line integrals. The developed technique involves the discretization of the line of sight integrals, and the allocation of volume emission rates to points in a discrete two dimensional grid that is representative of the atmosphere. The result is a discrete solution that is consistent with the measurements. The technique that is investigated in this thesis is an iterative Multiplicative Algebraic Reconstruction Technique (MART). This technique is one that is derived from a Maximum Probability (MP) technique and is similar to the Maximum Likelihood Expectation Maximization (MLEM) technique that is used in Emission Computed Tomography (ECT) in medical imaging.

1.3 The General Problem

Most two dimensional tomographic problems can be reduced to the solution of a field $f(x, y)$ from the knowledge of a set of line integrals through that field. A sample field

where $f(x, y) = 0$ outside the shaded region, and is some other value within the shaded region, is shown in Figure 1.1. The rays L_1 , L_2 , L_3 and L_4 constitute a set of discrete paths, through the given point in the top left corner, along which line integrals of the field can be taken. If the line integrals can be determined at every point within the field, which is continuous and square integrable, and the angular separation between the rays approaches zero then these line integrals reduce to the Radon transform. The inverse transform is the solution for the continuous field. However, if the line integrals are taken at discrete angular intervals (as in Figure 1.1) by a measuring instrument the solution for the field by means of the inverse Radon transform becomes difficult, although not impossible. These difficulties are due to the discrete nature of both the sampling and the recovery grid as well as noise due to the measuring instrument and the statistical nature of the field.

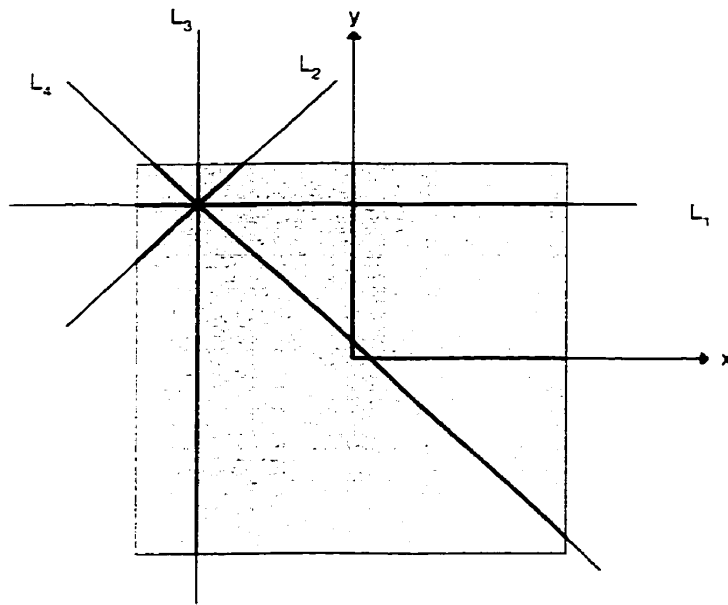


Figure 1.1: Description of the paths along which line integrals can be calculated.

Various techniques have been developed in medical imaging and geophysics to recover the field $f(x, y)$ from the measured line integrals. These techniques include discretization of the inverse Radon Transform and Algebraic Reconstruction Techniques (ARTs). The former is primarily used when the signal to noise levels are quite high and

Multiplicative ARTs (MARTs) are usually employed when the signal to noise levels are low. The techniques used in the medical imaging field rely on the fact that all of the line integrals are available over 180° . Although the measured line integrals are not continuous in angle, and are not available for every point, the set of integrals does cover the entire space.

1.4 The Particular Problem

The application of tomographic retrieval techniques for satellite measurements of the atmosphere has limitations that are not experienced with most ground based geometries, especially those in the medical imaging field; measurements of a patient may be made along any convenient line of sight. The geometrical constraints that are imposed by a satellite borne limb-looking imager are illustrated in Figure 1.2. The line integrals are the measurements of the volume emission profile along the shown rays. The solid nature of the Earth, and its associated albedo, limits the look directions that intersect it. Thus line integrals over the required 180° are not available. Three possible lines of sight that can provide line integrals are shown in Figure 1.2, the rays L_0 and L_r are tangent to the solid earth and represent boundary rays.

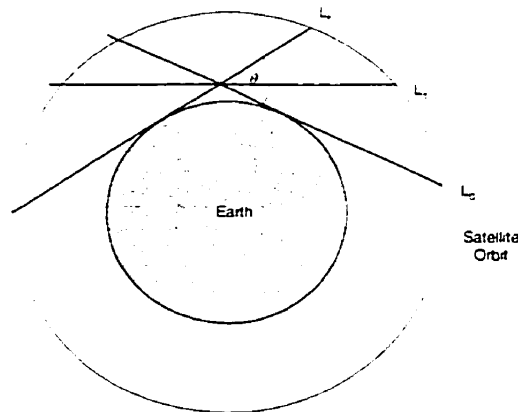


Figure 1.2: The first and last line integrals made from a satellite borne imager that do not intersect the solid earth.

The angle θ between the boundary rays (Figure 1.2) is a function of the altitude above the surface of the Earth. The angle between these boundary rays for points that are

below an altitude of 115 km are shown in Figure 1.3. As these angles are all much less than 180° (the required value for an accurate inverse Radon transform) a different technique is required to recover the two dimensional volume emission field contained within the earth's atmosphere.

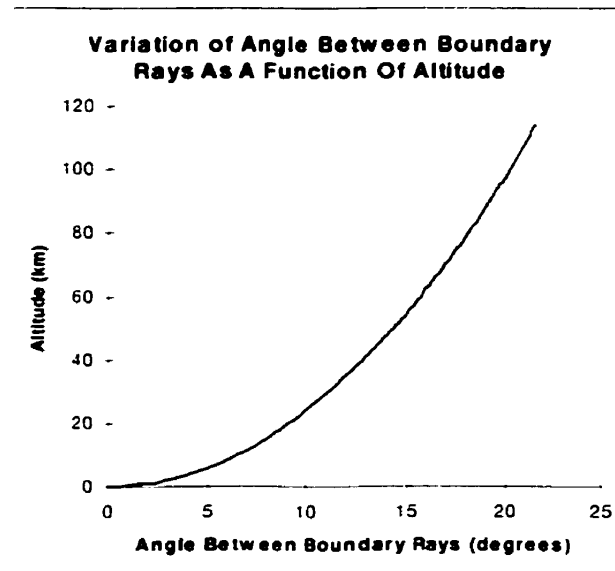


Figure 1.3: *The change in the angle between the boundary rays for line integrals for altitudes less than 115 km above the surface of the earth.*

Previous work by Lloyd and Llewellyn [1989] and McDade and Llewellyn [1991a, 1991b, 1993] provides a basis for such a two dimensional tomographic technique. The technique, called the Maximum Probability (MP) technique, was originally developed to deblur Fabry-Perot images and closely resembles the Maximum Likelihood Expectation Maximization (MLEM) Multiplicative Algebraic Reconstruction Technique (MART) that is currently used in Emission Computed Tomography (ECT) in medical imaging. The MLEM-MART is commonly used in those situations where the signal to noise associated with the line integral measurements is poor.

1.5 Outline

An extensive background to the tomographic retrievals that have been attempted in both geophysics and medical imaging is presented in Chapter 2. This chapter also highlights

the importance of the line integral (measurement geometry) to the chosen technique. The details of a single line integral measurement of the airglow by a satellite borne optical instrument are given in Chapter 3. A complete discussion of the measurements that are applicable for the developed tomographic technique is given in Chapter 4. The development of the current tomographic technique, and its similarity with the techniques used in other fields, is discussed in Chapter 5.

The geometry constraints that are imposed by the satellite borne imaging system are presented in Chapters 6 and 7. The particular geometry for limb observations is discussed in Chapter 6 and the optimization of the developed tomographic technique to use the satellite geometry in such a way that it yields solutions that converge both rapidly and accurately is presented in Chapter 7. The test procedures and the results of the performance tests for the current algorithm are given in Chapters 8, 9 and 10. These tests include: the effects of image rate and satellite nod (Chapter 8); the resolution of horizontal structure (Chapter 9); the modifications to the algorithm that are required to recover the oxygen infrared atmospheric band emission at $1.27\mu\text{m}$ that is attenuated through self absorption along the line of sight (Chapter 10). These modifications are especially important as Odin/OSIRIS is expected to make measurements as early as February 2000.

Finally a summary of the results and findings of the present work and some recommendations for future work are presented in Chapter 11. It is concluded that the developed technique is an accurate robust method that will permit the recovery of two dimensional structure in the atmospheric emissions measured from a satellite borne instrument. This technique, and the Odin/OSIRIS instrument, will recover both small and large scale structure in the oxygen infrared atmospheric band and so determine the two dimensional ozone profile above 40 km altitude.

CHAPTER II

AN INTRODUCTION TO TOMOGRAPHIC TECHNIQUES

2.1 Introduction

As noted previously tomography (from the Greek *tomos*, to slice) is the representation of a three dimensional object by means of its two dimensional cross sections. For most tomographic applications this requires the solution of a system of equations that consist of many line integrals that are represented in a discrete fashion. Tomographic techniques are not new, they have been used for many years in the field of medical imaging, although their application to the atmosphere is in its infancy. Techniques that have been employed are the Radon and Cormack transform methods, Algebraic Reconstruction Techniques (ARTs), Multiplicative Algebraic Reconstruction Techniques (MARTs) and the Maximum Likelihood Expectation Maximization Technique (MLEM); this last is just a special form of MART. The preferred method is very dependent upon the problem and no one method has been shown to be generally superior to any other. There has been some work on the tomographic recovery of geophysical quantities from measurements made from rocket and satellite platforms and it is this work that is the basis for the work presented in this thesis.

2.2 Some Tomographic Techniques

In general tomographic techniques have an associated geometry and mathematics that is quite involved. The background to four of the existing techniques is presented below.

2.2.1 The Abel Transform

The Abel transform is a technique that is used to recover a radially symmetric field from line integrals through the field. This transform method does not provide a true two dimensional recovery as it requires radial symmetry; this implies that the field is only a function of r , the radial distance. The line integrals are defined by paths that are tangent at distances r_0 from the origin according to equation 2.1.

$$F(r_0) = 2 \int_{r_0}^{\infty} \frac{f(r) dr}{(r^2 - r_0^2)^{\frac{1}{2}}} \quad [2.1]$$

A sample set of rays for the line integrals in an Abel transform is shown in Figure 2.1. The complete Abel transform requires that the tangent distance between successive rays be infinitesimally small. If this condition is met then the inverse Abel transform, given by equation 2.2,

$$f(r) = -\frac{1}{\pi} \int_r^{\infty} \frac{\left[\frac{dF(r_0)}{dr_0} \right] dr_0}{(r_0^2 - r^2)^{\frac{1}{2}}} \quad [2.2]$$

only requires the derivative of the Abel transform and an integral from the required radial distance out to infinity. This technique is suitable for the recovery of a one dimensional field from discrete data provided that the measurements give a reasonable estimate of the Abel transform derivative. However, special care must be taken with the singularity at $r = r_0$ when the integral is evaluated numerically.

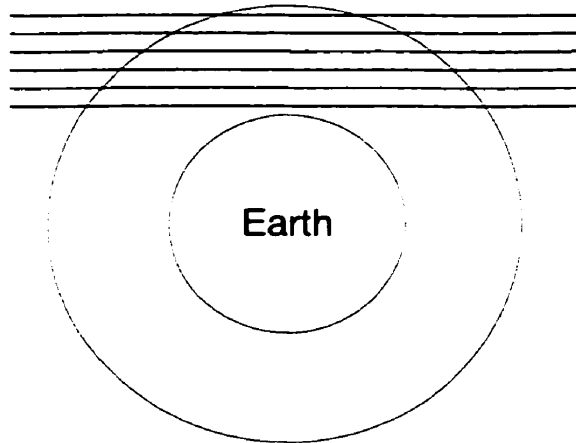


Figure 2.1: Sample rays for the line integrals in the Abel transform for atmospheric measurements.

2.2.2 The Cormack Transform

The Cormack transform (Cormack, 1963; 1964) was first introduced in radiology for the recovery of two dimensional fields, although it can be applied to the atmosphere. The Cormack geometry for atmospheric measurements is shown in Figure 2.2. If the radial

distance between the tangent points in a single set and the angular distance between the successive sets of parallel rays (black and red solid lines in Figure 2.2) are infinitesimally small, and the sets of line integrals are taken over 360° , then these measurements are a complete Cormack transform. The line integrals along the lines of sight (Figure 2.2) are given by equation 2.3,

$$f(l, \theta) = \int_{L(l, \theta)} g(r, \phi) ds \quad [2.3]$$

where the path is indicated by $L(l, \theta)$, and $g(r, \phi)$ is the measured field in polar coordinates. In equation 2.3 l is the perpendicular distance from the ray to the origin and θ is the angle of l from an arbitrary axis. A complete set of $f(l, \theta)$ is a Cormack transform. It should be noted that the variable naming convention used here is not consistent with the original work of Cormack. The changes were made in order to maintain consistency with the Radon transform variables (Section 2.2.3).

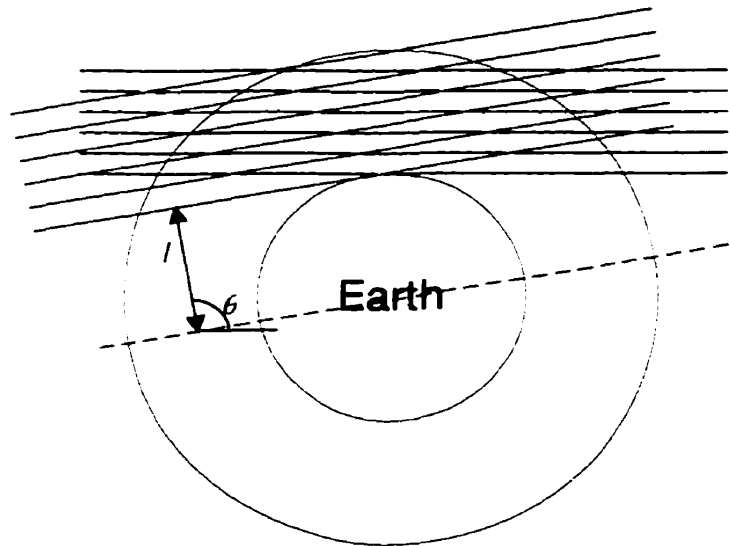


Figure 2.2: The geometry for the line integrals in the Cormack transform. For each set of rays (red and black) the angle θ is constant and l is varied.

The Fourier transform of the field $g(r, \phi)$ is given by equation 2.4 with each of the $g_n(r)$ coefficients defined by equation 2.5.

$$g(r, \phi) = \sum_{n=-\infty}^{\infty} g_n(r) e^{in\phi}. \quad [2.4]$$

$$g_n(r) = \frac{1}{2\pi} \int_0^{2\pi} g(r, \phi) e^{-in\phi} d\phi. \quad [2.5]$$

If the field $g(r, \phi)$ is zero outside a normalized unit circle Cormack showed that the transform $f(l, \theta)$, which if represented by a Fourier series (with coefficients given by equation 2.6) has the inverse $g_n(r)$ given by equation 2.7. In both equations $T_n\left(\frac{l}{r}\right)$ is the Tschebycheff polynomial of the first kind of degree n .

$$f_n(l) = \frac{1}{2\pi} \int_0^{2\pi} f(l, \theta) e^{-in\theta} d\theta = 2 \int_l^1 \frac{g_n(r) T_n\left(\frac{l}{r}\right) r dr}{(r^2 - l^2)^{\frac{1}{2}}}. \quad [2.6]$$

$$g_n(r) = -\frac{1}{\pi} \int_r^1 \frac{r f_n(l) T_n\left(\frac{l}{r}\right) dl}{(l^2 - r^2)^{\frac{1}{2}} l}. \quad [2.7]$$

It has been shown (Solomon *et al.*, 1984) that, after differentiation under the integral and integration by parts, the inverse $g_n(r)$ can be represented by equation 2.8 with the field no longer constrained to the unit circle.

$$g_n(r) = -\frac{1}{\pi} \int_r^{\infty} \frac{\frac{d}{dl} f_n(l) T_n\left(\frac{l}{r}\right) dl}{(l^2 - r^2)^{\frac{1}{2}}}. \quad [2.8]$$

The initial constraint was used by Cormack simply to ensure the square integrability of the field $g(r, \phi)$. In equation 2.8 the relationship between the Cormack and Abel inversions is readily apparent. As the Tschebycheff polynomial of degree 0 is equal to 1 equation 2.8 reduces to equation 2.9,

$$g_0(r) = -\frac{1}{\pi} \int_r^{\infty} \frac{\frac{d}{dl} f_0(l) dl}{(l^2 - r^2)^{\frac{1}{2}}} \quad [2.9]$$

which is equivalent to equation 2.2 (the inverse Abel transform).

2.2.3 The Radon Transform

The two dimensional Radon transform is used to transform a field $f(r, \phi)$, into a formulation that is based on line integrals through the field. The line integrals are dependent on two variables, an angle θ from the positive x -axis and a distance l from the origin. The line integral is taken perpendicular to the vector l along the path shown in Figure 2.3, the field $f(r, \phi)$ is assumed to be non-zero inside the white area and zero elsewhere. The exact definition of the Radon transform for any combination (l, θ) is given by

$$\begin{aligned} [Rf](l, \theta) &= \int_{-\infty}^{\infty} f\left(\sqrt{l^2 + z^2}, \theta + \tan^{-1}\left(\frac{z}{l}\right)\right) dz & \text{if } l \neq 0 \text{ and} \\ [Rf](0, \theta) &= \int_{-\infty}^{\infty} f\left(z, \theta + \left(\frac{\pi}{2}\right)\right) dz & \text{if } l = 0 \end{aligned} \quad [2.10]$$

where the integral is taken along the path shown in Figure 2.3 with $z = 0$ at the intersection of the path and the vector l . For the purpose of the present work it is assumed that the mathematical constraints such as the existence of this integral and the square integrability of $f(r, \phi)$ are met.

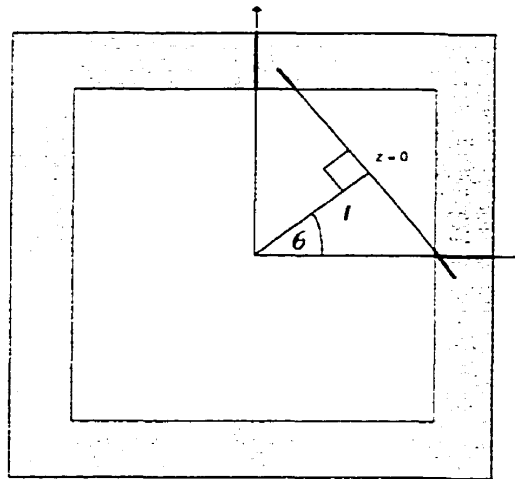


Figure 2.3: Definition of the ray for the line integral in the Radon transform.

In the Radon transform the combination (l, θ) can have any value and, therefore, each point (r, ϕ) can be characterized by a complete set of line integrals through it. This

complete set encloses any point (r, ϕ) over an angular range of 180° . An incomplete discrete set of rays, for which the line integrals may be taken, through a point (r, ϕ) is shown in Figure 2.4. The six rays (blue lines) extend over an angular range of 180° around (r, ϕ) and the vectors l are highlighted in red. Again the field $f(r, \phi)$ is assumed to be non-zero within the white area and zero elsewhere.

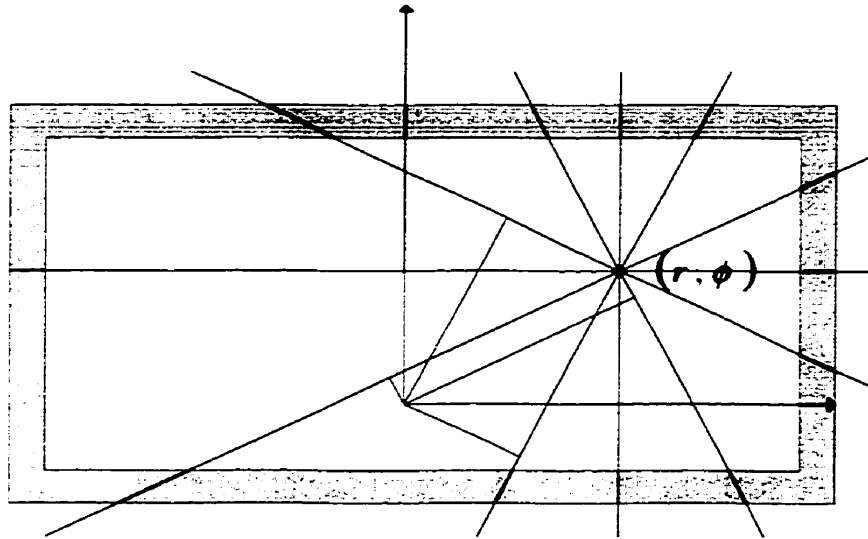


Figure 2.4: An incomplete set of line integral rays (6 in total) that characterize a given point (r, ϕ) . The line integrals are taken along the blue rays while the red lines, beginning at the origin, indicate the vectors l .

If the function $[Rf](l, \theta)$ in equation 2.10 is known for a range of θ (0 to π) and a sufficient range of l ($-E$ to E) to completely cover the field, $f(r, \phi)$, then the inverse Radon transform can be defined by equation 2.11,

$$[R^{-1}p](r, \phi) = \frac{1}{2\pi^2} \int_0^\pi \int_{-E}^E \frac{p_1(l, \theta)}{r \cos(\theta - \phi) - l} dl d\theta = f(r, \phi) \quad [2.11]$$

where $p = [Rf](l, \theta)$ and $p_1(l, \theta)$ is the partial derivative with respect to the first variable l . This is derived from the alternate definition of the inverse Radon transform (equation 2.12)

$$R^{-1} = \frac{1}{2\pi} BH_1 D_1 \quad [2.12]$$

where B is the back projection operator defined by equation 2.13,

$$[Bp](r, \phi) = \int_0^\pi p(r \cos(\theta - \phi), \theta) d\theta \quad [2.13]$$

H_1 is the Hilbert transform with respect to the first variable, and D_1 is the first partial derivative with respect to the first variable.

Equation 2.11 implies that the field $f(r, \phi)$ can be recovered if the Radon transform, and the partial derivative of the first variable of the Radon transform and the improper integral in equation 2.11 all exist. The integral is improper as the denominator may equal zero. Many applications that use tomography to recover the field $f(r, \phi)$ make measurements of the Radon transform and then simply apply the inverse transform. Other applications measure the Radon transform and attempt to recover the field through other techniques.

2.2.3.1 Solutions for the Inverse Radon Transform Method

The inverse Radon transform techniques that have been described in the literature (e.g. Herman, 1980) all require a nearly complete set of relatively noise-free measurements that represent the Radon transform. A complete description of the techniques that are used to solve inverse Radon transform problems when the data is discrete and contains noise has been given by Herman [1980] and Bertero and Boccacci [1998]. For completeness a brief discussion of some of these methods is included here.

There is a very simplistic discrete back projection operation to recover structures within a field $f(r, \phi)$ if there is a complete, or nearly complete, Radon transform. This method simply considers all measurements (line integrals) that intersect a discrete grid cell and sums the product of the path length through the grid cell and the measurements. This summation is an adequate representation of the Back Projection operator (equation

2.13). However, the method gives a dimensionally incorrect estimate of the field that requires multiplicative normalization and yields solutions that are usually a very blurred representation of the true field.

The more commonly used methods for the solution of the inverse Radon transform are convolutions that may require Fourier transforms. In these methods the Hilbert transform and the partial derivative seen in equation 2.12 are approximated by a convolution with a single function. One example of the convolution method is the Filtered Back Projection (FBP) in which a two dimensional Fourier transform of the Radon transform is made. A ramp filter $|\omega|$ and a suitable low pass filter, to remove the high frequency noise that is inherent in discrete measurements, are applied to the result. An inverse Fourier transform is then applied to recover the filtered projections and the back projection operator (equation 2.13) is applied to recover the field, $f(r, \phi)$, within a multiplicative normalization factor. It should be noted that this method is identical to applying the back projection operator to the convolution of the Radon transform with a well chosen regularization function, that has the same ramp and low pass filter characteristics as the functions in the FBP method. This approach is called the Convolution Back Projection (CBP) method.

2.2.4 The Maximum Likelihood Expectation Maximization (MLEM) Technique

The MLEM technique is used to estimate the vector \mathbf{x} (indexed by j) that is a solution to the discrete linear equation $\mathbf{Ax} = \mathbf{b}$ when the measurements \mathbf{b} (indexed by i) contain noise. The matrix \mathbf{A} , with elements a_{ij} , is geometry dependent. The problem may be restated as 'solve for \mathbf{x} such that $\mathbf{b} - \boldsymbol{\varepsilon} \leq \mathbf{Ax} \leq \mathbf{b} + \boldsymbol{\varepsilon}$ '. The technique used (De Pierro, 1991) is to maximize the log likelihood function

$$f(x^k, x^{k-1}) = \sum_i \left[\sum_j \left(\frac{b_i a_{ij} x_j^k}{\sum_{j'} a_{ij} x_{j'}^k} \log(a_{ij} x_j^{k-1}) \right) - \sum_j a_{ij} x_j^{k-1} \right] \quad [2.14]$$

which it has been shown converges, after iteration, to the maximum likelihood solution (Csiszar and Tusnady, 1984). The term x_j^k denotes the current iterative estimate of x_j and x_j^{k+1} indicates the next iterative value and the summations over i, j and j' are over all possible values. The maximization is achieved by setting the first partial derivative with respect to x_j^{k+1} equal to zero as in equation 2.15.

$$\frac{\partial f(x^k, x^{k+1})}{\partial x_j^{k+1}} = \sum_i \left(\frac{b_i a_{ij} x_j^k}{x_j^{k+1} \sum_{j'} a_{ij'} x_{j'}^k} - a_{ij} \right) = 0. \quad [2.15]$$

This equation (2.15) can be solved for x_j^{k+1} to give

$$x_j^{k+1} = x_j^k \sum_i \left(\frac{b_i}{\sum_{j'} a_{ij'} x_{j'}^k} \frac{a_{ij}}{\sum_i a_{ij}} \right) \quad [2.16]$$

where

$$\sum_i \left(\frac{a_{ij}}{\sum_i a_{ij}} \right) = 1. \quad [2.17]$$

Each term in the sum can be interpreted as a weighting filter function term with respect to the observation i . The MLEM technique is in fact a Multiplicative Algebraic Reconstruction Technique (MART) where the estimate of \mathbf{x} is adjusted through comparison of the measurements and the iterative estimate of the measurements.

2.3 Some Tomographic Applications

As noted previously tomographic reconstruction has been extensively used in the field of medical imaging although there have been applications in mining and some initial attempts to apply tomographic techniques to the determination of atmospheric constituents. Medical imaging applications include Photon Emission Tomography (PET), Single Photon Emission Computerized Tomography (SPECT) and transmission

Computed Tomography (CT) as in CAT scans. The two main algorithms that have been used include the Convolution Back Projection (CBP), and its derivatives, and the Algebraic Reconstruction Techniques, and their derivatives, that include the Multiplicative Algebraic Reconstruction Techniques, or MARTs, and the Maximum Likelihood Expectation Maximization (MLEM) technique.

2.3.1 Medical Imaging Applications

The ECT and x-ray transmission CT techniques that are used in medical imaging involve the solution of a problem that contains measured line integrals, or incomplete Radon transforms, of the form $O_i = \int_{\text{path } i} f(x, y, z) ds$ where O_i refers to a measurement along the i^{th} path through the unknown field $f(x, y, z)$.

2.3.1.1 X-Ray Tomography Discrete Inverse Radon Transform Technique

In CT, or x-ray tomography, discrete versions of the inverse Radon transform are usually applied. The Radon transform measurements typically have a very high signal to noise ratio and can be taken at sufficient resolution to approximate the complete set of (l, θ) values that is required for the inverse Radon transform. The geometry for the measurements used in x-ray (CT) tomography is illustrated in Figure 2.5. Typically a patient is illuminated by a linear x-ray transmitter that sends x-rays through the patient along lines perpendicular to the transmitter bank. The x-rays are received at a series of detectors that are parallel to the transmitter bank; it is the attenuation of these x-rays by the patient that is important. In this way the Radon transform (the line integral of the x-ray attenuation coefficients) is simultaneously measured for all relevant l values for any given angle θ . In order to complete the Radon transform measurements the transmitter and receiver banks must be rotated and the measurements performed at the new angle. It is obvious that if the measurements along the detector/transmitter banks are continuous

and the angle of rotation of the banks is also continuous these measurements are the complete Radon transform.

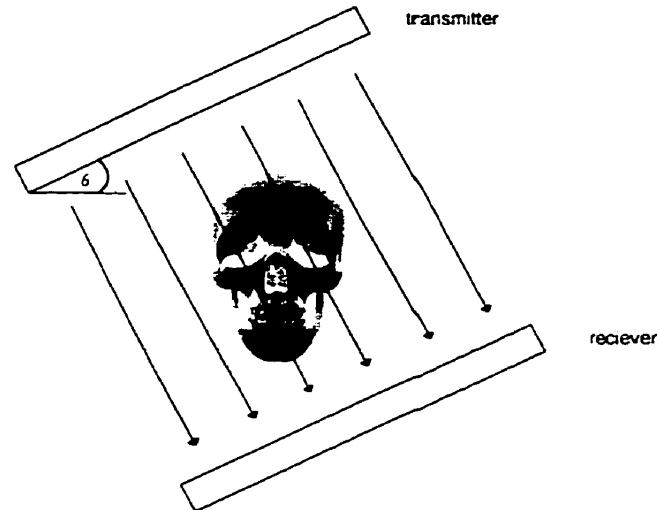


Figure 2.5: Geometry used for x-ray transmission (CT) Tomography.

A complete discussion of the techniques used in x-ray transmission tomography has been presented by Bertero and Boccacci [1998] and Herman [1980].

2.3.1.2 High Noise Level Algebraic Reconstruction Techniques for ECT

For some tomographic retrievals it has been necessary to develop techniques that are not seriously degraded by high noise levels associated with PET. In this method a patient is injected with a positron emitter that is deposited in proportion to the glucose uptake mechanism in the human brain. Thus a map of the resulting positron emissions is a map of the glucose consumption in the brain. The positron emissions are monitored through the detection of photon pairs that result from positron annihilation. The photon pairs travel in nearly opposite directions so that a detector ring, placed around the head of the patient, records the coincidences associated with the photon pairs. This is shown in Figure 2.6 where the straight lines indicate the paths of the photon pairs from positron annihilation. The two points marked with circles along one of the rays are important. In the PET method the simple detection of the coincident photon pair does not uniquely define the position of the positron annihilation. It is equally probable, in the absence of

photon attenuation, that the photon pair originated at either marked point. As each detector is opposite more than one other detector (as seen in Figure 2.6) many line integrals can be measured although the Radon transform is discrete due to the physical size of the detectors. Only if the detector banks were continuous could coincidences be measured along all rays for all values (l, θ) .

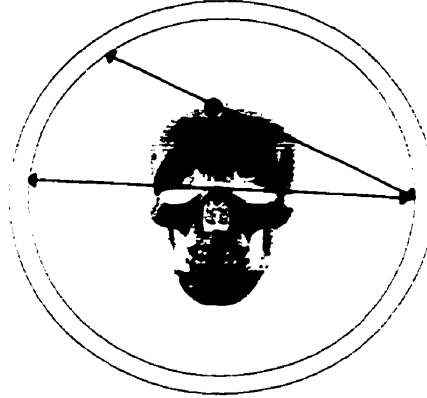


Figure 2.6: Geometry used with PET reconstruction of positron decay inside a human patient.

The tomographic methods used with PET differ from those used with x-ray CT because of the lower signal to noise levels in the PET measurements. As the signal quality does not allow the discrete inverse Radon transform methods (Section 2.2.3.1) Shepp and Vardi [1982] and Vardi and Shepp [1985] have developed a statistical technique that accounts for the high noise levels and the incomplete data set. This technique uses the statistical nature of the photon pair detection and gives a good recovery of the distribution of positron emitters. The technique is described as the Maximum Likelihood Expectation Maximization (MLEM) technique (Section 2.2.4) and uses an iterative procedure to recover a discrete two dimensional positron emission intensity field λ (indexed by b) from the coincidence measurements n^d (indexed by d).

For PET the MLEM technique yields

$$\lambda(b)^{new} = \lambda(b)^{old} \sum_{d=1}^D \frac{n^d(d)}{\sum_{b'=1}^B \lambda^{old}(b')p(b',d)} p(b,d) \quad [2.18]$$

where

$$n^{\bullet}(d) \equiv n(\bullet, d) \equiv \sum_{b=1}^B n(b, d) \quad [2.19]$$

is the total number of coincidences detected in detector pair d (the measurements). The summation in the denominator of equation 2.18 is the estimate of the measurements from the previous estimate of λ . If

$$n(b, \bullet) \equiv \sum_{d=1}^D n(b, d) \quad [2.20]$$

is the total number of coincidences from b that are detected and $p(b, d)$ is the probability of detecting a coincidence at b in detector pair d then

$$E(n(b, \bullet)) = \lambda(b) p(b, \bullet) \quad [2.21]$$

is the expected value of the coincidences detected in b that originated from d , and the problem has been reduced to estimating the mean $n(b, \bullet)$ given $n(\bullet, d)$.

2.3.1.3 Advances and Problems in PET

The MLEM technique (Shepp and Vardi, 1982) is the norm against which most new iterative techniques in the field of medical imaging are compared. One new iterative technique, based upon MLEM called the Image Space Reconstruction Algorithm (ISRA), has been developed by Daube-Witherspoon and Muehllehner [1986]. This technique is computationally faster than the MLEM technique although it does require back projections of both the measurements and their current estimates at each step in the iteration. The basic iterative equation (2.22) developed by these researchers is

$$\lambda_j^{(k+1)} = \lambda_j^{(k)} \frac{\sum_i a_{ij} n_i}{\sum_i a_{ij} \sum_j a_{ij} \lambda_j^{(k)}} \quad [2.22]$$

where the numerator is the discretely back projected data (Section 2.2.3.1) and the denominator is the discretely back projected estimates for the current iteration. This

technique has been shown to give comparable results to those from the MLEM technique and achieves its efficiency as the numerator only needs to be calculated once.

The results from the MLEM technique are characterized by edge effects and noise artifacts that are apparent in all unconstrained Maximum Likelihood (ML) solutions (Snyder *et al.*, 1987). In an attempt to limit these artifacts Snyder *et al.* proposed a modification to the existing MLEM technique. These authors suggested amending equation 2.18 with different probabilities in the numerator and denominator. The actual expression is

$$\lambda(b)^{new} = \lambda(b)^{old} \sum_{d=1}^D \frac{n(d)}{\sum_{b'=1}^B \lambda^{old}(b') p_2(b', d)} p_1(b, d) \quad [2.23]$$

where $p_1(b, d)$ is referred to as the kernel of the measurements. In this method some averaging mechanism, other than the standard back projection seen in the Shepp and Vardi MLEM, is applied to the observations. In their work Snyder *et al.* employed a trial and error approach to determine a set of $p_1(b, d)$ that reduced both the noise artifacts and edge effects.

In the original work of Shepp and Vardi the MLEM technique was unconstrained and an attempt to add constraints to the ML approach has been reported by Levitan and Herman [1987]. These authors called their method the Maximum A Posteriori (MAP) ML technique. In this technique a penalty function is added to the log likelihood function (equation 2.14) that requires the final solution to have a determined, but variable, degree of smoothness (or similarity) between neighbouring points in the recovery grid. This method reduces to the MLEM approach when the penalty term, a simple constant, is set equal to zero. Again Levitan and Herman used a trial and error approach to the penalty term in order to develop solutions with the required smoothness and accuracy.

Green [1990] has also developed a penalized ML technique that constrains the degree of smoothness of the final solution. In his work Green employed the One Step Late (OSL) approach in which partial derivatives of the previous estimate are included in the

iterative step. Once again a trial and error approach was used to determine a set of conditions for which the method converged faster and with fewer artifacts than the usual MLEM technique.

Many other modifications to the MLEM technique for ECT have been made during this decade. These include: corrections to the model used to forward project the estimates that account for both signal attenuation (Blankespoor *et al.*, 1996) and scatter (Welch and Gullberg, 1997); improved initial estimates (Pan *et al.*, 1997); and grid cell shape and size considerations (Matej and Lewitt, 1996). Other information that can improve the forward projection model has also been incorporated into the Maximum Likelihood approach, in particular Magnetic Resonance data has been used by Lipinski *et al.* [1997] to improve the MLEM recovery from Positron Emission Tomography data.

However, advances in the field of medical imaging have not been restricted to the MLEM algorithm. Other iterative techniques have also been investigated. These include: a Grouped-Coordinate Ascent (GCA) algorithm (Fessler *et al.*, 1997) that requires less computation than the MLEM technique; a Weighted Least Squares (WLS) approach (Anderson *et al.*, 1997); and regularization methods (Chinn *et al.*, 1997) that transform the original equations into a set of less ill-posed equations. In general it can be stated that the solution must be tailored to each particular problem.

2.3.2 Satellite Remote Sensing Tomography Applications

In the field of atmospheric remote sensing from satellite platforms a tomographic approach has been used on a number of occasions. One of the earliest attempts (Roble and Hays, 1972) used stellar occultation data to retrieve molecular oxygen and ozone vertical number density profiles. In that work the Abel transform (Section 2.2.1) was used with two different numerical schemes. The first considered an exponentially decaying concentration and the second considered a more complex profile that was similar to the expected result.

A later attempt to perform a two dimensional recovery of the 6300 Å OI, 5577 Å OI and 2800 Å Mg⁺ volume emission rates from the Visible Airglow Experiment on the Atmospheric Explorer spacecraft was reported by Fesen and Hays [1982]. These authors used a simple onion peel technique that divided the atmosphere into angular regions that are consistent with single limb scans. This technique is really a series of one dimensional inversions that are incorporated into a two-dimensional result. The problems associated with this technique are presented in Appendix A.

The first true two-dimensional recovery was reported in 1984 (Solomon *et al.*) using data from the same Visible Airglow Experiment. The actual technique used was a numerical solution to the Cormack transform (Section 2.2.2). In a series of papers Solomon *et al.* (1984 and 1985) showed that their self-described *ad hoc* approach, in which they combined nadir and limb measurements within the inverse Cormack transform, was a consistent and reliable way to obtain the altitude profile of isolated features.

The first use of an iterative approach to the two dimensional tomographic recovery of atmospheric constituents from measurements made with a satellite borne instrument was reported by Yee *et al.* [1987]. These authors used a minimum cross entropy approach to retrieve the two dimensional profile. In this approach there was no *ad hoc* smoothing of the observations or results because of noise limitations. The Yee *et al.* technique was tested on the same 6300 Å OI data used by Fesen and Hays [1982] and Solomon *et al.* [1984] and was shown to yield a stable iterative algorithm that was suitable for the inversion of airglow data.

2.3.3 Ground Based Ionospheric Remote Sensing Applications

There have been ongoing efforts to recover two dimensional electron density profiles in the ionosphere. Pryse *et al.* [1993] have used a tomographic imaging technique to show the development of a mid-latitude electron density trough from measurements of phase coherent signals at 150 MHz and 400 MHz transmitted by the Navy Navigational

Satellite System (NNSS) and simultaneously detected at several receivers along a meridional chain. The retrieval algorithm used was the Simultaneous Iterative Reconstruction Technique (SIRT) that was first proposed by Gilbert [1972] and described in detail by Austen *et al.* [1988]. With this technique Pryse *et al.* was able to identify a trough-like structure that had the characteristics of a mid-latitude trough.

Kersley *et al.* [1993] have also used a MART technique, described by Raymund *et al.* [1990], to recover two dimensional electron density profiles from similar NNSS and ground receiver data. In this case Kersley *et al.* used a standard ionosphere as the initial guess for the MART technique and verified their results with European incoherent scatter (EISCAT) ionospheric radar measurements. Raymund *et al.* [1993] have also published similar EISCAT verified results.

The methods described by the ground based tomographic researchers all suffer from a lack of near horizontal paths through the atmosphere and so limit the ability to recover vertical structure. In an attempt to improve on this situation Heaton *et al.* [1995] have adapted the technique of Kersley *et al.* [1993] by incorporating additional information from ionosondes, for the bottomside electron density profiles, and incoherent scatter radar measurements, for the topside profiles, in order to obtain a more accurate initial guess. The results obtained by Heaton *et al.* were also verified with independent EISCAT measurements. Similar work in ionospheric tomography has been reported by Mitchell *et al.* [1997] and Nygren *et al.* [1997].

2.4 Background Conclusions

In this background chapter many of the advances in tomographic analysis have been identified. The main conclusion that can be drawn from these advances and their applications is that while many techniques are available it is important to tailor the selected technique to the particular problem. Each problem has its associated limitations that are dependent specifically on the geometry and the measurements. In this thesis the investigation concentrates on the applicability of a particular tomographic technique to airglow observations.

CHAPTER III

A SINGLE MODEL OBSERVATION

3.1 Introduction

The tomographic techniques that have been discussed in Chapter 2 provide a retrieval of a two dimensional field from knowledge of line integrals through that field. The atmospheric tomography discussed in this thesis also uses a knowledge of line integrals, made by an optical instrument onboard a satellite platform, to recover the two dimensional volume emission rate profile of the atmosphere. A model for these line integrals, referred to as observations or measurements, is required to simulate the observed brightness for both algorithm test purposes and to provide estimates of the actual observations within the tomographic algorithm. The adopted modeling procedure, which is identical for both purposes, uses a discrete two dimensional volume emission profile for the atmospheric source function. This source function is sampled by an optical instrument with a non-stationary, finite, instrument field of view to simulate a single observation or measurement. This chapter includes an extensive discussion of the required parameters that pertain to the instrument, the satellite and the volume emission grid, and how these parameters are used in the observation model to generate a simulated brightness measurement.

3.2 Coordinate Systems Required to Define a Model Observation

Three coordinate system definitions are used in the simulation of an observation. Two of these coordinate systems are based on the orbit of the satellite and are described as the ascending node (asc) and the satellite (sat) systems. The third coordinate system is based on the model instrument and is called the instrument (inst) system. These three coordinate systems, and the set of transformations between them, provide a basis for a modeled observation.

The ascending node coordinate system (defined by the satellite orbit) is a fixed Earth

centred three dimensional Cartesian space. The x -axis of this system points towards the ascending node equator crossing and the z -axis is rotated 90° from the x -axis, within the orbit plane, in the direction of satellite motion. This coordinate system is illustrated in Figure 3.1. All satellite motion is in the x - z plane of this system and at any time the instantaneous satellite position is given by equation 3.1,

$$\underline{S}_{asc} = R_{sat} (\cos \alpha \hat{x}_{asc} + \sin \alpha \hat{z}_{asc}) \quad [3.1]$$

where R_{sat} is the radial distance of the satellite from the origin (centre of the Earth) and α is the angle of the satellite (along its track) from an arbitrary ascending node crossing. This coordinate system is effectively fixed in space so that the Earth rotates below the satellite and each ascending node crossing is at a different longitude. Thus the angle α can increase beyond 360° as the orbit number increases beyond the arbitrary 0^{th} orbit.

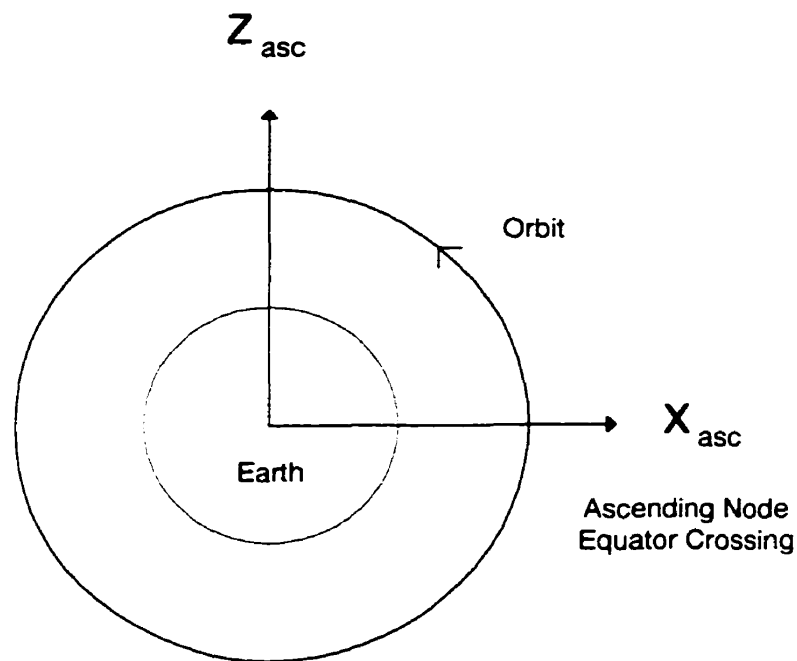


Figure 3.1: The Ascending node coordinate system is defined by the orbit plane and an arbitrary ascending node equator crossing. This coordinate system is used to define the two dimensional volume emission grid.

The satellite coordinate system is also Earth centred but, unlike the ascending node system, it rotates with the satellite motion. This is illustrated in Figure 3.2, which

includes both the ascending node and satellite systems, where the x -axis points through the local zenith and the z -axis is rotated 90° from the x -axis, within the orbit plane, in the direction of satellite motion. The x - z plane of the satellite system is identical to that for the ascending node system. The instantaneous position of the satellite in the 'sat' system is given by equation 3.2,

$$\underline{S}_{sat} = R_{sat} \hat{x}_{sat}. \quad [3.2]$$

In this system there is only an x component that is the satellite distance from the centre of the Earth.

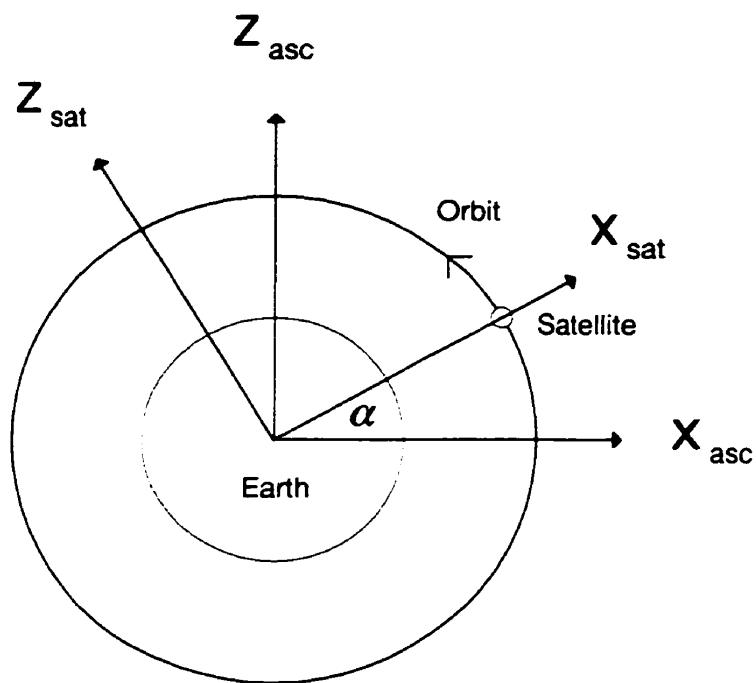


Figure 3.2: The Satellite coordinate system is defined by the orbit plane and the satellite position. This coordinate system is used to determine those regions of the volume emission grid that are sampled by the instrument.

The instrument coordinate system is based on the optical axis and a preferred direction within the focal plane of a single lens instrument. A schematic drawing of the single detector (lens-pixel) instrument is shown in Figure 3.3. Only one dimension, the preferred direction, of the two dimensional field of view is shown; this dimension is consistent with a vertical image of the atmosphere. It is assumed that there is cross-track

homogeneity in the atmospheric source function so that the orthogonal dimension of the field of view is unimportant. The x -axis of the instrument system is defined to be along the preferred direction while the z -axis is coaligned with the optical axis of the instrument. The unit vector for any field of view look direction in the orbit plane is defined by an angle β that is an offset from the optical axis. This unit vector is defined according to equation 3.3,

$$\underline{P}_{inst}(\beta) = \sin \beta \hat{x}_{inst} + \cos \beta \hat{z}_{inst}. \quad [3.3]$$

As there is an assumption of cross track homogeneity there is no \hat{y}_{inst} component.

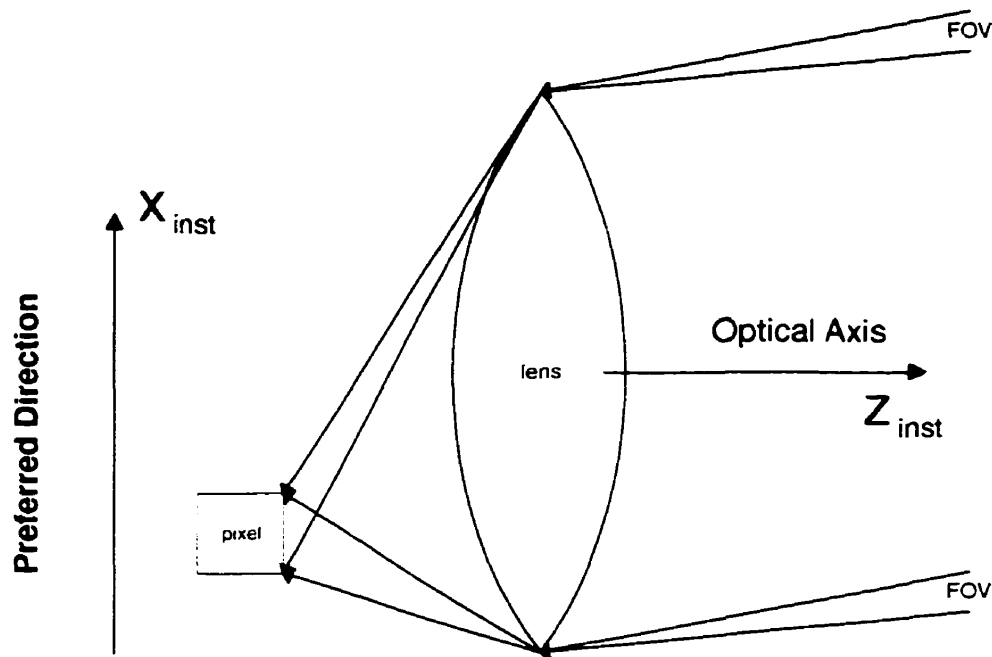


Figure 3.3: *The Instrument coordinate system is defined by the optical axis of the lens and a preferred direction. This coordinate system is used to define the instantaneous field of view of the simple instrument.*

3.3 Inputs to a Modeled Observation

Three input sets are required to generate the simulated brightness measurement made by the optical instrument on the satellite platform. These inputs are related to the instrument that makes the measurement, the satellite on which the instrument is located and the atmospheric source function that the instrument measures. These three

parameter sets are discussed in detail below.

3.3.1 The Model Instrument Definition

An instrument model is required to simulate an observation. The adopted instrument model is based on the single detector (lens-pixel) instrument shown in Figure 3.3. The instrument model must accurately represent the instantaneous field of view and the detection sensitivity of the entire system as a function of the view angle, *i.e.* the look direction. This representation is made with a discrete set of look direction unit vectors, $\underline{P}_{inst}(\beta)$, that cover the entire instrument field of view and a corresponding set of values, $\delta(\beta)$, that represent the sensitivity of the instrument with respect to these unit vectors.

The field of view and the throughput of the instrument are defined by the lens and the size of the pixel as well as their relative separations. However, it is convenient to group all three parameters and define a single field of view as input to the instrument model. Any lens-pixel system with a similar field of view, whatever the pixel size and lens focal length, can be similarly modeled. The required inputs are upper and lower bounds to the angle β that define the sensitivity range (field of view) of the instrument.

For an accurate representation of the instrument, non-ideal performance such as vignetting or a non-uniformity in the pixel sensitivity across its surface must be included in the model. A convenient approach for this is to introduce a function $\delta(\beta)$ that is a normalized representation of the system sensitivity (as a function of the look direction β) such that the integral over the entire field of view is unity.

The continuous field of view of the simple instrument is represented in a discrete fashion with a resolution factor. This factor, $NumFOV$, defines the total number of discrete look direction angles that are considered; if $NumFOV$ approaches infinity then the field of view is exactly modeled as continuous. The field of view resolution factor allows the total field of view to be subdivided into smaller fields of view that are each assumed to observe the same source brightness and collect light with a uniform

sensitivity.

The output from the instrument model is a set of $NumFOV$, indexed by k starting at 0, look direction unit vectors $\underline{p}_{inst}(\beta_k)$ (equation 3.3) and a set of sensitivities $\delta(\beta_k)$. A sample set of three look direction vectors, bounded by angles β_{lower} and β_{upper} , is shown in Figure 3.4. A uniform set of sensitivity parameters for this set of unit vectors would have $\delta(\beta_k) = 0.333$, for all k .

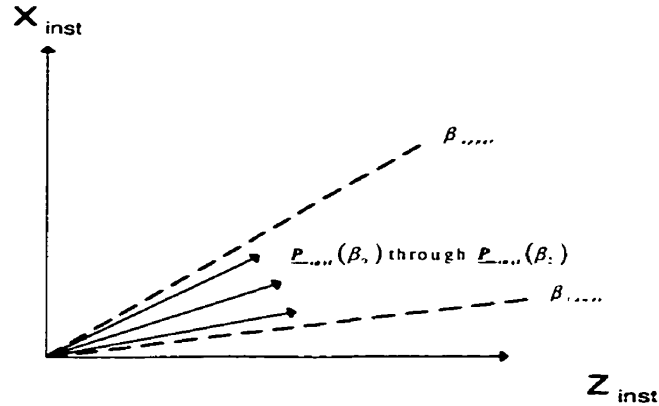


Figure 3.4: The Instrument coordinate system and three sample look direction unit vectors that make up the discrete field of view. Each vector can sample a different atmospheric source function.

3.3.2 The Model Satellite Attitude and Position Parameters

The discrete set of look direction vectors, defined in Section 3.3.1, that cover the instantaneous instrument field of view must have an origin and orientation in the two Earth centred coordinate systems. This orientation and origin must be available throughout the duration of the measurement in order to provide a complete non-stationary field of view that samples the atmospheric source function. The required satellite attitude and position parameters are three angles of rotation and two position coordinates for various times during the measurement.

The origin of the look direction vectors is given by the spacecraft position in both the ascending node and satellite systems. In the ascending node system the parameters R_{sat} , the satellite distance from the centre of the Earth, and α , the satellite angle from the

arbitrary ascending node crossing, are both required. In the satellite coordinate system only R_{sat} is required as this system moves with the satellite (see equations 3.1 and 3.2).

The look direction unit vector $\underline{P}_{inst}(\beta_k)$ must be oriented into both coordinate systems. A series of transformations, or rotations, are required to align the \hat{x}_{inst} , \hat{y}_{inst} and \hat{z}_{inst} axes first with the satellite coordinate system and then with their ascending node system counterparts. The first three rotation angles that take the vectors into the satellite system are defined as ω , θ and ϕ and are related to the yaw, pitch and roll of the optical axis; the final rotation is through the satellite angle α (Figure 3.2) and completes the transformation into the ascending node system.

If the satellite and instrument coordinate systems are aligned then the angle ϕ is the rotation of the optical axis about the \hat{x}_{sat} axis that moves the optical axis, or \hat{z}_{inst} axis, out of the orbit plane. The optical axis is still directed tangent to the radius defined by the satellite distance from the centre of the Earth but it is no longer within the orbit plane. The second rotation (θ) is about the new \hat{y}_{inst} axis, and is negative due to the coordinate system orientation, and places the tangent radius of the optical axis look direction at a different distance from the centre of the Earth than the satellite radius. This rotation maintains the alignment of the preferred instrument direction with the local zenith at the tangent point of the optical axis. The third rotation (ω) is about the new optical axis and rotates the new preferred direction axis of the instrument coordinate system so that it is no longer aligned with the local zenith at the optical axis tangent point.

The process involved in the transformation of the look direction vectors $\underline{P}_{inst}(\beta_k)$ into the satellite coordinate system is shown in Figures 3.5, 3.6 and 3.7 and is simply a reversal of the three rotations described above. The resulting field of view vectors are defined as $\underline{P}_{sat}(\beta_k)$ and describe the instantaneous field of view in the satellite system. Figure 3.5 illustrates the $-\omega$ rotation required to align the \hat{x}_{inst} axis with the local zenith at the optical axis tangent point. Figure 3.6 shows the rotation θ that is required to align

the \hat{x}_{inst} axis with the satellite zenith. The final transformation, a rotation of $-\phi$ that aligns the instrument and satellite axes as shown in Figure 3.7. The complete transformation from \underline{P}_{inst} to \underline{P}_{sat} , for any look direction vector, is given in equation 3.4,

$$\underline{P}_{sat}(\underline{R}_t) = \begin{pmatrix} 1 & 0 & 0 \\ 0 & \cos \varphi & -\sin \varphi \\ 0 & \sin \varphi & \cos \varphi \end{pmatrix} \begin{pmatrix} \cos \theta & 0 & -\sin \theta \\ 0 & 1 & 0 \\ \sin \theta & 0 & \cos \theta \end{pmatrix} \begin{pmatrix} \cos \omega & -\sin \omega & 0 \\ \sin \omega & \cos \omega & 0 \\ 0 & 0 & 1 \end{pmatrix} \underline{P}_{inst}(\underline{R}_t). \quad [3.4]$$

This transformation of the entire set of vectors is sufficient to define the instantaneous field of view in the non-stationary satellite system that is used, together with the satellite angle α , to determine those atmospheric model cells that are intersected by the different lines of sight (Appendix B).

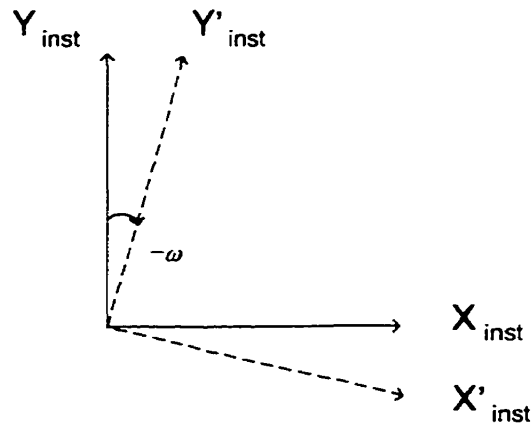


Figure 3.5: The rotation $-\omega$ about the \hat{z}_{inst} axis that is used to align the \hat{x}_{inst} axis with the local zenith at the tangent point of the optical axis.

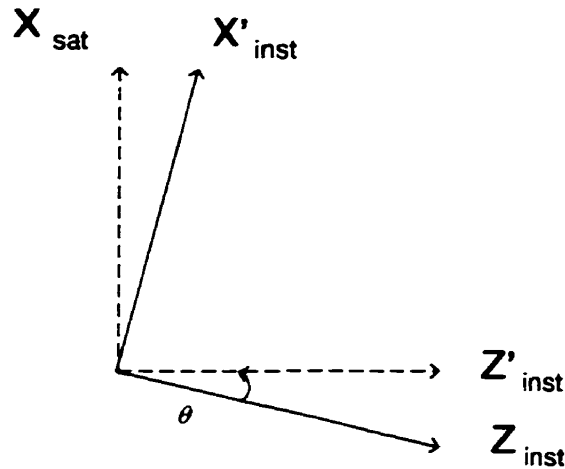


Figure 3.6: The rotation θ about the new \hat{y}'_{inst} axis that is used to align the \hat{x}'_{inst} axis with the \hat{x}_{sat} axis.

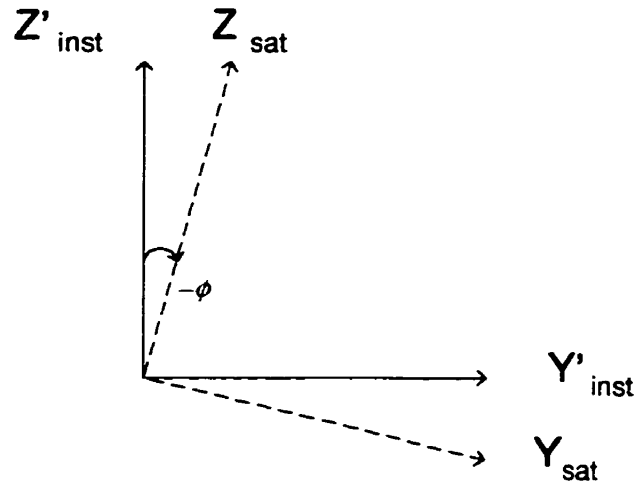


Figure 3.7: The rotation $-\phi$ about the \hat{x}_{sat} axis that is used to align the \hat{z}'_{inst} axis with the \hat{z}_{sat} axis and the \hat{y}'_{inst} axis with the \hat{y}_{sat} axis.

To complete the transformation into the ascending node system only a simple rotation of α , about the \hat{y}_{sat} axis is required. This rotation takes the look direction vectors, $\underline{P}_{sat}(\beta_k)$, and yields a set of $\underline{P}_{asc}(\beta_k)$ that completely define the instantaneous field of view in the ascending node system. The transformation definition is given by equation 3.5,

$$\underline{P}_{asc}(\beta_k)_l = \begin{pmatrix} \cos\alpha & 0 & -\sin\alpha \\ 0 & 1 & 0 \\ \sin\alpha & 0 & \cos\alpha \end{pmatrix} \underline{P}_{sat}(\beta_k)_l. \quad [3.5]$$

The set of $\underline{P}_{asc}(\beta_k)$ look direction vectors are used to determine the geometric path length of the line of sight through each cell in the observed grid (Appendix B).

Because each measurement is made with a finite exposure time and the spacecraft changes its orientation and position during this time a set of *NumTimes* attitude $(\omega, \phi, \theta)_l$ and position $(R_{sat}, \alpha)_l$ parameters are required to define the complete non-stationary field of view; the index *l* ranges from 0 to *NumTimes* - 1, and *NumTimes* is defined as the temporal resolution factor. Each instantaneous field of view, defined by the set of $\underline{P}_{sat}(\beta_k)$ or $\underline{P}_{asc}(\beta_k)$ unit vectors, is transformed (for each step *l*) to define the total field of view during the measurement. The result is a set of *NumFOV* x *NumTimes* unit vectors, $\underline{P}_{sat}(\beta_k)_l$ or $\underline{P}_{asc}(\beta_k)_l$, in either of the Earth centred coordinate systems. If the instrument sensitivity is assumed to be constant during the measurement the weighting factors $\delta(\beta_k)$ must be adjusted so that $\delta(\beta_k)_l = \frac{\delta(\beta_k)}{NumTimes}$. In this way a normalized set of weighting factors, $\sum_{k,l} \delta(\beta_k)_l = 1$, are maintained.

In summary the outputs of the spacecraft attitude model are two sets of unit vectors, $\underline{P}_{sat}(\beta_k)_l$ and $\underline{P}_{asc}(\beta_k)_l$, and a set of sensitivities $\delta(\beta_k)_l$. These parameters are sufficient to define completely the non-stationary field of view in both Earth centred coordinate systems and the sensitivity of the (lens-pixel) instrument over this field of view.

3.3.3 The Two Dimensional Discrete Volume Emission Grid

The atmospheric source function that is the input for a model observation is contained within a discrete two dimensional volume emission grid that is coplanar with the *x-z* plane of the ascending node coordinate system. The grid cells are bounded by the angle

along the satellite track and the radial distance, from the centre of the Earth. An arbitrary volume emission profile is assumed to exist throughout the grid. In the following discussion only the geometry and the associated parameters for the two dimensional volume emission grid are considered.

The volume emission grid geometry is shown in Figure 3.8. As illustrated in this figure the grid cell number, indexed by the subscript j , increases with respect to radial shell and then with respect to angular division. The first angular division is at an arbitrary ascending node point. As the satellite orbits the Earth the longitude of the ascending node changes and there is no requirement for the volume emission profile to be the same at each ascending node. Thus the angular dimension of the grid can increase beyond 360° and while the starting angle is defined as 0° the end boundary is arbitrary.

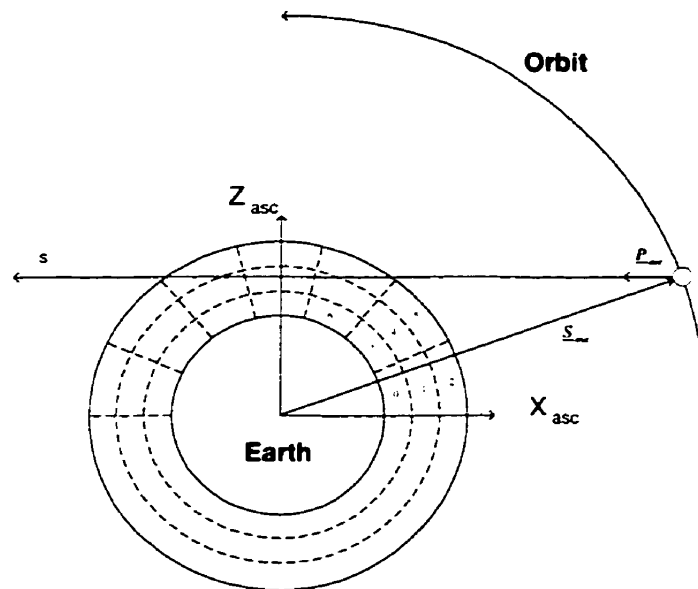


Figure 3.8: The two dimensional volume emission grid geometry in the ascending node coordinate system. A sample line of sight, P_{asc} , is shown.

The definition of the two dimensional volume emission grid requires both upper and lower boundaries for the radial shells, as well as radial shell and angular resolution parameters. The minimum and maximum radial shells are defined as *ShellMin* and *ShellMax* respectively. The radial shell resolution and the angular resolution are defined

as $\Delta Shell$ and $\Delta Angle$. The number of radial shells, $NumShells$, at any angle is defined by equation 3.6,

$$NumShells = \frac{ShellMax - ShellMin}{\Delta Shell} . \quad [3.6]$$

For the grid shown in Figure 3.8 the appropriate values are $NumShells = 3$ and $\Delta Angle = \frac{\pi}{7} rad$; the minimum and maximum shell distances are not included in this figure. The index j (equation 3.7) is known if both the shell number and angle number of the cell are known.

$$j = AngleNumber \times NumShells + ShellNumber . \quad [3.7]$$

The radial distance and angular values of the grid cell boundaries are defined by the $ShellNumber$ and $AngleNumber$. The radius r of any shell is given by equation 3.8 and the angular distance γ , from the predefined 0, of any angular division is given by equation 3.9. Both the $ShellNumber$ and $AngleNumber$ have an initial value 0.

$$r = ShellNumber \times \Delta Shell + ShellMin , \quad [3.8]$$

$$\gamma = AngleNumber \times \Delta Angle . \quad [3.9]$$

As already noted the volume emission grid is two dimensional within the orbit plane. However, the look directions may sample out of this plane if either, or both, of the attitude parameters ω and ϕ is non-zero. In this case it is necessary to assume that the source function is uniform out of the orbit plane.

The lines that define the angular divisions within the ascending node $x-z$ plane can also be translated into planes, orthogonal to the $x-z$ plane, that intersect the original line. Any point that is out of the orbit plane, with radial distance $r = \sqrt{x^2 + y^2 + z^2}$ and angle $\gamma = \tan^{-1}\left(\frac{z}{x}\right)$, is considered to have the same volume emission as the point within the plane at the same radial distance and the same angle γ . Thus there is a constraint for radial uniformity between successive planes.

3.4 The Definition of a Modeled Observation

A modeled observation includes contributions from all look directions in the non-stationary field of view as defined by either of the vector sets $\underline{P}_{sat}(\beta_k)_i$ or $\underline{P}_{asc}(\beta_k)_i$. The first step in the construction of a model observation requires the determination of the brightness along each line of sight. The second step requires a calculation of the weighted average of the brightness values, seen along each line of sight, to determine the simulated measurement.

3.4.1 The Observed Brightness Along a Single Line of Sight

The observed brightness in any look direction is defined by the integral representation given in equation 3.10. If the satellite is used as the origin for the look direction then the integral is along a path from the satellite to infinity. It is assumed that the only significant contributions to the integral are between *ShellMin* and *ShellMax*, the boundaries of the discrete two dimensional volume emission grid. The observed brightness $O_{\underline{P}_{asc}} [kR]$ is the integral of the volume emission contributions $V(s) [kR/km]$ along the line of sight.

$$O_{\underline{P}_{asc}} = \int_{sat}^{\infty} V(s) ds. \quad [3.10]$$

The integral in equation 3.10 can be discretely represented by equation 3.11.

$$O_{\underline{P}_{asc}} = \sum_j L_{\underline{P}_{asc},j} V_j [kR] \quad [3.11]$$

where the summation is over all grid cell elements j intersected by the line of sight $\underline{P}_{asc}(\beta_k)_i$ and $L_{\underline{P}_{asc},j} [km]$ is the geometric path length through each element. The value $V_j [kR/km]$ is the volume emission contribution from each element j (Section 3.3.3).

Equation 3.12 is an expansion of the summation given in equation 3.11 for the particular line of sight, $\underline{P}_{asc}(\beta_k)_i$, shown in Figure 3.8.

$$O_{\underline{p}_{asc}} = L_{\underline{p}_{asc}.8}V_8 + L_{\underline{p}_{asc}.7}V_7 + L_{\underline{p}_{asc}.10}V_{10} + L_{\underline{p}_{asc}.13}V_{13} + L_{\underline{p}_{asc}.14}V_{14} \quad [kR]. \quad [3.12]$$

It is readily apparent that some method for the determination of the path through each grid cell is required to calculate the summation. The actual representation of the summation requires a knowledge of the relevant grid cell at any distance s along the line of sight and the intercept lengths $L_{\underline{p}_{asc}.j}$. The actual process used to determine these parameters is given in Appendix B.

3.4.2 The Complete Modeled Observation

The complete simulated brightness measurement consists of the averaged, or blurred, contributions over the lines of sight, $\underline{p}_{asc}(\beta_k)_l$, that constitute the entire field of view. The method for determining the brightness along these individual lines of sight has been given in Sections 3.4.1, together with Appendix B, and a simple method to determine the simulated measurement from the observed brightness values in the complete non-stationary field of view is given by equation 3.13,

$$O = \sum_l \frac{1}{NumTimes} \left(\sum_k \delta(\beta_k) O_{\underline{p}_{asc}(\beta_k)_l} \right) \quad [kR], \quad [3.13a]$$

$$O = \sum_{l,k} \delta(\beta_k)_l \left(\sum_j L_{\underline{p}_{asc}(\beta_k)_l,j} V_j \right) \quad [kR]. \quad [3.13b]$$

These equations describe the weighted average of the entire set of observed brightness values along the lines of sight that cover the total field of view. In the first representation, equation 3.13a, the two sums represent the weighted average of the observed brightness values contained within an instantaneous field of view, and the weighted average over the successive instantaneous fields of view that make up the entire field of view. In equation 3.13b the interior summation represents the contributions of each grid cell to the observed brightness along a single line of sight, $\underline{p}_{asc}(\beta_k)_l$, and the outer double summation represents the weighted average over these brightness values. The three summations in this representation are in fact symbolic of

the three input sets that are required to model an observation: the Instrument; the Satellite and the Two Dimensional Volume Emission Grid.

CHAPTER IV

SIMULATED OBSERVATION SETS

4.1 Introduction

In order to evaluate the effectiveness of the tomographic technique for the retrieval of two dimensional atmospheric volume emission profiles (from measurements made by an optical instrument on a satellite platform) it is necessary to generate simulated observations that can be used for test purposes. The actual tomographic procedure requires thousands of individual measurements in an observation set for the inversion technique to be effective. These simulated measurements have been generated in an identical fashion using the same procedure as that for a single observation (Chapter 3). The individual measurements are linked by an imager and the orbit of the satellite that contains the imager.

For the simulated observations the imager, which is defined as multiple single pixel instruments (Section 3.3.1), is considered to be viewing a discrete two dimensional grid that contains an arbitrary volume emission profile (Section 3.3.3). The imager, the satellite parameters and the volume emission profiles that have been used to generate the modeled observations are presented in this chapter together with a discussion of the required observational resolution (Chapter 3) and the expected noise parameters.

4.2 The Model Imager Used for Test Data

The simulated observations assume that the imager has a linear array vertical detector, *i.e.* each pixel observes a different tangent altitude. Thus the imager may be described as multiple (*NumPixels*) single pixel instruments (Section 3.3.1). Each of these single pixel instruments share the same objective lens and make simultaneous observations, although each pixel has a different look direction. The set of simultaneous measurements is referred to as an image. For the present work the number of illuminated pixels (*NumPixels*) has been limited to 100; this is consistent with the

Odin/OSIRIS instrument where there are 128 pixels, but those at the top of the detector array are masked-off to provide dark current measurements.

The preferred axes of each pixel (see Section 3.2 and Figure 3.3) are aligned so that the optical axes are parallel for each of the single pixel instruments. A schematic representation of this simple imager is shown in Figure 4.1, the \hat{x}_{inst} axis points along the preferred direction and \hat{z}_{inst} is along the imager optical axis. The labeled field of view is for the entire detector array; the pixel numbering defines the bottom pixel as index 0. The field of view of each pixel is only a fraction of the total imager field of view. In the present work the model imager has a total field of view of approximately 2° , this corresponds to 100 km of vertical limb coverage for a satellite at 600 km altitude. These values are consistent with those for OSIRIS on Odin.

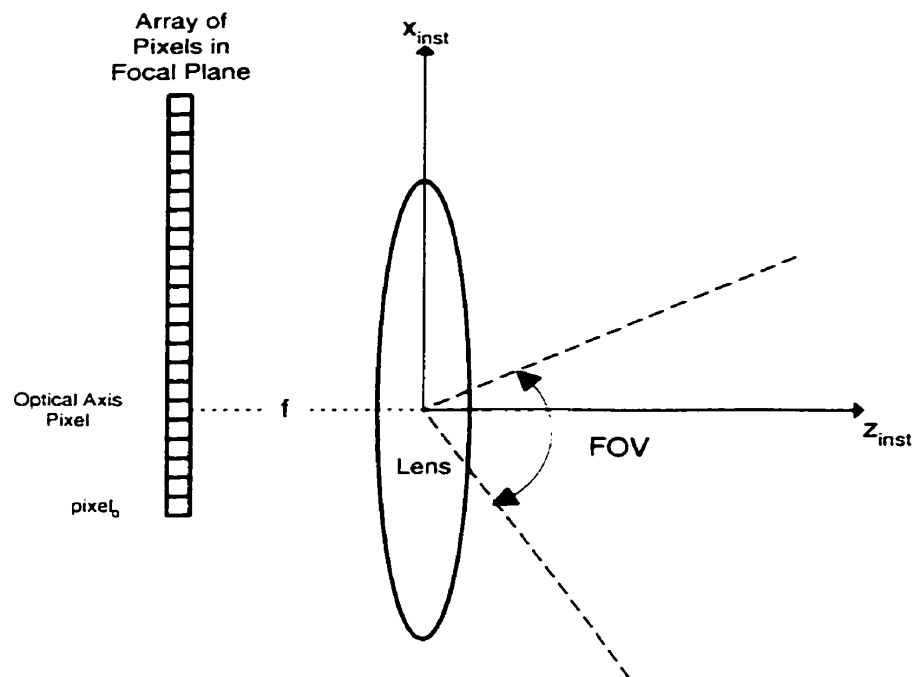


Figure 4.1: A schematic representation (not to scale) of the one dimensional vertical imager used throughout this work. The imager consists of multiple single pixel instruments (identical to those discussed in Section 3.3.1) that all share the same coordinate system and objective lens.

For an imager with $NumPixels$ pixels and a total field of view of FOV_t , the field of view of any single pixel is given by equation 4.1,

$$FOV_p = \frac{FOV_t}{NumPixels}, \quad [4.1]$$

if there is no overlapping of the fields of view of adjacent pixels. The index of the pixel with a central field of view that corresponds to the imager optical axis is designated as the *OptAxisPixelNumber*; for the present work this is pixel number 20. The lower and upper field of view angles, β_{lower} and β_{upper} , for each single pixel instrument (Section 3.3.1) are given by equations 4.2 and 4.3 respectively:

$$\beta_{lower} = (PixelNumber - OptAxisPixelNumber - 0.5)FOV_p; \quad [4.2]$$

$$\beta_{upper} = (PixelNumber - OptAxisPixelNumber + 0.5)FOV_p. \quad [4.3]$$

Each pixel is divided into sub-pixels, for which the sensitivity and the source brightness are assumed to be uniform, according to the value of the field of view resolution factor, $NumFOV$ (Section 3.3.1). In this way the entire set of $NumFOV$ look direction vectors and sensitivities that are required for the single pixel instrument model (Section 3.3.1) are defined. For the purpose of the test data presented throughout this thesis $NumFOV$ was set equal to 7.

In the present work the sensitivity, $\delta(\beta)$, of each pixel has been considered to be uniform and only the source brightness has been allowed to vary within the pixel field of view. This implies that all angles β associated with the field of view of any single pixel have the same sensitivity (equation 4.4).

$$\delta(\beta_k) = \frac{1}{NumFOV}. \quad [4.4]$$

This simple representation is considered adequate for test purposes but the ability to handle a non-uniform sensitivity is essential for the complete observation set model.

The output from the imager model is a $NumPixels \times NumFOV$ set of look direction vectors $\underline{P}_{inst}(\beta_k)$ and sensitivities $\delta(\beta_k)$ that define the instantaneous field of view of the complete imager. The values of k ranges from 0 to $NumFOV-1$ for each pixel. Thus the total field of view is broken into $NumPixels \times NumFOV$ separate look directions, grouped into sets of $NumFOV$, that correspond to a single measurement. In the present work there are 100 separate measurements (the array has 100 pixels) each of which requires 7 field of view divisions. Hence the complete imager model consists of 700 look directions and the corresponding sensitivities.

4.3 The Model Spacecraft and Imaging Parameters Used for the Simulated Images

To calculate a complete image set both the orbit and the spacecraft orientation must be defined. This is consistent with the method described for the generation of a single measurement (Section 3.3.2). However, additional parameters which describe the duration of the measurements and the temporal resolution are also required to define the complete observation set.

4.3.1 The Orbit and Orientation of the Spacecraft

The model orbit used throughout the present work is a 6978 km circular orbit. This corresponds to a 600 km altitude at the equator, a 96.7 minute period, a tangential velocity of 7.56 km/s and an angular velocity of 1.09×10^{-3} radians/s. These parameters are those for Odin/OSIRIS. Thus, it is a simple procedure to determine the satellite position \underline{S}_{avc} (in the ascending node coordinate system, Section 3.2) at any time.

The inclination of the satellite orbit is also required as it determines the geographic latitude and longitude of any point around the orbit, and of any point along a line of sight that originates within the orbit plane. As the oblateness of the Earth must also be considered in the determination of model altitudes the latitude is a required parameter. For the present work the orbit inclination has been set to 97° ; for the model orbit

altitude this corresponds to a sun-synchronous orbit and is consistent with the Odin mission.

The three spacecraft rotation angles ω , θ and ϕ (Section 3.3.2) are also required for modeling the observation sets. For the present work the out of orbit plane look direction angle ϕ and the roll angle ω , the deviation from the local vertical at the tangent point, were both set equal to zero for all observations. Only the angle θ associated with the radial shell tangent distance from the centre of the Earth is allowed to vary.

Two modes have been considered for the variation of the angle θ . One involves a continuous adjustment of θ that maintains the tangent point of the optical axis, and therefore each pixel look direction, at a fixed altitude above the surface of the Earth. The variation of θ in this "stare" mode is due to the oblateness of the Earth. The second, or nod, mode allows the tangent altitude of the optical axis to vary in a regular sawtooth fashion from a minimum, to a maximum, to a minimum altitude. The variation of θ over an entire orbit for the two different modes is shown in Figure 4.2. The low frequency line corresponds to variations in θ that correct for Earth oblateness. The high frequency curve shows the same low frequency Earth oblateness envelope and a superimposed tangent altitude nod. For this curve the tangent altitude nod rate was set to 1 km/s. The effects of these different nod conditions on the observations and the inversions are discussed in Chapter 8.

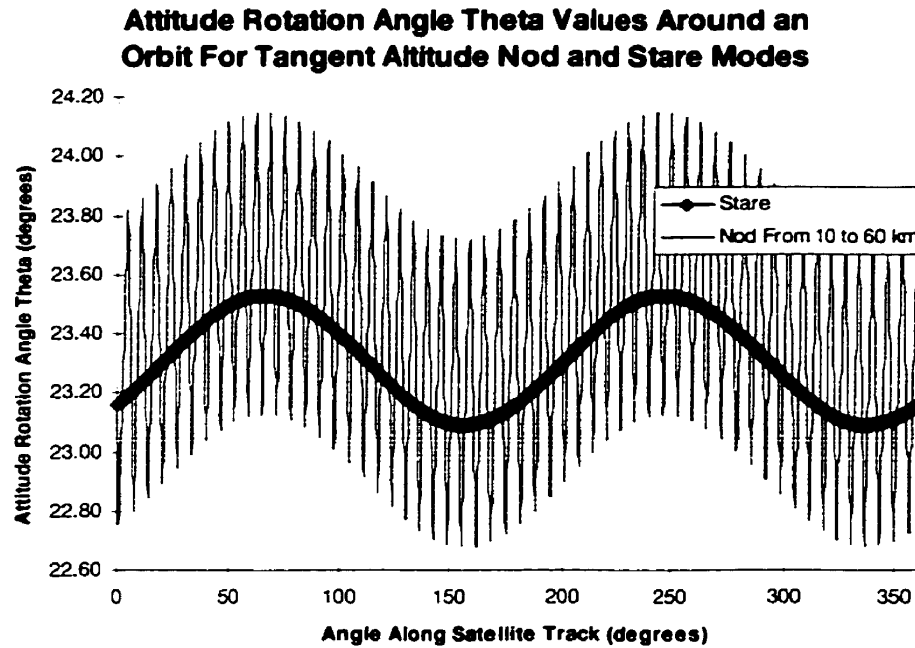


Figure 4.2: The orbital variation of the attitude angle θ for two operational modes.

While the attitude for the model satellite is exact this is not expected to be the case for the real satellite as the reported attitude will contain both systematic and random errors associated in each of the parameters. The impact of a range of errors, both systematic and random, has been tested and it has been found that for typical attitude errors the effect is much smaller than that from other uncertainties in the tomographic inversion.

4.3.2 The Duration of an Observation Set

The angular extent of the input volume emission grid is determined from the total observing time that is defined by the total number of images in the observation set and the image rate. These two parameters define the distance traveled by the spacecraft during the total observing time.

Typically in the present work the number of images (*NumImages*) in an observation set has been set at 700. This matter is discussed in some detail in Section 6.6 and Appendix D. The 700 image set implies that there 70,000 observations (700 images x 100 pixels)

in the typical observation set. For an image rate of one every two seconds, this is consistent with the expected rate for Odin/OSIRIS, the model satellite will travel for 1400 seconds, or approximately 87° , around the orbit during the collection of the observation set. As the imager samples the atmosphere ahead of the spacecraft the actual angular grid coverage (for a satellite that travels 87°) is from 14° to 121° in front of the initial satellite position.

4.3.3 The Temporal Resolution of an Observation Set

The temporal resolution parameter, *NumTimes* (Section 3.3.2), is the final imaging parameter that is required for generation of the model observations. This parameter defines the number of instantaneous fields of view that are considered in a single measurement. Larger values of *NumTimes* correspond to higher resolution observations. A value of 7 implies that seven instantaneous fields of view are defined in both the satellite and ascending node coordinate systems. This, together with a value of 7 for the field of view resolution parameter (*NumFOV*) implies that 49 different vectors for each set, $\underline{P}_{sat}(\beta_k)_l$ and $\underline{P}_{asc}(\beta_k)_l$ (Section 3.3.2), are required for a single measurement. Thus, for a linear detector array with 100 pixels there are 9800 look direction vectors associated with a single image and so for an image set with 700 images there are 6,860,000 line of sight look direction vectors in the entire observation set.

The orbit position and the orientation of the spacecraft are also required *NumTimes* for each image. Hence the number of $(\omega, \phi, \theta)_l$ and $(R_{sat}, \alpha)_l$ (Section 3.3.2) parameters that must be calculated for an observation set is *NumImages* x *NumTimes*. For the typical image set this is 4900 (700 x 7) position and attitude values.

The required output from the spacecraft model contains three data sets: the complete satellite system field of view vectors $\left[\underline{P}_{sat}(\beta_k)_l \right]_{pl}$; the complete ascending node field of view vectors $\left[\underline{P}_{asc}(\beta_k)_l \right]_{pl}$; and the position parameters $\left[(R_{sat}, \alpha)_l \right]_l$. The values of

the subscripts in these sets are: $k = 0$ to $NumFOV - 1$; $l = 0$ to $NumTimes - 1$; $p = 0$ to $NumPixels - 1$; and $I = 0$ to $NumImages - 1$.

4.4 The Input Volume Emission Profiles for Test Purposes

It was noted previously (Section 3.3.3) that for the generation of the model observations a two dimensional volume emission grid, based on the ascending node coordinate system and completely contained within the orbit plane, is required. The associated grid parameters *ShellMin*, *ShellMax*, *DeltaShell* and *DeltaAngle* are also required. *ShellMin* and *ShellMax* provide a range that encloses the volume emission profile at all angles and *DeltaShell* and *DeltaAngle* are made sufficiently small that no further decrease in the grid cell size causes a significant change ($> 0.01\%$) in the modeled observation. The angular extent of this grid is dependent on both the satellite and imaging parameters.

The vertical volume emission profile shown in Figure 4.3 has been used as the basis profile for the emission grid in the present work. The radius of the Earth at the centre of each angular division has been calculated for the latitude determined from both the orbit inclination and the angle along the satellite track. In this way the central altitude (above the surface of the Earth) of each grid cell in an angular division is known so that a cubic spline interpolation of the vertical profile can be used to give the volume emission for each cell. The calculated two dimensional volume emission profile is shown in Figure 4.4; the low frequency oscillation is due to the oblateness of the Earth that is superimposed upon the rectangular representation of the radial grid. It should be noted that the ordinate scale in this figure, and in many others presented in this work, is a geocentric altitude above *ShellMin*. It is not the altitude above the surface of the Earth.

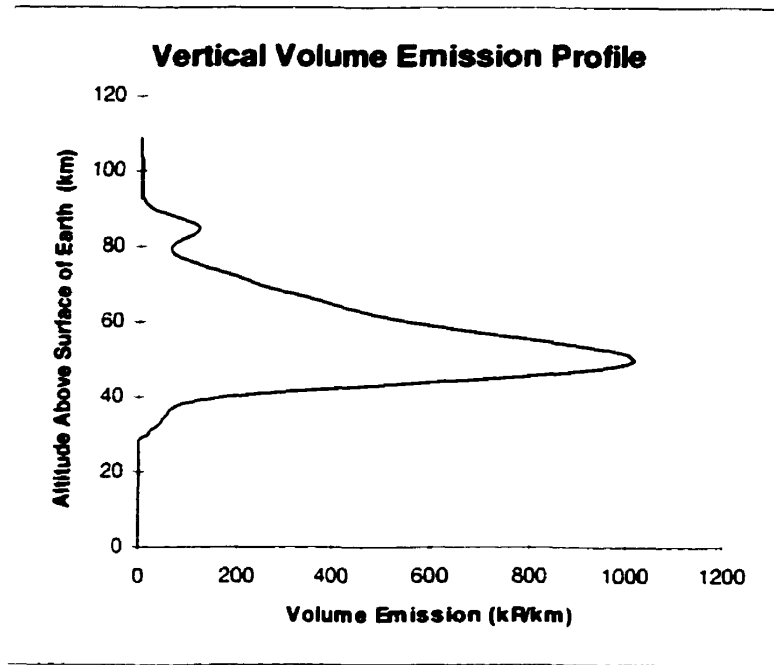


Figure 4.3: *The basis vertical volume emission profile for each angular division in the two dimensional input grid. This is a typical daytime emission profile for the oxygen infrared atmospheric band.*

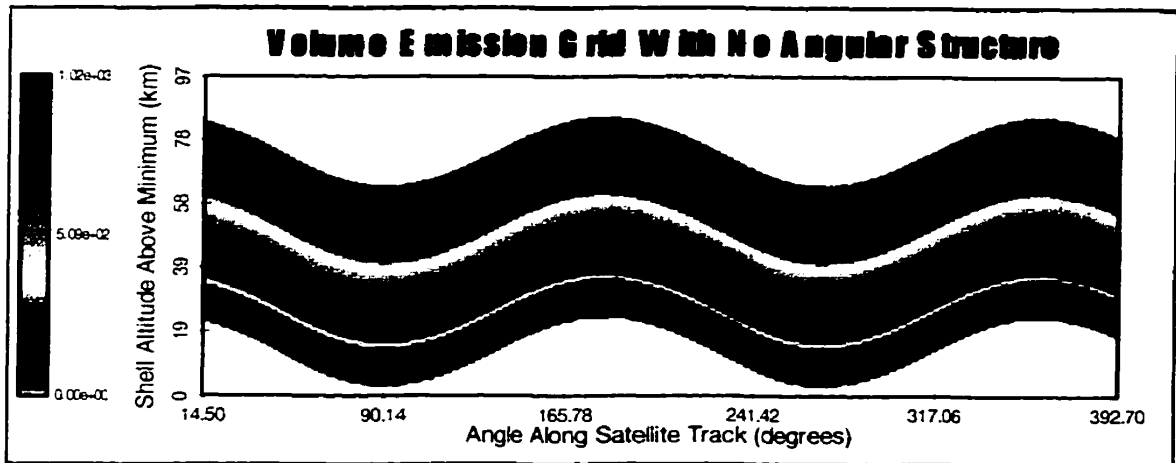


Figure 4.4: *The two dimensional volume emission grid, with no angular structure. The low frequency oscillation is due to the oblateness of the Earth. The colour scale represents the volume emission rate in kR/km.*

The two dimensional volume emission grid shown in Figure 4.4 has been used as the basis for all test input in the present work. This volume emission grid is modulated to give profiles that contain additional structure in both the angular and the radial

dimensions. Two types of modulation, both multiplicative, have been used; one is a simple angular modulation and the other is a combined angular and vertical modulation.

The simple angular modulation is given by equation 4.5,

$$M=1+0.3\cos\left(2\pi\gamma/\lambda\right)+0.2\sin\left(4\pi\gamma/\lambda\right)+0.1\cos\left(6\pi\gamma/\lambda\right)+0.1\cos\left(8\pi\gamma/\lambda\right)+0.02\cos\left(10\pi\gamma/\lambda\right). \quad [4.5]$$

The volume emission in each grid cell with central angle γ , the angle from the ascending node equator crossing (Section 3.3.3), is multiplied by M . The wavelength λ of the angular structure is varied for different test cases. An example of the modulated grid, with the wavelength λ set to 30° , is shown in Figure 4.5. The multiple frequency components defined by equation 4.5 are clearly visible in this figure; again the low frequency envelope is due to the oblateness of the Earth.

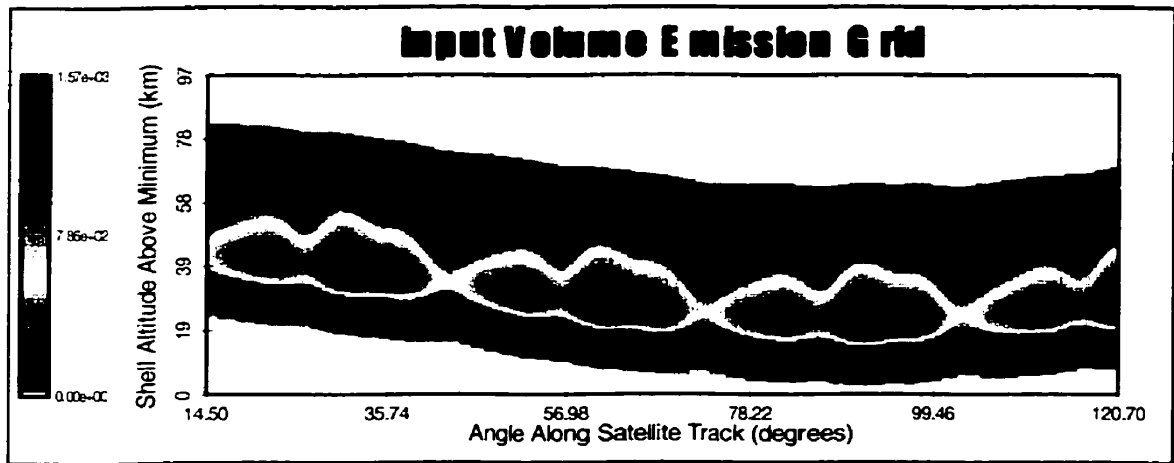


Figure 4.5: A sample volume emission grid derived using equation 4.5 and a value of λ equal to 30° . This grid which covers only a partial orbit corresponds to 700 images taken once every two seconds.

The second type of structure is defined by equations 4.6 and 4.7 and involves a modulation in both angle and radial distance.

$$M = 1 - \left(A_{\min} + \frac{e^{\beta(r-r_{\min})}}{H} \right) e^{-\frac{(\gamma-\gamma_0)^2}{2\sigma^2}} \cos(k_{alt}r) \cos(k_r\gamma). \quad [4.6]$$

$$A_{\min} + \frac{e^{\beta H}}{H} = A_{\max}. \quad [4.7]$$

The wavenumbers k_{ult} and k_{γ} in equation 4.6 represent radial and angular oscillations respectively. Throughout the present work the wavelength in the radial dimension was fixed at 10 km and k_{γ} was allowed to vary so that the angular wavelength ranged from 1.0° to 5.0° . These angular oscillations correspond to horizontal structures in the 100 to 500 km range. The other two terms in equation 4.6 are an exponential that represents a Gaussian decay from some central angle, γ_0 , and a growth term with respect to radial distance, this is represented by the formulation in braces. For test purposes γ_0 was set to the angular centre of the grid and σ was set to give the decay halfwidth equal to 20° .

The radial growth term is somewhat more complicated. H is the total radial extent of the grid, or $ShellMax - ShellMin$, and the growth term β in equation 4.6 is determined from equation 4.7. For the present work A_{\min} and A_{\max} have been defined as 0.2 and 0.8 respectively. The growth term results in oscillations that grow with radial distance from A_{\min} (at $ShellMin$) to A_{\max} (at $ShellMax$). An example of this type of radial and angular modulation, with a 4.0° angular wavelength, is shown in Figure 4.6. Angular and radial shell cross sections from this grid are shown in Figures 4.7 and 4.8 and clearly illustrate the angular and radial structure introduced by the modulation.

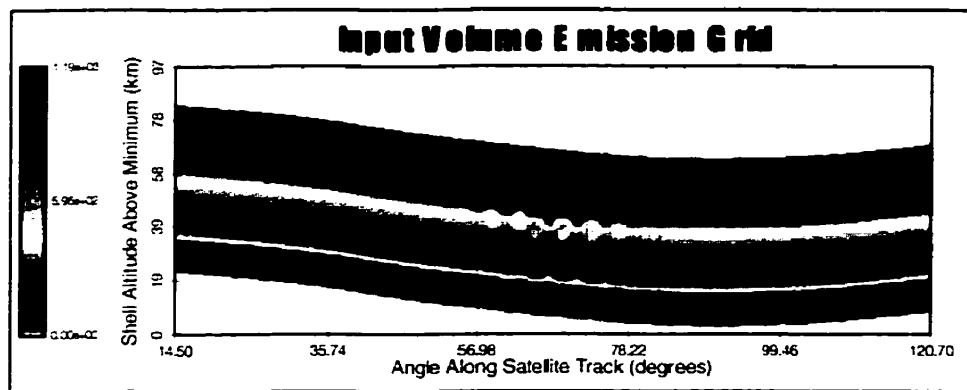


Figure 4.6: A sample two dimensional volume emission grid with 10 km vertical structure and 400 km horizontal structure derived from equation 4.6. The grid covers only a partial orbit and corresponds to 700 images taken once every two seconds.

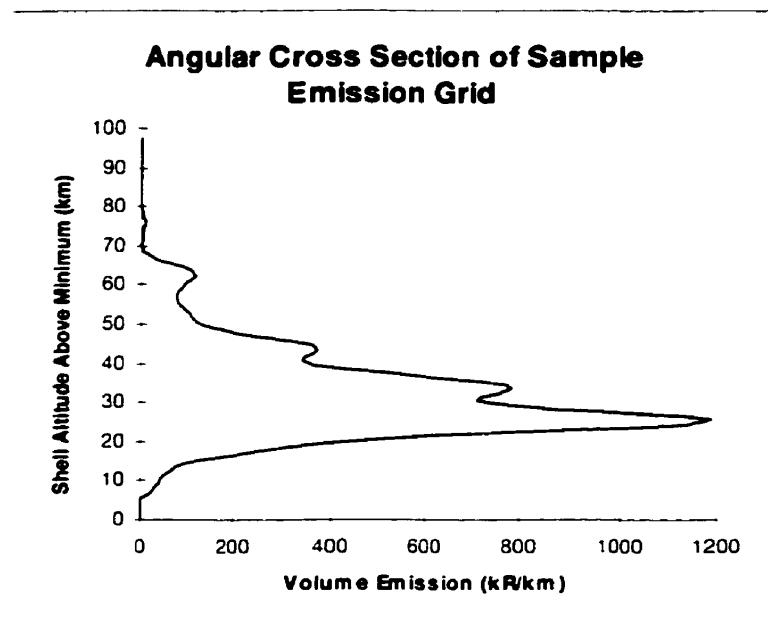


Figure 4.7: An angular cross section taken from the centre of the grid shown in Figure 4.6. This plot clearly illustrates the vertical modulation of the basis vertical profile shown in Figure 4.3.

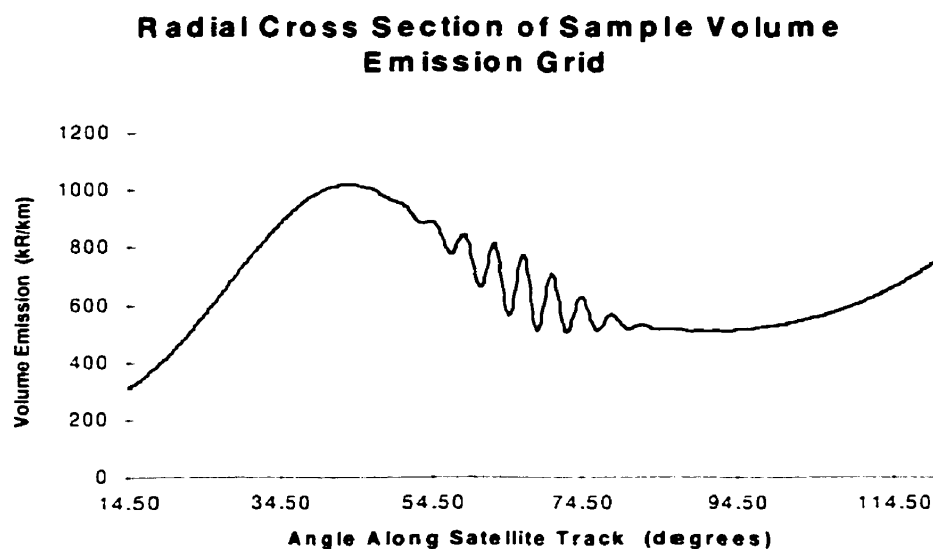


Figure 4.8: A radial shell cross section taken from the centre of the grid shown in Figure 4.6. This plot clearly illustrates the angular modulation imposed by equation 4.6.

4.5 The Resolution Parameters and Grid Cell Size

In order to provide accurate model data the resolution parameters *NumTimes* and *NumFOV*, and the grid cell size must be set to give high resolution modeled input data. This implies that any further increase in resolution, through either an increase in the resolution parameters or a decrease in grid cell size, does not result in a significant change ($> 0.01\%$) in the simulated input signal.

The two plots shown in Figure 4.9 represent modeled observations for a 700 image observation set that consists of 100 pixels, or measurements, for each image. These measurements were simulated using the stare mode (Section 4.3.1) with the tangent altitude locked at 40.5 km and a 0.5 Hz image rate. The upper plot in Figure 4.9 represents a low resolution construction of the observation set. The resolution parameters *NumTimes* and *NumFOV* were both set to unity so that only one line of sight was traced through the emission grid for each measurement. The grid cell size was 0.2° by 1.0 km. The lower plot in Figure 4.9 corresponds to a high resolution set of modeled observations that use the same volume emission profile with a different resolution grid. The parameters *NumTimes* and *NumFOV* were both set to 7 so that 49 lines of sight were traced for each measurement. The grid cell size used for these simulated measurements was 0.02° by 0.100 km. The two dimensional representations shown in this figure suggest that there are only very small differences between the two observation sets.

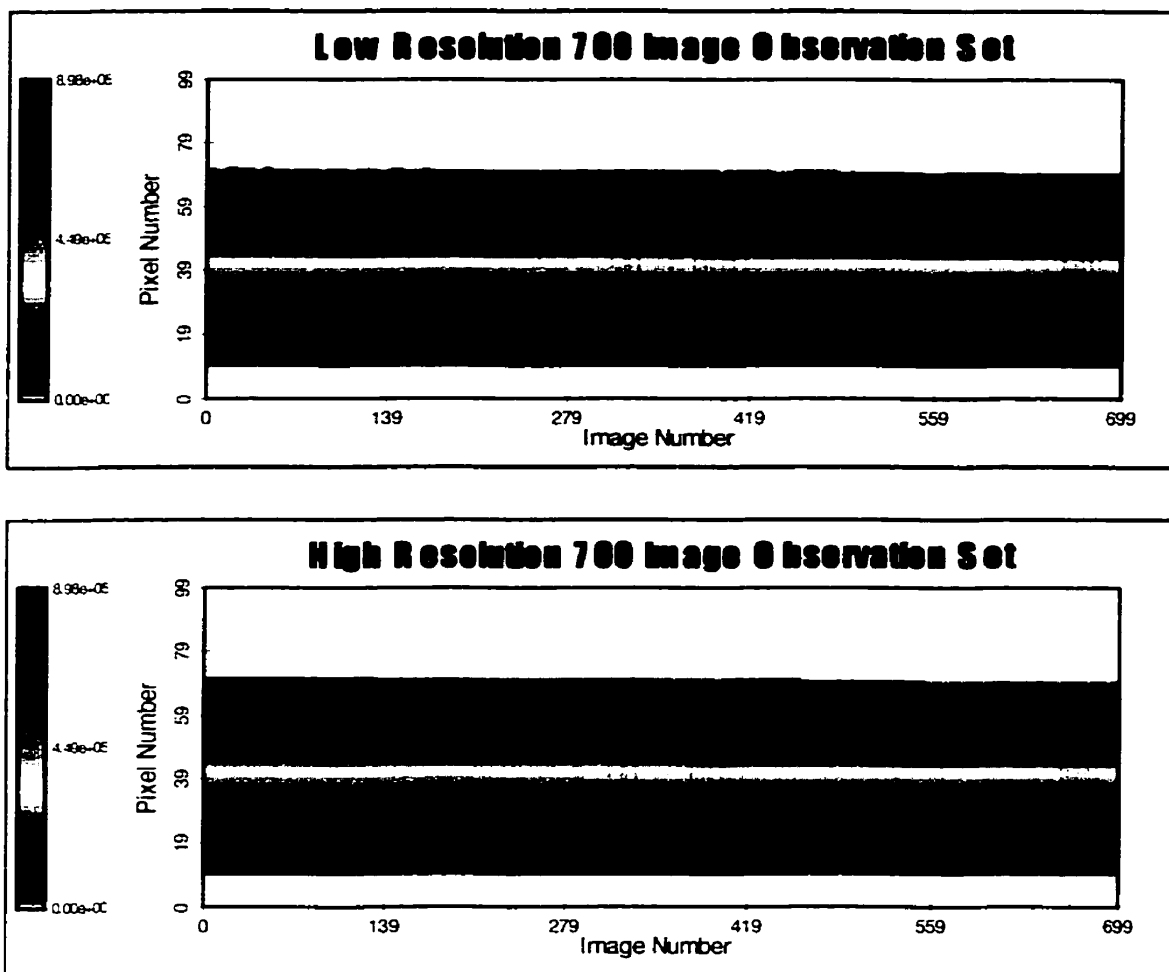


Figure 4.9: *Low and high resolution observation sets constructed using an unstructured volume emission grid similar to that shown in Figure 4.4. The colour scale represents the observed brightness in kR.*

The modeled brightness values at a single pixel are shown in Figure 4.10 and clearly illustrate the differences between the modeled observations for the different resolutions. The low resolution cross section exhibits an oscillation about the high resolution value that is due to the combined effects of both the Earth oblateness and the grid cell size.

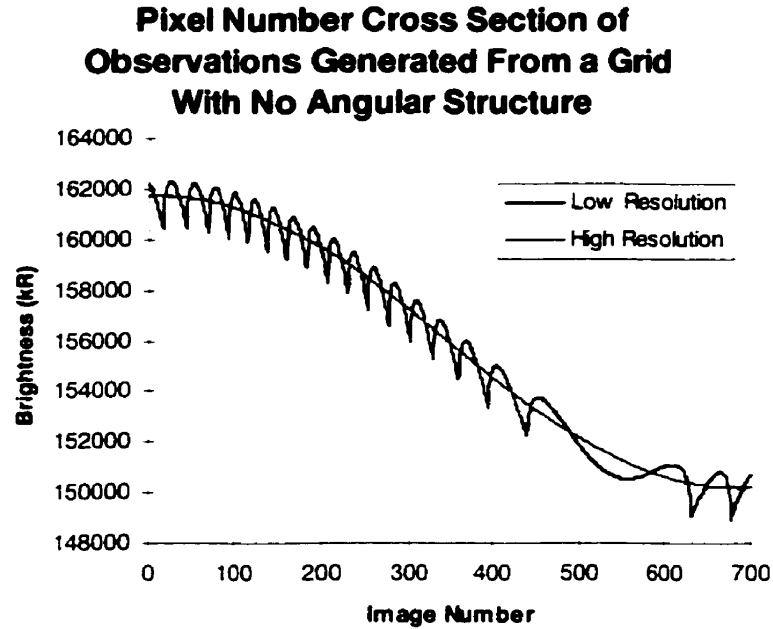


Figure 4.10: Pixel cross sections for the two dimensional plots seen in Figure 4.9. This plot illustrates the differences between the high and low resolution observations.

As the satellite moves around its orbit a line of sight that is tangent at 40.5 km above the surface of the earth is not tangent within the same radial shell throughout the entire volume emission grid. This is due to both the Earth oblateness and the radial shell boundaries of the volume emission grid. This is illustrated in Figure 4.11 which shows the progression of the line of sight through a grid that is characterized by 1 km thick shells. In each case the central altitude of the shell above the surface of the earth is indicated and the lowest 226 km (highlighted in red) of the path is symmetric about the tangent point.

For a line of sight that is tangent above the emission peak a very large fraction of the measured signal comes from the highlighted region near the tangent point. It is readily apparent from the different panels shown in Figure 4.11 that the central altitude and, therefore, the volume emission assigned to the cell changes due to Earth oblateness. The cyclic nature is due to the progression of the tangent point from the top of a shell through to a tangent point at the bottom of the same shell which is equivalent to the

tangent point at the top of the adjacent lower shell. In the top panel of Figure 4.11 the line section only samples emissions from 41.0 km. The following panels illustrate that the line segment samples a weighted average of only two different emissions until the last panel where it samples the same emission as in the top panel. This process repeats itself as the line of sight becomes tangent lower in the grid and, therefore, the contribution of the volume emissions from the lowest 226 km of this line of sight to the pixel brightness is cyclic.

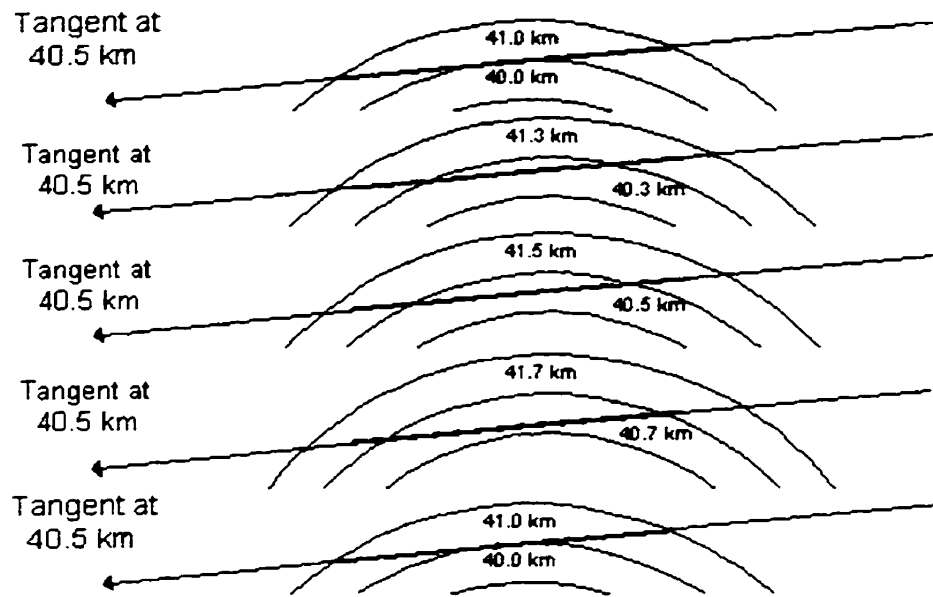


Figure 4.11: Progression of a line of sight that is tangent at 40.5 km above the surface of the Earth. The central altitude of the geocentric shells is marked on the figure.

For a much finer resolution grid the lowest 226 km of the same line of sight samples many more shells and the distribution of the volume emission along this 226 km is more consistent with the distribution between 40.5 and 41.5 km. If the grid cell size is reduced to 0.1 km then the range of volume emissions that the line segment samples is from 40.45 to 41.55, not from 40 to 42 km as shown in Figure 4.11. The cyclic nature still exists but the amplitude of the oscillation is much smaller with the decreased grid cell size.

It is apparent from Figure 4.10 that the low resolution approach cannot provide high quality simulated observations. In Figure 4.12 the high resolution observations are compared with those made at a moderate resolution; in this latter case the resolution parameters *NumTimes* and *NumFOV* were both set to 5 and the grid cell size was 0.04° by 0.200 km. The oscillations that are readily apparent in the low resolution data are still visible at moderate resolution, although they are much smaller, and the shape of the plot more closely matches the almost obscured high resolution data. However, as there is an improvement with increased resolution the values of the parameters *NumTimes* and *NumFOV* were set equal to 7 and a grid cell size of 0.02° by 0.100 km was used for the test data.

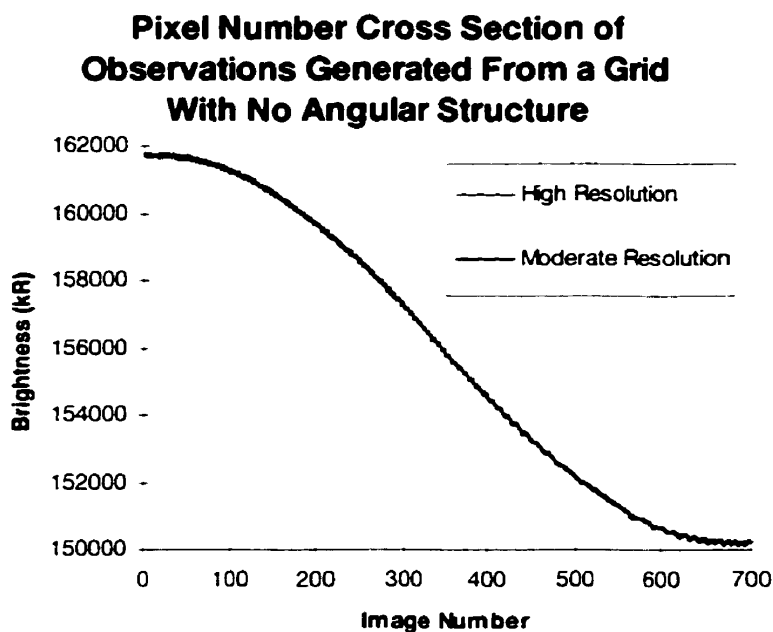


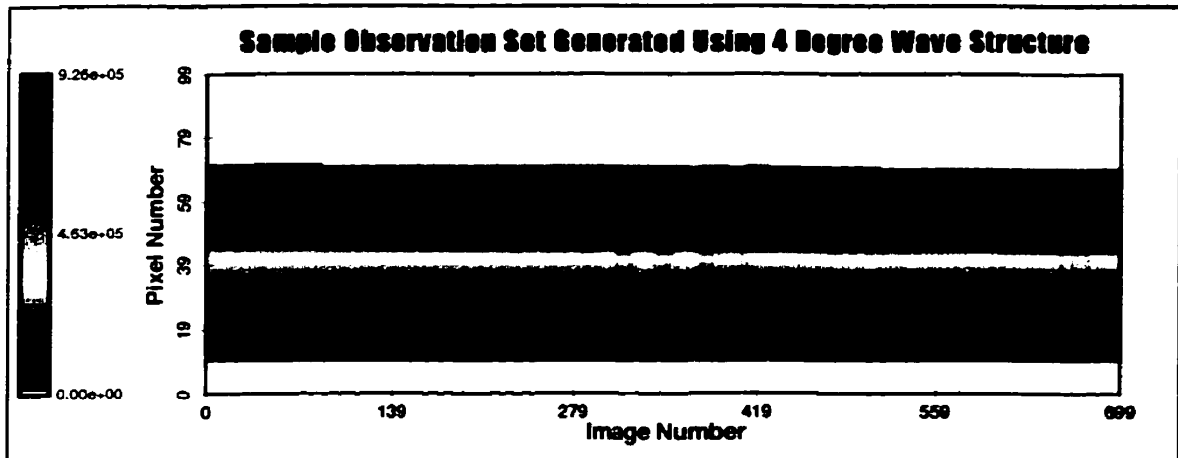
Figure 4.12: Comparison of the pixel cross section for moderate and high resolution observations.

4.6 Sample Observation Sets

The colour plots shown in Figure 4.13 illustrate high resolution observations for different structures and nod modes. These are typical data sets that have been used as input for testing the tomographic retrieval technique. All three data sets correspond to

one image every two seconds. In the top panel the input emission grid corresponds to the 4.0° wave structure shown in Figure 4.6. In the middle panel the input emission grid corresponds to a 30° angular structure (Figure 4.5). In both of these observation sets the imager is operating in the tangent altitude stare mode with the optical axis fixed at 40.5 km.

The data shown in the bottom panel of Figure 4.13 corresponds to that for a nodding satellite. The input volume emission grid had the same 30° angular structure that was used for the stare mode observations shown in the middle panel. In the nod mode the rotation angle θ was varied so that the tangent altitude of the optical axis oscillated between 10.0 km and 60.0 km at a nod rate of 1.0 km/s at the tangent point (Figure 4.2). The white areas in this plot indicate those measurements that contained lines of sight that were tangent outside the emission grid. It is readily apparent that when the optical axis is at a low tangent altitude the bottom pixels of the detector array do not contain valid measurements and as the satellite nods up so the upper pixels do not contain valid measurements. Thus the effect of satellite nod is to eliminate data from the observation set.



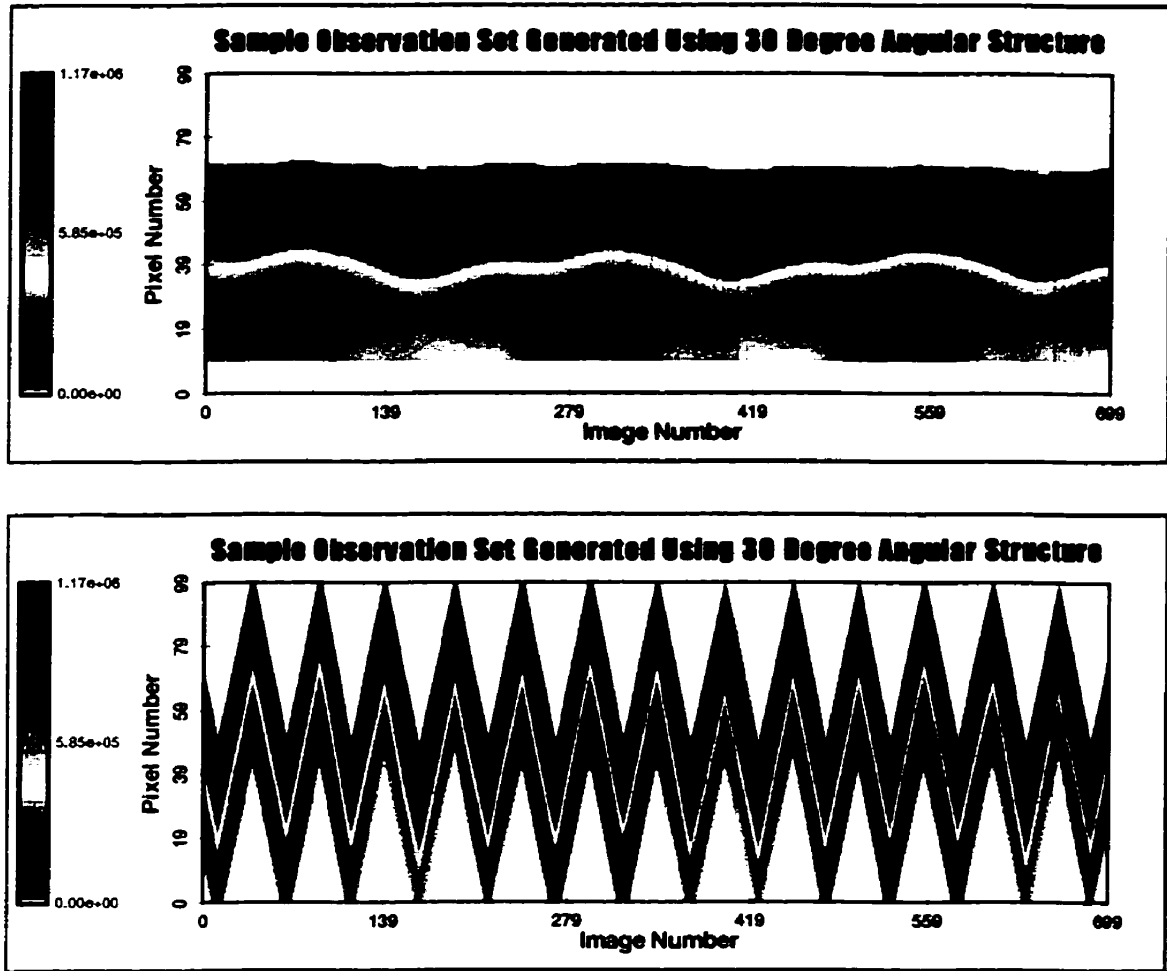


Figure 4.13: Three sample observation sets for different structure types and attitude modes. The top plot was generated using emissions with a four degree wave structure while the lower plots used emissions with thirty degree angular structure.

4.7 Observational Noise Values

One of the primary objectives of the present work has been to determine the effect of noise and missing data on the tomographic recovery technique. Measurement errors that correspond to absolute Gaussian random noise and different signal to noise ratios have been applied to the simulated observation sets and their effects, together with those of missing data (both images and individual pixels), have been evaluated.

These poor data effects are shown in Figure 4.14 which uses the same observation set as that seen in the top panel of Figure 4.13. However, in Figure 4.14 there is a uniform

20% probability of missing each image in the set and each measurement has an associated noise that is absolute Gaussian random, with a standard deviation of 2 MR. It is readily apparent that there are many differences between the plot in Figure 4.14 and that in the top panel of Figure 4.13.

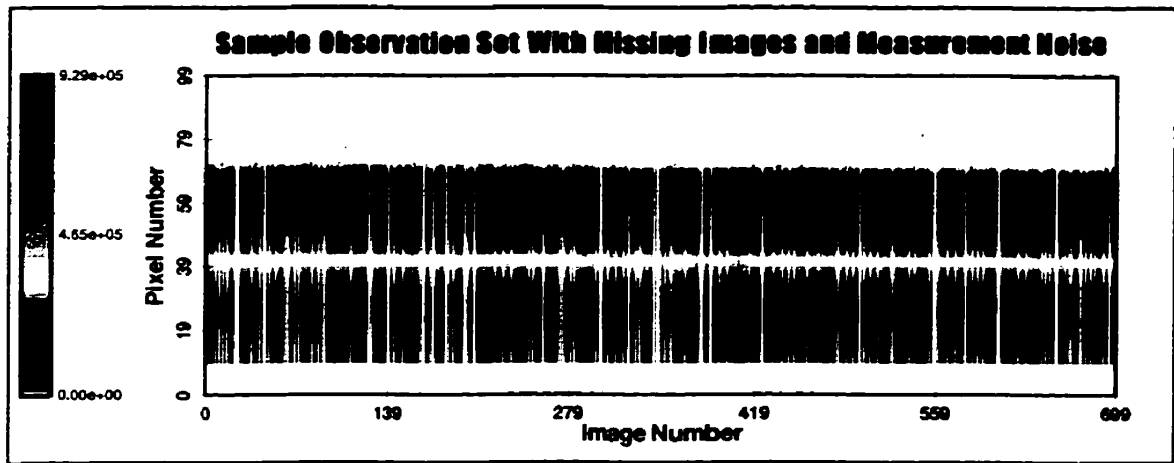


Figure 4.14: A sample observation set with a uniform 20% probability of having each image missing and Gaussian random noise, standard deviation of 2 MR.

4.8 The Image Set Parameters

The values shown in Table 4.1 represent both the fixed parameters and the parameters that were allowed to vary between the different tests. The fixed parameters are constant for each set of observations; the final fixed parameter the *Nod Rate* is only valid for the nod mode and does not apply to the stare mode. Test conditions that are discussed in later parts of this thesis have used different values for the variable parameters in the calculation of the model observations.

Fixed Parameters	Variable Parameters
<i>NumPixels</i> : 100	<i>NumImages</i> : Normally 700
<i>OptAxisPixelNumber</i> : 20	<i>Image Rate</i> : 1, 2 and 3 s/image
<i>FOV</i> : 2.03°	<i>Nod Range</i> : Stare, 10 to 60 km and 10 to 110 km
<i>NumFOV</i> : 7	<i>Signal to Noise Levels (S/N)</i> : 10, 20, 50, 100 and 200
<i>R_{sat}</i> : 6978 km	<i>Absolute Noise Levels</i> : 500, 1000, 2000, 5000 and 10000 kR
<i>Speed Sat</i> : 7.559 km/s	<i>Missing Pixel Levels</i> : 1 in 100, 50, 20, 10, 5 and 2; and every other pixel
<i>Inclination</i> : 97°	<i>Missing Image Levels</i> : 1 in 100, 50, 20, 10, 5 and 2
<i>Nod Rate</i> : 1 km/s	<i>Structure Levels</i> : NONE, 180°, 60° and 30° <i>Angular Structure</i> together with 1°, 2°, 3°, 4° and 5° <i>Wave Structure</i>
<i>NumTimes</i> : 7	
<i>Integration Time</i> : 1 s	
<i>DeltaShell for Observations</i> : 100 m	
<i>DeltaAngle for Observations</i> : 0.02°	
<i>ShellMin</i> : 6384 km	
<i>ShellMax</i> : 6482 km	

Table 4.1: The image set parameters used for various test conditions in this thesis.

CHAPTER V

THE TWO DIMENSIONAL ATMOSPHERIC TOMOGRAPHY TECHNIQUE

5.1 Introduction

The tomographic technique presented in this chapter provides a basis for the current work on satellite based atmospheric tomography. The basic algorithmic approach, including the inputs, initial starting conditions and termination conditions for the developed technique, is presented here. This chapter, together with the material in Chapters 3 and 4, provides all of the necessary background information for the developed satellite atmospheric tomography technique.

5.2 The Current Technique

The tomographic technique that is presented in this thesis began development as a tool to deconvolve Fabry-Perot images (Lloyd and Llewellyn, 1989). In that work Lloyd and Llewellyn also showed how the Fabry-Perot algorithm could be adapted to allow retrieval of vertical airglow profiles from rocket photometer data. McDade and Llewellyn [1991a] expanded on these ideas and successfully modified the technique to recover a two dimensional airglow profile from rocket photometer data. McDade and Llewellyn also extended this work further with simulations of both rocket [1991b] and satellite [1993] tomography. It is the satellite tomography simulations that are the basis for the present work.

5.2.1 Background to the Current Technique

As a part of a thermospheric wind study regular observations of the airglow were made with a Fabry-Perot interferometer (resolving power 10^6) and the ring pattern images were stored as compressed column vectors. Subsequent analysis indicated that these ring patterns were not in fact circular so that the stored images were blurred and the retrieval of the atmospheric winds required that the stored images be de-blurred. In their

approach to this deblurring Lloyd and Llewellyn [1988] presented the problem as a linear system of equations

$$\mathbf{B} = \mathbf{AT} \quad [5.1]$$

where the matrix \mathbf{B} (indexed by i) is the measured image of the discrete object \mathbf{T} (indexed by j) which is blurred, or distorted, by the apparatus dependent matrix \mathbf{A} . Lloyd and Llewellyn developed a technique, the Maximum Probability (MP) method, that considered the most probable contribution of any element j to the measurement B_i , given that the T_j values are distributed according to photon counting, or Poisson, statistics. They developed the concept that each T_j value is the mean value, given that the contribution of that object element to the image is P_{ij} , and in the mean $P_{ij} = A_{ij}T_j$. Lloyd and Llewellyn used a Lagrange multiplier technique to develop the two equations (5.2 and 5.3) that were required for their work

$$P_{ij} = \frac{(B_i + n_i)A_{ij}T_j}{\sum_j A_{ij}T_j} - 1 \quad [5.2]$$

$$T_j = \frac{\sum_i P_{ij}}{\sum_i A_{ij}} \quad [5.3]$$

where P_{ij} is the most probable value of the contribution to the measurement B_i , given that the mean value of the object is T_j and n_i is the number of elements that contribute to measurement i . These equations are iterative. Thus the application of equation 5.2 to an initial estimate of the \mathbf{T} object elements yields a set of P_{ij} values that may be used with equation 5.3 to give a new set of object elements. Lloyd and Llewellyn showed that this technique was effective for the deconvolution of Fabry-Perot images. They further demonstrated that a system of linear equations

$$\mathbf{O} = \mathbf{LV} , \quad [5.4]$$

where \mathbf{O} is a set of rocket photometer data, \mathbf{V} is a vertical airglow profile and \mathbf{L} is a set of geometry and instrument dependent weights, could be solved in a similar manner to determine the vertical airglow profile.

Later McDade *et al.* [1991] were able to extend the MP technique to recover the two dimensional N_2^+ volume emission profile in an aurora from rocket photometer data. The matrix L was calculated from a knowledge of the rocket attitude and instrument performance. This matrix also included albedo contributions to the measured signals. The two dimensional volume emission profile obtained by these investigators is shown in Figure 5.1.

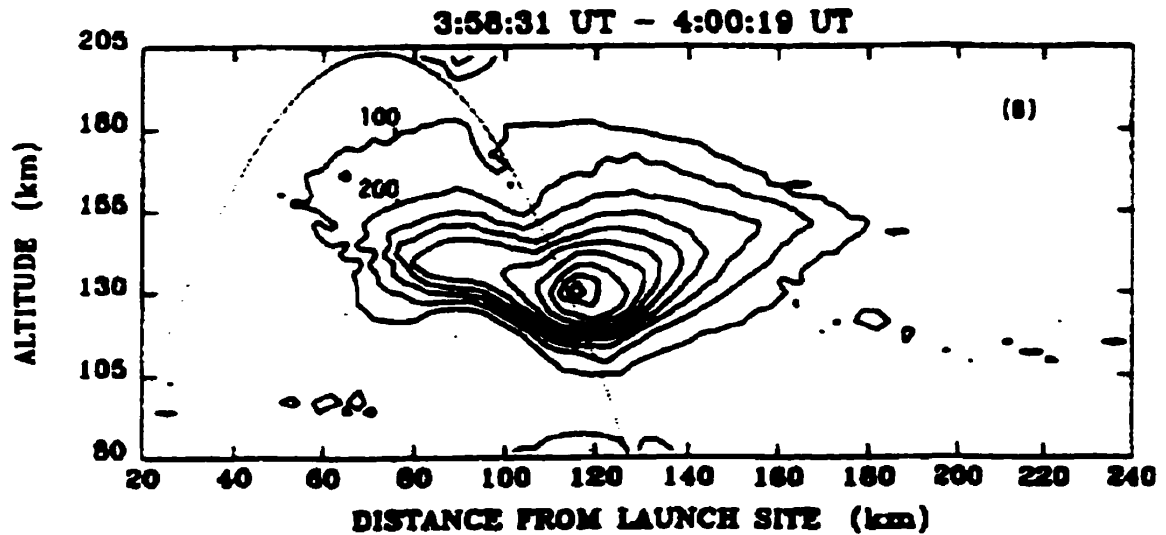


Figure 5.1: The distribution of the 391.4 nm emission obtained from a tomographic inversion of observations made in a rocket tomography experiment (McDade et al., 1991).

In an extension of their work McDade and Llewellyn [1991] simulated other rocket experiments that considered a non-stationary auroral form. These same authors (McDade and Llewellyn, 1993) also developed a simulation of photometric measurements made with a simple vertical imaging instrument on a satellite platform. They demonstrated that the modified tomographic equations, 5.5 and 5.6,

$$P_{ij} = \frac{(O_i + n_i)L_{ij}V_j}{\sum_j L_{ij}V_j} - 1 \quad [5.5]$$

$$V_j = \frac{\sum_i P_{ij}}{\sum_i L_{ij}} \quad [5.6]$$

could be used to retrieve horizontal structure in an arbitrary two dimensional airglow profile, where O_i is a single photometric measurement, n_i is the number of atmospheric grid cells sampled by the measurement, L_{ij} is the path length of the i^{th} measurement through the j^{th} cell, V_j is the retrieved volume emission at grid cell j , and P_{ij} is the expected contribution of volume emission V_j to measurement O_i .

The remainder of this thesis deals with, changes to and the application of, these equations and the analysis of the results produced by the adapted tomographic technique.

5.2.2 Changes to the Original Equations

As noted above equations 5.5 and 5.6 were used by McDade and Llewellyn [1993] in their model representation of two dimensional tomography from a satellite platform. However, if equation 5.5 is substituted into 5.6 the modified representation shown in equation 5.7 is obtained;

$$V_j^{(n)} = \frac{\sum_i \left(\frac{(O_i + n_i) L_{ij} V_j^{(n-1)}}{\sum_j L_{ij} V_j^{(n-1)}} - 1 \right)}{\sum_i L_{ij}} \quad [5.7]$$

superscripts (n) and $(n-1)$ indicate the volume emission at the current (n^{th}) and previous $([n-1]^{\text{th}})$ iterations respectively.

While equation 5.7 is complete it may be simplified for certain assumptions. If O_i , the brightness measurement, is large compared to n_i , the number of volume emission elements the measurement samples, then n_i may be omitted from the equation. Similarly the -1 term can be eliminated if it is small compared with the other term in the numerator. If these terms are both removed from equation 5.7, then the $V_j^{(n-1)}$ term in the numerator of the summation can be taken outside the summation as it does not depend on the observations i . The resulting formulation is given in equation 5.8,

$$V_j^{(n)} = V_j^{(n-1)} \frac{\sum_i \left(\frac{O_i L_{ij}}{\sum_j L_{ij} V_j^{(n-1)}} \right)}{\sum_i L_{ij}}. \quad [5.8]$$

The denominator in equation 5.8 is dependent only on the volume emission element j and those observations that sample it. It is simply the sum of the geometric path lengths of the observations i through the volume emission element j . This summation can be represented by the value W_j (equation 5.9) and, as it has no dependence on the observation i , placed in the summation in the numerator of equation 5.8, as shown in equation 5.10.

$$\sum_i L_{ij} = W_j. \quad [5.9]$$

$$V_j^{(n)} = V_j^{(n-1)} \sum_i \left(\frac{O_i}{\sum_j L_{ij} V_j^{(n-1)}} \frac{L_{ij}}{W_j} \right). \quad [5.10]$$

The right hand fractional term contained within the summation in equation 5.10 divides the path length, for each observation i through element j , by the sum of the path lengths that intersect that element. Obviously

$$\sum_i \frac{L_{ij}}{W_j} = 1 \quad [5.11]$$

must hold as the summation of these terms, over all observations that intersect the element j must equal unity (see equation 5.9). This implies that the term L_{ij} / W_j , within the summation in equation 5.10, is simply a normalized weighting factor. For convenience this term is defined (equation 5.12) as β_{ij} ,

$$\frac{L_{ij}}{W_j} = \beta_{ij} \quad [5.12]$$

and is only geometry dependent. In the present work other weighted averages, such as those given in equation 5.13,

$$\frac{L_{ij}^m}{\sum_i L_{ij}^m} = \beta_{ij} \quad [5.13]$$

where m is an arbitrary integer, have also been examined.

In their work McDade and Llewellyn [1993] used the summation in the denominator of equation 5.10 to represent the modeled observation. This modeled observation is based on the previous estimate of the volume emission elements and can be represented by equation 5.14.

$$\sum_j L_{ij} V_j^{(n-1)} = O_{i_{cr}}^{(n-1)}. \quad [5.14]$$

This is a single line of sight simplification of the modeled observations, that were discussed in detail in Chapter 3, although a more accurate representation of $O_{i_{cr}}^{(n-1)}$ is given by equation 3.13a or 3.13b. The substitution of equations 5.12 (or 5.13) and 5.14 into equation 5.10 gives the simplified iterative expression shown in equation 5.15,

$$V_j^{(n)} = V_j^{(n-1)} \sum_i \left(\frac{O_i}{O_{i_{cr}}^{(n-1)}} \beta_{ij} \right). \quad [5.15]$$

This equation simply states that the next estimate of the volume emission, V_j , is the current value multiplied by a weighted average of all observations that sample that cell, divided by their estimates from the previous volume emission solution.

5.2.3 Comparison of McDade and Llewellyn Approach to MLEM Technique

A direct comparison of equations 5.15 and 2.16 indicates that the McDade and Llewellyn technique is actually the MLEM technique if β_{ij} is defined by equation 5.13 with $m = 1$. One part of this thesis work investigated the possibility of adjusting m , in equation 5.13, to suit the satellite geometry and provide better, but not necessarily MLEM, solutions for the problem of imaging in the limb. This is similar to the work of Snyder *et al.* [1987] (Section 2.3.1.3).

5.2.4 Algorithm Concept for Atmospheric Emissions Measured from a Satellite Platform

Section 5.2.2 outlined the tomographic equations that are used in the present work. These equations can also be represented by block diagram models, Figures 5.2 and 5.3, that illustrate the integration of the equations into an effective algorithm for the retrieval of a two dimensional volume emission profile from the satellite airglow measurements. Figure 5.2 shows the block diagram approach to the entire tomographic inversion procedure. The observations O_0 through $O_{NumObs-1}$, the brightness measurements made by the optical instrument (Section 4.6), are the primary inputs to the tomographic inversion algorithm. The value $NumObs$ is the number of measurements contained within the entire observation set where $NumPixels$ measurements are taken simultaneously in a single image (Chapters 3 and 4).

A set of ancillary data is required with the actual observations in order to model the estimated signals and to define the size and resolution of the volume emission recovery grid. This data set includes the ω , ϕ , θ , R_{sat} and α values, (for each image I) that define the orientation and position of the spacecraft at relevant times during the measurements. These five parameters (Sections 3.3.2 and 4.3.3) are the three spacecraft rotation angles, the satellite distance from the centre of the Earth and the angle along the satellite orbit respectively. The parameters are required $NumTimes$ for each image in the observation set where $NumTimes$ is the temporal resolution factor in the retrieval.

A second ancillary data set (β and δ values) contains the parameters that are needed (for each pixel p) to model the optical instrument (Section 3.3.1). A set of angles, β_k , define the instrument field of view and the values δ_k define the instrument sensitivity over the field of view. There are $NumFOV$ values of these parameters for each pixel in the imager where $NumFOV$ is the field of view resolution factor in the retrieval. The final set of ancillary data refers to the grid used for the volume emission profile recovery. The required grid parameters are the minimum and maximum radial shell distances and the radial and angular grid cell sizes. These ancillary data sets are required to forward model

the observations (equation 5.15) and determine the β_j weighting factors (equation 5.13) that are used in the inversion.

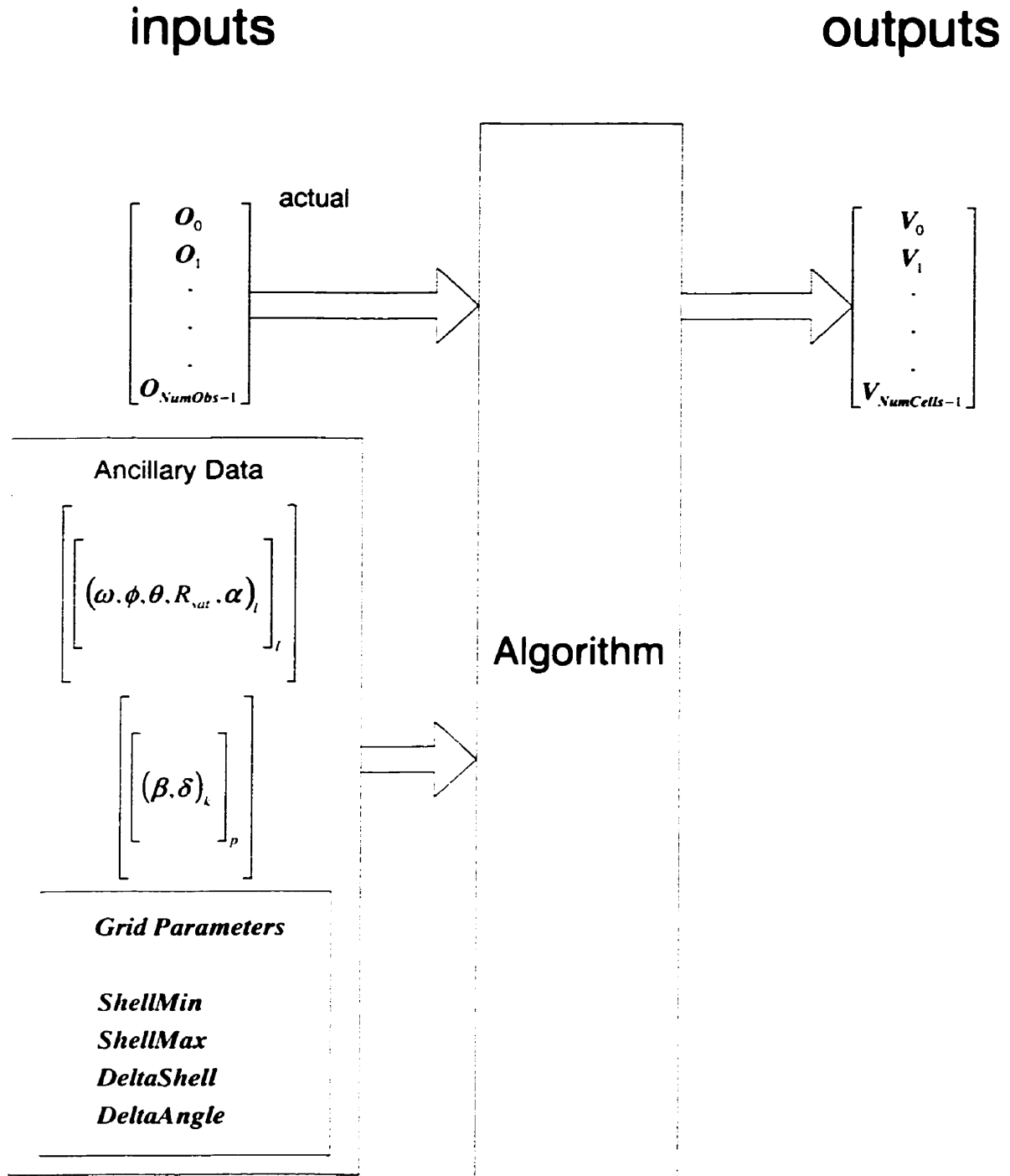


Figure 5.2: The inputs and outputs of the tomographic algorithm used to retrieve the two dimensional volume emission profiles from the brightness observations made from a satellite platform.

Figure 5.3 illustrates how the iterative equations manipulate the observations to produce the final volume emission profile. The current iterative estimate, the $(n-1)^{th}$, of the volume emission profile is used, together with the ancillary data, as input to a model that provides the next estimate of the observations. The estimates of the observations and the actual observations are compared and, as shown in equation 5.15, the observations i that sample an element j are divided by their modeled counterparts. If the weighted average of these ratios is high (*i.e.* greater than unity) then the volume emission value contained within that element is raised (*i.e.* multiplied) by the weighted average. Similarly if the weighted average is low the contribution from the cell is decreased. This process is repeated at every cell location to yield a new set of volume emission elements.

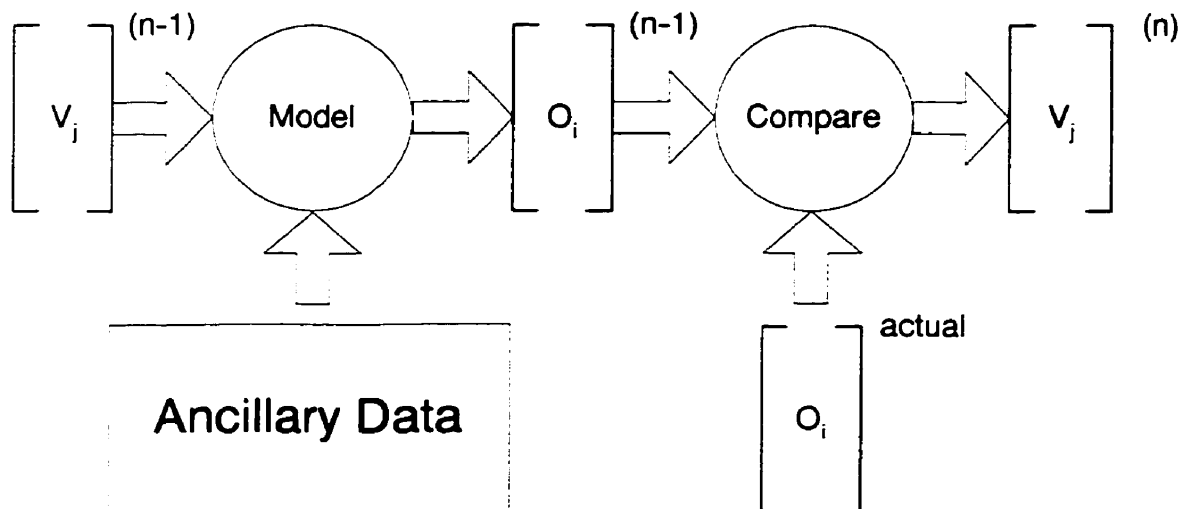


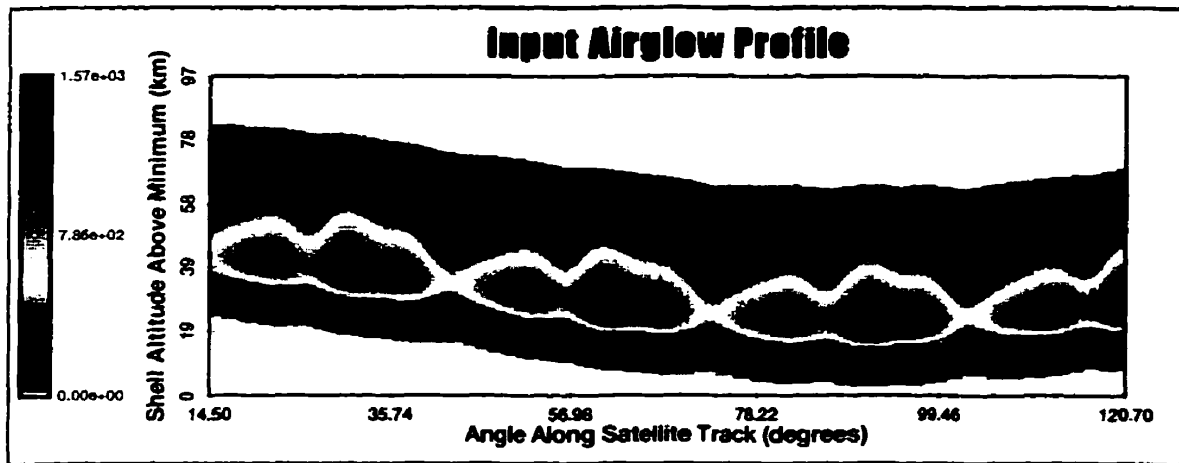
Figure 5.3: A block and data flow diagram for the satellite tomography algorithm.

5.2.5 The Initial Estimate

The process outlined in Figure 5.3 requires an initial estimate for the volume emission profile. In agreement with McDade and Llewellyn [1993] the present work has used a uniform volume emission profile. If the volume emission values, $V_j^{(0)}$, in equations 5.14 and 5.15 are identical then the actual initial estimate is given by equation 5.16,

$$V_j^{(1)} = \sum_i \left(\frac{O_i}{\sum_j L_{ij}} \beta_{ij} \right). \quad [5.16]$$

Thus the actual initial estimates, $V_j^{(1)}$, for the algorithm are the weighted averages, over all observations, for the assumption that the profile is uniform only along each line of sight. In this way the geometry and the magnitudes of the observations dictate the initial estimate. The top panel in Figure 5.4 is an input volume emission profile and the middle panel is the initial estimate based on equation 5.16. It is readily apparent that even the initial estimate indicates some of the structure that is seen in the input volume emission. For completeness the final recovered solution, after 30 iterations of equation 5.15, is given in the bottom panel of Figure 5.4.



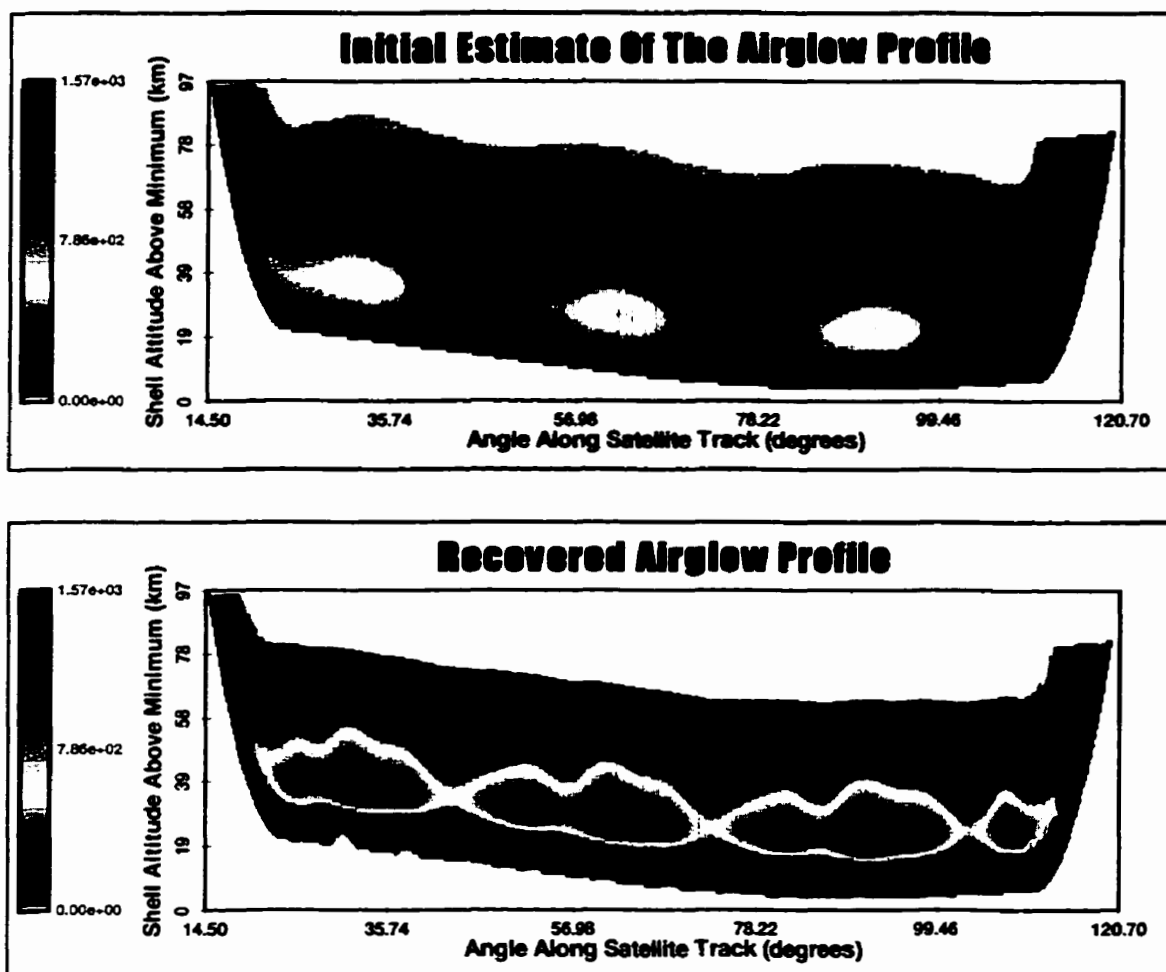


Figure 5.4: An input volume emission profile, the initial estimate of the profile given by equation 5.16, and the final estimate of the profile after 30 iterations.

5.2.6 Estimate of Retrieval Accuracy

It is necessary to estimate the accuracy of each tomographic retrieval. This is done by a percentage difference comparison between the retrieved and the known input profiles. A percentage error distribution is obtained from this comparison and fitted with a quadratic function. There are two parameters from this quadratic fit. They are the width of the error distribution and the offset of the peak percentage error from 0%; a narrow width and small offset implies an accurate retrieval. A more complete discussion of this error analysis technique is given in Appendix C.

5.3 Computational Considerations

The algorithm concept discussed in Section 5.2.4 is computationally intensive and techniques have been developed to minimize the computational load without compromising the retrieval accuracy. This section, together with Appendix D, outlines the major computational considerations and presents the techniques that have been used to optimize the speed of the retrieval process.

5.3.1 The Termination Condition

The termination condition for the algorithm corresponds to the number of iterations that are needed to produce the required solution. As each iteration requires significant computation it is important the retrieval not be continued beyond the point of insignificant gain. In agreement with McDade and Llewellyn [1993] the termination condition in the present study is a defined number of iterations.

The typical shape of the curves that represent the widths of the quadratic fits to the error distribution histograms (Appendix C), for the recovered volume emission profile and the observation estimates, are shown in Figure 5.5. In this case the input volume emission grid was compared to the solution grid after each iteration of the algorithm. The observation estimates were similarly compared to the actual measurements after each iteration. Only the quadratic fit widths for the fifth iteration and beyond are shown as the error distributions are non-Gaussian for the first few iterations. Since a narrow width implies an accurate match between the estimate and the true volume emission profile it is apparent from Figure 5.5 that there is no significant improvement after about 30 iterations. The error curves flatten at this point and the estimated observations are not significantly closer to the measurements with further iteration. For this reason the majority of inversions in this thesis have used a termination condition of thirty iterations. The reconstructed estimates of the observation sets and the actual input observation sets for Figure 5.5 are shown in Figure 5.6. Again it is readily apparent that there are no obvious differences in the two data sets after 30 iterations.

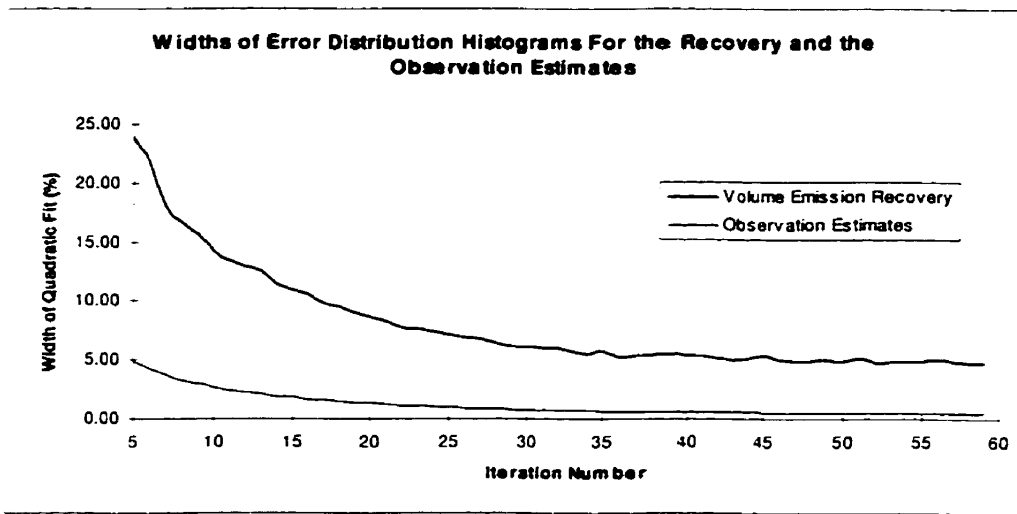


Figure 5.5: The error distribution histogram widths for both the recovered volume emissions and the estimate of the observations. This plot is typical of all good recoveries where there is effectively no decrease in the histogram width after 30 iterations.

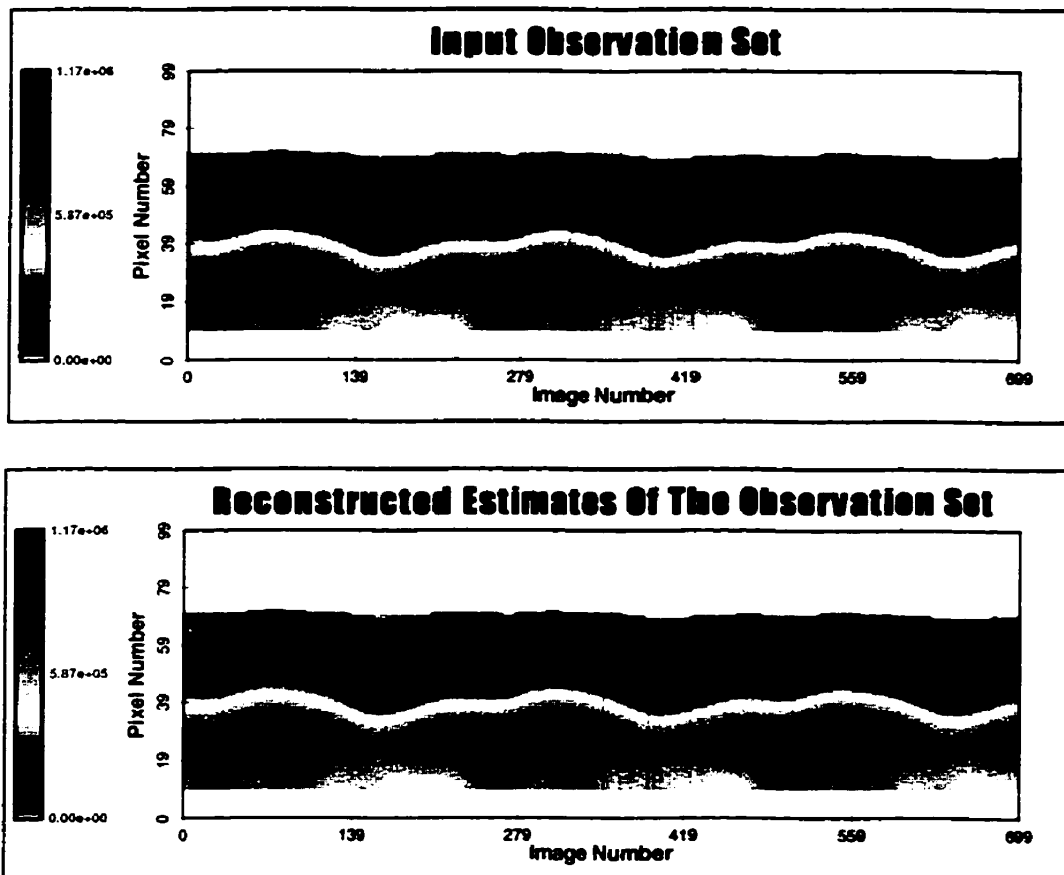


Figure 5.6: An input observation set and the estimate of the observation set based on the recovery grid after 30 iterations.

5.3.2 Observation Estimate Precision

There are two important considerations for the precision and speed of the observation estimates used in the tomographic retrieval process; these are the resolution factors *NumFOV* and *NumTimes* and the computational precision of the path length terms, L_{ij} .

A modified floating point scheme has been employed (Section D.1) to store the calculated path lengths (L_{ij} values in Section B.3) internally in the computer memory. This approach uses only two bytes to store the integer and decimal parts of the L_{ij} values. A series of tests (Section D.1) have indicated that this scheme is much more computationally efficient than a floating point representation and does not compromise precision.

The temporal and field of view resolution factors, *NumTimes* and *NumFOV*, are also required parameters for the modeled observations used in the tomographic technique. A number of tests with higher resolution factors indicated that these did not improve the quality of the recoveries. As higher resolution parameters require additional computation time, the values for *NumTimes* and *NumFOV* used for the estimates of the observations were both set to one. This means that it is only necessary to generate a single line of sight modeled observation estimate within the inversion process. This is different from the values of seven, for *NumTimes* and *NumFOV*, that have been used to calculate the test data. For the remainder of this thesis equation 5.14 is used to generate the observation estimates in the tomographic retrieval.

5.3.3 The Number of Observations in a Retrieval and Joining Retrievals

The available computational power also influences the number of observations (images) that can be included in a single tomographic retrieval. As noted the path lengths are computationally intensive and are required at each iteration. Therefore, these values must be calculated only once and stored in order to optimize the retrieval process. The available RAM and the path length precision (Section D.1) determine the number of path lengths that can be efficiently stored and retrieved. Limiting the number of

observations that can be used in a single recovery also impacts the inversion accuracy as well as having a direct correlation with the 'edge effect' that is discussed in Section 6.5.

The fact that only a limited number of images can be used in a single inversion implies that successive recoveries must be merged to produce the final solution. The technique that has been developed to merge recoveries is discussed in Appendix D (Section D.2). This appendix also includes the computational optimization results for different imaging rates and the total number of images used in a single inversion. The results given in Section D.2 indicate that an image set size of 700, which is the maximum that the current computational power can handle efficiently, is sufficient although not optimal. Therefore, unless otherwise stated, an image set size of 700 has been used throughout this thesis, independent of the imaging rate.

CHAPTER VI

THE SAMPLING GEOMETRY AND ITS EFFECT ON THE INVERSIONS

6.1 Introduction

For any tomographic technique the number of times and the way in which each grid cell is sampled impacts on the quality of the retrieval. This is especially true for atmospheric tomography from a satellite platform because of the restrictive geometry. These restrictions result in three main regions for the recovery grids used in the current technique. Each of these regions, primarily identified by their sampling, can be subdivided with retrieval characteristics that are different in each of the sub-regions. The number of times and the way in which each grid cell is sampled are discussed in this chapter particularly in connection with the 'edge effect' that results in a region of poorly recovered data at the angular extremes of the retrieved volume emission grids.

6.2 Intersection Geometry

There are eight different ways that a grid cell, with minimum and maximum radii and two angular bounds, can be intersected by a straight line of sight. The line of sight can intersect the boundaries of the cell in a *Shell-Shell*, *Angle-Angle* or *Shell-Angle* fashion. However, there are variations within these three intersection types that produce eight separate and important intersection types.

Figure 6.1 shows a grid cell that is intersected by three different lines of sight. Line of sight 1 cuts directly through the cell in an *Angle-Angle* manner; intersections of this type only occur when the line of sight is tangent in the same shell as the cell or in a nearby shell. The maximum difference in the radial distance between the tangent point of the line of sight and the shell that contains the cell, for these *Angle-Angle* intersections, is determined by the angular size of the cell.

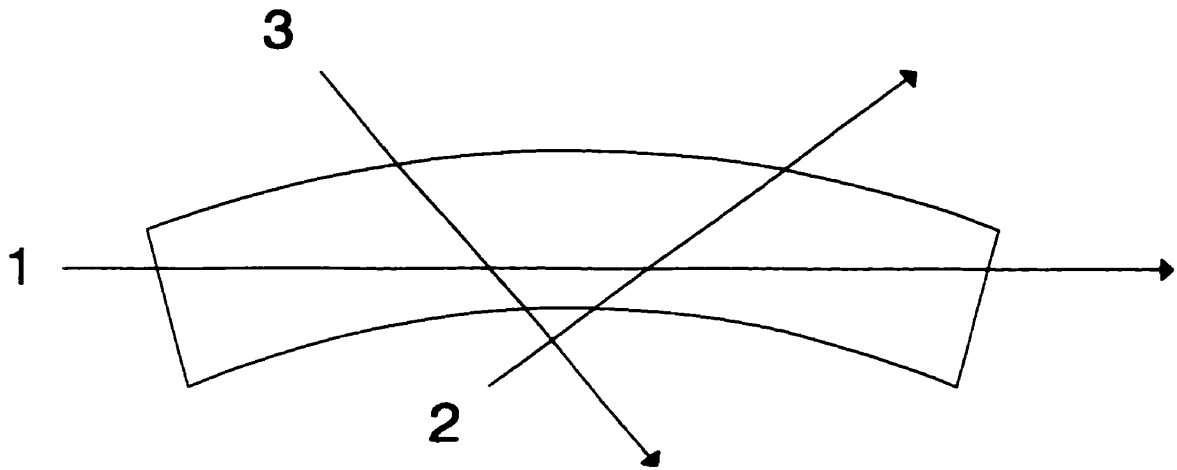


Figure 6.1: The three standard intersection types for lines of sight that sample a grid cell. These are: 1) Angle-Angle, 2) Shell-Shell, tangent before the cell and 3) Shell-Shell, tangent after the cell.

The two other lines of sight (2 and 3) in Figure 6.1 are both *Shell-Shell* intercepts. While these lines-of-sight appear to be the same there is an important difference between them. Line of sight 2 is tangent, with respect to the radial grid, before it intersects the cell and line of sight 3 is tangent after it leaves the cell. This seemingly minor difference is important for the tomographic retrieval.

The remaining five possible types of intersection for a line of sight with a grid cell are shown in Figure 6.2. These include four different *Shell-Angle* intercepts and one *Shell-Same Shell* intercept. Intercept types 4 and 5 can occur if the line of sight is tangent before it enters the cell while intercept types 6 and 7 can only result if the line of sight is tangent after it leaves the cell. While these four types appear to be quite similar they have slightly different effects on the tomographic recovery. The last intercept type (8) is the *Shell-Same Shell* intercept that has only a minor effect on the quality of the tomographic recovery. The effects of these different intercept types on the tomographic recovery are discussed in more detail in Chapter 7.

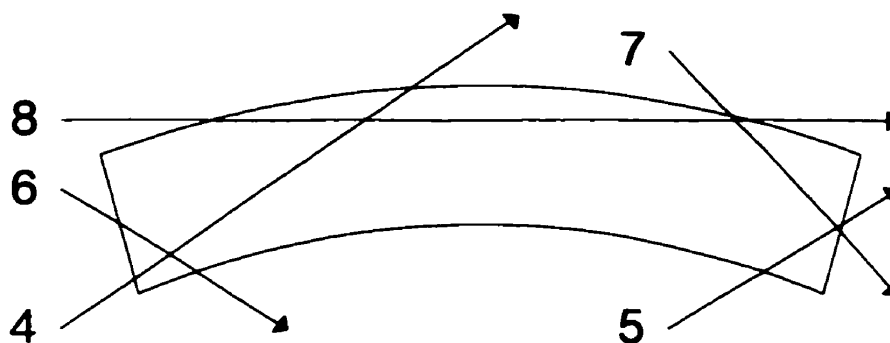


Figure 6.2: The five other intersection types for lines of sight that sample a grid cell.

6.3 Sampling Density

The sampling density is defined as the number of times that each cell, in the two dimensional recovery grid, is sampled by different lines of sight. The sampling density for a grid with cells 0.2° by 1.0 km is shown in Figure 6.3. This plot corresponds to a 700 image observation set, with the tangent altitude of the optical axis fixed at 40.5 km above the surface of the Earth, and a 0.5 Hz imaging rate. Nine different lines of sight are superimposed on the sampling density grid. These lines of sight appear to be parabolic due to the rectangular representation of the radial grid and correspond to the first, central and last image in the set for pixel numbers 10, 50 and 80 respectively (from bottom to top). Pixel 10, the lowest line of sight drawn for each image, is always tangent at an altitude near 30.5 km.

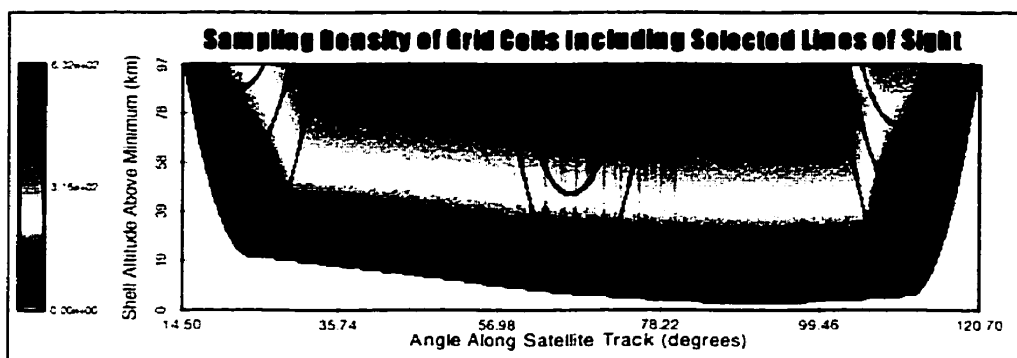


Figure 6.3: The number of times that each grid cell, 0.2° by 1.0 km, is sampled by 700 images taken once every two seconds. The superimposed lines of sight are for pixels 10, 50 and 80 for each of the images 0, 349 and 699.

As already noted previously there are three distinct regions within the recovery grid and these are indicated by the selected lines of sight superimposed on the sampling density plot shown in Figure 6.3. Clear evidence for these regions is shown in the cross section plot presented in Figure 6.4. In the centre of the grid (with respect to the angular dimension) each shell has a nearly uniform sampling density. The slow rise in the sampling density seen in this figure is due to the earth oblateness, the high frequency variation is due to the discrete (non-continuous) sampling. At the angular edges of the grid the uniformity in the sampling density associated with the central region is absent. This is apparent from the two dimensional sampling density grid (Figure 6.3) and the radial shell cross section (Figure 6.4) where there are large changes in the sampling density at both the left and right edges of the grid.

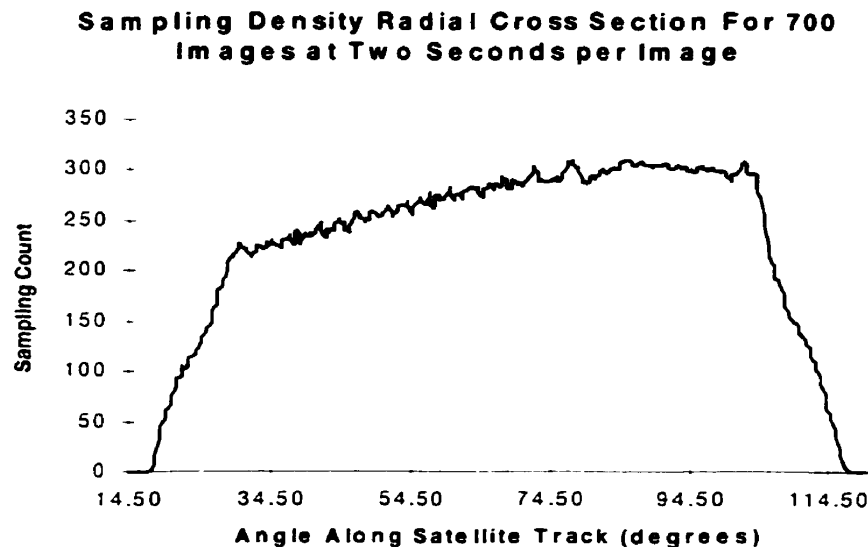


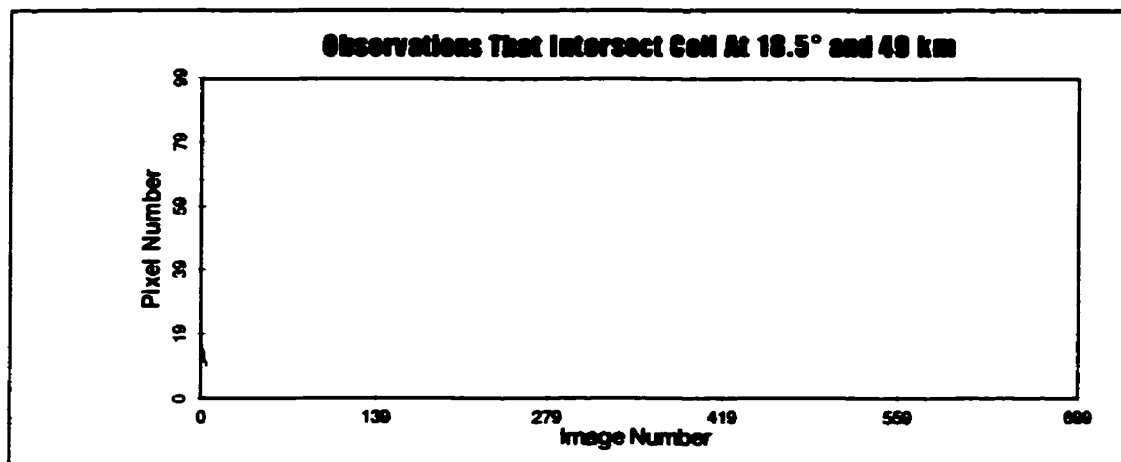
Figure 6.4: A radial shell cross section from the plot shown in Figure 6.3. This cross section illustrates the flat central region, where almost constant sampling occurs, and the left and right regions where there are large changes in the sampling density.

6.4 The Three Regions of Interest

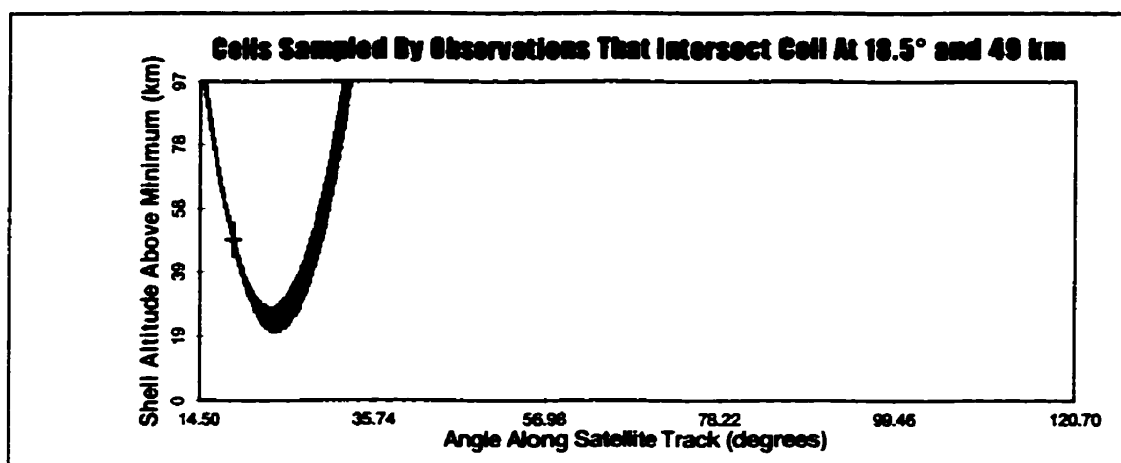
The three regions defined by the sampling density plot shown in Figure 6.3 are sampled differently. These regions are the left and right hand sides of the grid, or regions (L) and (R), where the sampling is non-uniform (with respect to angle) for a given radial shell,

and the centre of the grid, region (C), where the sampling is approximately uniform for a given radial shell. These regions can also be characterized by the way in which the lines of sight intersect the different grid cells. If the minor intersections, types 4 through 8, are ignored then the regions (L) and (R) are both characterized by a predominance of *Shell-Shell* type intercepts. On the extreme left of the grid all lines of sight are tangent after they have intersected the cell of interest while on the extreme right all lines of sight are tangent before they enter the cell. These are the type 3 and 2 intersections respectively. In the central (C) region the dominant intersection type is altitude dependent.

It is of value to divide each of the (L) and (R) regions into two separate sub-regions. Regions (L-1) and (R-1) are found at the angular extremes of the recovery grid. The region (L-1) is defined as being to the left of the line joining the tangent points of the lines of sight of the first image; the region (R-1) is defined in an analogous way. For region (L-1) and image 0 the geometry severely restricts *Angle-Angle* intercepts; similarly, for image 699, *Angle-Angle* intercepts to the right of the line joining the tangent points are also restricted. The upper panel in Figure 6.5 indicates those observations that intersect cell (92,49), or the cell at *AngleNumber* 92 and *ShellNumber* 49 (highlighted by a cross in Figure 6.5b), in Region (L-1). The very limited nature of this observation set is indicated by the short curve in the bottom left hand corner of the Image-Pixel observation grid. Each of the observations in this set (ignoring the minor intersection types 4 through 7) enter the cell through the top of the shell and exit at the bottom. This is more clearly seen in the lower panel in Figure 6.5 which illustrates those cells sampled by the observations. The lower plot is the superposition of all lines of sight that intersect cell (92,49) with the lowest points indicating the tangent points. The sampled set of cells is not symmetric about the cell of interest and includes only a small fraction of the entire grid. Other cells in this (L-1) region of the grid are sampled in an almost identical manner.



(a)

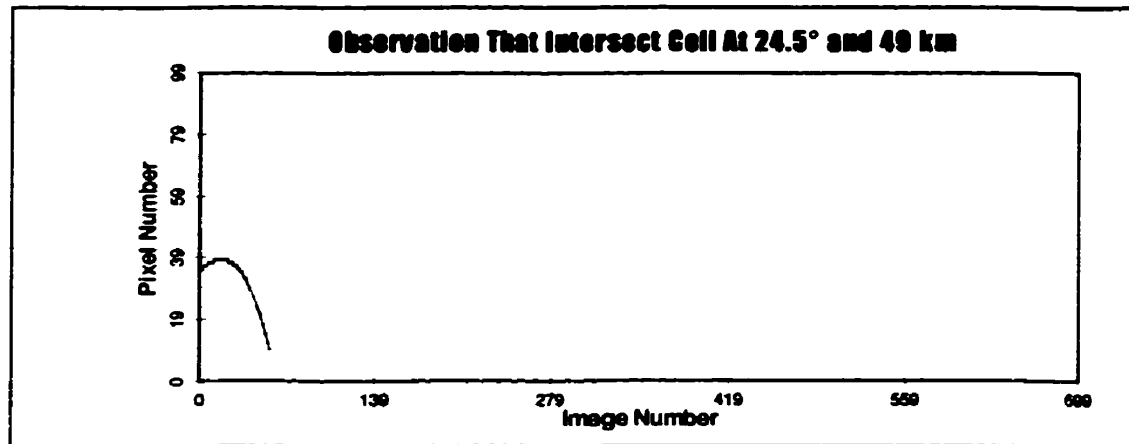


(b)

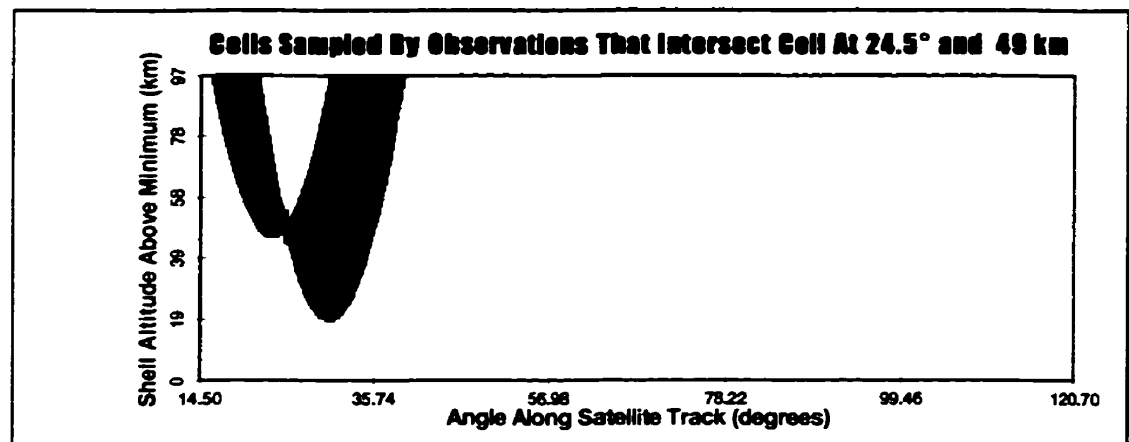
Figure 6.5: Observations that intersect the grid cell at AngleNumber 92 and ShellNumber 49 in the (L-1) region (a) and the other grid cells that these observations sample (b).

The upper plot in Figure 6.6 shows those observations that intersect a cell 6° to the right of the cell shown in Figure 6.5. In this case there is a much larger observation set. The lower plot in Figure 6.6 indicates the grid cells that are sampled by these observations. While the sampled cells fill a larger fraction of the grid the sampling is still not symmetric as the majority of the observations are tangent after passing through the cell. This region is defined as the (L-2) transition region; it includes some type 1, *Angle-Angle*, intercepts and some type 2, *Shell-Shell*, intercepts but the type 3 intersection (*Shell-Shell*) still dominates. The combined (L-2) transition region and the (L-1) region

cover approximately 20° ; this is from the start of the grid through to the point where the line of sight associated with the bottom pixel of the first image in Figure 6.3 leaves the grid.



(a)



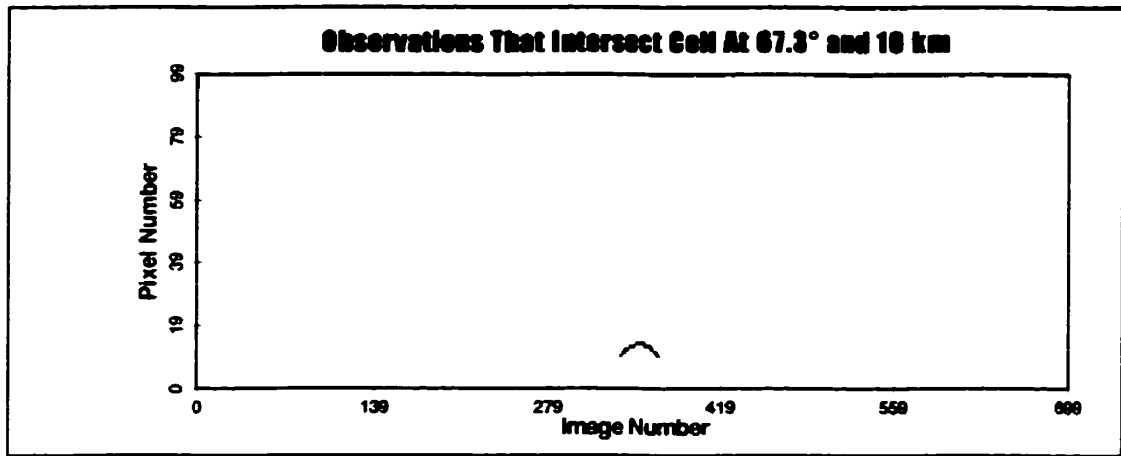
(b)

Figure 6.6: *Observations that intersect the grid cell at AngleNumber 122 and ShellNumber 49 in the (L-2) region (a) and the other grid cells that these observations sample (b).*

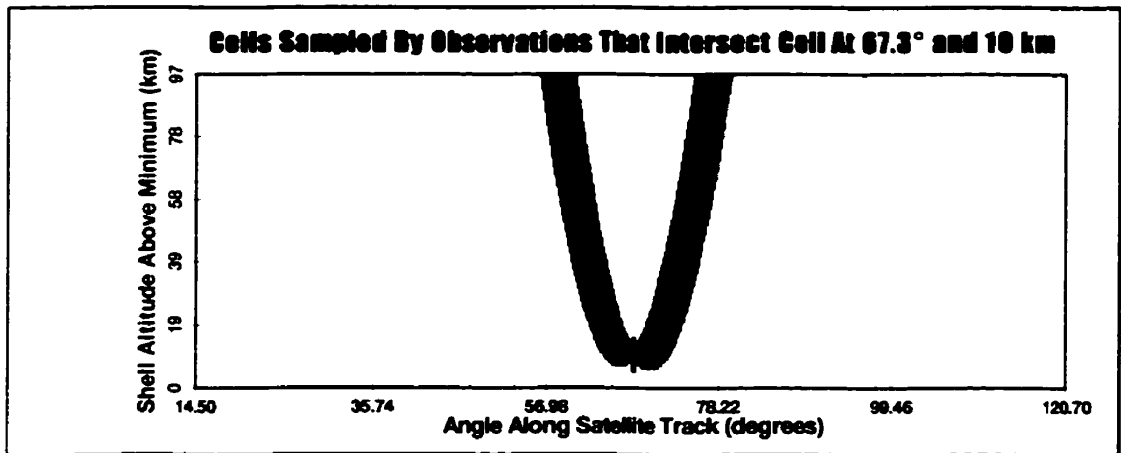
The central region is to the immediate right of the (L-2) region. In this region all cells associated with a particular radial shell are sampled in a nearly uniform fashion. The dominant type of intersection in these cells depends on their distance from the bottom of the grid. Hence, the central region of the grid can be divided into separate sub-regions. These regions are: the (C-1) region near the bottom of the grid which is dominated by *Angle-Angle* intercepts; the (C-3) region near the top of the grid where most

intersections are of the *Shell-Shell* type; and region (C-2) in the middle of the grid. This last is a transition region where the intersections are almost equally distributed between the *Angle-Angle* and *Shell-Shell* types.

The extent of the observations and the cells sampled for each of these three sub-regions is illustrated in Figures 6.7, 6.8 and 6.9. Region (C-1) is characterized by a small number of observations that cover a narrow, and almost symmetric, set of grid cells. The lack of complete symmetry is due to the Earth oblateness. It should be noted that in this region these observations follow almost the same path through the grid.



(a)



(b)

Figure 6.7: Observations that intersect the grid cell at AngleNumber 336 and ShellNumber 10 in the (C-1) region (a) and the other grid cells that these observations sample (b).

As shown in Figure 6.8, a typical cell in region (C-2) is sampled by a wider range of observations than the typical cell in region (C-1) and the grid coverage is also almost symmetric. However, unlike the (C-1) sub-region the different observations in the (C-2) region do not follow similar paths through the grid. Some observations have a line of sight that is tangent near the cell, while others travel to the bottom of the grid and intersect the cell either before or after the tangent point.

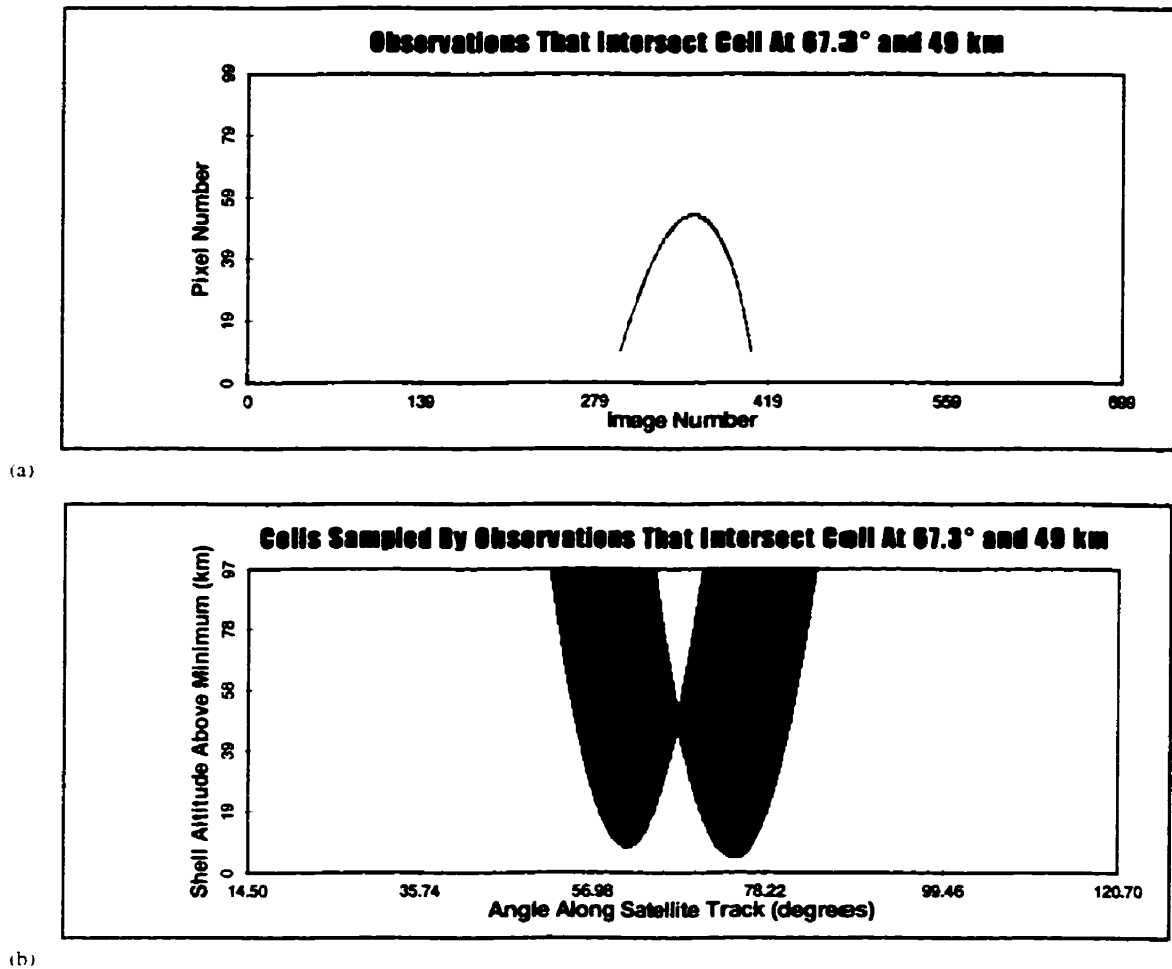


Figure 6.8: Observations that intersect the grid cell at AngleNumber 336 and ShellNumber 49 in the (C-2) region (a) and the other grid cells that these observations sample (b).

The largest range of observations, both with respect to pixel and image, that intersect cells is for the (C-3) sub-region. This is shown in Figure 6.9 where most observations sample from below the shell that contains the cell of interest and are characterized by

Shell-Shell type intersections. Only a small fraction of the total number of observations that intersect region (C-3) cells are tangent near the cell and result in *Angle-Angle* type intercepts. The observations that sample the (C-3) region are also characterized by a wide range in the measured brightness as the lines of sight sample different parts of the volume emission profile. The lower panel in Figure 6.9 indicates that the coverage associated with these lines of sight is almost symmetric and ranges over some 40° of the grid.

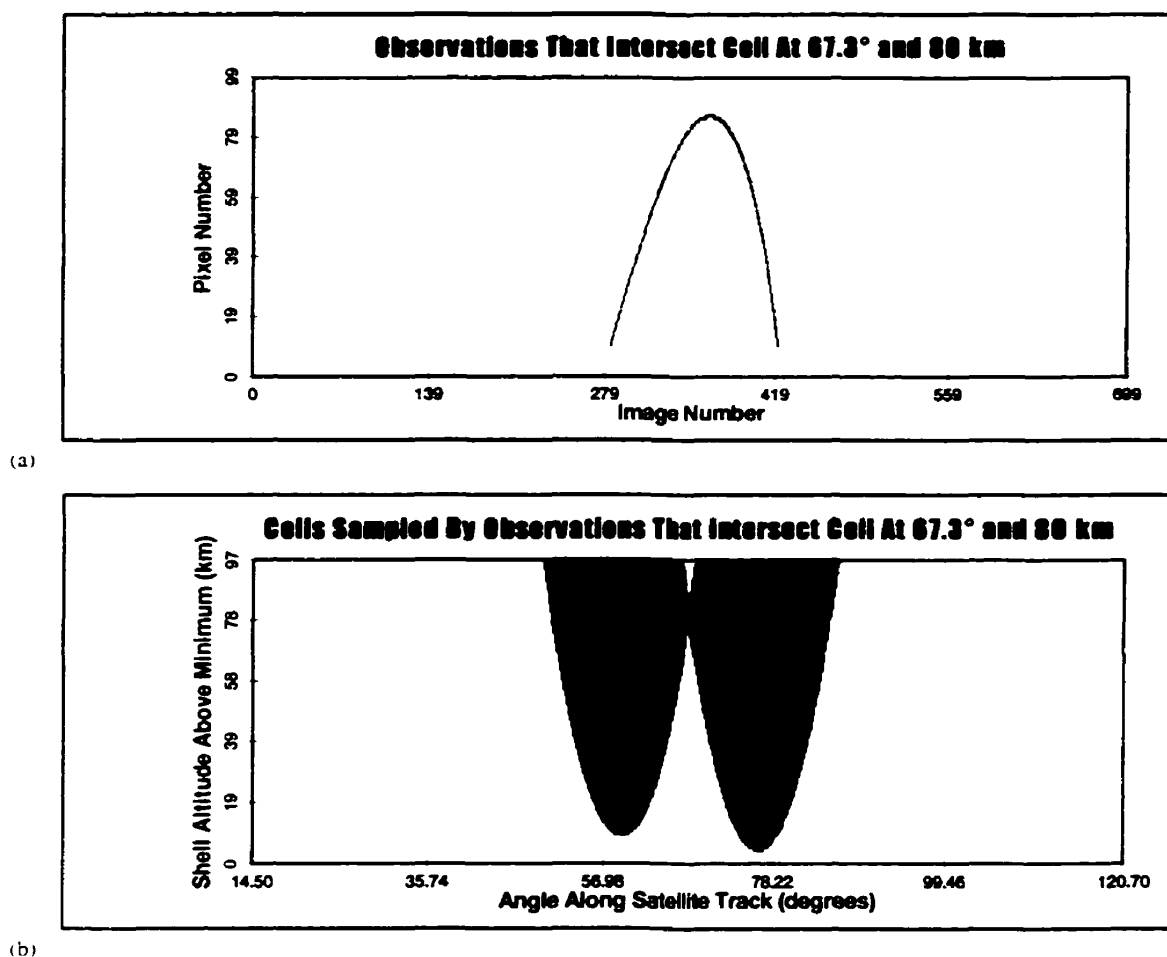


Figure 6.9: Observations that intersect the grid cell at AngleNumber 336 and ShellNumber 30 in the (C-3) region (a) and the other grid cells that these observations sample (b).

Figures 6.10 and 6.11 illustrate a behaviour for cells on the right hand side of the grid that is similar to that for cells on the left. There is a transition region, (R-2), in which

there are some *Angle-Angle* intercepts and some type 3 (*Shell-Shell*) intercepts, although the type 2 (*Shell-Shell*) intercepts dominate.

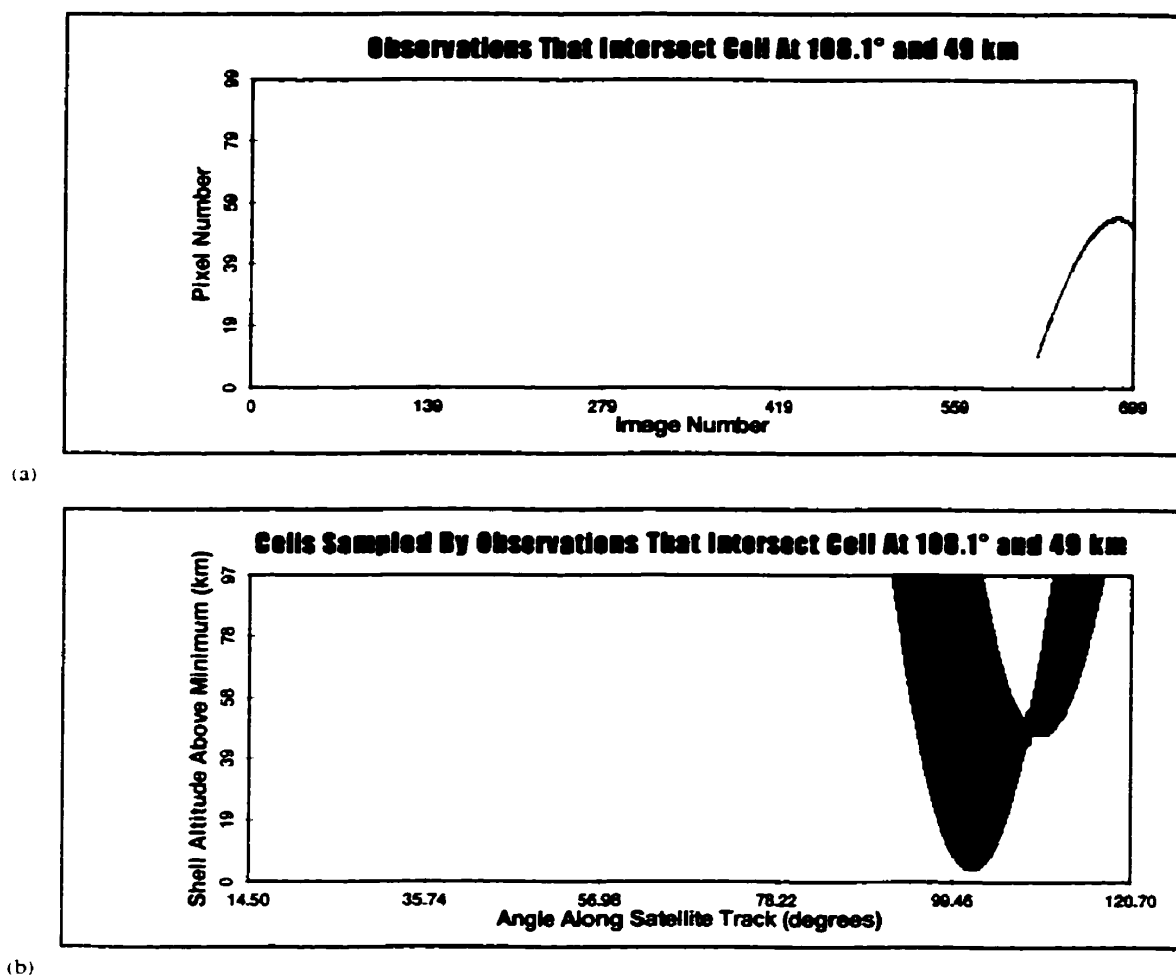
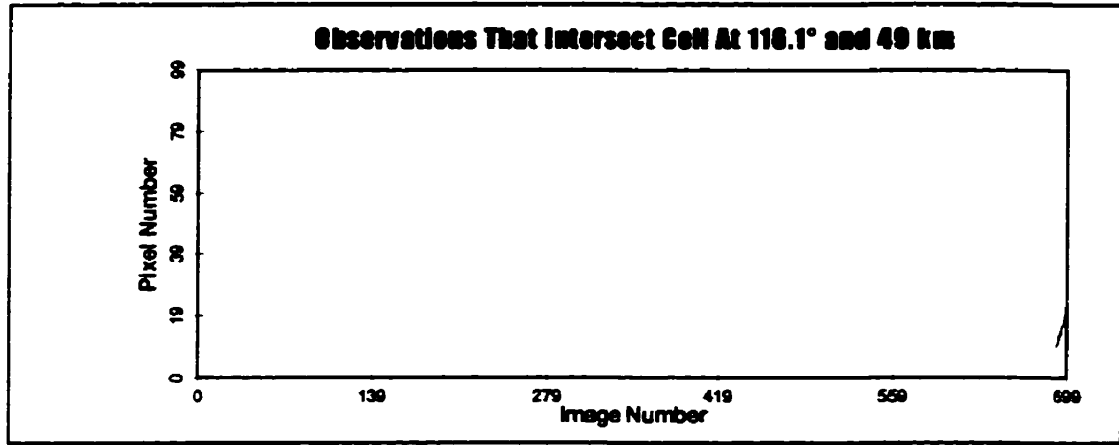
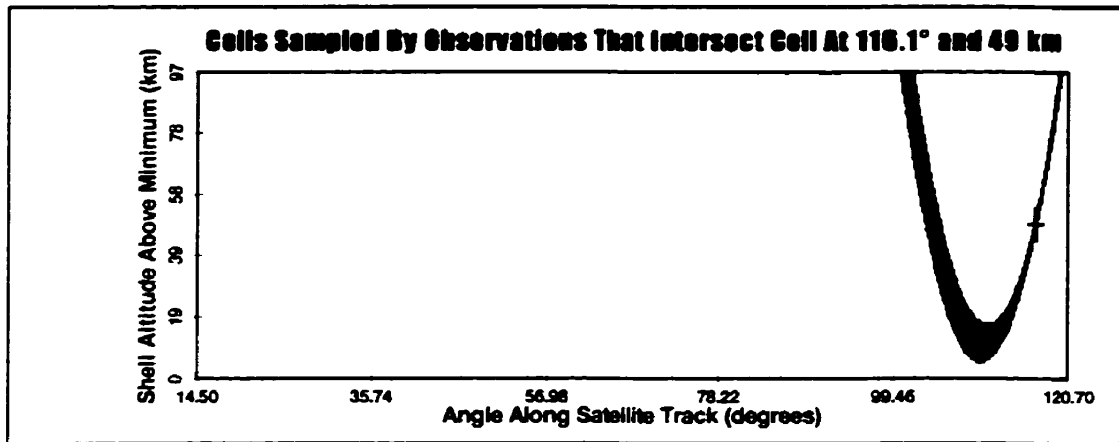


Figure 6.10: Observations that intersect the grid cell at AngleNumber 540 and ShellNumber 49 in the (R-2) region (a) and the other grid cells that these observations sample (b).

The behaviour of the observations and the sampled cells for the extreme right hand side of the grid are shown in Figure 6.11. This is similar to the (L-1) region except the intersections are almost entirely type 2 rather than type 3.



(a)



(b)

Figure 6.11: Observations that intersect the grid cell at AngleNumber 580 and ShellNumber 49 in the (R-1) region (a) and the other grid cells that these observations sample (b).

6.5 The Edge Effect

It is apparent from the retrieval presented in Figure 6.12 that there are obvious differences between the input and the retrieved volume emissions at the left and right hand edges of the two dimensional recovery grid. This 'edge effect', which is present in the (L-1) and (L-2) and the (R-1) and (R-2) sub-regions, is due to the way in which the observations sample each of the cells in these regions. The geometry of the observations causes an undersampling of the cells in these regions, this undersampling is compounded as the observations have almost the same path and, therefore, the same apparent brightness.

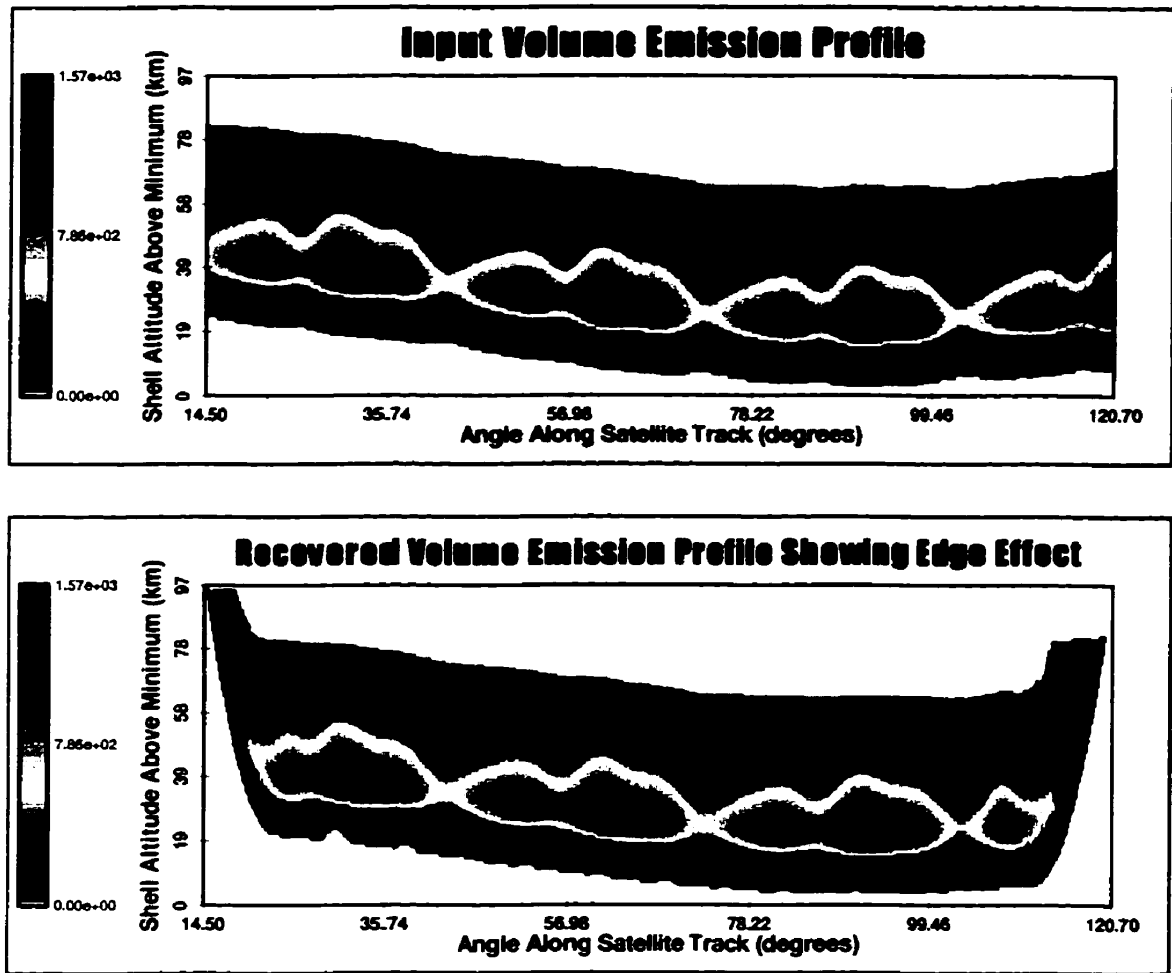


Figure 6.12: Input and recovered volume emission profiles that illustrate the edge effect in both the (L) and (R) regions.

At each iteration in the recovery process the volume emission associated with each cell is multiplied by a fractional value in order to estimate the volume emission for the next iteration (equation 5.15). This fractional value is derived from a filtered contribution of those observations that intersect, or sample, the particular cell. Each observation 'requests' that the volume emission at the cell either be raised, or lowered, by the amount that the measured observation is either higher, or lower, than the modeled observation as determined by the previous volume emission solution. Each observation makes the same fractional 'request' for all cells that it samples and the 'request' is derived from the volume emission values contained within the entire set of sampled cells. In order to achieve the best solution, and to determine the optimum multiplicative

factor for each cell, many observations with completely different characteristics and 'requests', are required for each cell. For cells in regions (L) and (R), and especially in the (L-1) and (R-1), regions the observations do not have the required range of characteristics.

The edge effect region is defined by the envelope within which the sampling method and density is inadequate. This envelope is bounded on the left side by the lowest line of sight in the first image; this line of sight also intersects the top leftmost cell of the grid and is tangent low in the atmosphere (Figure 6.3). For the retrieval shown in Figure 6.12 the observation and recovery geometry are the same as for the sampling density plot shown in Figure 6.3; the lowest line of sight of the first image is the only observation that intersects the top leftmost cell. The cells sampled by this line of sight are shown in Figure 6.13 and it is apparent that the line of sight extends deep into the grid and exits the grid nearly 20° from the entry point. It is over this 20° that the edge effects occur.

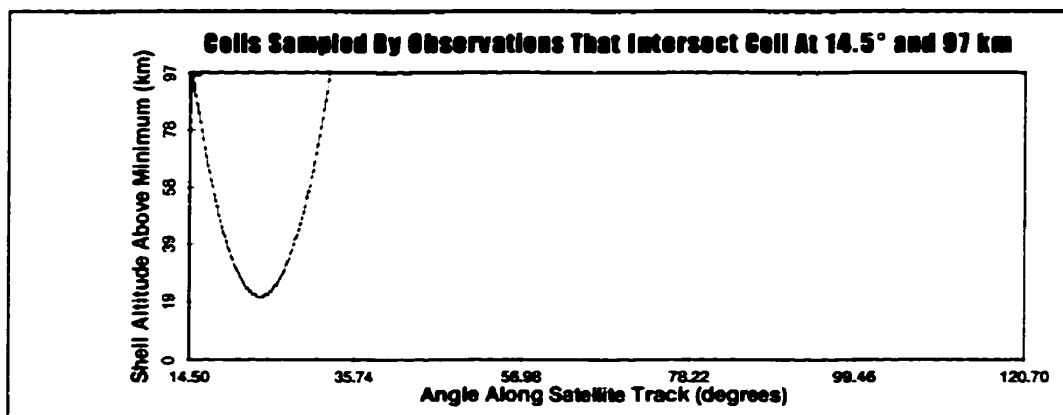


Figure 6.13: *The cells that are sampled by the first observation that intersects the top leftmost cell (72,97) of the volume emission grid. This observation and the cells that it samples define the left hand envelope of the edge effect.*

Figures 6.14 through 6.19 illustrate the cells that are sampled by other observations that also intersect cells along the first line of sight shown in Figure 6.13. In Figures 6.14, 6.15 and 6.16 these measurements correspond to cells that are before the tangent point of the first observation. Only a small set of observations (three or four for a 0.5 Hz imaging rate) intersect any given cell that is before the tangent point of the first line of

sight shown in Figure 6.13. These observations follow nearly the same path through the grid and so have approximately the same magnitude (apparent brightness) and intersect the given cell in nearly the same manner.

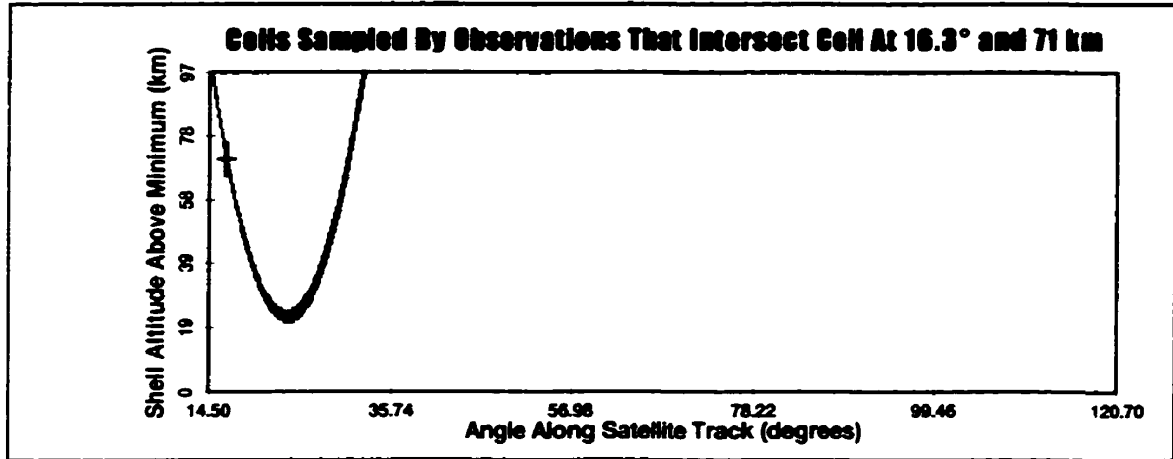


Figure 6.14: The other cells that are sampled by observations that intersect grid cell (81,71) which is along the first line of sight shown in Figure 6.13.

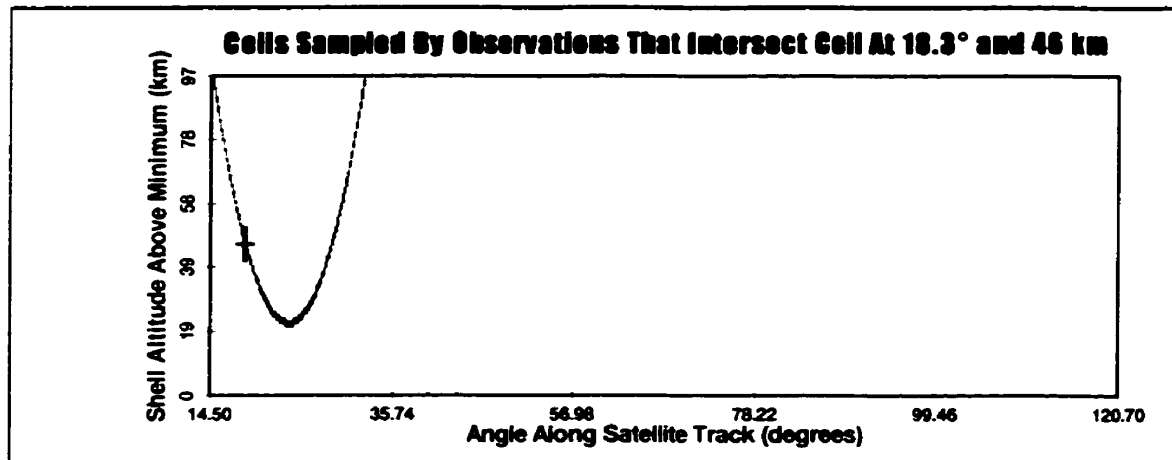


Figure 6.15: The other cells that are sampled by observations that intersect grid cell (91,46) which is further along the first line of sight shown in Figure 6.13. These are approximately the same set of cells as those shown Figures 6.13 and 6.14.

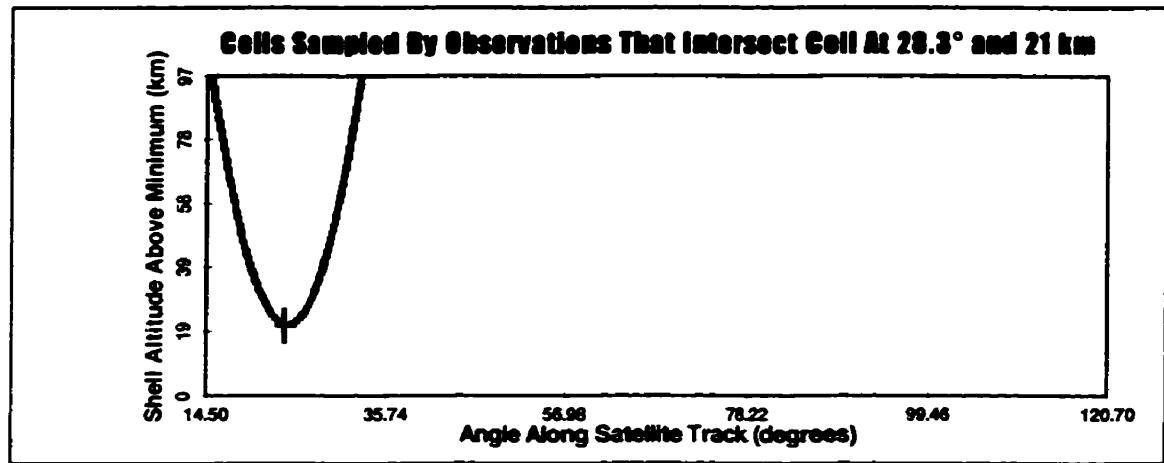


Figure 6.16: Other cells that are sampled by observations that intersect the cell (141,21) at the tangent point of the first observation. These are approximately the same set of cells as those shown in Figures 6.13, 6.14 and 6.15.

The averaging mechanism used in the iterative inversion algorithm depends on both the magnitude of the observation and the estimate of the observation. If all observations and their corresponding estimates are almost identical (this is the case for all cells along the original line of sight that are before the tangent point) then these cells will converge to approximately the same value. This is apparent from the plot shown in Figure 6.12 where the solution contours follow the parabolic lines of sight in region (L-1). The cells in this region are undersampled by very similar observations.

As shown in Figures 6.17, 6.18 and 6.19 cells that occur after the tangent point of the first observation are sampled by a large and diverse set of observations. In these cases the cells sampled by the observations are almost symmetric about the cell of interest. This is a characteristic of cells in region (C) (Section 6.4). In this region all types of intersections occur and the multiplicative value for the volume emission element, after each iteration, is obtained from the filtered weighted average of a large set of diverse observations. In this case the retrieved solution (Figure 6.12) for the (C) region is appropriate.

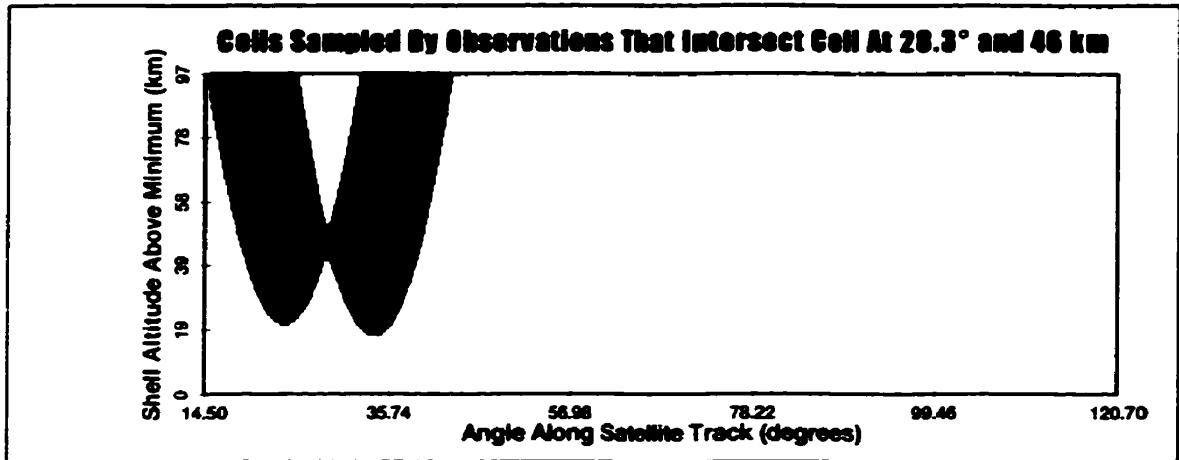


Figure 6.17: A far broader range, compared to those in Figures 6.14, 6.15 and 6.16, of cells are intersected by observations on the far side of the tangent point of the first observation.

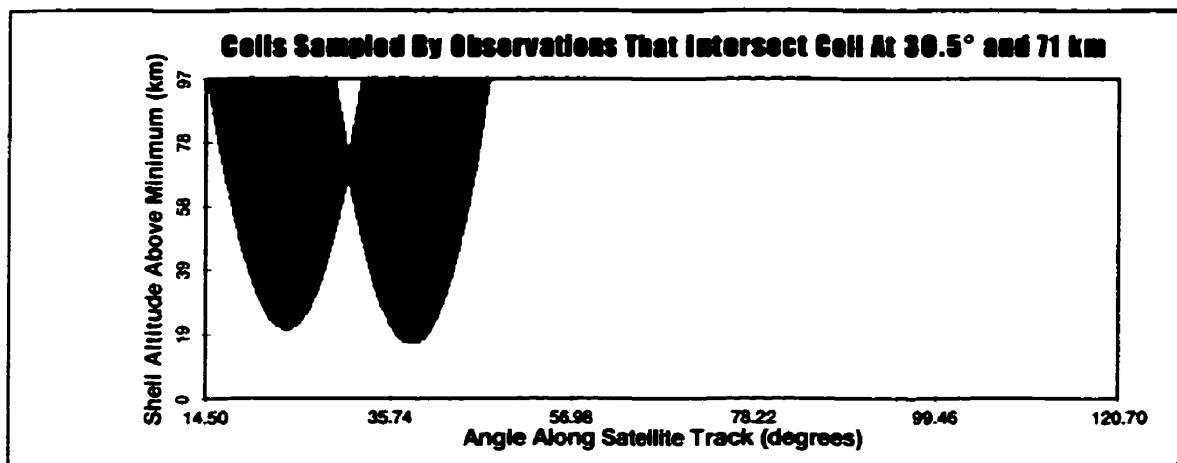


Figure 6.18: An even broader range of cells is sampled by observations that intersect a cell further along the first observation path than the cell shown in Figure 6.17.

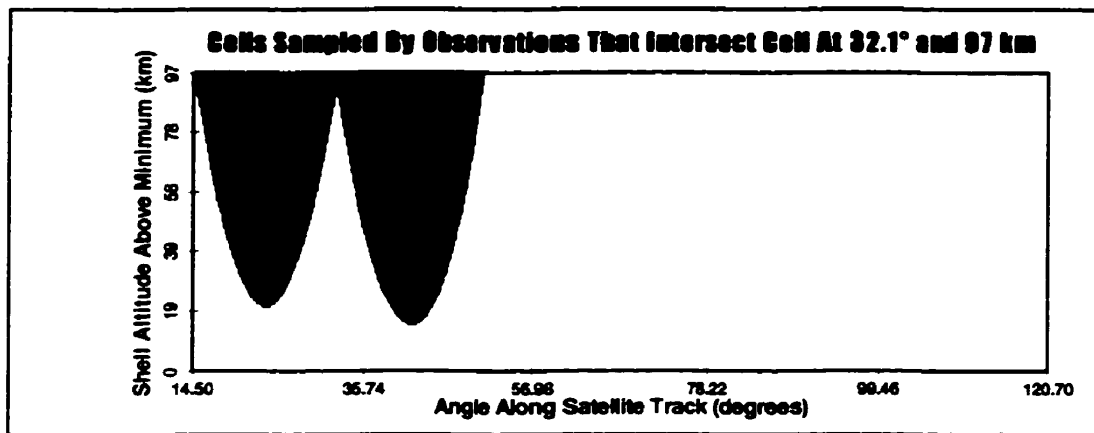


Figure 6.19: A complete range of cells is sampled by observations that intersect a cell near the end of the first observation path.

The behaviour of the observations in the transition regions, that go from a limited set of nearly identical observations to a large diverse set of observations that sample each cell, are shown in Figures 6.20 and 6.21. It is apparent from Figure 6.20 that the cell (102,49) that is within the (L-1) region is only associated with observations that intersect it in a top shell to bottom shell (type 3) fashion. However, this set of observations is larger and more diverse than the set that samples the boundary cells in the (L-1) region. The range of tangent altitudes for the former observations covers approximately 25 km so that the magnitudes (apparent brightnesses) of the measurements can be quite different. Thus, the retrieval in this region is better than closer to the edge, but it is still not reliable.

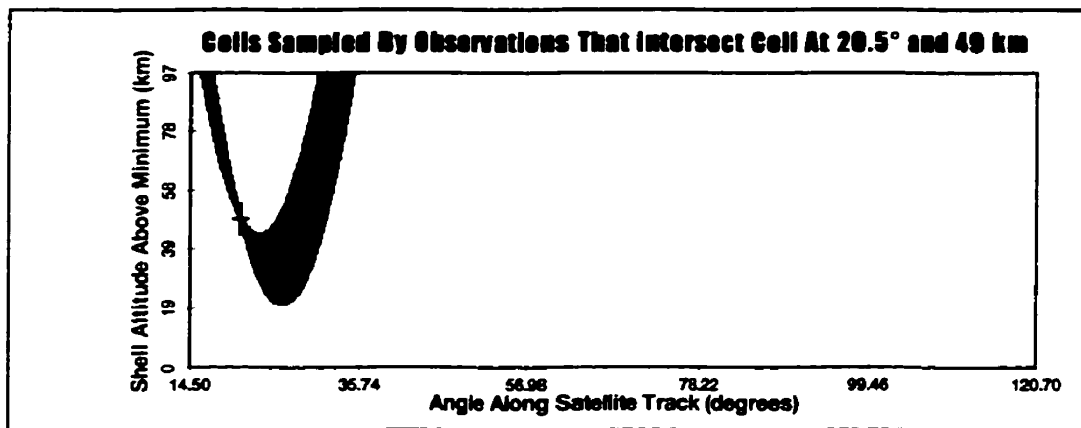


Figure 6.20: The cells sampled by observations that sample a cell (102,49) in the transition region where no intersections occur before the tangent point of any line of sight.

The observations for cell (132,46) in the (L-2) region are shown in Figure 6.21. It is apparent in this case that the observations are tangent both before and after the cell of interest. The range of cells sampled by these observations is wider than for cell (102,49) (Figure 6.20) but the distribution is not symmetric. The recovery in the (L-2) region is still affected by inconsistencies in the solution determined for cells in the (L-1) region. For this reason the solution is still low quality, although its contours do not follow the lines of sight.

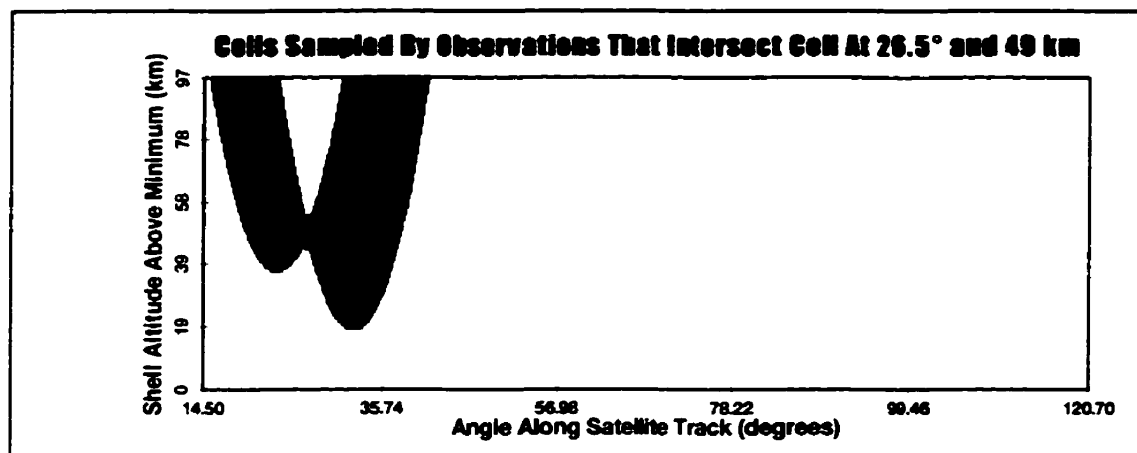


Figure 6.21: Cells intersected by observations that sample cell (132,46) in the transition region where the intersections are of all three types.

As discussed the edge effect has a defined boundary and, therefore, a known angular extent within the grid. This is true for both the left and right angular extremes of the grid. For the given satellite geometry the lowest lines of sight (consistent with the boundary line of sight shown in Figures 6.3 and 6.13) cover an angular extent of approximately 20° . This implies that for both the initial and final boundaries of the retrieval grid there is at least 20° of the retrieved solution that may contain significant errors. It has been determined from a series of tests that the edge effect is completely eliminated 22° away from both the left and right boundaries. This is the amount of poorly recovered data that must be discarded from each inversion. The angular extent of this edge effect region is independent of all inversion and observation parameters,

except for the radial distance of the tangent point of the boundary line of sight and the maximum shell radius (*ShellMax*).

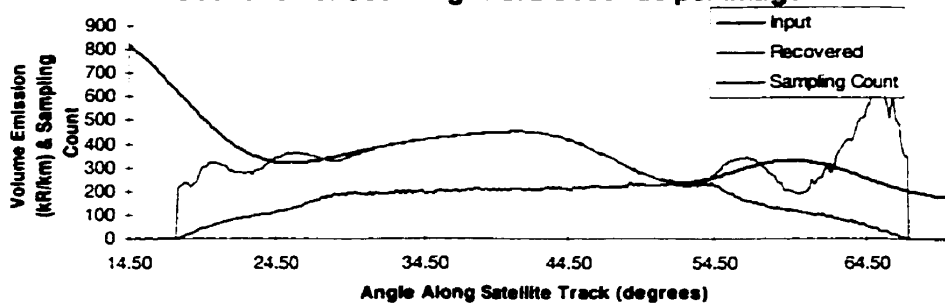
6.6 The Number of Images Used in a Single Inversion

The edge effect discussed in Section 6.5 also affects the number of images that must be included for each inversion. It was noted that the angular extent of the poor recovery depends only on the extent of the boundary lines of sight at both the left and right edges of the grid and is independent of the number of images that are simultaneously inverted. However, the total angular extent of the retrieved grid does depend on the imaging rate and the number of images used in the retrieval. Hence, for a fixed imaging rate, the more images that are used in the tomographic recovery the larger the angular extent of accurate retrieval, and the smaller the fraction of the grid that must be discarded due to the edge effect.

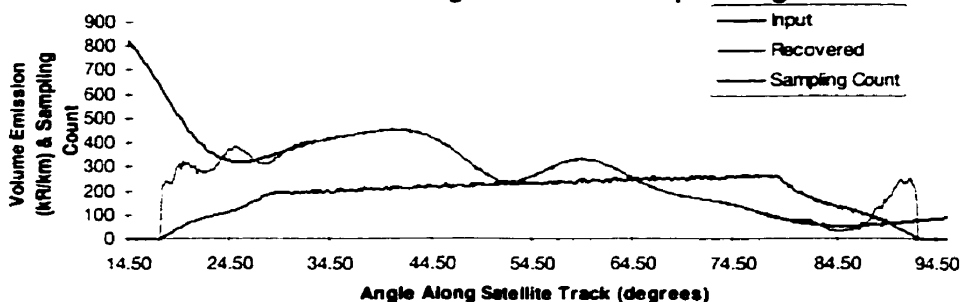
The various plots shown in Figure 6.22 illustrate the radial shell cross sections of the input and recovered volume emission profiles for inversions made with 300, 500, 700 and 900 images. The imaging rate for these observations was constant at 0.5 Hz, except for the last plot where the imaging rate was 1.0 Hz. The sampling density cross sections for the corresponding cells (the number of times that the cell is sampled by the observations) are also included in these plots. It is readily apparent from these plots that the boundaries between both the left (L) and right (R) regions and the central (C) region, can be clearly identified and are in agreement with the interpretation presented in Section 6.5.

The plot in Figure 6.22 that corresponds to the retrieval for 300 images indicates that only about 20° of data has been accurately retrieved. The cross sections for 500, 700 and 900 images have accurate retrieval regions that span approximately 45°, 70° and 95° respectively. The addition of 200 images to the inversion with an imaging rate of 0.5 Hz has added almost 25° of angular extent to the accurate retrieval. This increase is expected as the satellite travels nearly 25° during the 400 seconds required to obtain the additional 200 images.

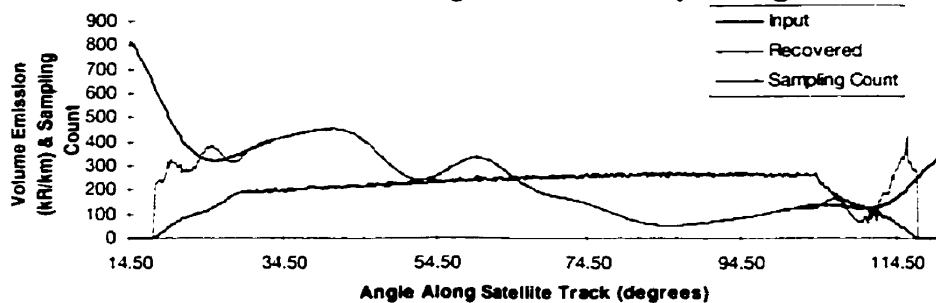
Recovery and Sampling Density Radial Shell Cross Sections For 300 Images at 2 Seconds per Image



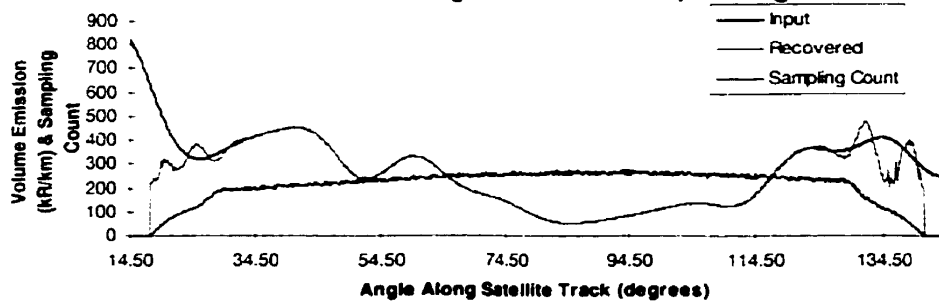
Recovery and Sampling Density Radial Shell Cross Sections For 500 Images at 2 Seconds per Image



Recovery and Sampling Density Radial Shell Cross Sections For 700 Images at 2 Seconds per Image



Recovery and Sampling Density Radial Shell Cross Sections For 900 Images at 2 Seconds per Image



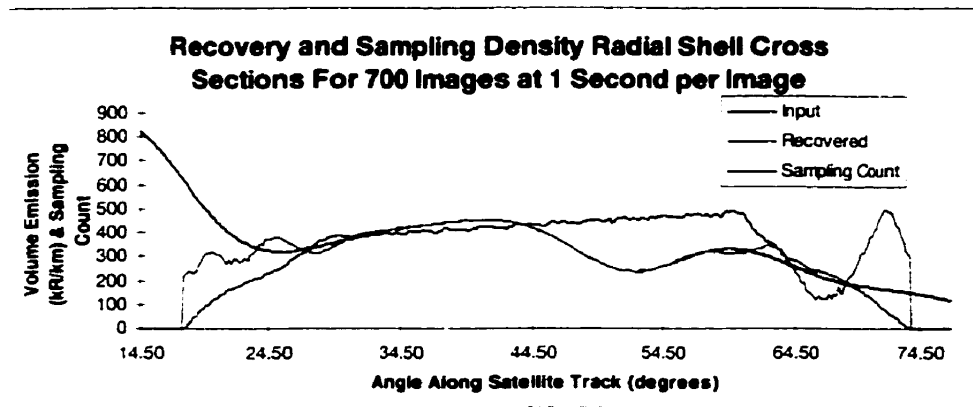


Figure 6.22: *Five recovered volume emission radial shell cross sections together with the sampling densities at each of the relevant grid cells. The recoveries are for observation sets that include different numbers of images and imaging rates.*

Computational limitations (Appendix D) necessarily influence the number of images that can be simultaneously inverted. When this modeling work was initially undertaken the available computer system was heavily loaded even for image sets of 700 images. For a 0.5 Hz imaging rate 700 images provides an angular range of 70° of accurate retrieval. The last plot in Figure 6.22 shows that if the imaging rate is increased to 1 Hz the recovery range is necessarily decreased to approximately 25° and, although not optimal, it is still acceptable. It is for this reason that observation sets with 700 images have been used in most of this thesis.

While the edge effect, and the region over which the retrieval is acceptable, is influenced by both the sampling density and geometry the angular extent of the poorly recovered volume emission profile is constant for the present satellite geometry. However, the impact of the sampling geometry is not limited to the edge effect as it can also influence the retrieval in a more fundamental manner through the observation weighting filter (Chapter 7).

CHAPTER VII

THE OBSERVATION WEIGHTING FILTER

7.1 Introduction

The observation weighting filter is unique for each cell in the recovery grid and defines the importance of the individual observations in the iterative solution at that cell. This filter function is dependent on the geometry and the way in which each observation intersects the grid cell. It is also normalized so that the sum of the values of the weighting filter function for any cell is equal to unity. Modifications to the shape of this geometry dependent function allow for faster and more accurate volume emission retrievals.

The basic tomographic equation (equation 5.15), the weighting term β_{ij} (equation 5.13) and the single line of sight observation estimate $O_{i_{ev}}^{(n-1)}$ (equation 5.14) have been presented in Chapter 5. For convenience these equations are repeated here.

$$V_j^{(n)} = V_j^{(n-1)} \sum_i \left(\frac{O_i}{O_{i_{ev}}^{(n-1)}} \beta_{ij} \right). \quad [7.1]$$

$$\frac{L_{ij}^m}{\sum_i L_{ij}^m} = \beta_{ij}. \quad [7.2]$$

$$\sum_j L_{ij} V_j^{(n-1)} = O_{i_{ev}}^{(n-1)}. \quad [7.3]$$

As described in Section 5.2.2 the set of i (observation) dependent terms β_{ij} provide (for any cell j) a weighted average comparison mechanism that modifies the volume emission within the cell at each iterative step of the tomographic retrieval. This geometry dependent (through the path length of the observation within the given cell) set of β_{ij} values is defined as the observation weighting filter for the grid cell j , and determines the relative effect of each observation on the convergence of the tomographic procedure and the final retrieved solution.

The shape of the observation weighting filter, which is dependent on the types of intersection (Figures 6.1 and 6.2) that dominate the cell, also is important for the tomographic routine. The shape of the weighting filter is different within each region of the grid (Section 6.4) and is affected by both the weighting factor exponent m (equation 7.2) and the grid cell dimensions. In the present work the radial dimension of the grid cells for all recoveries has been fixed at 1 km and the angular dimension has been varied. The effect of varying the two parameters m and *DeltaAngle*, with respect to solution accuracy and convergence speed, are presented in this chapter.

7.2 Path Length Envelopes

The path length envelope is the maximum geometric length that any observation tangent at a given radial distance can have through a particular cell. This envelope is specific to the radial distance and the angular dimension of the cell and contains only the type 1, 2 and 3 intersections shown in Figure 6.1. Any other intersections for a given line of sight, or observation, will traverse the shell with a shorter distance. In every case the path length envelope has a standard shape; it is symmetric about the centre and contains a flat central region (a plateau).

7.2.1 The Shape of the Path Length Envelope

The shape of the path length envelope is dictated by the path lengths that observations with a particular tangent altitude below a grid cell can have through that grid cell. The maximum path length if only *Shell-Shell* intersections are considered is close to 113 km. However, if angular boundaries are present the maximum intercept length is decreased.

If the recovery grid contains cells that are only bounded by radial shells and there are no angular divisions then only type 2 and 3 intersections (Figure 6.1) occur. The path length for these intersection types is given by equation 7.4,

$$L = \sqrt{r_1^2 - r_{\tan}^2} - \sqrt{r_2^2 - r_{\tan}^2} \quad [7.4]$$

where r_1 and r_2 are the upper and lower radial distances of the cell respectively and r_{tan} is the tangent distance of the line of sight. All distances are defined with respect to the centre of the Earth, the centre of the grid.

The path lengths through three cells on different radial shells, for lines of sight that are tangent below the cells, are shown in Figure 7.1. The minimum tangent distance included in this figure is 6384 km and the one kilometer thick shells have the indicated minimum and maximum radii.

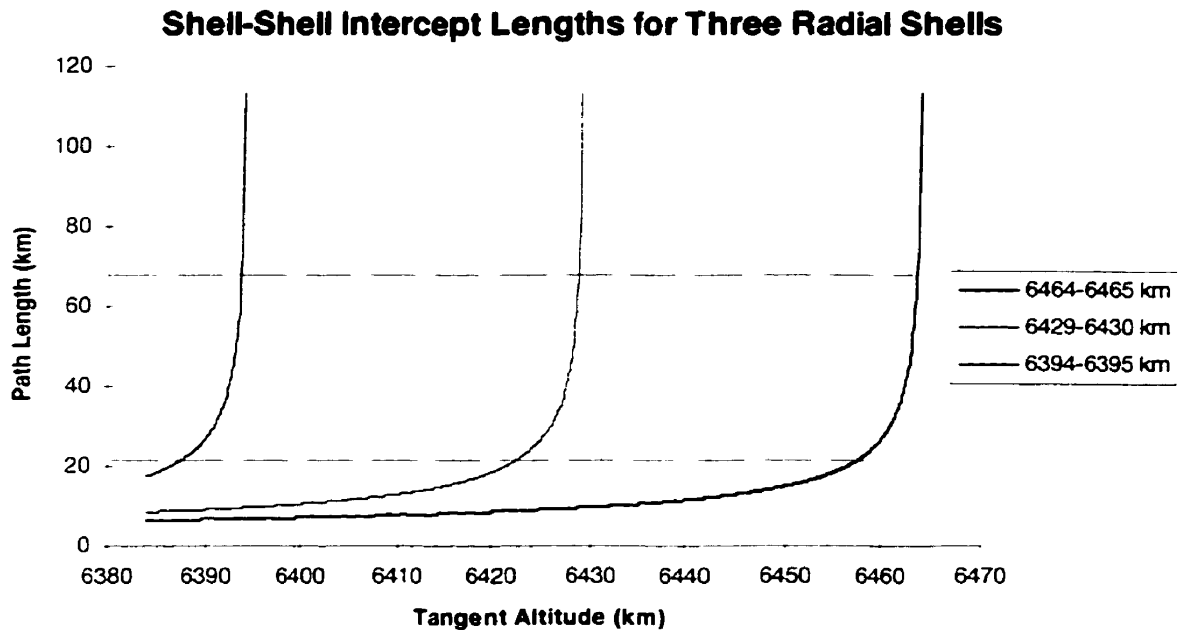


Figure 7.1: The path length through different grid cells in the absence of angular boundaries. These paths include type 2 and 3 intercepts where the tangent altitude is always below the shell of interest.

It is apparent from this figure that shells at larger radial distances are intersected by a wider range of tangent altitudes. The curve for the 6464-6465 km shell is intersected, in a *Shell-Shell* fashion, by lines of sight with tangent altitudes that approach 6464 km while the 6394-6395 km shell is only intersected by lines tangent below 6394 km. Thus more lines of sight intersect the higher shells. This interpretation is in agreement with the sampling density plot that was shown in Figure 6.3.

The dashed lines in Figure 7.1 illustrate the typical length of type 1 (*Angle-Angle*) intercepts for cells with different angular widths. The upper dashed line is located at about 67 km and corresponds to an angular cell size of 0.6° , the lower line is located at approximately 22 km and corresponds to an angular size of 0.2° . These lengths are representative of the real values as the linear distance between the angular bounds changes with radial distance from the centre of the grid. As no line of sight, that intersects a grid cell with angular bounds, can have a path length through the cell that is greater than the diagonal distance between the angular bounds the dashed lines shown in Figure 7.1 are the typical maximum path lengths for the two different grid cell sizes. If only *Angle-Angle* and *Shell-Shell* intercepts are considered then the intercept path lengths are constrained by these maximum values. This is illustrated in Figure 7.2 for the case of *Shell-Shell* and *Angle-Angle* intercepts through a 1 km by 0.2° cell located in the 6429-6430 km shell. The plateau in the path lengths near the tangent distance 6425 km is due to the angular divisions.

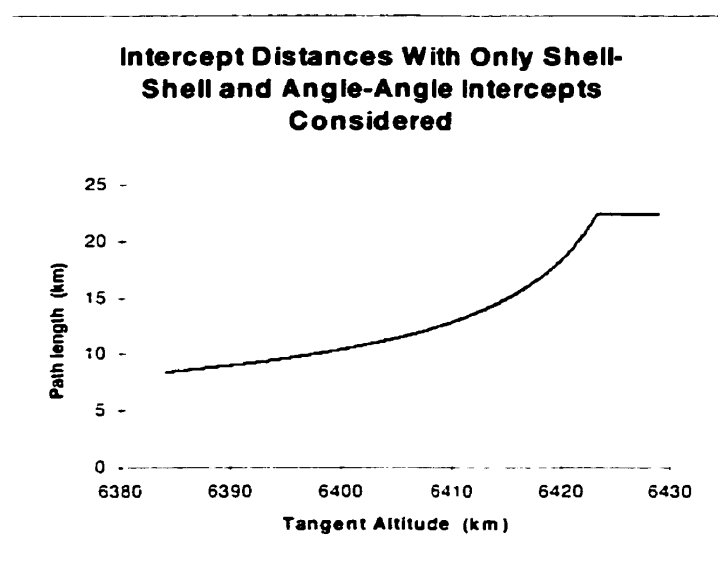


Figure 7.2: Intercept path lengths through a 0.2° by 1.0 km cell with minimum and maximum radii of 6429 and 6430 km. All lines of sight that are tangent above 6425 km and intercept the cell do so in an *Angle-Angle* manner and so are constrained to the maximum length.

It was previously noted (Section 6.2) that the type 2 and 3 intercepts shown in Figure 6.1 are different. Lines of sight that are tangent before the cell of interest have a

different effect on the inversion than those that are tangent after the cell. To accommodate this distinction the curve shown in Figure 7.2 has been reflected about its end point to give the curve shown in Figure 7.3. All data points to the left of the centre in this new curve correspond to type 1 and 2 intercepts and all points to the right of the centre correspond to type 1 and 3 intercepts. This curve is called the path length envelope and represents the maximum path lengths through the cell for lines of sight that are tangent at the given altitudes.

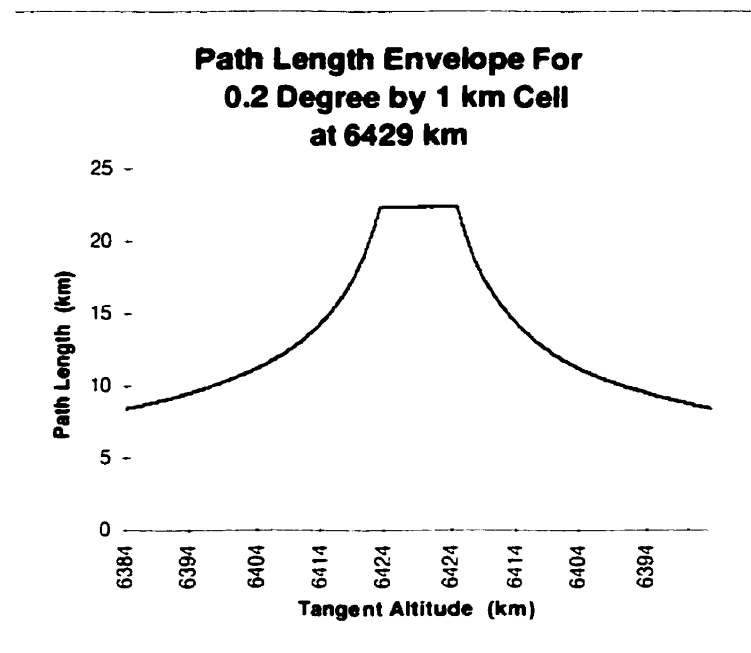


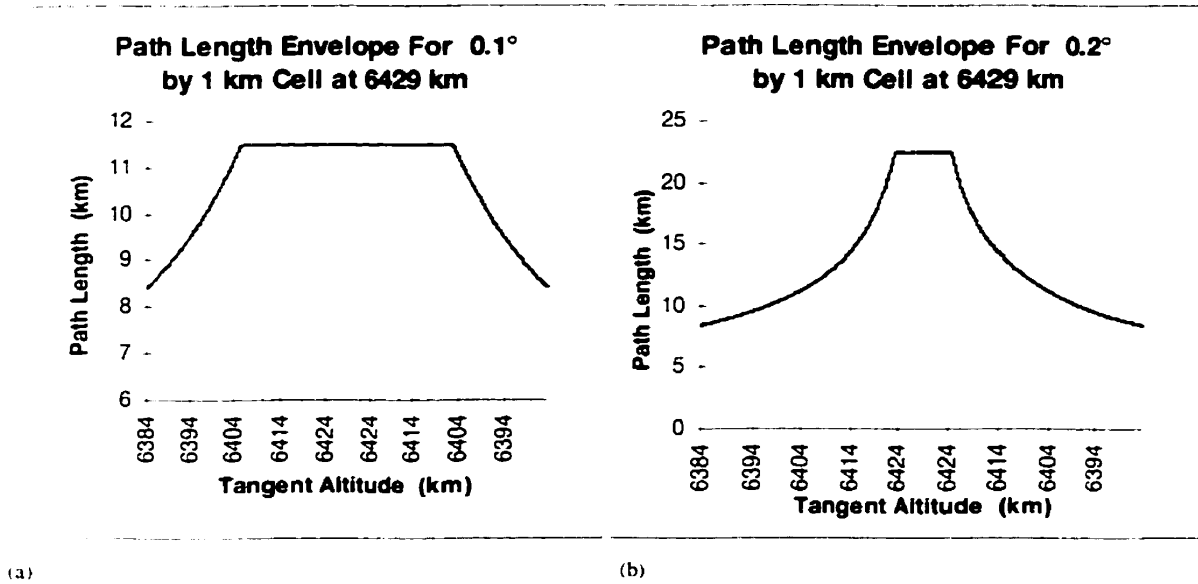
Figure 7.3: Path length envelope if only Shell-Shell and Angle-Angle intercepts of a grid cell are allowed. All other types of intercept for a line of sight that is tangent at the given altitude are shorter.

The path length envelope exhibits a particular shape. For lines of sight that are tangent before entering the cell there is a smooth increase in the envelope as the tangent altitude increases. These path lengths all represent type 2 *Shell-Shell* intercepts. The smooth increase is followed by a plateau over a range of tangent altitudes where only *Angle-Angle* intercepts occur. As the tangent altitude decreases after the plateau so there is a decrease in the path length envelope with the intercepts all being type 3 *Shell-Shell*.

All path length envelopes, whatever the grid cell angular dimension, exhibit this basic shape. A smooth rise, a plateau followed by a smooth decrease. However, the angular size of the grid cells is important for the actual path lengths in the envelope.

7.2.2 The Dependence of the Path Length Envelope on the Grid Cell Size

The three plots shown in Figure 7.4 illustrate the variation of the path length envelope for different angular dimensions of the cells. The path length envelope for a cell 1 km by 0.1°, at radial distance 6429 km, is shown in plot (a). In this case the path length envelope has a wide plateau, or central region, because lines of sight that are tangent well below the cell can intersect the relatively small cell in an *Angle-Angle* fashion.



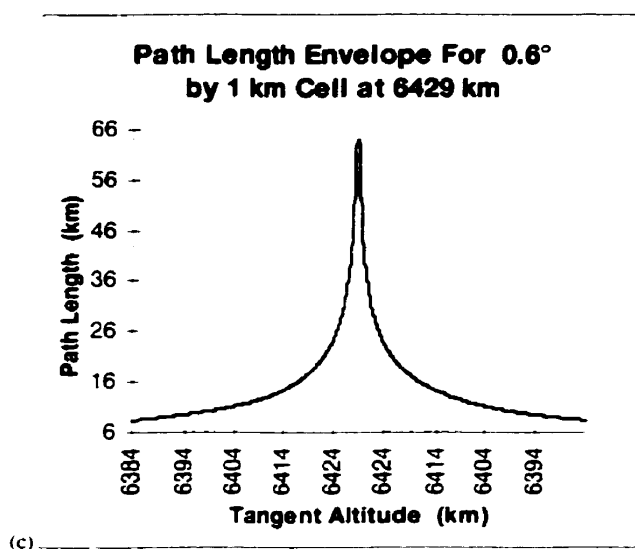


Figure 7.4: The path length envelopes for cell sizes of 0.1° , 0.2° and 0.6° . The envelopes for cells with larger angular sizes have a smaller range of tangent altitudes with Angle-Angle type intercepts.

If the angular dimension of the cell is doubled to 0.2° the plateau (Figure 7.4b), for a cell at the same radial distance, is narrowed. The increased separation between the angular boundaries requires that for *Angle-Angle* intercepts to occur the tangent points of the lines of sight must be radially close to the cell of interest. The final plot (c) in Figure 7.4 corresponds to a cell at the same radial distance but with a 0.6° angular size. In this case the plateau in the path length envelope is almost completely eliminated. Only lines of sight that are tangent in the adjacent lower shell (6428 km radial distance) can intersect in an *Angle-Angle* fashion.

Thus it is apparent that an increase in cell size causes a decrease in the width of the plateau in the path length envelope. There is also an associated decrease in the relative length of the lower tangent altitude path lengths, with respect to those at higher tangent altitudes, as the angular cell size increases. The actual observation weighting filter is dependent on both these relative path lengths and the modification caused by the weighting factor exponent.

7.3 Weighting Function Envelopes

The weighting function envelope is the maximum weight (maximum β_i value in equations 7.1 and 7.2) that any observation i can have on the recovery at element j if i is tangent at a particular altitude. This envelope is related to the path length envelope; if m , the weighting factor exponent in equation 7.2, is equal to 1 then the weighting function envelope is the normalized path length envelope. However, as the weighting factor exponent is quite arbitrary the weighting factor envelope and the path length envelope can have different shapes.

7.3.1 The Importance of the Weighting Function Envelope

Each observation in the tomographic recovery affects the calculated volume emission rate in every cell that it samples. However, there is little value in having the same weight for each observation that intersects a particular cell. Some observations contain information that is more relevant to the cell of interest than others that also intersect the same cell. The weighting function envelope defines the maximum influence of each observation on the retrieval for a particular cell.

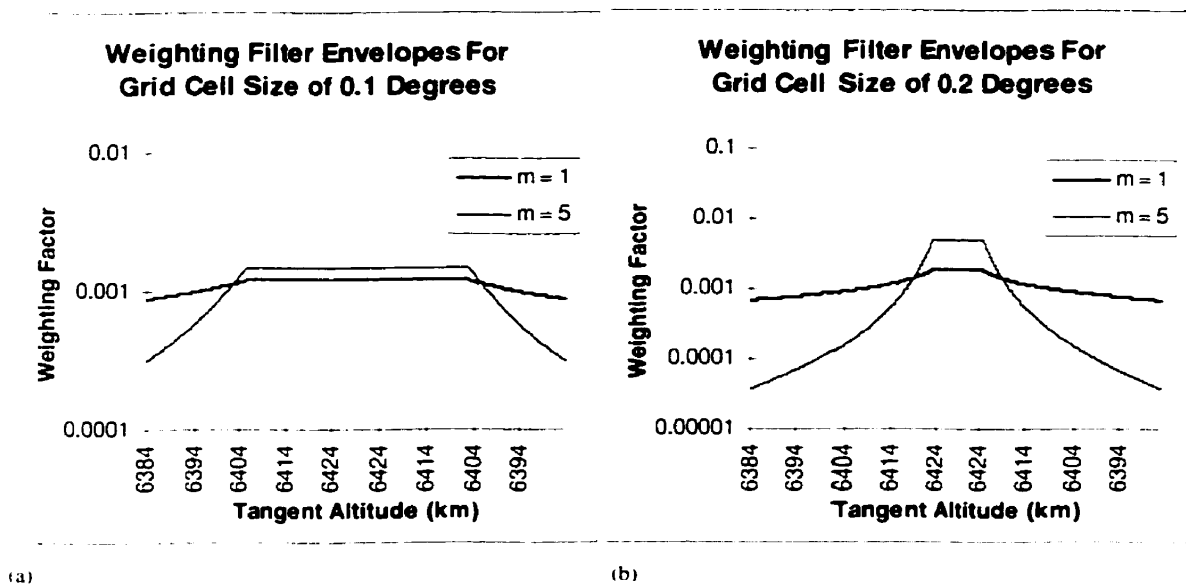
An observation that is tangent low in the grid contains information from a wide range in both angle and radial distance. Conversely, an observation that is tangent high in the grid contains information from only a limited set of angles and radial shells. If both of these observations sample the same cell (necessarily high in the grid) the higher tangent altitude observation contains information that relates to the region close to the cell of interest. Obviously this observation should have a larger weight in the recovery of information for that cell. The weighting function envelope ensures that this is the case.

As noted above the path length and the weighting function envelope (Figure 7.4) are related and have a similar variation in characteristic shape with cell size. Hence, for all cell sizes observations that are tangent at radial distances close to the cell of interest are more important for the solution at that cell than observations that are tangent away from the cell. The major difference between the weighting function envelopes for the

different cell sizes is the number of tangent altitudes that are included in the plateau, *i.e.* are given the same relative weight, and the change in the relative weight as the tangent altitude decreases away from that of the plateau. These differences are important factors in the tomographic inversion and can also be modified by changing the weighting factor exponent.

7.3.2 The Effect of the Weighting Factor Exponent on the Weighting Function Envelopes

Plots of the weighting filter envelopes for different cell sizes are shown in Figure 7.5. The two curves in each plot correspond to the envelope for a different weighting factor exponent. In Figure 7.5a the falloff of the envelope as the tangent altitude moves down from the cell is minimal; it is less than a factor of ten even for an exponent equal to five. This implies that observations that are tangent well below the cell of interest can still have a significant influence on the solution for that cell. The reason for this is the small angular cell size.



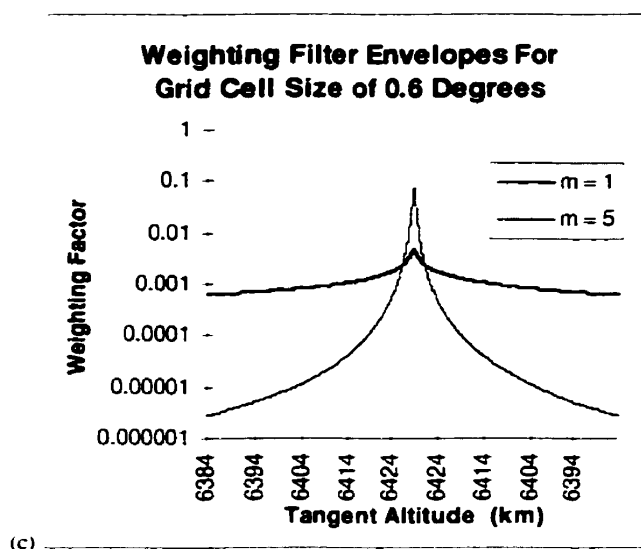


Figure 7.5: Observation weighting filter envelopes for different cell sizes and different weighting factor exponents.

The weighting factor envelopes for the 0.2° cell (Figure 7.5b) have narrower plateaus and a more rapid fall off at lower tangent altitudes than those for the 0.1° cell. The lowest tangent altitude, for a weighting factor exponent equal to one, has about one third the weight of the plateau but for an exponent equal to five the lowest tangent altitude has a weight that is only 0.4% of the plateau weight. While this size of cell has a wide plateau it can effectively eliminate the influence of observations that are tangent well below the cell.

The final plot (c) in Figure 7.5 shows the weighting function envelopes for a 0.6° cell size. These envelopes have almost no plateau and, even for a weighting factor exponent equal to one, effectively eliminate the influence of observations that are tangent below the cell. For this cell size only those observations that are tangent very near the cell of interest have any influence on the recovery. This may be considered detrimental to the tomographic concept as it eliminates all but a few observations that sample each cell.

7.4 The Region of Influence of a Cell as a Result of the Observation Weighting Filter

As discussed in Section 7.3 the observation weighting filter provides an averaging mechanism that determines the effect of individual observations on the solution for the

volume emission rate in any cell. In practice the observation weighting filter determines those cells around the cell of interest that have the most significant effect on the solution for that cell. In this section the basic observation weighting filters are examined further and the concept of an averaging kernel, or the kernel of cells and their relative importance in the solution for a particular cell, is developed.

7.4.1 The Basic Shape of the Observation Weighting Filter

The observation weighting filter is bounded by the weighting filter envelopes. These filters exhibit a rise, from the first observation that intersects the cell, up to a flat plateau and then a decrease to the last observation that intersects the cell.

The actual observation weighting filters for a retrieval using images collected every two seconds are shown in Figure 7.6. In this case the recovery grid cell size is 1 km by 0.2° and the weighting factor exponent is equal to one. The observations are numbered where the bottom pixel of the first image is the 0th observation and then increase through pixel number and image number as indicated by equation 7.5,

$$i = \text{PixelNumber} + \text{ImageNumber} \times \text{NumPixels} . \quad [7.5]$$

The plot in Figure 7.6a corresponds to a cell in the (C-1) region (Section 6.4) where most of the line of sight that intersect the cell do so in a type 2 *Angle-Angle* fashion. This is apparent from the flat maximum seen in the filter function as many observations intersect this cell with the maximum possible path length. However, even in the central region of the weighting filter there are some observations that have an intersection length that is much smaller. These latter observations all have secondary intersection types, 4 through 8. While it is not readily apparent from Figure 7.6a there are also some type 2 and 3 intersections. However, overall the weighting filter functions in the (C-1) region are dominated by *Angle-Angle* intercepts.

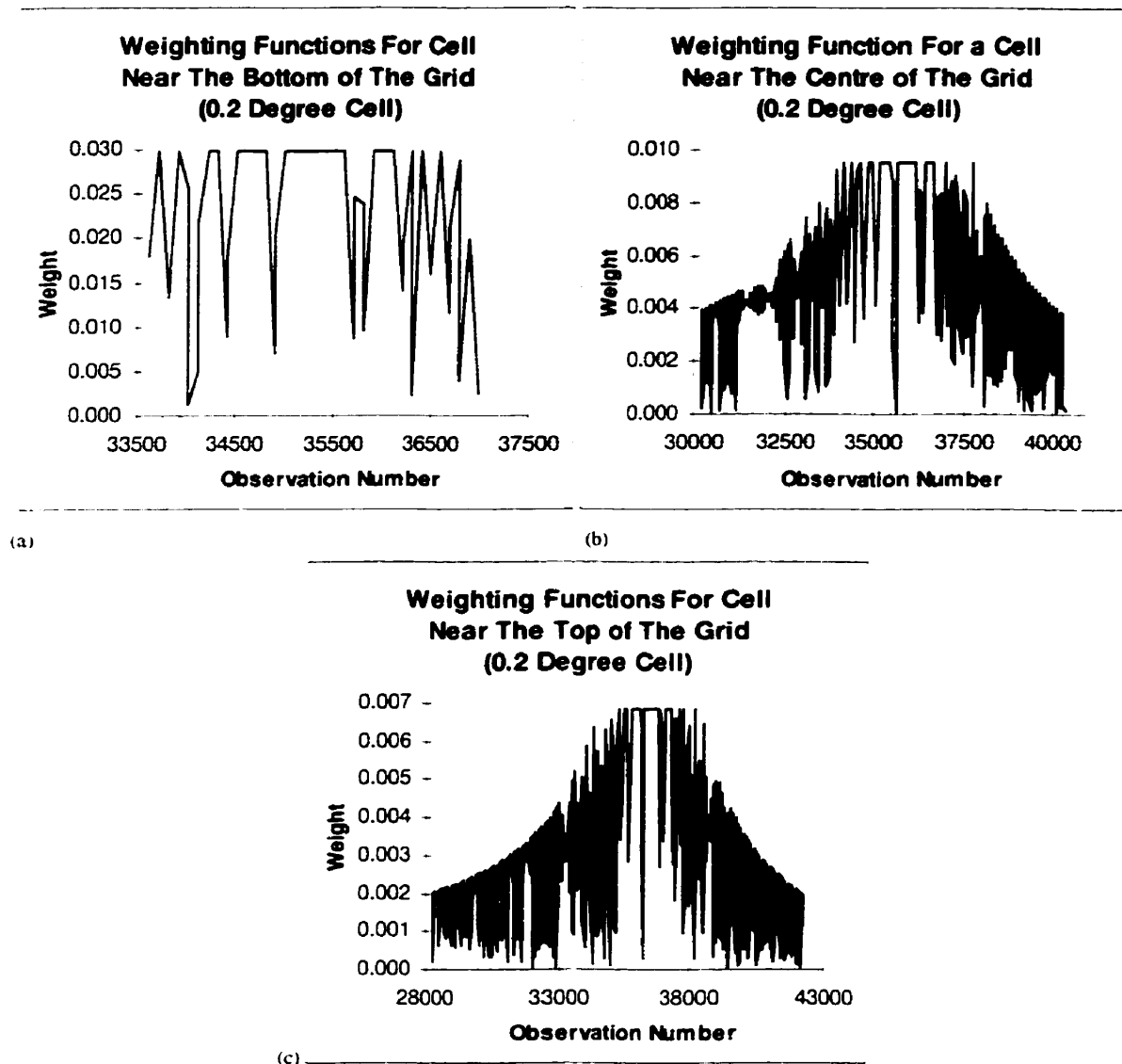


Figure 7.6: Three observation weighting filters for lines of sight that sample 1 km by 0.2° grid cells in the (C-1), (C-2) and (C-3) regions.

The weighting filter function for a cell in the (C-2) region is shown in Figure 7.6b. In this case the filter function exhibits the rise, plateau and fall characteristics that are seen in both the path length and weighting filter envelopes. The deviations from the envelope are due to type 4 through 8 intersections. The first observations that intersect the cell are associated with the lowest looking pixels of the first image that includes information from that cell: in this case the lines of sight are tangent before the cell of interest. As the satellite moves along its orbit subsequent observations that are tangent at higher

altitudes also sample the cell of interest. This causes the rise in the envelope in the first region of observations. In every case these observations are tangent before intersecting the cell. The observations associated with the central region of the weighting filter function are tangent in and near the cell and the dominant intersection is the *Angle-Angle* type. As the satellite moves further along its orbit, corresponding to an increase in the observation number, only those observations that are tangent after intersecting the cell of interest can sample that cell. The tangent altitude of these observations necessarily decreases as the satellite moves towards the cell and there is a consequent decrease in the observation weighting filter. The observation weighting filter shape (Figure 7.6c) for cells in the (C-3) region near the top of the grid is quite similar to that for (C-2) region cells.

It is the observation weighting filter that determines the influence of each observation on the retrieval in any given cell (equations 7.1 and 7.2). The lines of sight and the observation weighting filter functions determine the kernels for each cell that impact the retrieval in that cell.

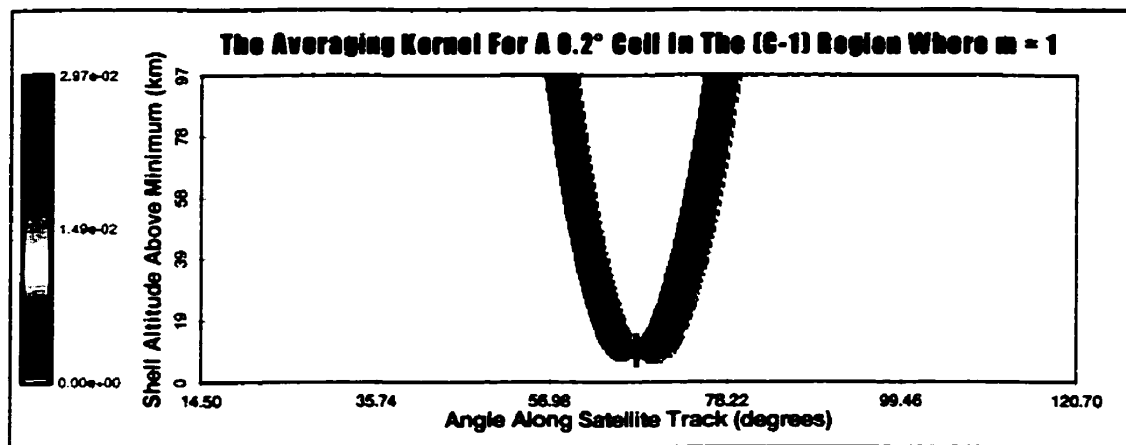
7.4.2 The Averaging Kernel Formed by the Observation Weighting Filter

As noted the volume emission rates in grid cells that are in the 'neighbourhood' of the cell of interest influence the solution for that cell. The 'neighbourhood' does not imply close physical proximity rather it includes all those cells that are sampled by lines of sight that intersect the cell of interest. Examples of cells that are in the neighborhood of another cell were given in Chapter 6 (Figures 6.7b, 6.8b and 6.9b which showed those other cells that are sampled by observations that intersect the particular cell). These plots also demonstrate that the neighbourhood of a given cell depends on its position in the grid.

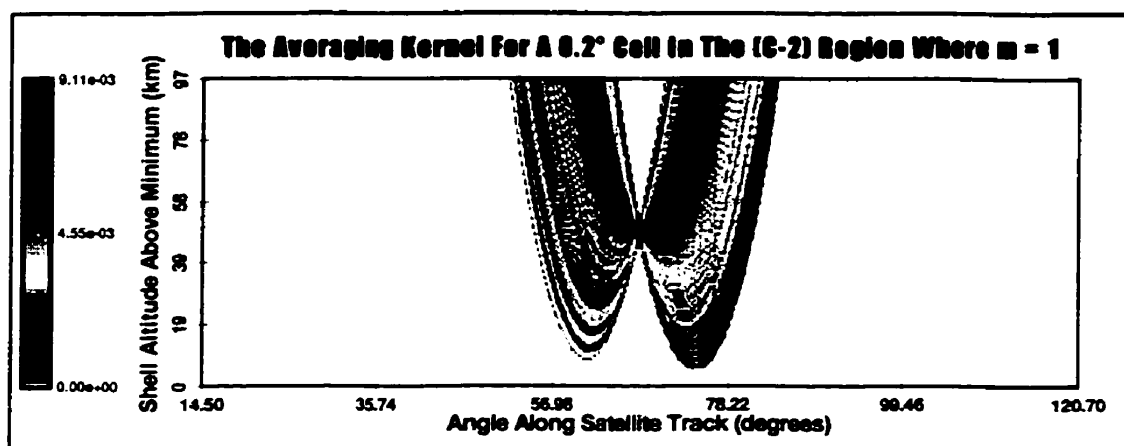
While these figures highlight those cells that are sampled by lines of sight that intersect a given cell they do not indicate the relative importance of the other cells to the volume emission rate solution for the given cell. In an effort to interpret this relative importance

of cells in the neighbourhood the concept of an averaging kernel has been introduced. The averaging kernel is determined from the weighting filter function value for each observation that intersects the cell. In practice every cell sampled by each observation is incremented by the weighting filter function for that observation and the simple average is obtained for each of the sampled cells. In this way an average weight is determined for the effect of each cell, in the neighbourhood of the given cell, on the retrieval in the cell of interest.

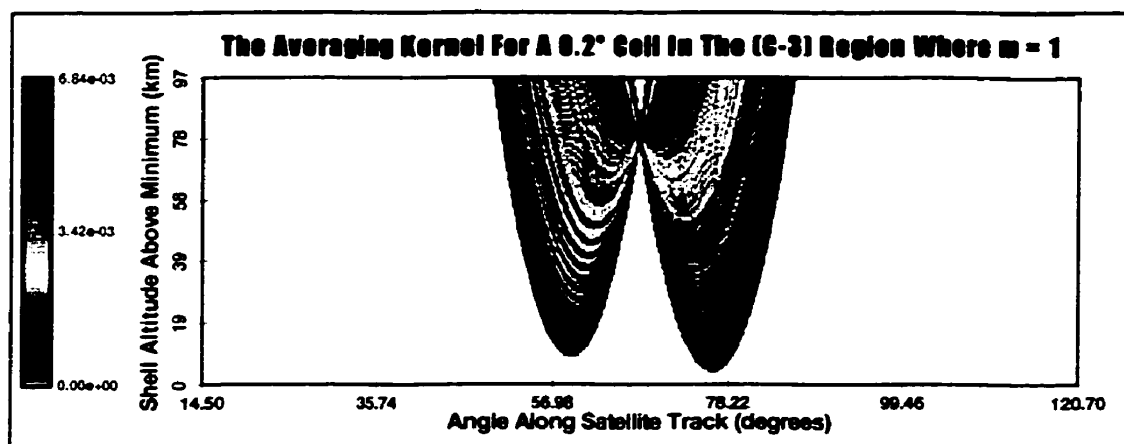
Three sample averaging kernels, for cells in each of the (C-1), (C-2) and (C-3) regions, are shown in Figure 7.7. In each case the cell size is 1 km by 0.2° and the imaging rate is 0.5 Hz, the weighting factor exponent is equal to one. The colour scale indicates the averaging kernel value, or the relative weight, on the recovered value at the cell identified by the cross. The white areas contained within these plots have no immediate impact (for the current iteration) on the recovery of the highlighted cell. The contours in these plots indicate that cells sampled by those observations that are tangent near the cell of interest are more important for that cell. This is to be expected as these observations predominantly sample in the *Angle-Angle* fashion (in the plateau region).



(a)



(b)



(c)

Figure 7.7: The averaging kernels for the observation weighting filters shown in Figure 7.6 for cells in regions (C-1), (C-2) and (C-3).

The plot in Figure 7.7a illustrates the averaging kernel for a cell in the (C-1) region and corresponds to the observation weighting filter shown Figure 7.6a. The neighbourhood of cells is quite narrow and each cell in the neighbourhood has approximately the same effect on the cell of interest. The weight for each cell is approximately 0.03. For a (C-2) region cell (Figure 7.7b) the average weight for each cell in the neighbourhood is not uniform. Cells that correspond to lines of sight that are tangent near the cell of interest have nearly maximum weight, while those cells that are sampled by observations that are tangent at a considerable distance from the cell of interest have a lower weight. This is significant for the identification of small scale structures as the volume emission rates in distant cells are not expected to be as highly correlated with that of the cell of interest

as those in cells that are physically close. The averaging kernel for a cell in region (C-3) is shown in Figure 7.7c. This cell has a very large neighbourhood and a wide range of weights within the neighbourhood. Again those cells that are in the neighbourhood yet physically far away from the cell of interest have little relative importance to the solution at that cell.

The averaging kernel is the most important factor associated with the tomographic inversion technique. It is important that the correct kernel, as dictated by the observation weighting filter function, be determined for the inversion. As with the weighting filters the averaging kernel can be modified by a variation in either the angular grid cell dimension or the weighting factor exponent.

7.5 The Averaging Kernels in Each of the Three Central Regions

As noted the averaging kernel is different in each of the three central regions, (C-1), (C-2) and (C-3), of the retrieval grid.

7.5.1 Region (C-1)

In region (C-1), near the bottom of the grid, the observation weighting filter (Figure 7.6a) is approximately uniform as all observations that sample cells in this region are tangent near the cell of interest and so follow nearly the same path through the grid. However, if the angular dimension of the grid cells is large so that there are no Angle-Angle intercepts the weighting filter becomes essentially random since it is dominated by secondary intersection types. The relative uniformity of the weighting filter function in this region leads to an averaging kernel (Figure 7.7a) that is also uniform. This uniformity is maintained even for an increased weighting factor exponent (Figure 7.8). In practice as all observations of cells in the (C-1) region have almost identical paths there is no requirement to adjust the weight of the different observations.

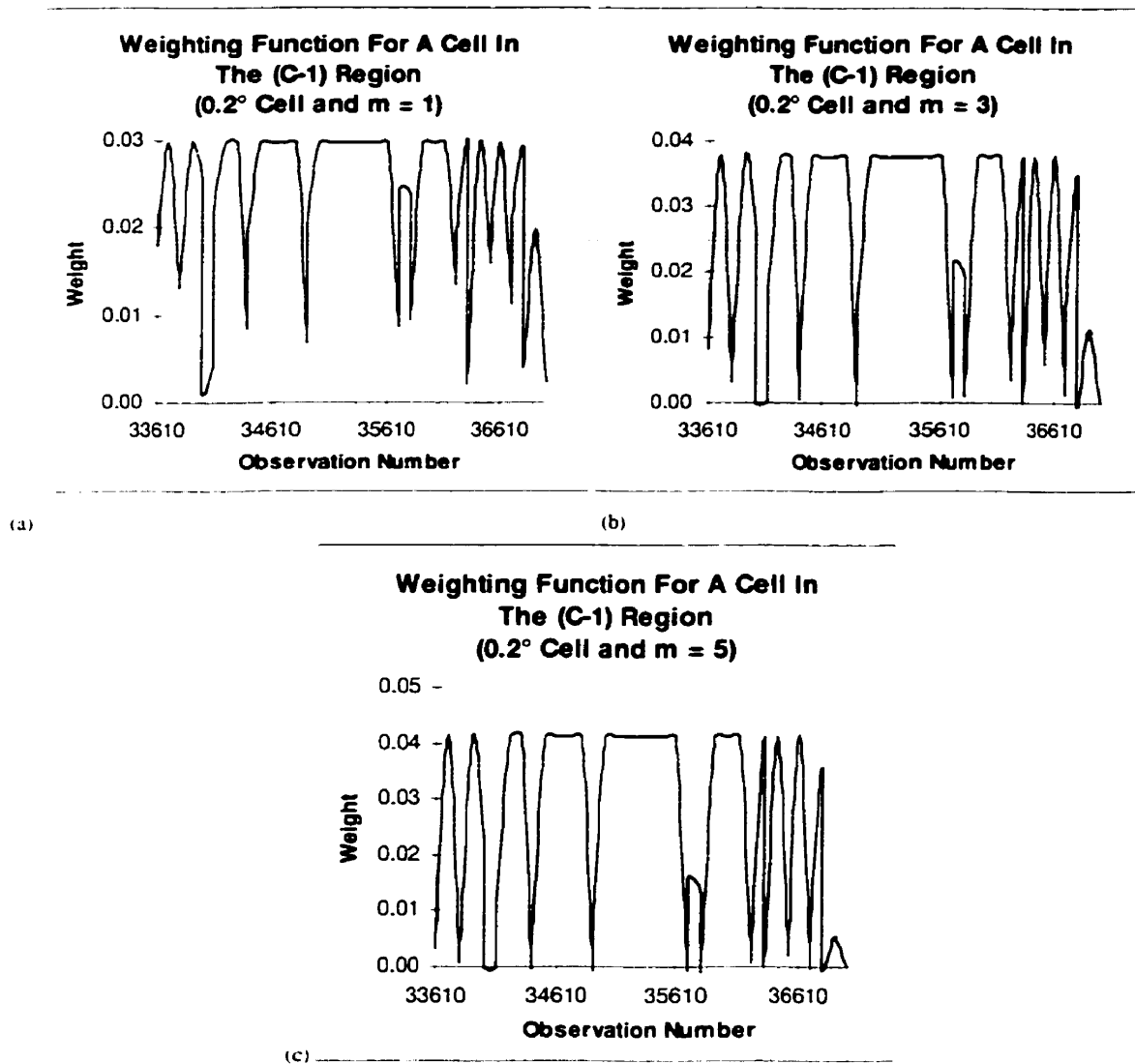


Figure 7.8: *The weighting filter functions for a cell in the (C-1) region, the angular dimension of the grid cell is 0.2°. The filter function is essentially independent of the weighting factor exponent.*

7.5.2 Region (C-2)

In region (C-2) the weighting filter function is dependent on both the grid cell size and the weighting factor exponent. It was shown in Sections 7.2 and 7.3 that the path length and weighting filter envelopes, and therefore the weighting filter function, changed shape if either the grid cell size or the weighting factor exponent changed. The example shown in Figures 7.6b included a wide range of tangent altitudes below the cell of interest that is characteristic of the (C-2) region. As the averaging kernel in the (C-2) region is affected by both a change in the grid cell size and the weighting factor exponent three different grid cell sizes and exponents have been considered. The kernels, and the weighting filter functions, for cells in the (C-2) region are shown in Figures 7.9 through 7.14 and illustrate the important differences that result from the different parameters.

The weighting filter functions for a grid cell size of 0.1° and three different exponents ($m = 1, 3$ and 5) are shown in Figure 7.9. In each case there is a wide range of observations that fall within the central plateau of the weighting filter functions where the dominant intersection type is *Angle-Angle*. As with the (C-1) region, where *Angle-Angle* intercepts also dominate, the weighting filter functions and, therefore, the averaging kernels are not significantly changed as the weighting factor exponent is varied. However, for those observations away from the plateau that intersect the cell in a secondary fashion the normalized relative weights are moderately attenuated by an increase in the exponent.

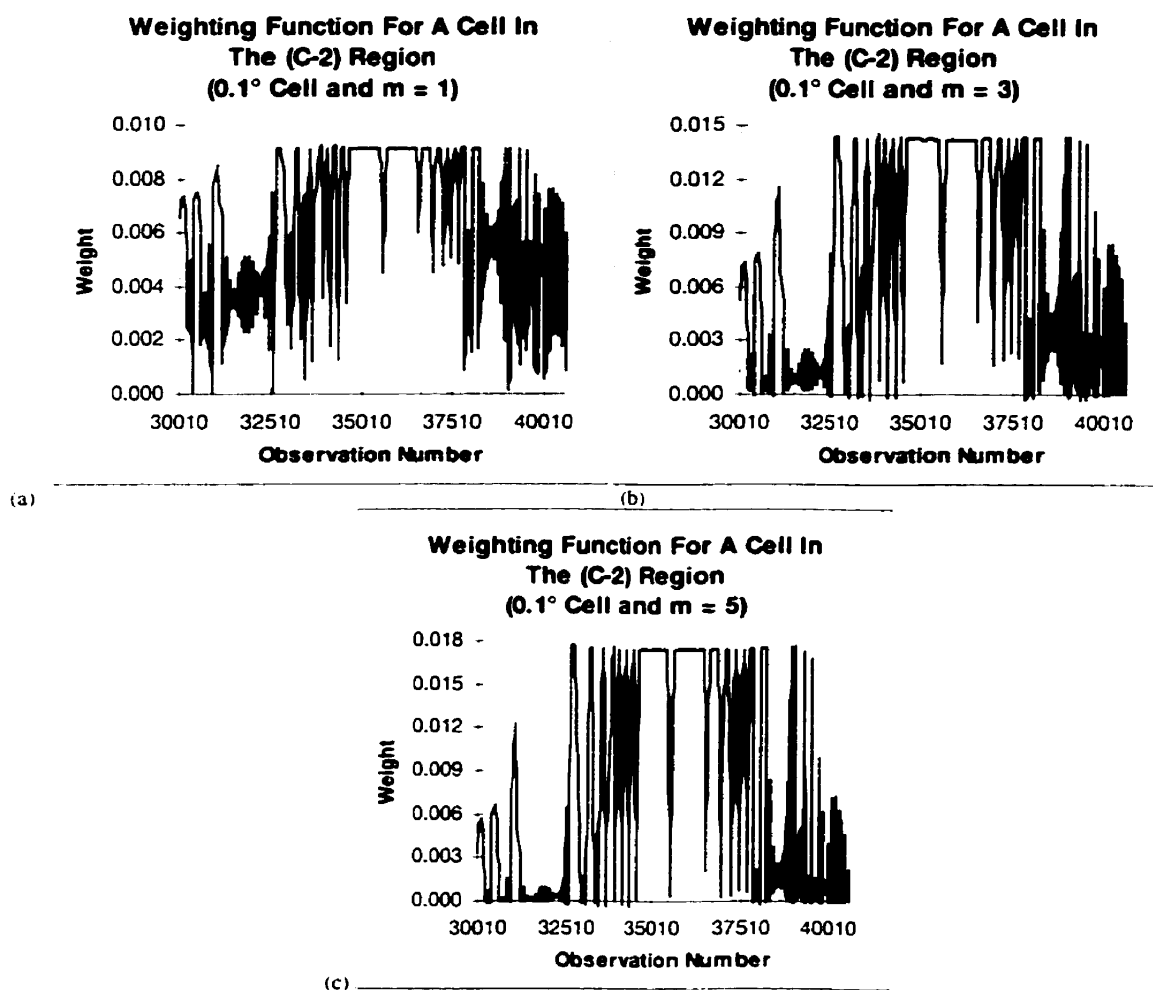
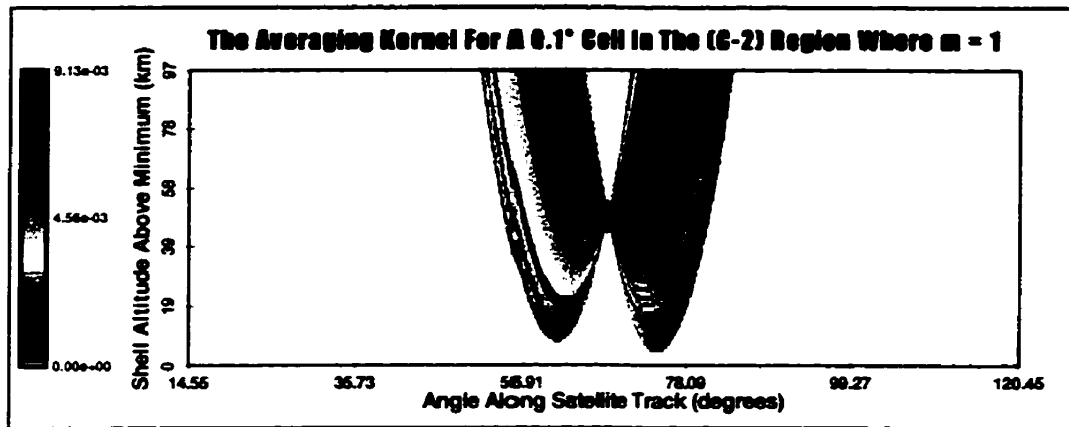
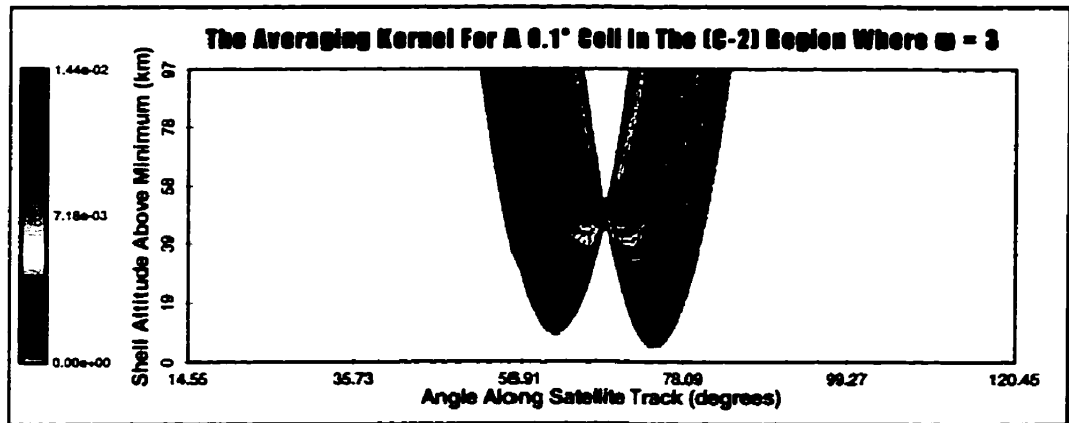


Figure 7.9: The weighting filter functions for a cell in the (C-2) region that correspond to a grid cell size of 0.1° and $m = 1, 3$ and 5 .

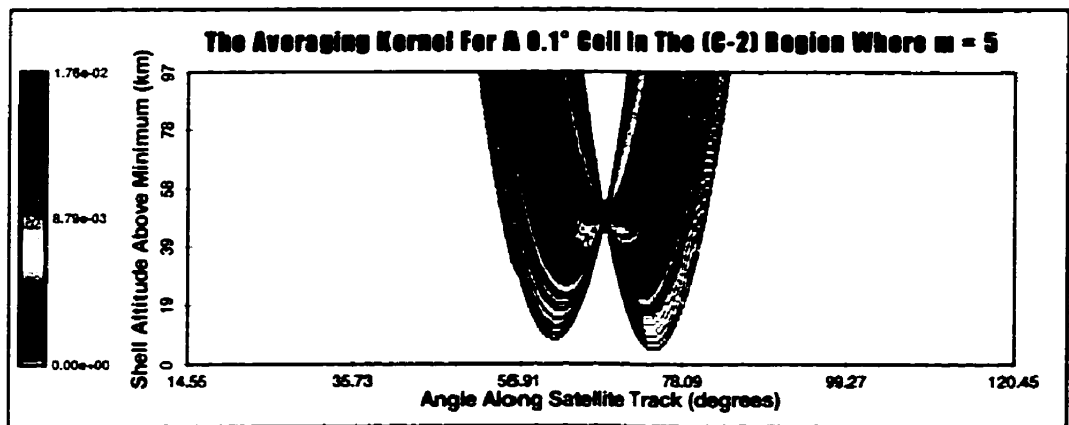
The averaging kernels for the weighting filter functions shown in Figure 7.9 are illustrated in Figure 7.10. As the weighting factor exponent is increased so there is a small attenuation in the relative importance of cells that are physically distant from the cell of interest. For $m = 1$ all of the sampled cells have approximately the same importance. When the weighting factor exponent is increased to 3 the averaging kernel tightens and there is an increased (relative) importance for those cells that are physically close to the cell of interest. When m is increased to five the kernel tightens even more. However, although the averaging kernel has tightened with the increased exponent those cells that are in the neighbourhood of the cell of interest, but physically far away, still have significant weight.



(a)



(b)



(c)

Figure 7.10: The averaging kernels for a grid cell in the (C-2) region, the cell size is 0.1° and $m = 1, 3$ and 5 . These averaging kernels are almost independent of the weighting factor exponent.

The weighting filter functions for a 0.2° grid cell are shown in Figure 7.11. In this case for each value of the exponent there is a narrow plateau in the weighting filter function

and attenuation of the weighting for observations that are tangent below the cell of interest. The attenuation increases as the weighting factor exponent increases. Those observations that are tangent at large distances from the cell of interest have little influence on the solution at that cell.

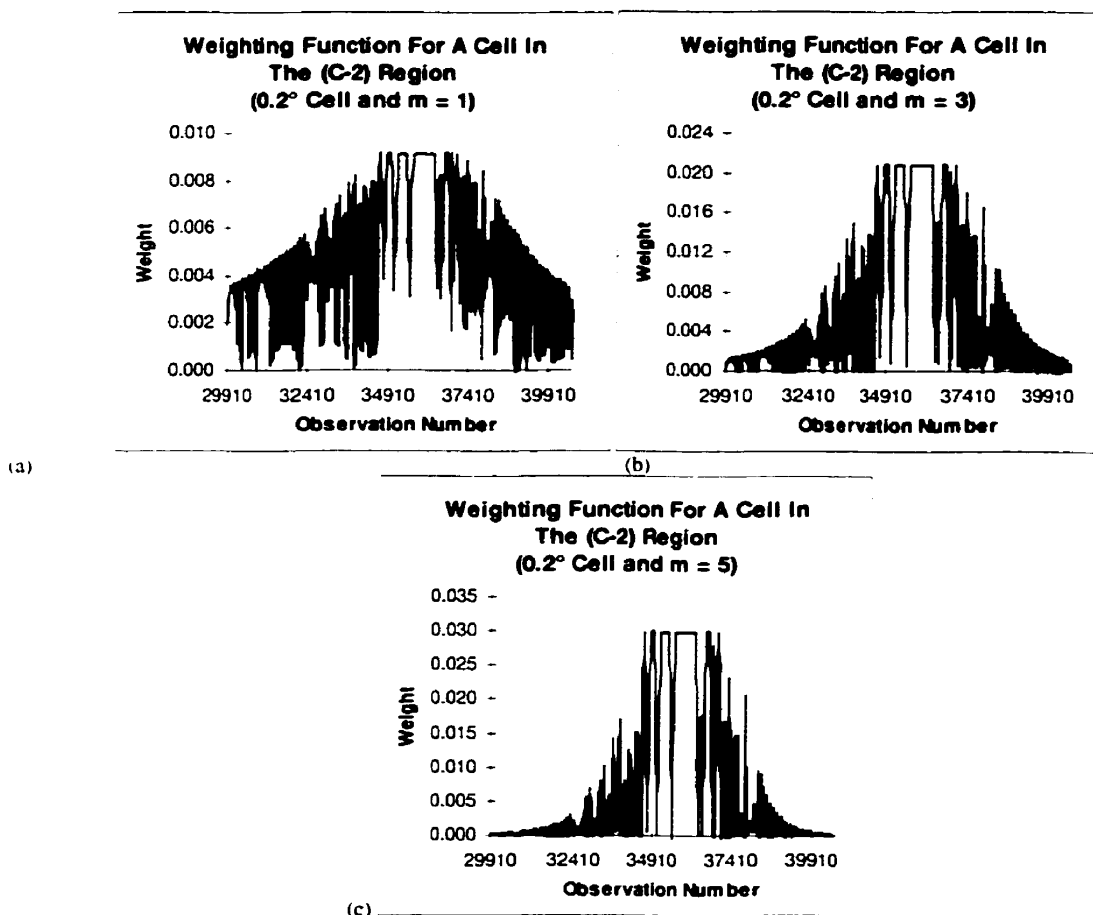
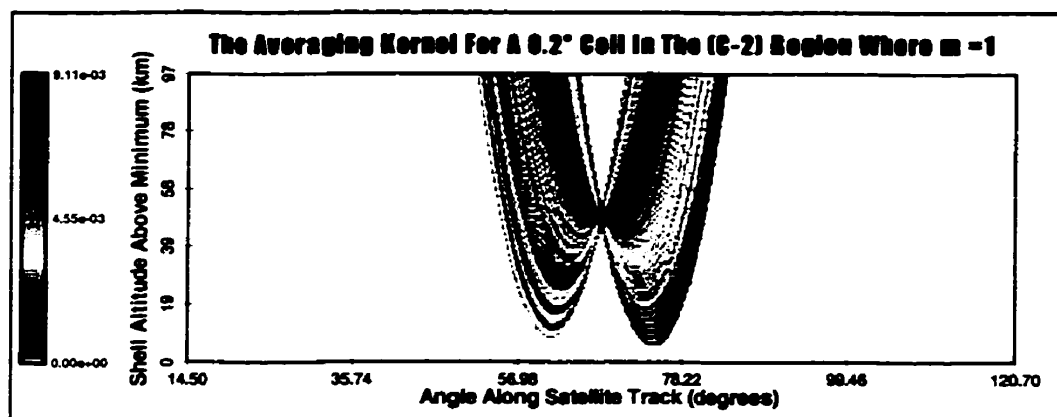


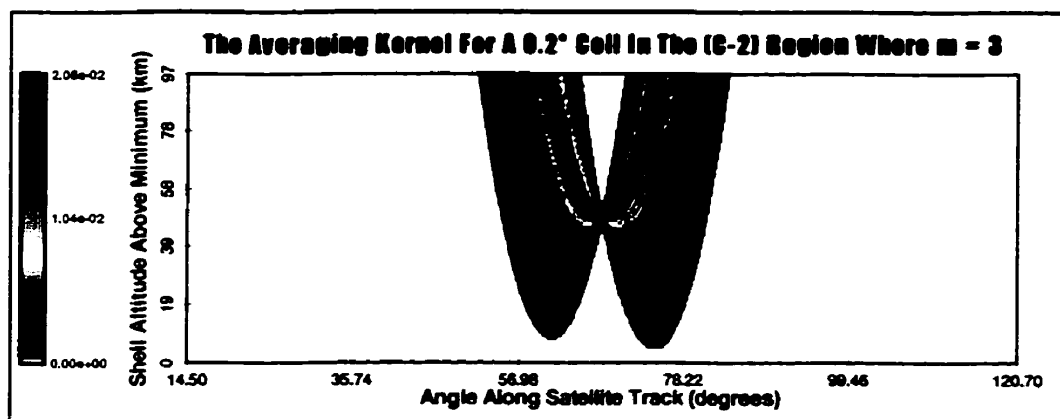
Figure 7.11: The weighting filter functions, in the (C-2) region, that correspond to a grid cell size of 0.2° and $m = 1, 3$ and 5.

The relative importance of the neighbourhood cells for the 0.2° grid cell is shown in the averaging kernel plots in Figure 7.12. For this cell size the relative importance of the cells physically distant from the cell of interest is noticeably decreased from that for the 0.1° grid cell with the same exponent. As m is increased there is significant tightening of the averaging kernel. Observations that are tangent well below the cell of interest have little effect on the solution at that cell. Many of the cells in the neighbourhood, but physically far removed, do not register on the colour scale for $m = 5$. In Figure 7.12c

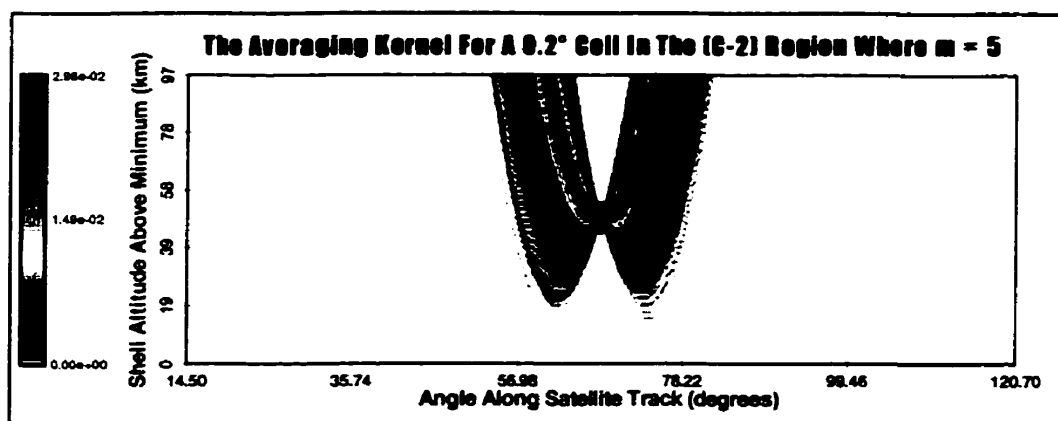
only those observations that are tangent very near the cell of interest have a high weight, although the effect of those cells a moderate distance away has not been completely eliminated.



(a)



(b)



(c)

Figure 7.12: The averaging kernels for a grid cell in the (C-2) region, the cell size is 0.2° and $m = 1, 3$ and 5 . These averaging kernels tighten as the weighting factor exponent is increased.

If the grid cell size is increased to 0.6° then the averaging kernels for cells in the (C-2) region tighten in an extreme fashion (Figure 7.14) as the weighting factor exponent increases. The weighting filter functions for a 0.6° grid cell size with the different exponents are shown in Figure 7.13 and illustrate the reason for the extreme tightening. In each case the plateau region is very narrow as few observations intersect in the *Angle-Angle* fashion and have the maximum weight. In addition because of the large distance between the angular boundaries the maximum weight is large, compared to the *Shell-Shell* intercept weights. The increase in the exponent significantly increases the relative importance of this limited number of *Angle-Angle* observations.

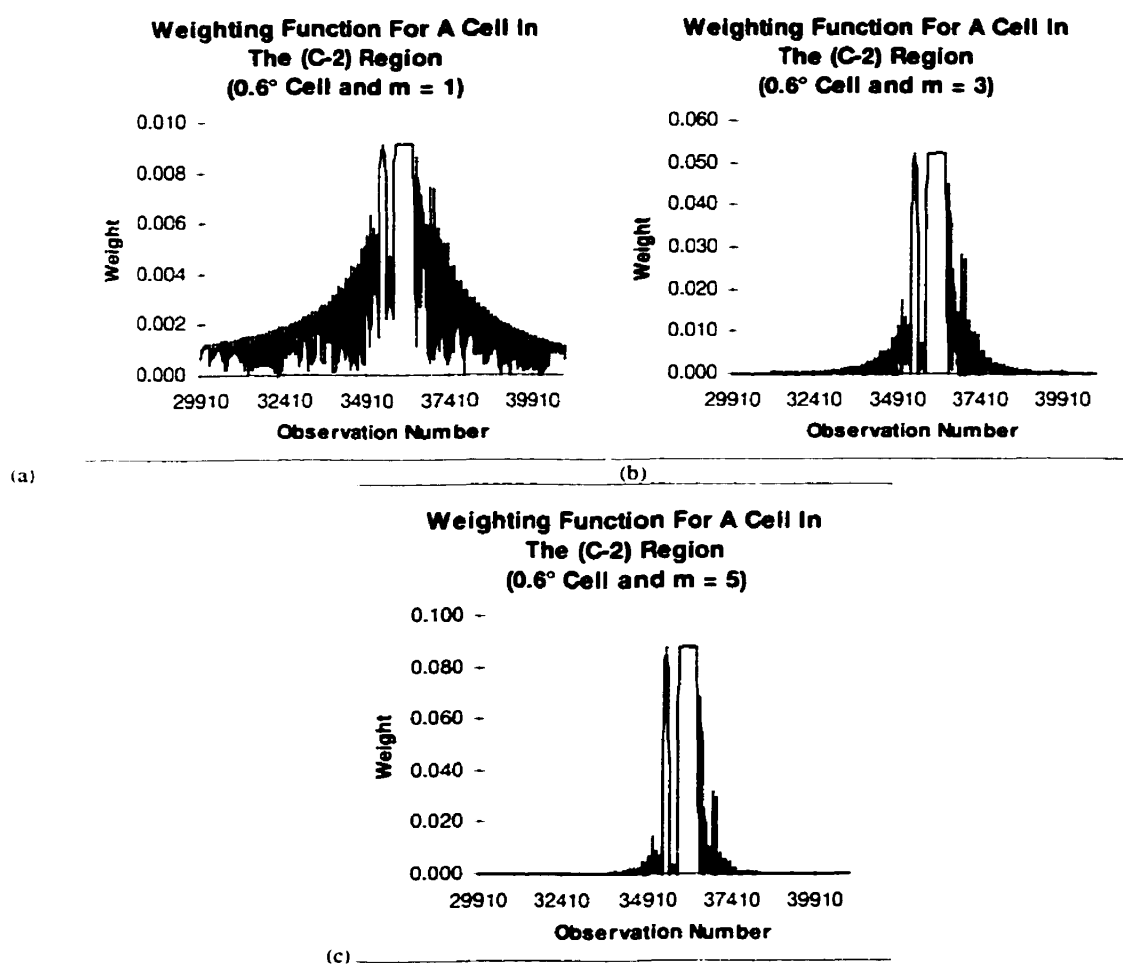


Figure 7.13: The weighting filter functions, in the (C-2) region, that correspond to a grid cell size of 0.6° and $m = 1, 3$ and 5 . There are considerable differences as the weighting factor exponent is increased.

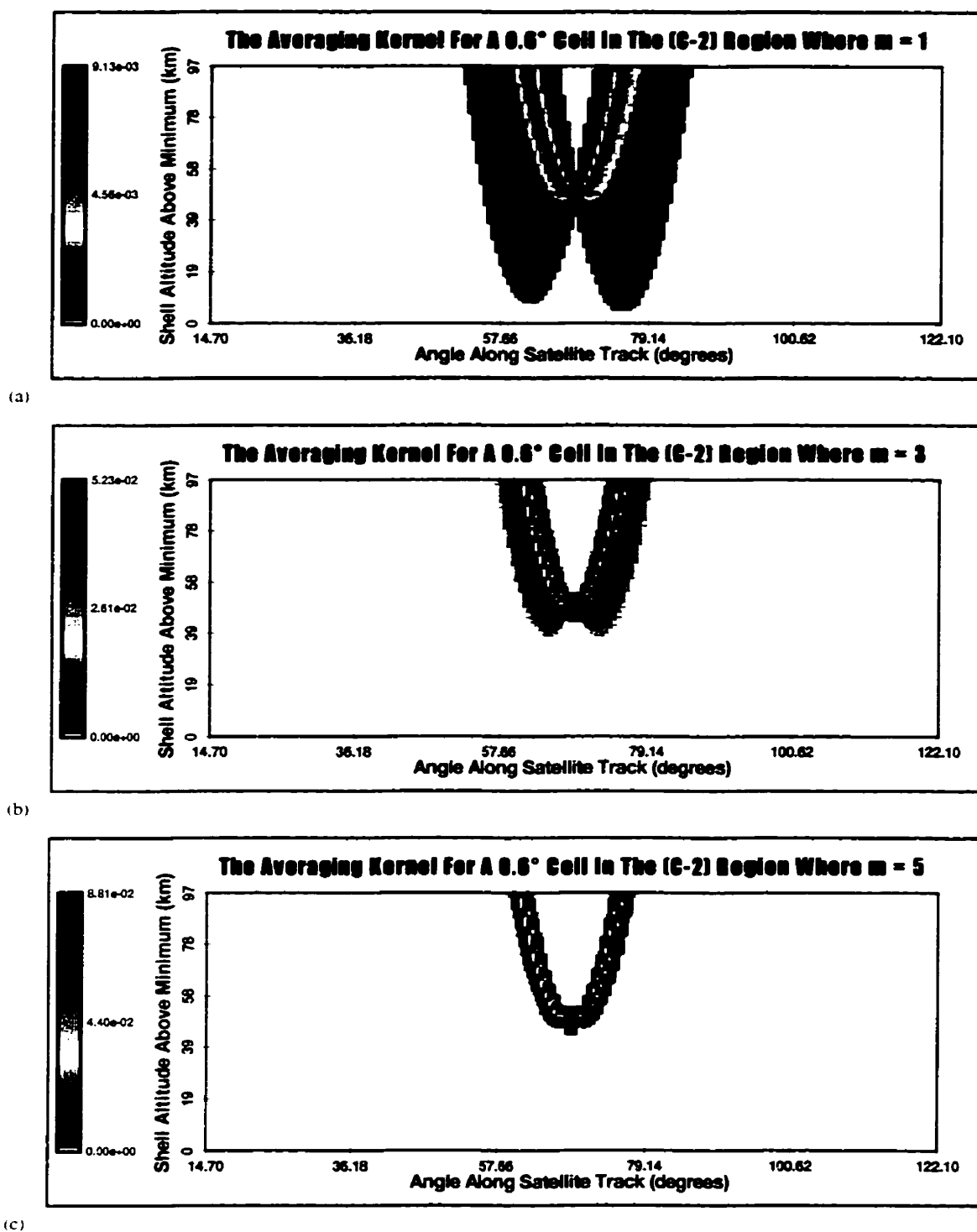


Figure 7.14: *The averaging kernels for a grid cell in the (C-2) region, the cell size is 0.6° and $m = 1, 3$ and 5 . These averaging kernels tighten significantly as the weighting factor exponent is increased.*

The averaging kernels for the weighting filter functions shown in Figure 7.13 are given in Figure 7.14. For all but the lowest weighting factor exponent the kernels are severely tightened. Only those cells that are sampled by lines of sight that are tangent very near the cell of interest have an effect on the solution for that cell. The fundamental concept of the tomographic algorithm has been violated by these averaging kernels as a large number of the observations have been eliminated from the solution. In effect each cell becomes undersampled for these parameters.

7.5.3 Region (C-3)

Cells in the (C-3) region have a similar characteristic to those in the (C-2) region with respect to the averaging kernel and the observation weighting filter. However, as there is a wider range of observations that sample cells in the (C-3) region the filter functions and the averaging kernels exhibit some important differences from those in the (C-2) region. The averaging kernels are more susceptible to tightening with an increase in either the weighting factor exponent or the grid cell size, even for those parameters that result in predominantly *Angle-Angle* intercepts in the other regions.

This tightening is illustrated in Figure 7.15 for a 0.1° grid cell. In the (C-2) region there was almost no tightening of the averaging kernel (Figure 7.14) as the weighting factor exponent increased, but in the (C-3) region there is a noticeable attenuation of the weighting filter functions. This implies that the averaging kernel tightens as the weighting factor exponent increases and is illustrated in Figures 7.16a and 7.16b for a weighting factor exponent increase from 1 to 3. However, further the tightening is less apparent as m increases from 3 to 5 (Figure 7.16c). The reason for this is that the major contribution of the observation weighting filter is contained in the plateau observations and the increase in m from 1 to 3 has already reduced the effect of *Shell-Shell* and secondary intercepts. Thus for a grid cell size of 0.1° there is little effect on the averaging kernel as the weighting factor exponent is increased beyond 3.

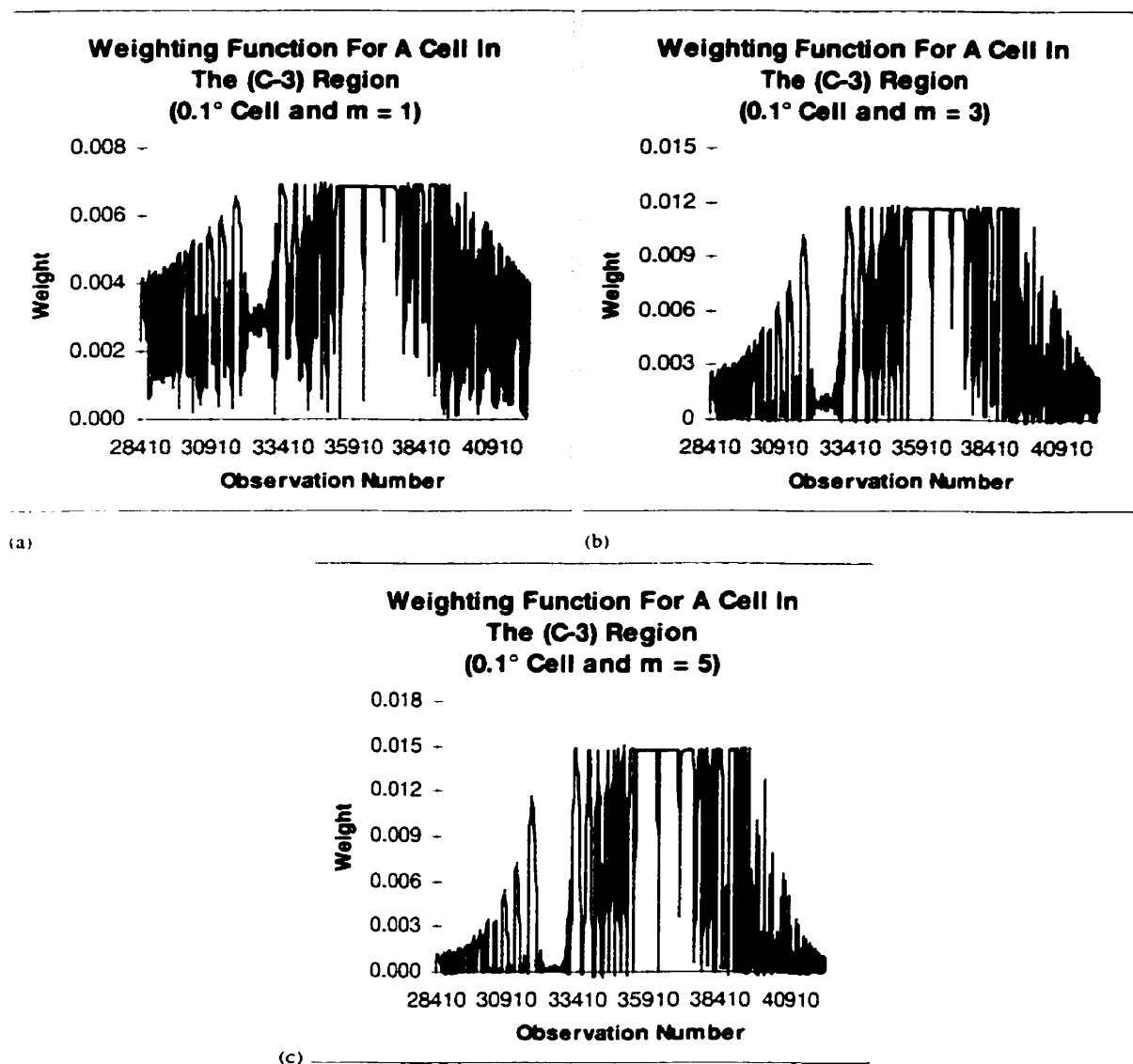
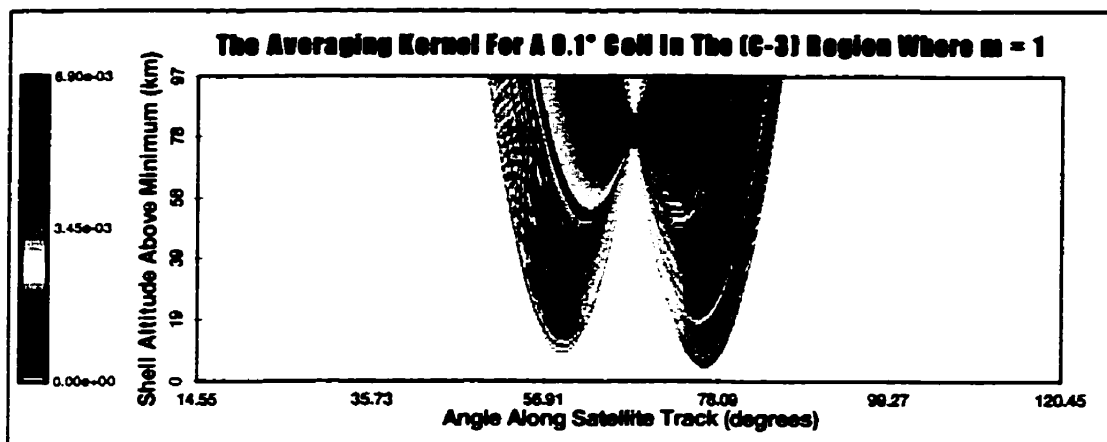
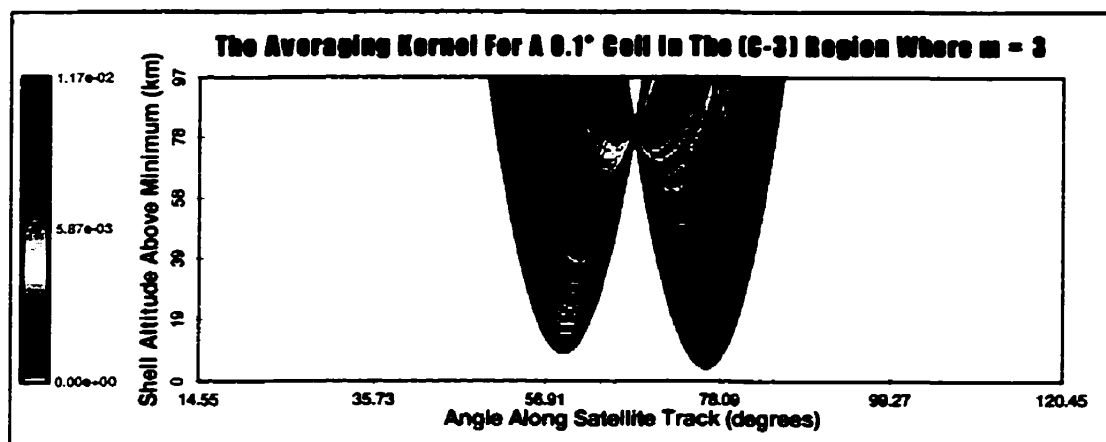


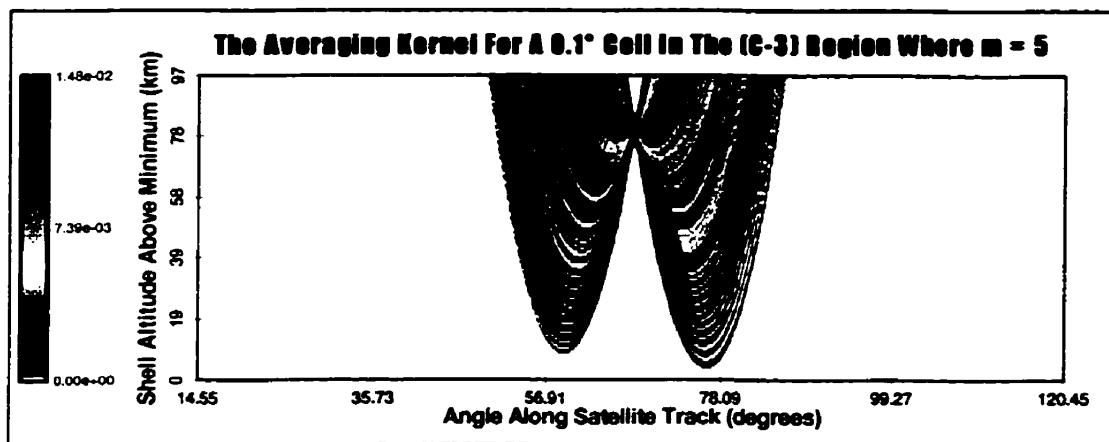
Figure 7.15: *The weighting filter functions, in the (C-3) region, that correspond to a grid cell size of 0.1° and $m = 1, 3$ and 5. As the weighting factor exponent is increased there is a noticeable change in the weighting filter function.*



(a)



(b)



(c)

Figure 7.16: The averaging kernels for a grid cell in the (C-3) region, the cell size is 0.1° and $m = 1, 3$ and 5 . These averaging kernels tighten as the weighting factor exponent is increased.

For a 0.2° grid cell size the weighting filter functions (Figure 7.17) and averaging kernels (Figure 7.18) for a cell in the (C-3) region indicate that as the weighting factor exponent is increased so the shapes of these functions change significantly. It is apparent that for the averaging kernels shown in Figure 7.18 that as the exponent is increased the contributions from observations that are tangent near the bottom of the grid have been completely removed and only those observations that are tangent near the cell of interest have an effect. The overall effect for a 0.2° grid cell in the (C-3) region is for the averaging kernel to tighten as the exponent increases but it still allows many cells to effect the retrieval at any given cell.

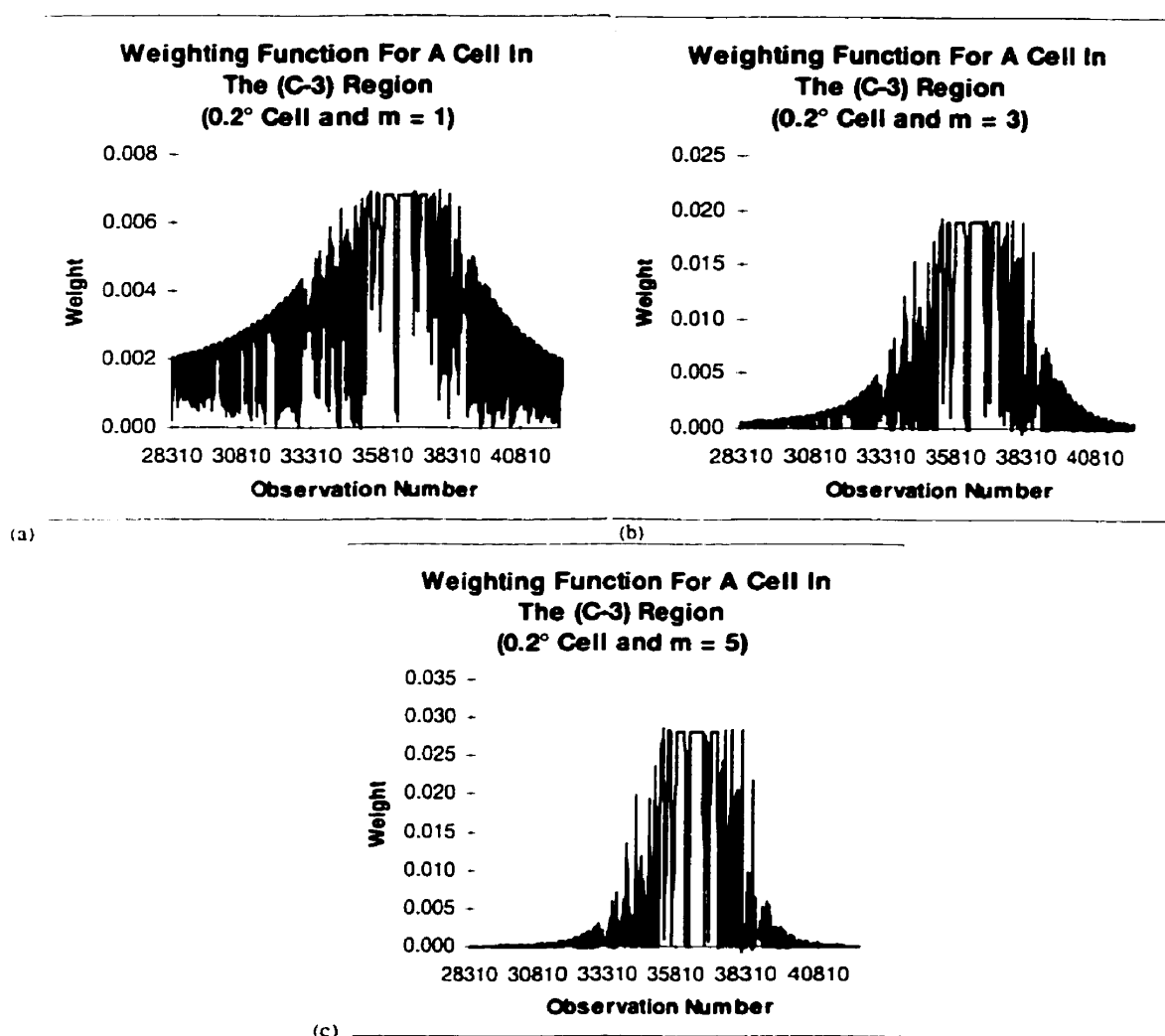
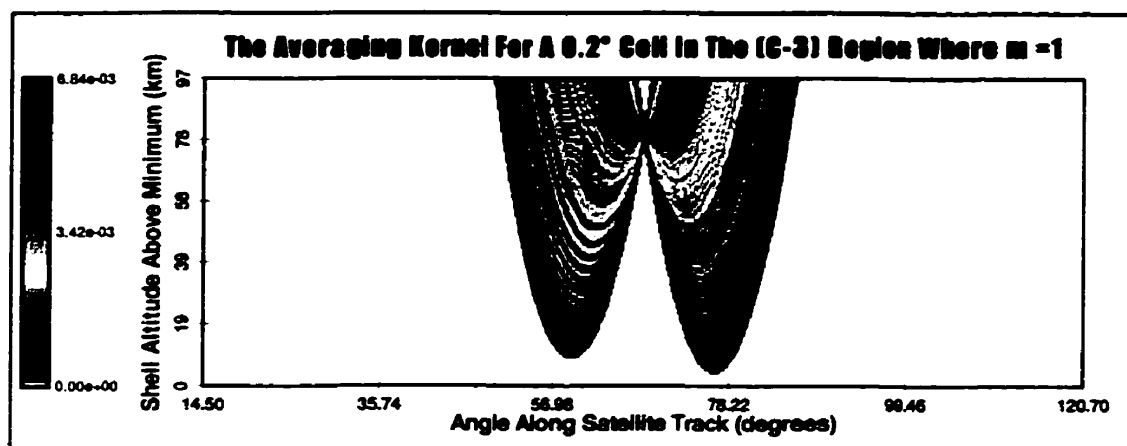
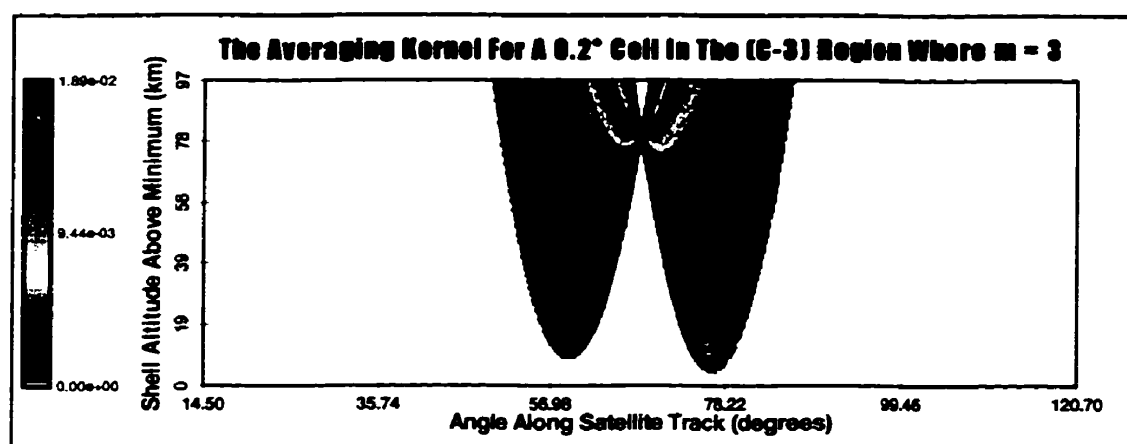


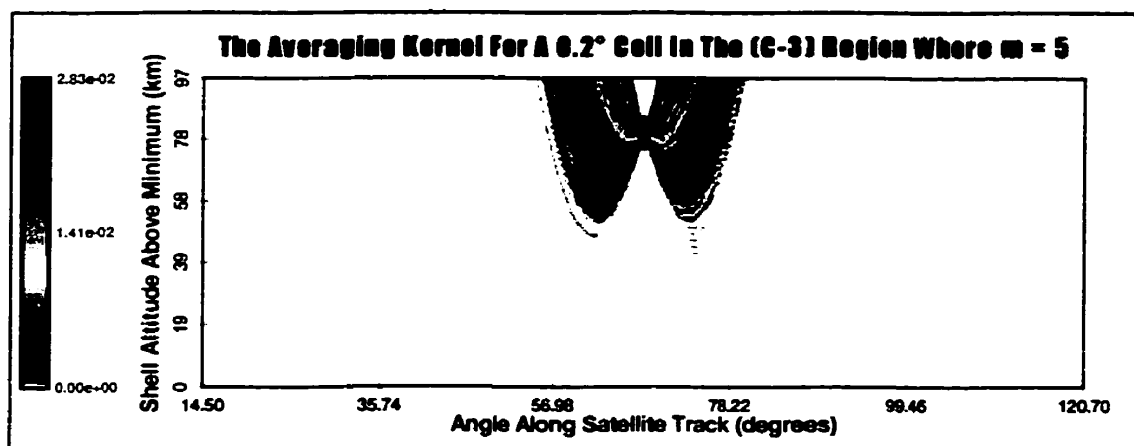
Figure 7.17: The weighting filter functions, in the (C-3) region, that correspond to a grid cell size of 0.2° and $m = 1, 3$ and 5 . As the weighting factor exponent increases there is a significant change in shape.



(a)



(b)



(c)

Figure 7.18: The averaging kernels for a grid cell in the (C-3) region, the cell size is 0.2° and $m = 1, 3$ and 5 . These averaging kernels significantly tighten as the weighting factor exponent is increased.

For a 0.6° grid cell in the (C-3) region the averaging kernel is tightened extremely as the weighting factor exponent increases. The weighting filter functions, shown in Figure 7.19, indicate that only a small fraction of those observations that intersect cells in the (C-3) region have any effect on the solution when the exponent equals 5. Although the attenuation at the extremes of the filter is not as dramatic for $m = 3$ (Figure 7.19b) it is still readily apparent.

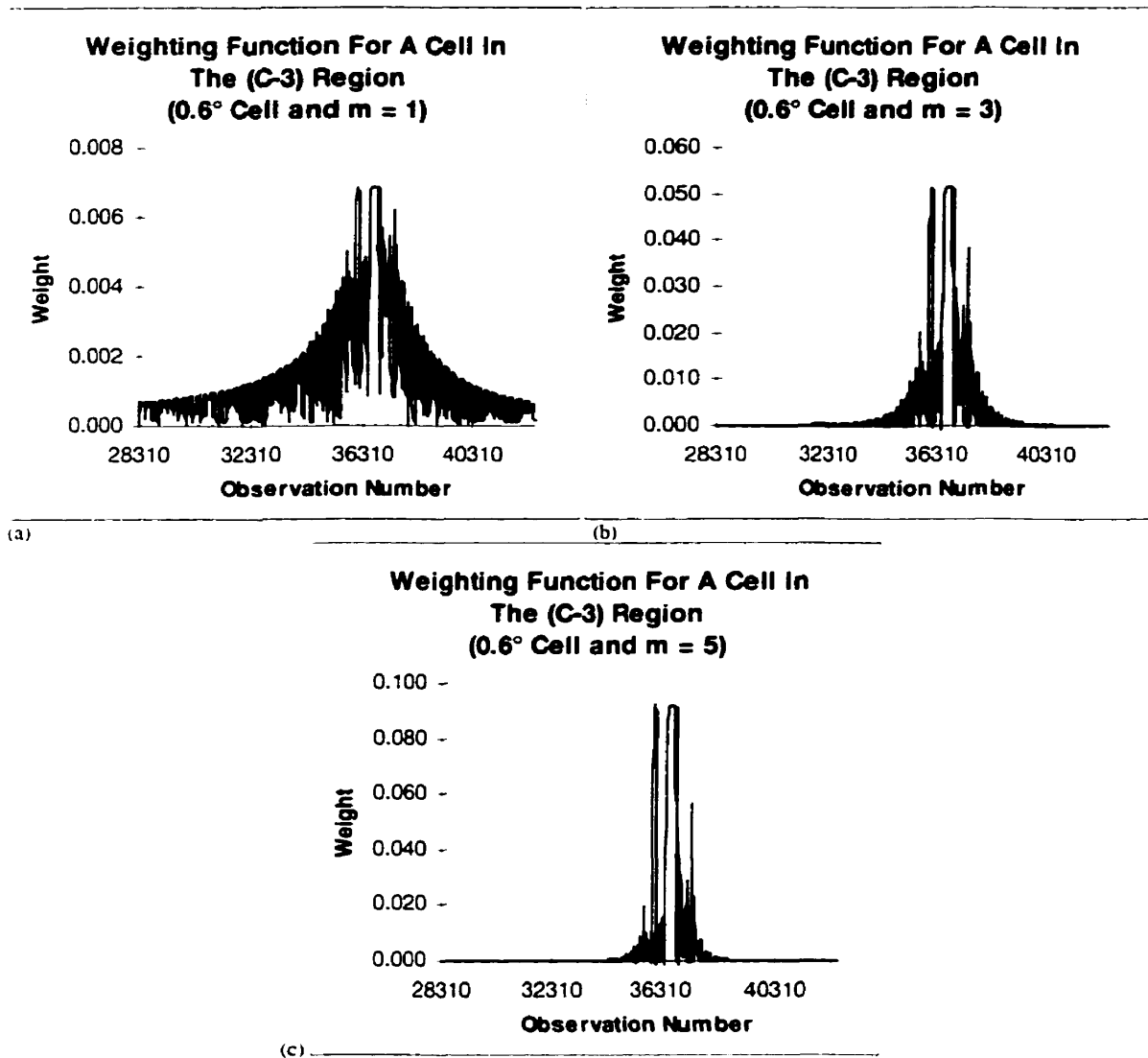
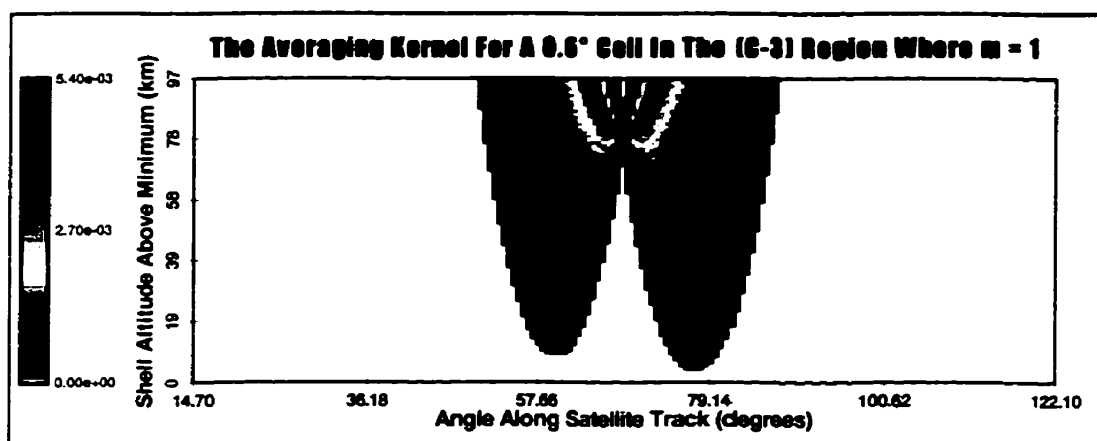
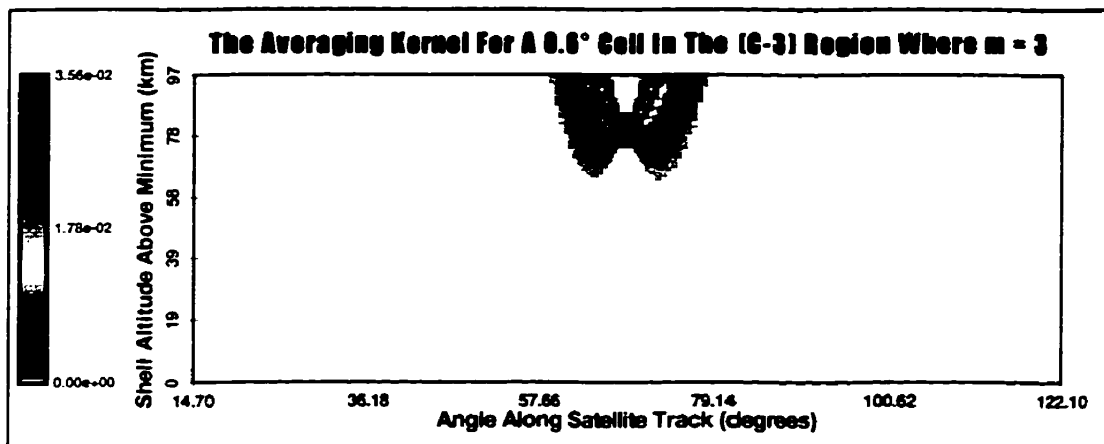


Figure 7.19: The weighting filter functions, in the (C-3) region, that correspond to a grid cell size of 0.6° and $m = 1, 3$ and 5 . There are very severe differences between the plots for different values of the weighting factor exponent.

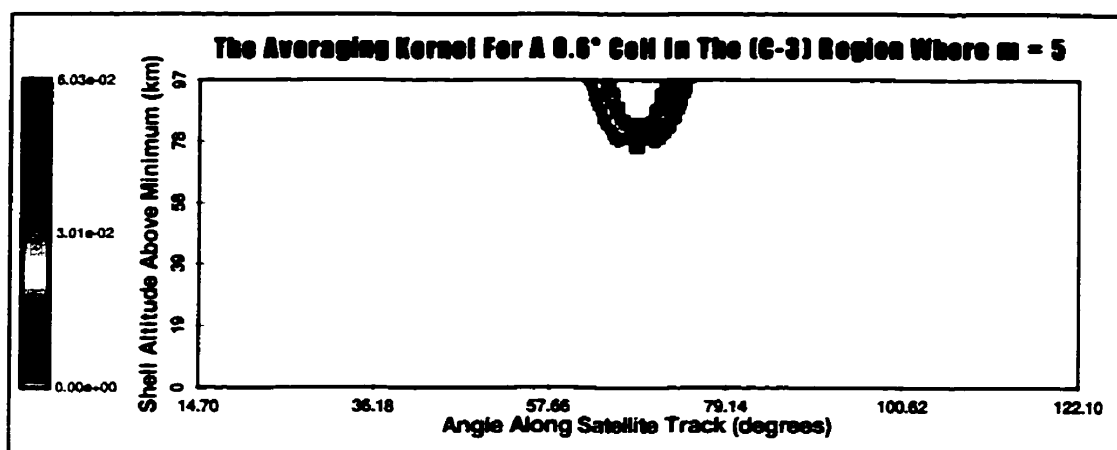
The averaging kernels for a 0.6° grid cell in the (C-3) region shown in Figure 7.20 illustrate the extreme tightening of the weighting function. The averaging kernel for all exponent values for this cell size is so tight that it effectively eliminates the influence of most of the observations to the solution at the cell of interest. Only those observations that are tangent near to the cell of interest have a significant effect on the solution for that cell. Thus for a grid cell size of 0.6° there is a significant undersampling of the cell and so a poor retrieval.



(a)



(b)



(c)

Figure 7.20: The averaging kernels for a grid cell in the (C-3) region, the cell size is 0.6° and $m = 1, 3$ and 5 . These averaging kernels severely tighten as the weighting factor exponent increases.

7.6 Convergence for Different Filter Shapes

The different observation weighting filters modify in a unique fashion the effects of the observations that sample a cell. Those weighting filters that exclude observations that are tangent well below the cell of interest allow the solution to begin at a more favourable position within the solution space and so converge more rapidly to the correct result. This is due to the shape of the vertical volume emission profile above the peak (Figure 7.21) and the fact that those observations that are tangent near the cell of interest sample cells with similar volume emission rates.

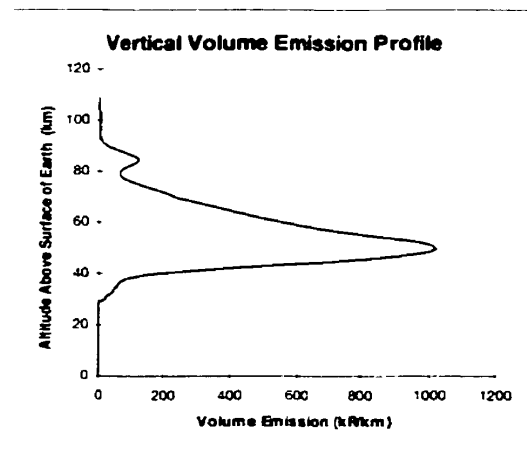


Figure 7.21: A typical vertical volume emission profile.

7.6.1 Reasons for Superior Convergence with Higher Weighting Factor Exponents

The associated brightnesses of the lines of sight that intersect any given cell cause some observation weighting filter functions to have superior convergence rates and more accurate results. For those filters where m is high the observations that are tangent at, or at least near to, the cell of interest are given a large weighting. These observations necessarily sample only a limited amount of the grid and so have an associated brightness that is more consistent with the particular cell. The brightness values for observations that sample cells in the (C-1), (C-2) and (C-3) regions are shown in Figure 7.22. These observations were generated for 0.5 Hz sampling rate of the input volume emission grid shown in Figure 6.12.

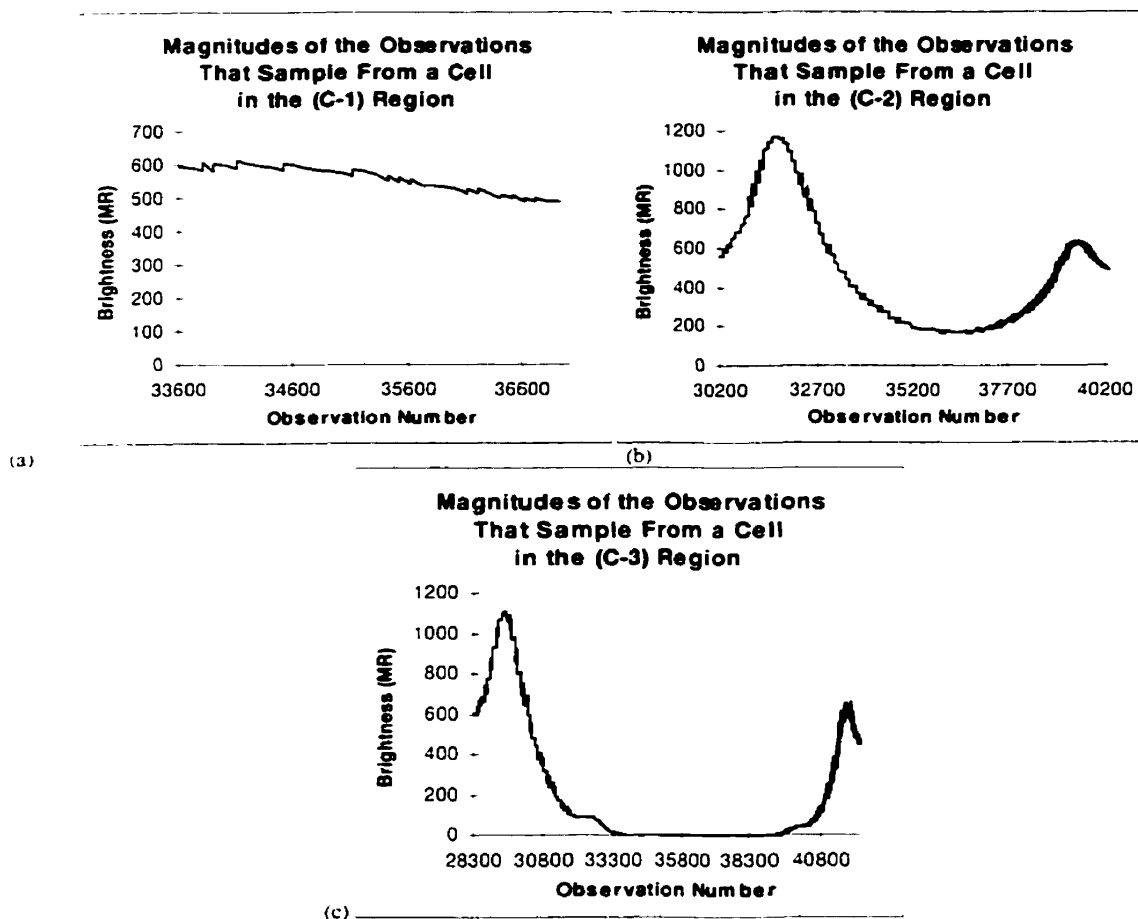


Figure 7.22: Typical line of sight brightnesses for observations that sample cells in the three grid regions. The discontinuities are due to discrete sampling.

Those observations that sample cells in the (C-1) region all have approximately the same brightness (Figure 7.22a) as they follow similar paths through the two dimensional volume emission grid. However, this is not the case for lines of sight that sample cells in the (C-2) region (Figure 7.22b). In this region the central observations, those that are tangent near the cell of interest all have similar magnitudes although the brightness is only 20% of that for observations that are tangent well below the cell of interest. The difference in the brightnesses of observations are even larger for cells in region (C-3) (Figure 7.22c). In this case there is a wide range of observations that are tangent at many different altitudes that sample these cells.

For cells in the (C-2) and (C-3) regions it is important to attenuate the contributions from those observations that are tangent near the peak of the volume emission profile as their contribution would otherwise dominate the initial estimate for the volume emission solution. The initial volume emission estimate for cells in the (C-2) and (C-3) regions should be dominated by those observations that are tangent in the region.

The initial estimate in the tomographic retrieval that is used to start the iterative procedure is a flat uniform profile (Section 5.2.5). As the previous observation estimate, $O_{i_{ev}}^{(n-1)}$ in equation 7.1, is a linear combination of the volume emission rates contained within the grid (equation 7.3) the $V_j^{(0)}$ values may be canceled to give equation 7.6 as the first iterative solution to the volume emission rate contained within cell j .

$$V_j^{(1)} = \sum_i \left(\frac{O_i}{\sum_j L_{ij}} \beta_j \right) \quad [7.6]$$

The interior summation in the denominator is the path length for the observation i through the entire grid. This implies that the initial estimate, for each observation that samples a given cell, is just the measured value divided by the path length through the grid, *i.e.* each observation is considered to have a uniform profile along its line of sight.

Figures 7.23 and 7.24 illustrate the total path lengths through the grid and the first estimate of the volume emission rate contained within the cell of interest for the observations shown in Figure 7.22. In the (C-1) region the volume emission rates predicted by the observations (Figure 7.24) are nearly uniform so that all observations should be equally weighted. However, for cells in the (C-2) and (C-3) regions the predicted volume emission rates for each observation cover a large dynamic range and it is the lower values, that correspond to observations that are tangent near the cell of interest, that are the most relevant. The large volume emission rates associated with the peak in the emission intensity must be assigned a smaller weight.

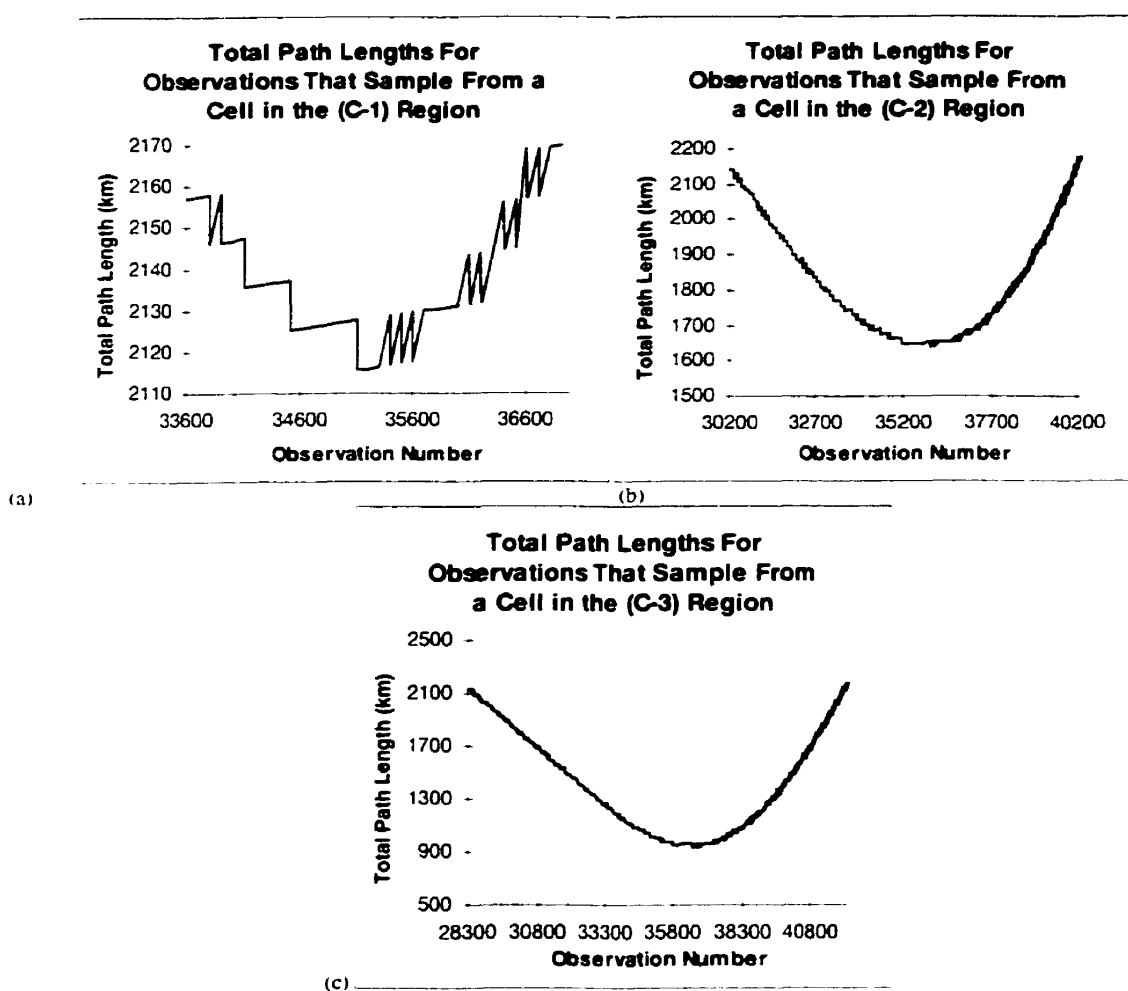


Figure 7.23: The path lengths through the entire grid for observations that sample cells in each of the (C-1), (C-2) and (C-3) regions. Apparent discontinuities in these path lengths are due to the discrete nature of the grid.

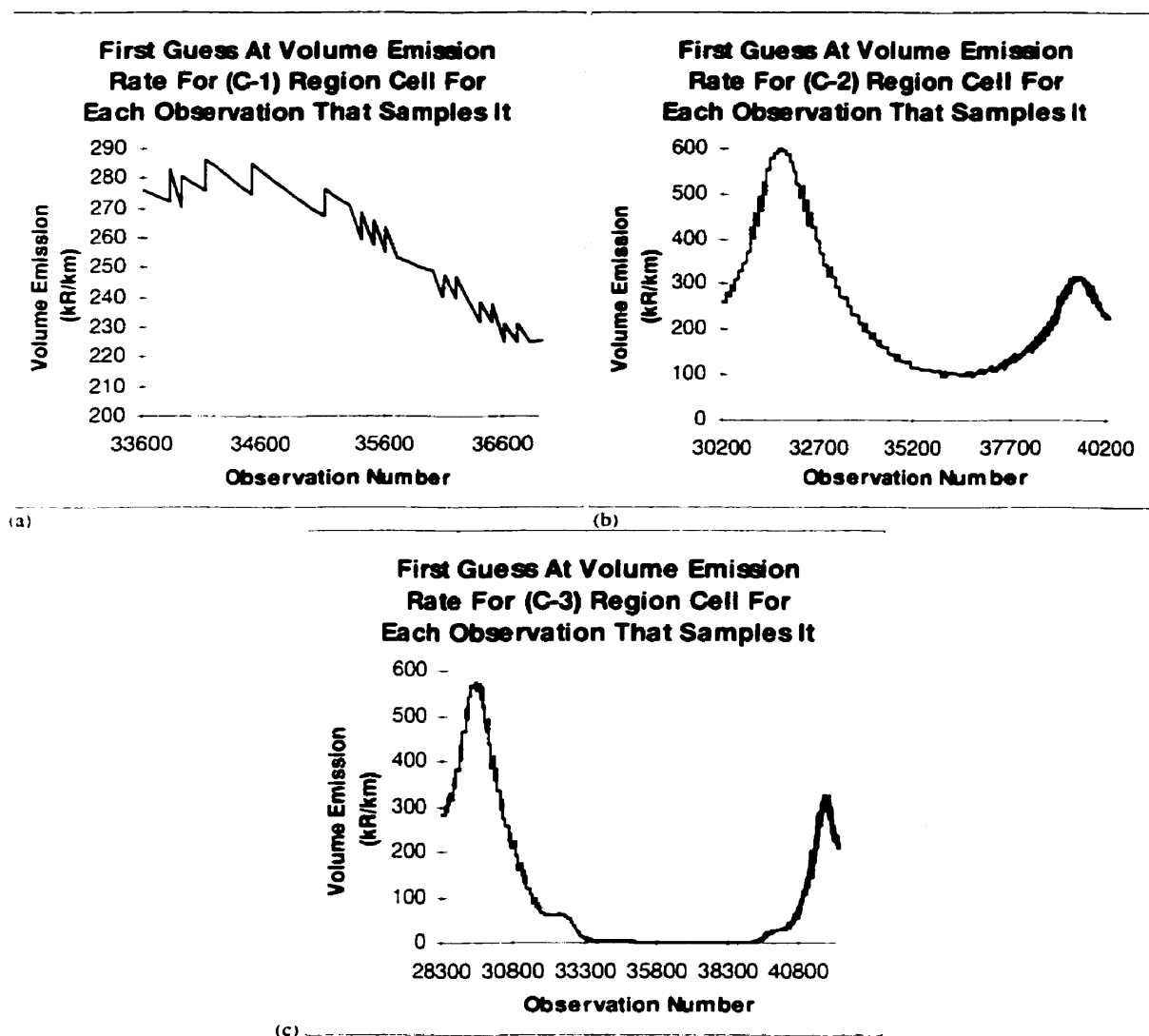


Figure 7.24: The initial estimate of the volume emission rate contained within cells in the (C-1), (C-2) and (C-3) regions. These initial estimates are based on equation 7.6 and the data in Figures 7.22 and 7.23.

The initial estimates for the volume emission rates contained within the troughs in Figure 7.24 do not accurately represent the volume emission rates in the associated

cells. Hence, it is important that the effect of observations that are tangent lower in the grid not be completely eliminated. As the filter functions (Sections 7.3 and 7.4) depend on both the grid cell size and the weighting factor exponent a careful search of the associated parameter space was made to determine the optimal parameters. The criteria considered both the time to convergence and accuracy of the final result.

7.6.2 Convergence Results for Different Weighting Factor Exponents

The parameter space search resulted in the selection of a grid cell with a radial shell dimension of 1 km and an angular dimension of 0.2° . Although this value was adopted the results were marginally improved for a smaller angular cell size. However, the improved accuracy did not justify the large increase in the time required to calculate the volume emission rates.

The weighting factor exponent in the filter functions is the critical parameter for both the convergence time and the accuracy of the final results when small scale structures are present in the grid. Figures 7.25 through 7.30 illustrate the benefit of increasing the weighting factor exponent and so attenuating the effect of observations that are tangent at a large distance from the cell of interest. Comparisons (angular cross sections) between the retrieved solution and the input volume emission profile (Figure 6.12) for the first three iterations of the tomographic recoveries with various weighting factor exponents are shown in Figure 7.25, 7.26 and 7.27. It is readily apparent from these figures that the attenuation of the less relevant observations by, the higher weighting factor exponents, better directs the solution towards the final value. Each increase in the weighting factor exponent results in solutions (at almost every point and after each iteration) that are closer to the true value.

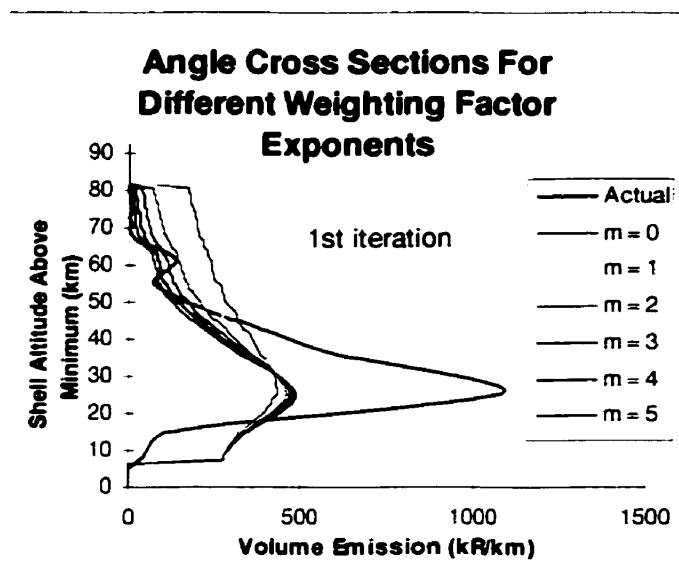


Figure 7.25: Angular cross sections for the calculated volume emission rates (after the first iteration) and the actual input values for six different weighting factor exponents.

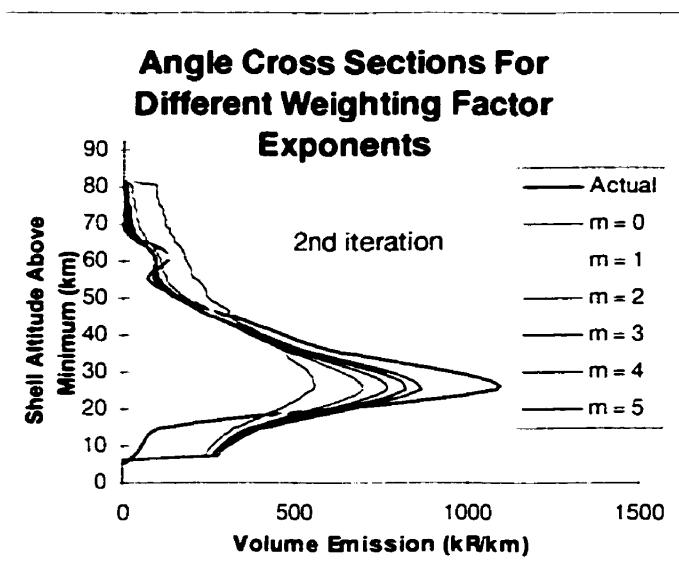


Figure 7.26: Angular cross sections for the calculated volume emission rates (after the second iteration) and the actual input values for six different weighting factor exponents.

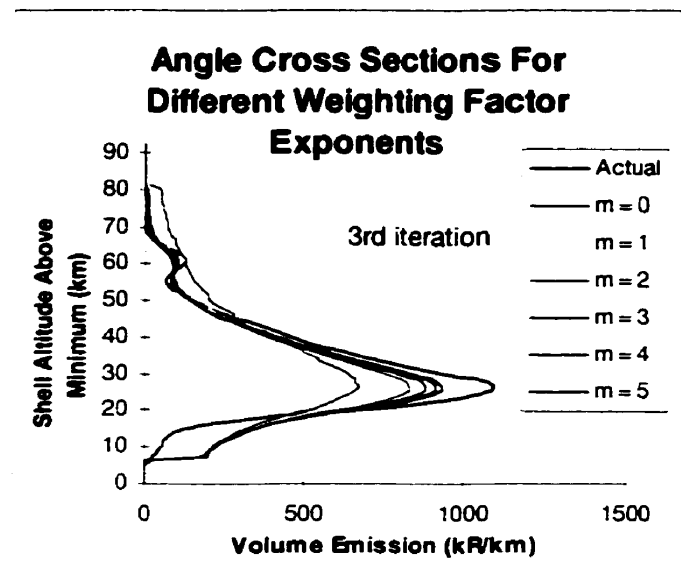


Figure 7.27: Angular cross sections for the calculated volume emission rates (after the third iteration) and the actual input values for six different weighting factor exponents.

Similar results are also seen in Figure 7.28, 7.29 and 7.30 where the radial shell cross sections that correspond to the actual input volume emissions and the solutions after each of the first three iterations are compared. Again each increase in the weighting factor exponent leads to more desirable solutions. It can also be seen from these figures that the benefits associated with increasing m also converge. Thus values of the weighting factor exponent greater than 5 give no obvious advantage. Hence the 1.0 km by 0.2° grid cell size and an exponent value of 5 have been adopted for the tomographic inversions presented in this thesis.

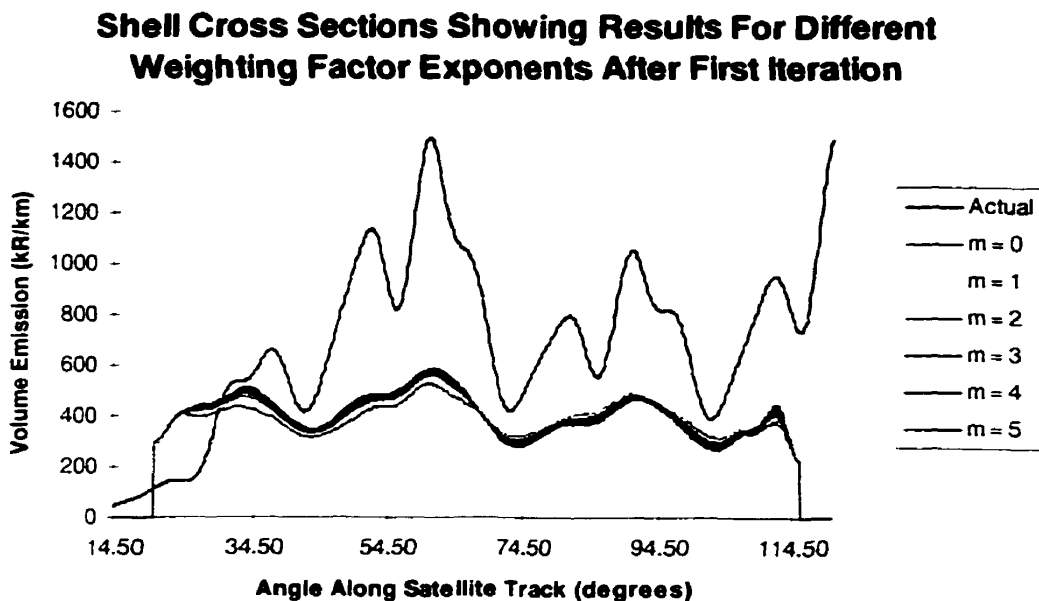


Figure 7.28: Radial shell cross sections for the calculated volume emission rates (after the first iteration) and the actual input values for six different weighting factor exponents.

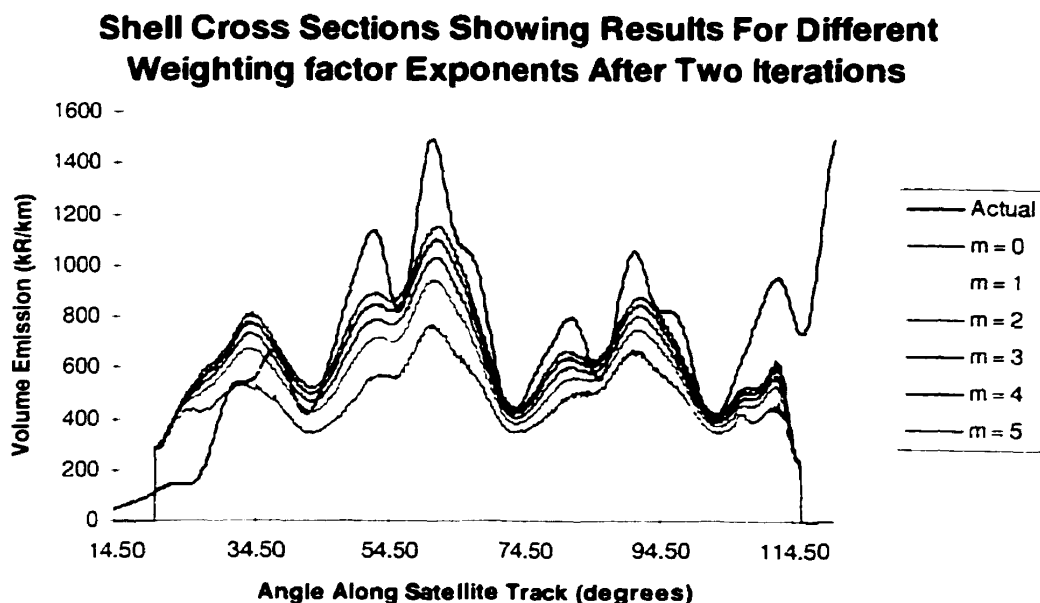


Figure 7.29: Radial shell cross sections for the calculated volume emission rates (after the second iteration) and the actual input values for six different weighting factor exponents.

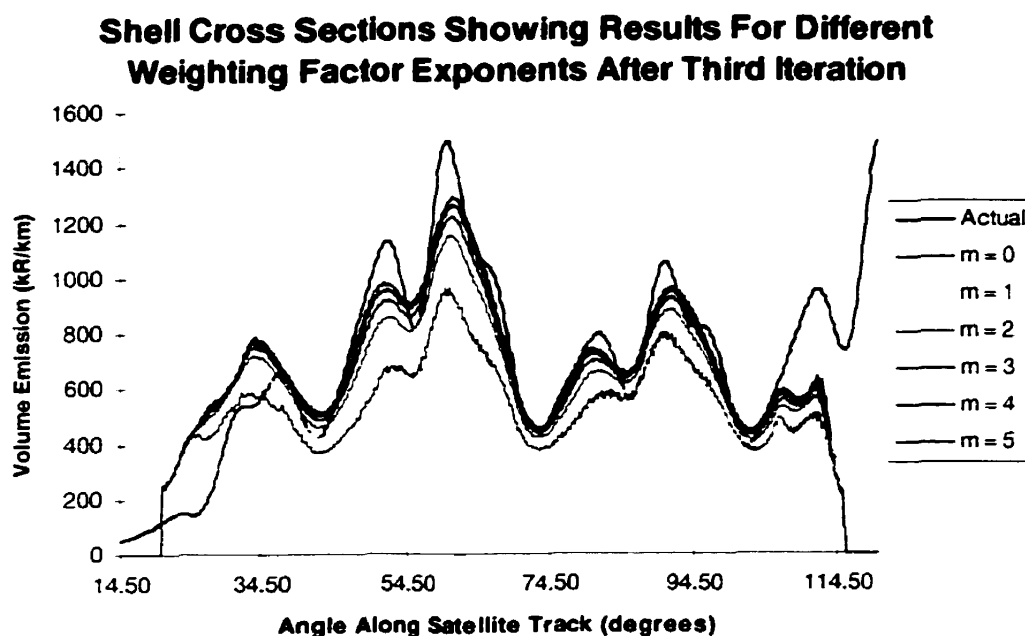


Figure 7.30: Radial shell cross sections for the calculated volume emission rates (after the third iteration) and the actual input values for six different weighting factor exponents.

7.7 Examples of the Tomographic Recovery for Different Weighting Factor Exponents and Grid Cell Sizes

The two dimensional input volume emission profile and the recoveries for both the optimal parameters and a poor choice of weighting factor exponent and grid cell size are shown in Figure 7.31. The well recovered profile (Figure 7.31b) shows little obvious difference from the input profile except for the expected edge effect. The error distribution (Appendix C), and the quadratic fit to this distribution, are shown in Figure 7.32. The recovery is very good. The width of the error distribution is 3.61% and there is no visible offset from zero. This is typical of the results for the optimal grid cell size and weighting factor exponent.

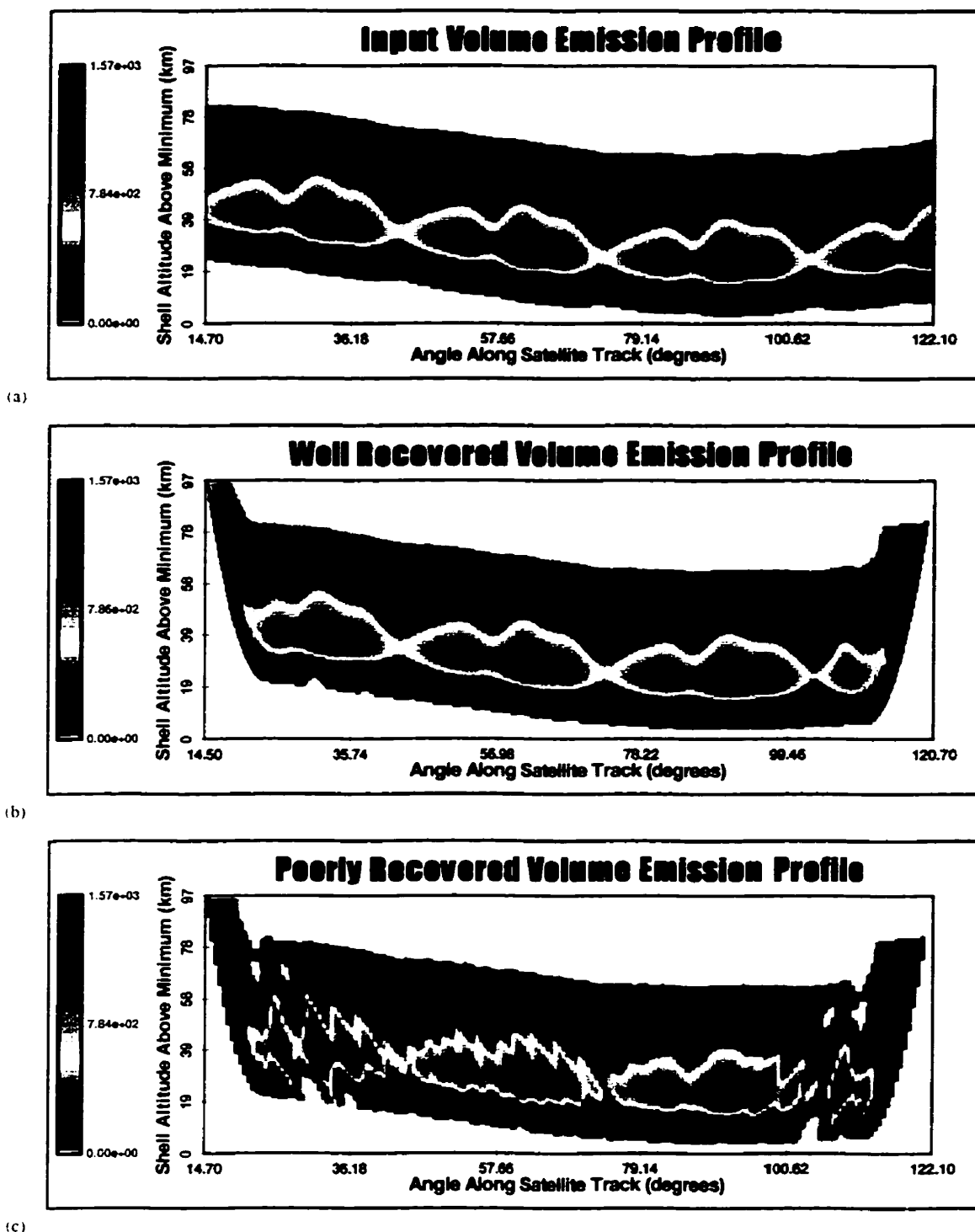


Figure 7.31: The two dimensional volume emission profiles that correspond to the input grid (a) and two recoveries (b and c). These grids were chosen to illustrate the effect of using the optimal parameters as well as an ill-conditioned set.

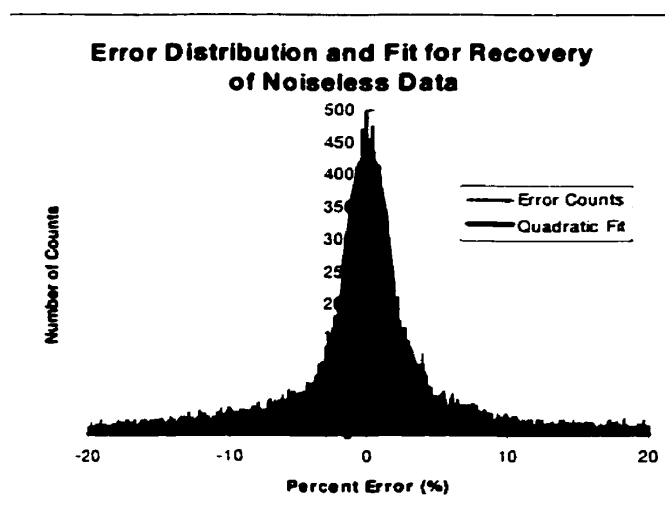


Figure 7.32: *The error distribution and quadratic fit for the well recovered profile shown in Figure 7.31. The peak is not offset and the distribution width is 3.61%.*

However, for the poorly recovered volume emission profile (angular grid cell size 0.6° and a weighting factor exponent of 5) there are obvious differences between the retrieval and the input volume emission profile. The weighting filter functions and averaging kernels for these parameters were presented in Figures 7.13, 7.14, 7.19 and 7.20. The weighting filter functions are very narrow and so the averaging kernels are extremely tight with a consequent undersampling and a poor recovery.

The solutions for a 0.2° grid cell are shown in Figure 7.33. In this case the recovered radial shell cross sections are compared with their input values for different weighting factor exponents and the number of iterations. It is apparent from Figure 7.33a and 7.33b that the volume emission profile is accurately retrieved after 50 iterations with either a weighting factor exponent of one or five. However, there are some small differences between the recovered and input values in Figure 7.33b. The weighting filter functions associated with the exponent equal to one do not recover some of the subtle structure that is retrieved with a weighting factor exponent equal to five.

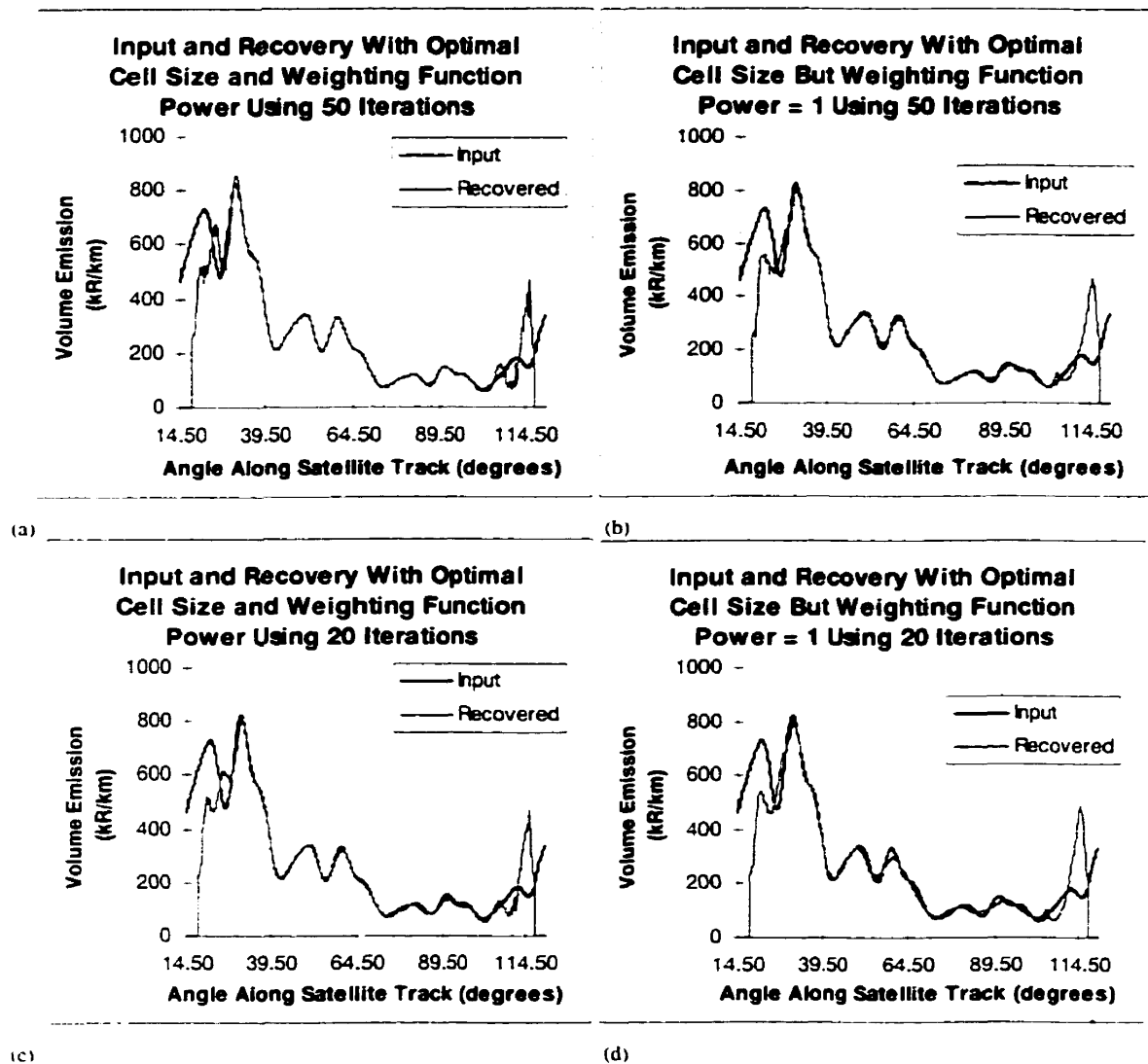


Figure 7.33: Radial shell cross sections for optimal and non-optimal choices of the weighting filter functions.

The plots in Figures 7.33 (c) and (d) further illustrate the advantage of a weighting factor exponent value equal to five. As each iteration requires extensive calculation it is important that the number of iterations be minimized. With the optimal grid cell size and weighting factor exponent even the very subtle angular structure has been almost completely resolved in only twenty iterations. This is not the case for the weighting factor exponent equal to one.

7.8 Concluding Remarks

The observation weighting filter function is fundamental to the accuracy and speed of convergence of the final solution. It is a geometry dependent term defined by equation 7.2 in which the weighting factor exponent can be varied. A careful search of the angular grid cell size and weighting factor exponent parameter space gave the optimal weighting filter functions for the entire set of grid cells. These values are 0.2° and $m = 5$ for a 1 km thick cell. These values are used throughout the remainder of this thesis as they provide accurate and rapid convergence.

CHAPTER VIII

OPERATIONAL MODES

8.1 Introduction

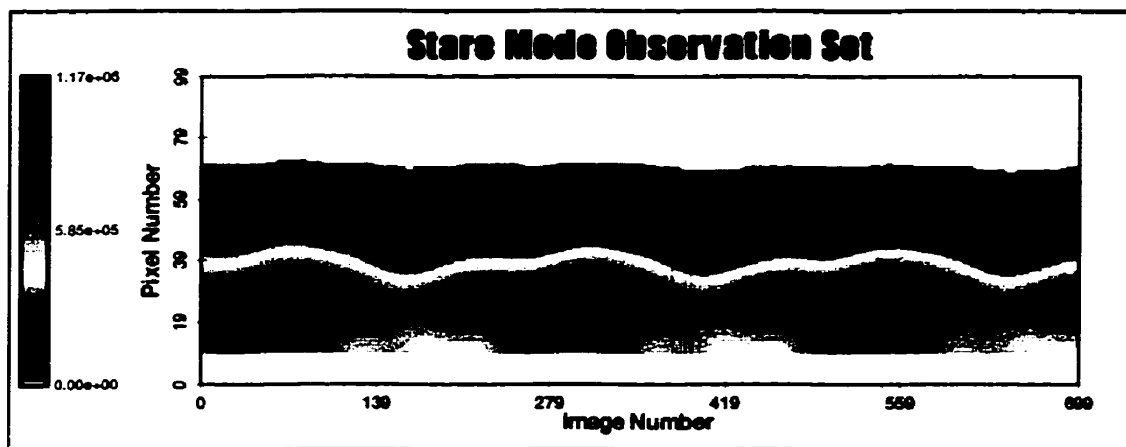
The operation a satellite borne imager requires the definition of a number of parameters called modes. In the present work two independent operational modes that are consistent with the Odin/OSIRIS infrared imager (scheduled for launch in early 2000) have been studied in detail. These are the nod mode, that is required by other instrumentation on the satellite, and the imaging rate mode which is limited by the data downlink capability of the satellite. Each of these operational modes impacts the tomographic recovery. For the present work three separate nod modes and three different imaging rates have been investigated, and their effect on the recovery of a moderately structured emission profile in the presence of observational noise has been studied.

8.2 Comparison of Observations, Sampling Densities and Results Using Three Different Nod Modes

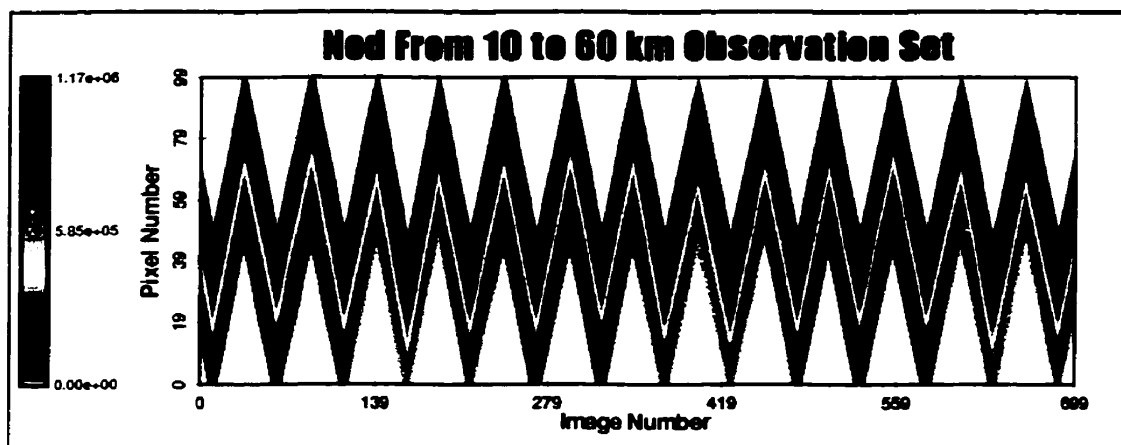
It was noted in Section 4.3.1 that the optical axis of the instrument can be made to nod through different rotations of the satellite about its pitch axis. The first type corresponds to tangent altitude tracking in which the optical axis is maintained at a fixed tangent altitude above the surface of the Earth. Even for this simple 'stare' mode the Earth's oblateness demands motion of the satellite about the pitch axis. The two other nod types studied correspond to a sawtooth variation of the tangent altitude of the imager optical axis from 10 to 60 km and from 10 to 110 km. Both of these atmospheric scan modes have a fixed 1 km/s (at the tangent point) nod rate for the entire scan (in both up and down directions) and are consistent with the planned Odin operation.

Three different observation sets that would be collected by the different nod modes are shown in Figure 8.1. Each of these simulated observation sets sampled the volume emission grid (Figures 6.12 and 8.3a) at a rate of one image every two seconds. Those

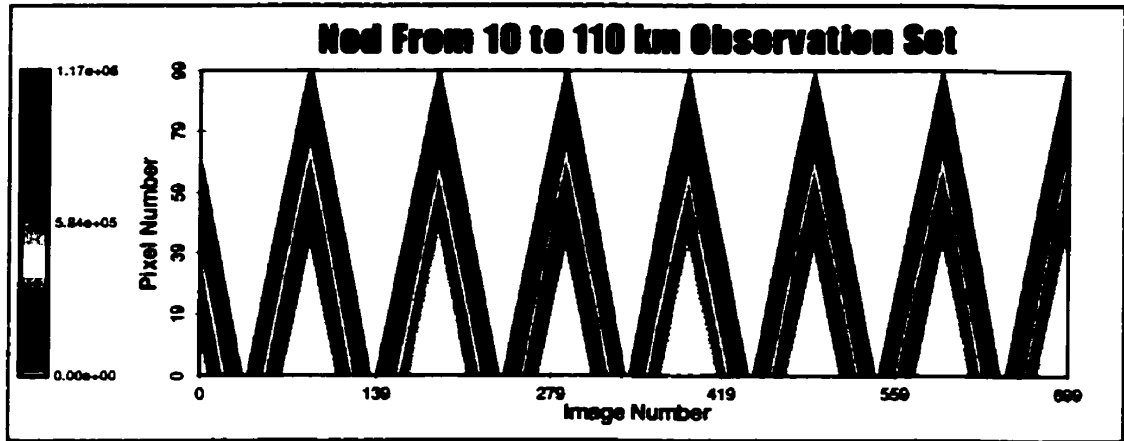
pixels that sample regions outside the recovery grid have been set to zero and are represented as white in these two dimensional plots. It should be noted that in the stare mode (Figure 8.1a) many more pixels sample the relevant parts of the atmosphere than in the other two modes. In particular for the nod from 10 to 110 km (Figure 8.1c) only a very small fraction of the measurements sample the grid.



(a)



(b)

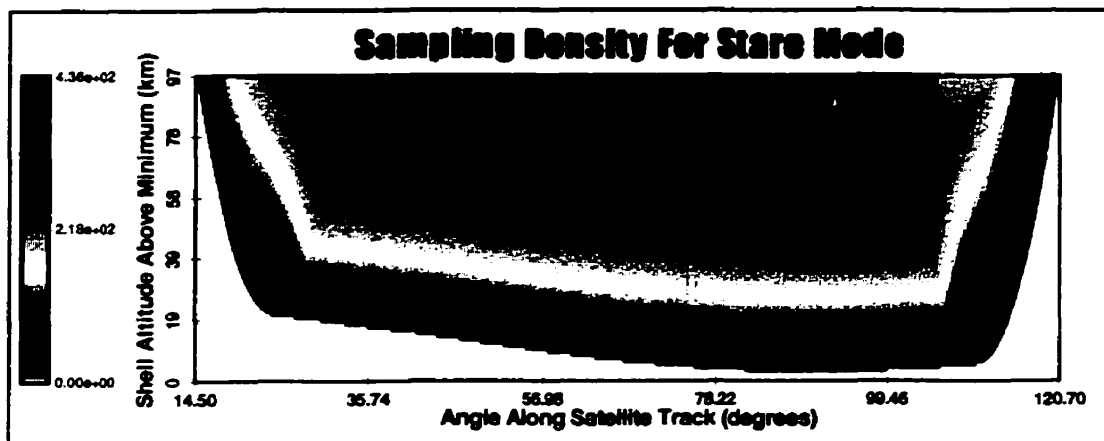


(c)

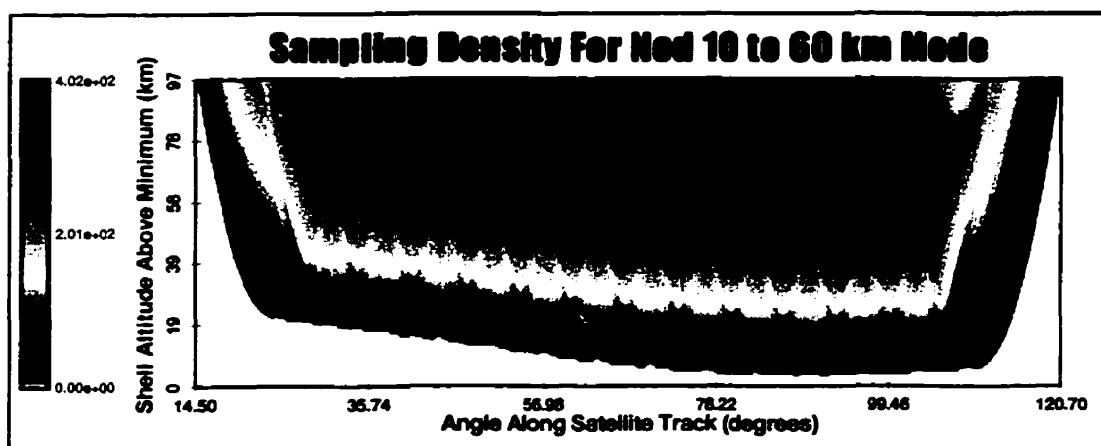
Figure 8.1: *Three observation sets that correspond to the different nod modes. These are the stare, nod from 10 to 60 km and the nod from 10 to 110 km. The colour scale represents the limb brightness in kR.*

The sampling densities associated with each of these different modes are illustrated in Figure 8.2; as noted in Section 6.3 this density is the number of times each grid cell is sampled by the complete observation set. The stare mode (Figure 8.2a) has a uniform density distribution with respect to radial distance and this distribution is only slightly distorted in the 10 to 60 km nod mode (Figure 8.2b). Despite the apparent periodic sampling in Figure 8.2b the sampling density for the interior radial shells in this nod mode is almost identical to that for the stare mode. This occurs as the vertical imager continuously samples the central cells even with the 10 to 60 km nod.

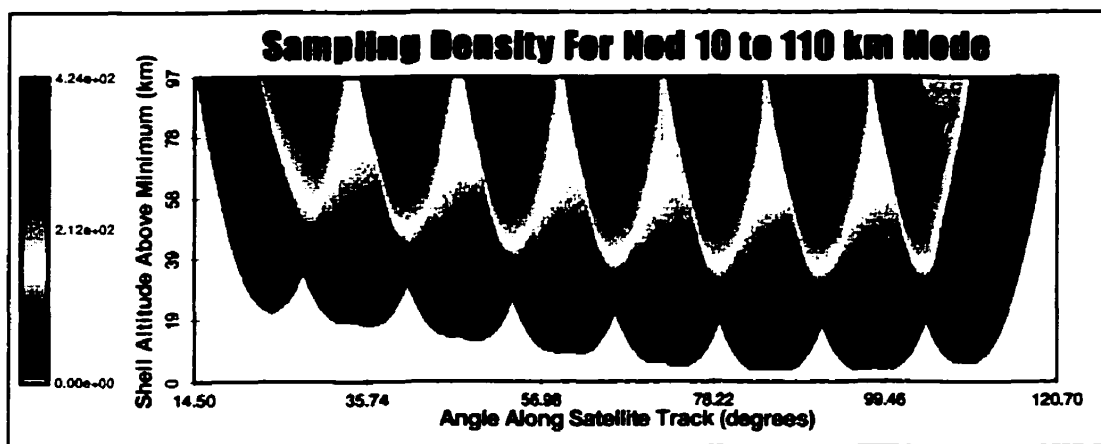
Figure 8.2c illustrates the sampling density for the 10 to 110 km nod mode. It is readily apparent from this figure that the sampling density distribution is significantly modified from that for the stare mode. Although all cells in the interior of the grid are sampled a periodic change in the sampling density of any radial shell, with the same frequency as the nod, is clearly evident.



(a)



(b)

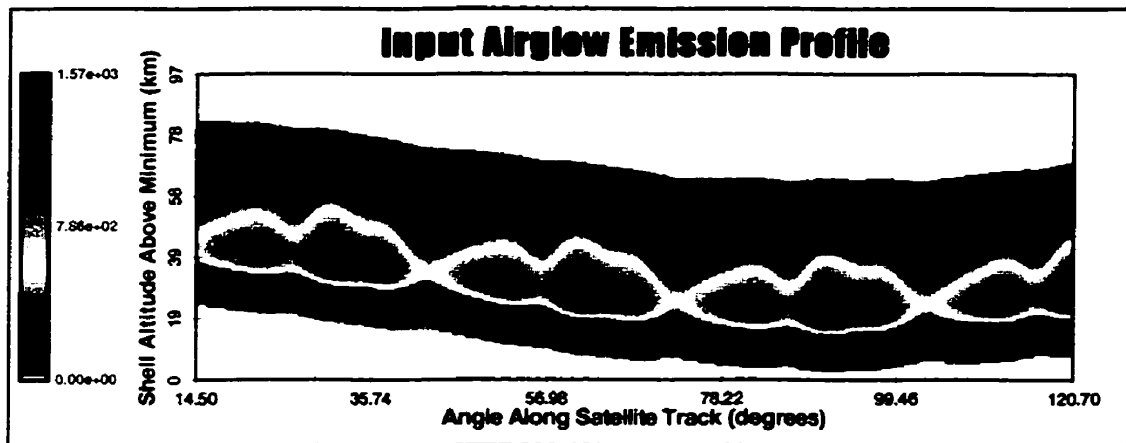


(c)

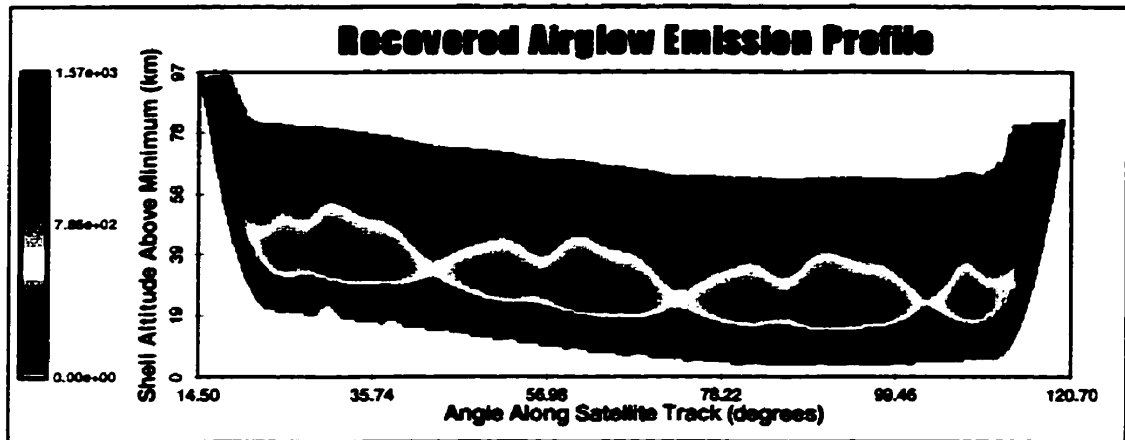
Figure 8.2: The sampling densities for the observations shown in Figure 8.1. The colour scale represents the number of times that each grid cell is sampled.

The input and the recovered volume emissions for the observations shown in Figure 8.1 are presented in Figure 8.3. It should be noted that the observations were generated with a grid cell size 0.02° by 100 m while the tomographic inversions recovered the volume emissions in a grid with a cell size of 0.2° by 1 km (Section 7.6.2). It is apparent from a visual inspection of the retrievals that the stare and the 10 to 60 km nod modes (Figures 8.3b and 8.3c) achieve a good recovery of the input profile. The error histograms (Appendix C) for these recoveries have widths of 4.21% and 4.68% respectively. The nearly equal error histogram widths indicates that the 10 to 60 km nod mode does not degrade the recovered profile.

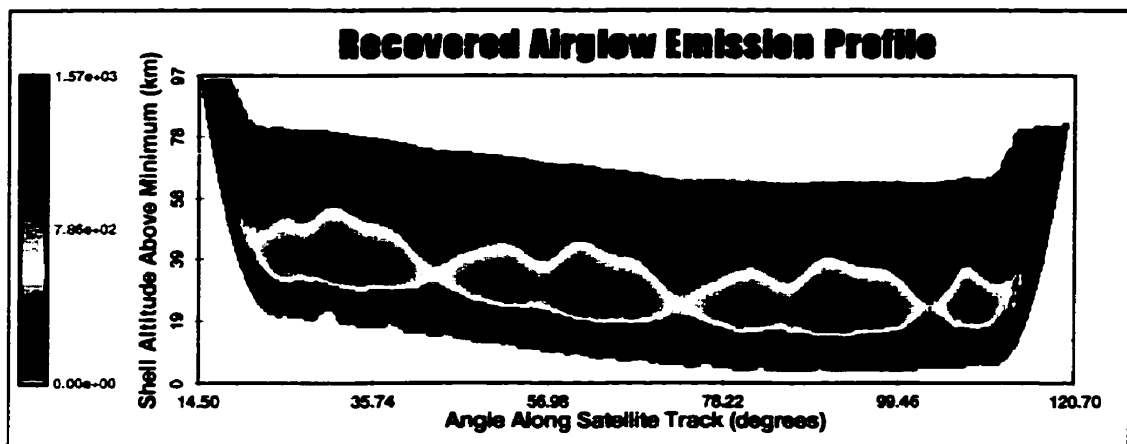
The final panel (d) in Figure 8.3 corresponds to the tomographic recovery for the observations corresponding to the 10 to 110 km nod mode. It is apparent that in this case the recovered volume emission profile follows the sampling density contours (Figure 8.2c). The reason for this is, as for the edge effect (Section 6.5), an undersampling of the cells with similar observations. Thus for the modeled imager with a 2° field of view a tangent altitude nod from 10 to 110 km at a rate of 1 km/s does not provide an observation set that allows the accurate tomographic recovery of the emission profile.



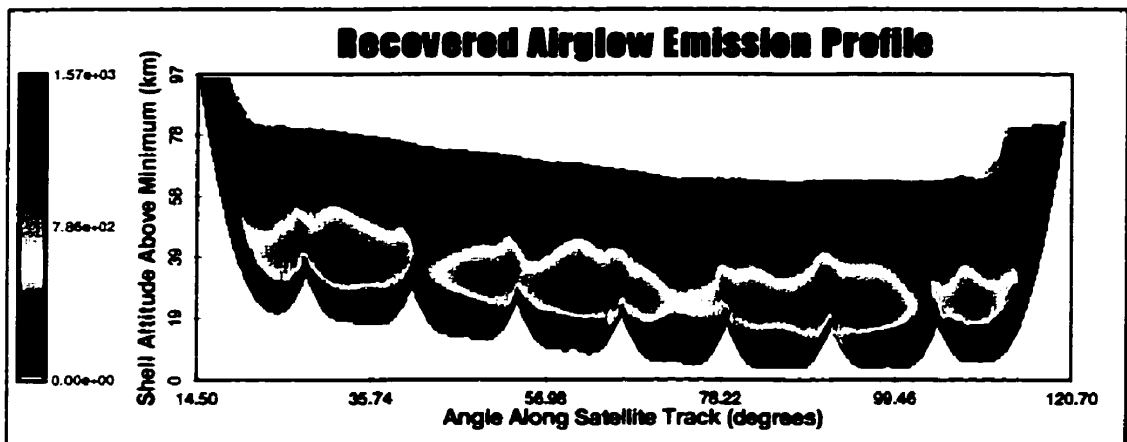
(a)



(b)



(c)



(d)

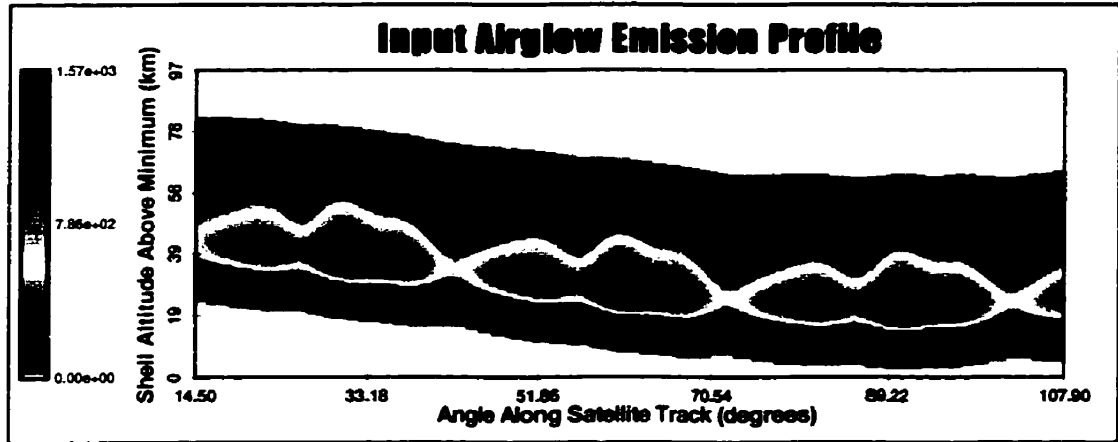
Figure 8.3: Sample recoveries of the input volume emission profile shown in the top panel (a), for the three different nod modes: stare (b), nod from 10 to 60 km (c) and nod from 10 to 110 km (d). The colour scale is the volume emission rate (kR/km).

8.3 Comparison of the Results for Three Different Imaging Rates in the Absence of Noise

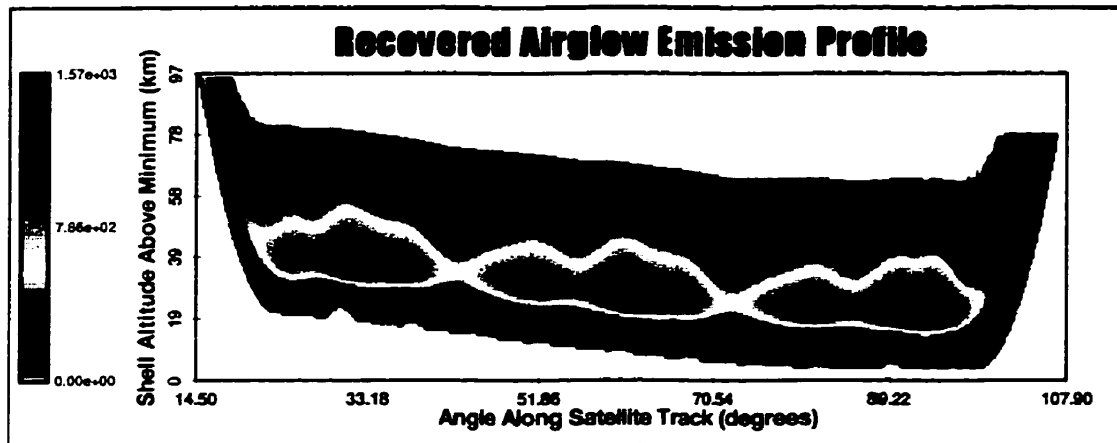
The imaging rate is an important operational parameter for the tomographic recovery as it determines the number of observations that sample each cell. However, the number of cell samples must be coupled with the computing time required for the tomographic retrieval; if more observations sample each cell then the retrieval time is necessarily increased. Thus the adopted imaging rate must be consistent with both the inversion accuracy and the computational speed requirements. In order to examine the probable Odin/OSIRIS operations the effects of imaging at 1.0 Hz, 0.50 Hz and 0.33 Hz (one image every one, two and three seconds respectively) in the stare mode have been evaluated.

The input and the recovered two dimensional volume emission profiles for a 0.5 Hz imaging rate are shown in Figure 8.4. The observation set consisted of 600 images with an angular coverage from 14.50° to 107.90° . For the image sets taken once per second and once every three seconds the number of images required to achieve the same angular coverage is 1200 (the absolute maximum number of images possible given the computational power) and 400 respectively. As the recovered profiles from each of the different imaging rates are visually identical only the recovered profile for the 0.50 Hz imaging rate is shown in Figure 8.4.

The error histograms and quadratic fits for the three inversions are shown in Figure 8.5. In each case the error histogram has an approximately Gaussian shape and is narrowest for the 1.0 Hz imaging rate. The width of each of the quadratic fits and their associated offset is listed in Table 8.1. These also indicate that the best retrieval is obtained with the highest imaging rate although the differences in the retrievals for the three different imaging rates are not necessarily significant.



(a)



(b)

Figure 8.4: *The input and recovered grids for one of the three inversions considered in the imaging rate study. Only a single recovery is shown as the grids are visually identical for all three imaging rates. The colour scale represents the volume emission rate in kR/km*

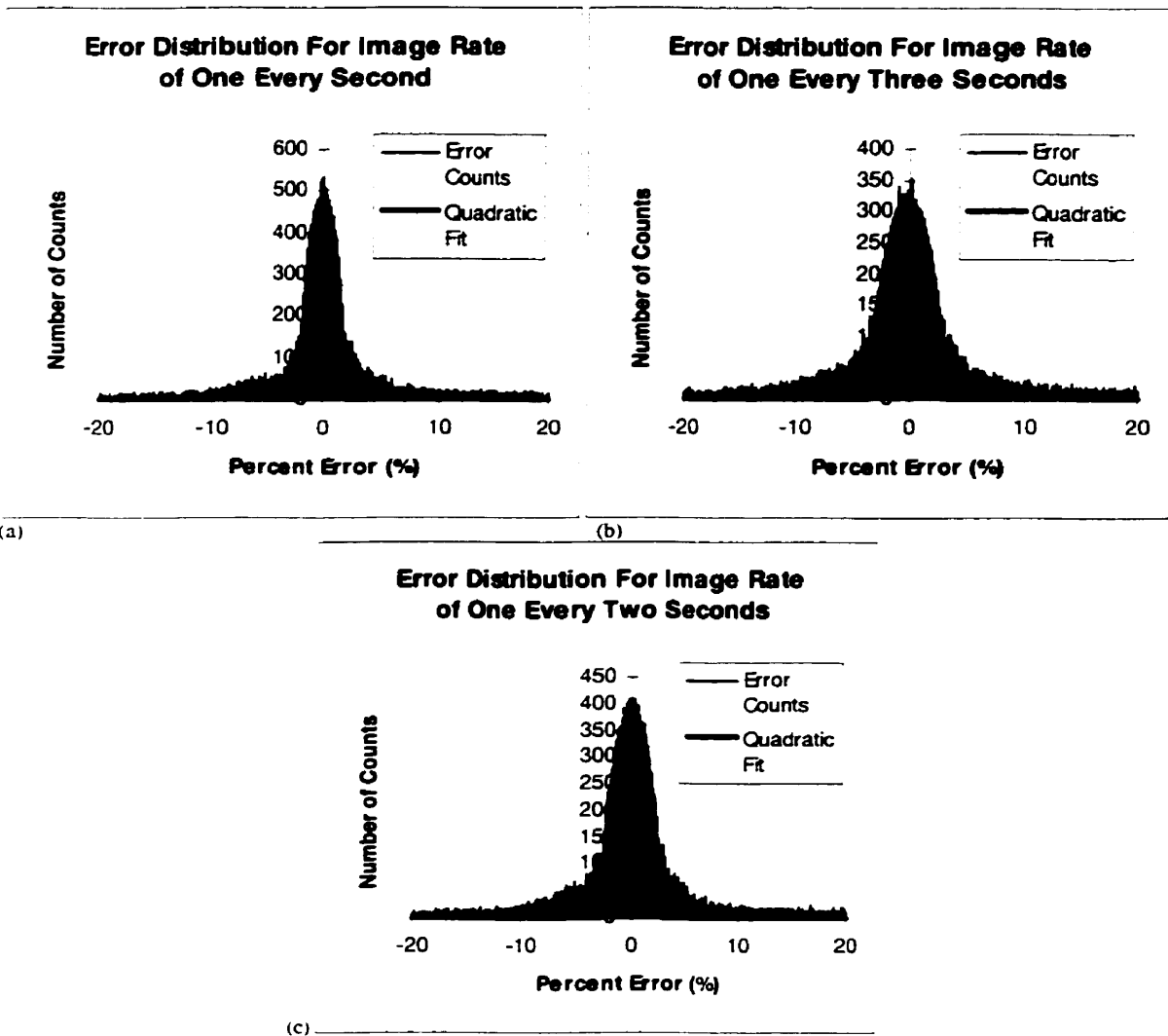


Figure 8.5: The error histograms and quadratic fits for the three inversions made for the different imaging rates.

Image Rate (Seconds/Image)	Error Histogram Total Width (%)	Error Histogram Peak Offset (%)	Time For Inversion (Seconds)
1	3.09	-0.02	320
2	4.08	-0.02	156
3	4.94	-0.00	104

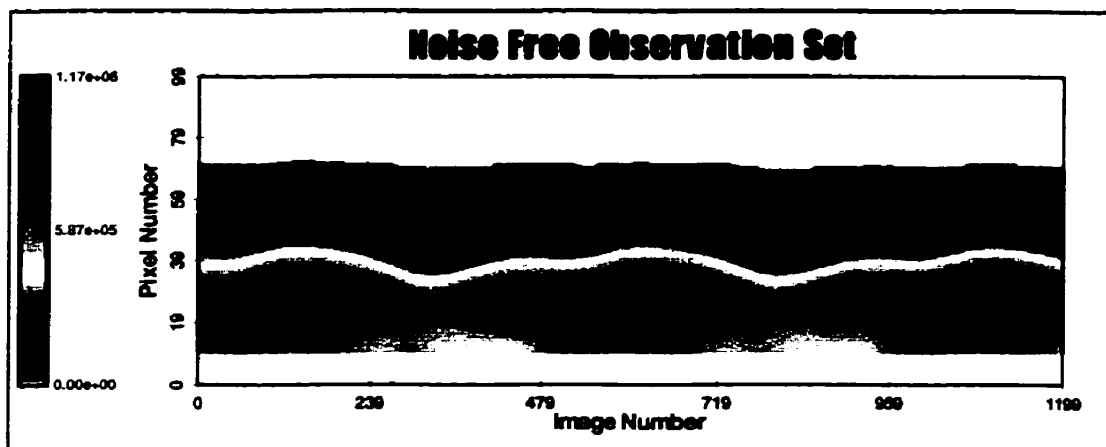
Table 8.1: The error histogram width and peak offset parameters for the three retrievals made for data generated at different imaging rates. The computing time for each retrieval is also listed.

As already noted the choice of the imaging rate must also consider the computing time for the retrieval. The time required to complete each of the three tomographic retrievals

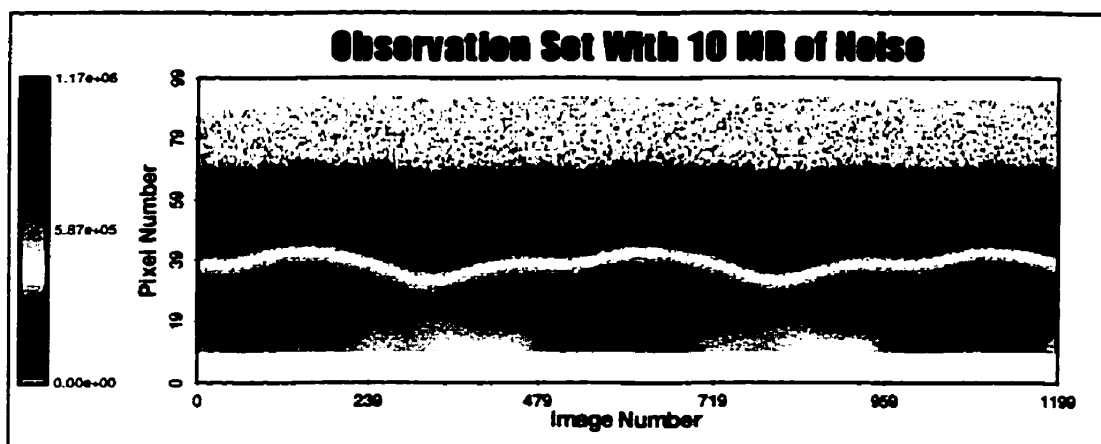
for the same angular extent, with the present computing resources, is included in Table 8.1. While these times are only relevant to these particular inversions they do indicate the relative time required to recover the same two dimensional space for the three different imaging rates. In each case the time required for the tomographic retrieval is, on a per image basis, nearly identical at 0.25 seconds. Thus, it would appear that in the absence of noise a 0.33 Hz imaging rate is optimum as the retrieval can be made in less time with no significant degradation in the retrieval accuracy. However, as real measurements include noise it is necessary to consider the effect of noise on the retrieval.

8.4 Choice of Imaging Rate in the Presence of Noise

Observation sets both with and without noise are presented in Figure 8.6. These observations were generated from the volume emission profile shown in Figure 8.4a for a 1 Hz imaging rate in the stare mode. The Gaussian noise was added to the noise free observation set with an input parameter of 10 MR as the halfwidth of the noise distribution. This is appropriate as in most infrared detectors the major noise contribution is from the detector. The difference between these observation sets is particularly apparent at high altitudes where the line of sight signal is comparable to the noise signal.



(a)



(b)

Figure 8.6: Two observation sets in the absence and presence of noise. The colour scale is the measured pixel brightness in kR.

The cross sectional views for these two dimensional images are shown in Figure 8.7. The single image cross sections (Figure 8.7a) illustrate the magnitude of the noise imposed on the measurements. It is readily apparent that the measurements made at higher altitudes (higher pixel numbers) where the signal is considerably weaker have a much larger relative error. The noise associated with measurements at the limb peak are quite visible in this figure.

The cross section shown in Figure 8.7b illustrates the noise in each of the simulated measurements seen at pixel 50 in the imager. In this case the error associated with each measurement is readily apparent as pixel number 50 samples well above the limb peak.

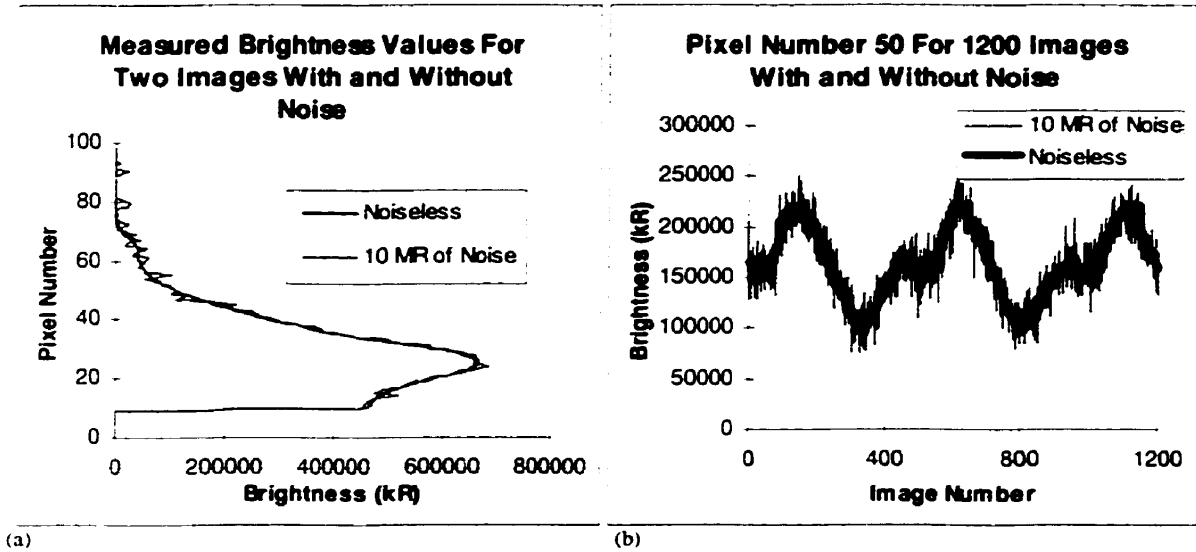
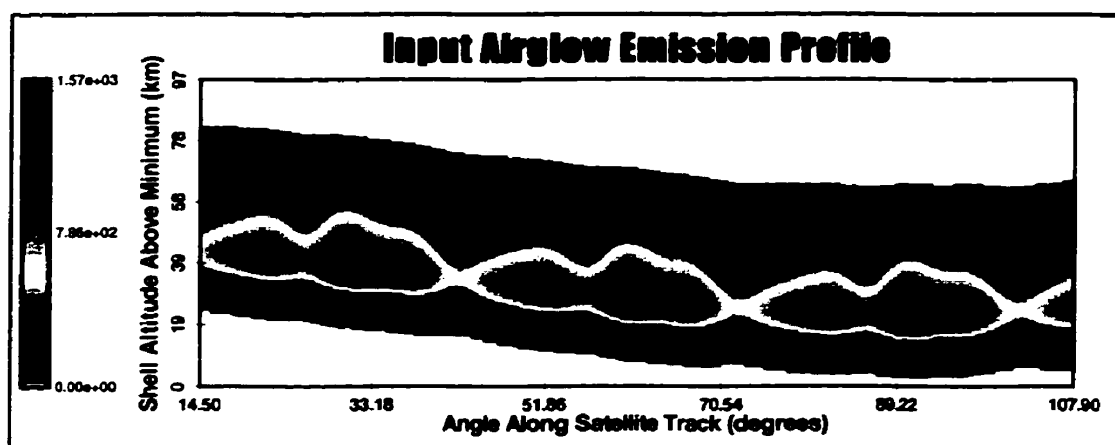


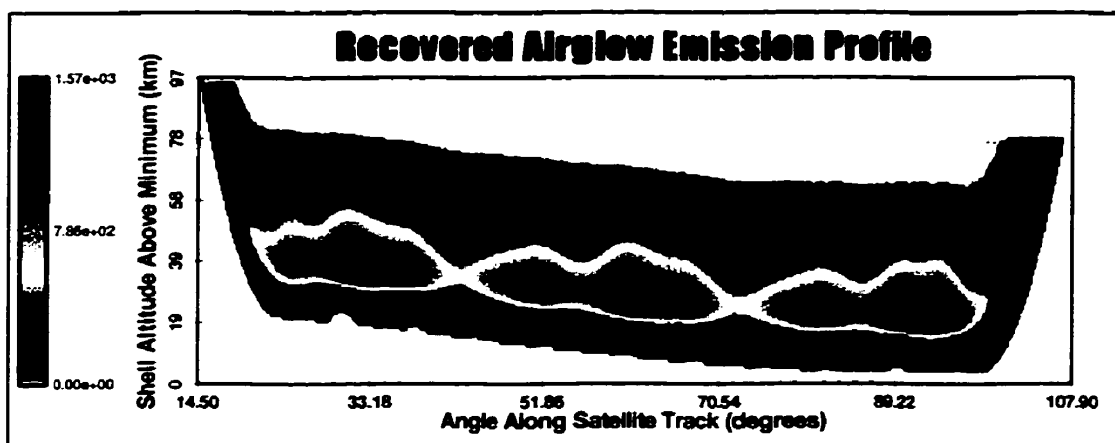
Figure 8.7: Cross sections of the observation data shown in Figure 8.6.

Fifteen separate tomographic retrievals that correspond to three different imaging rates and five different absolute noise values have been made. The input volume emission profile used in these tests is that shown in Figure 8.8a and the best and worst case retrievals, based on the error histograms, are shown in Figures 8.8b and 8.8c. For the best case recovery there are very slight visual differences between the input and recovered profiles. However, for the worst case retrieval there are obvious differences although the large scale structures contained within the volume emission profile are preserved.

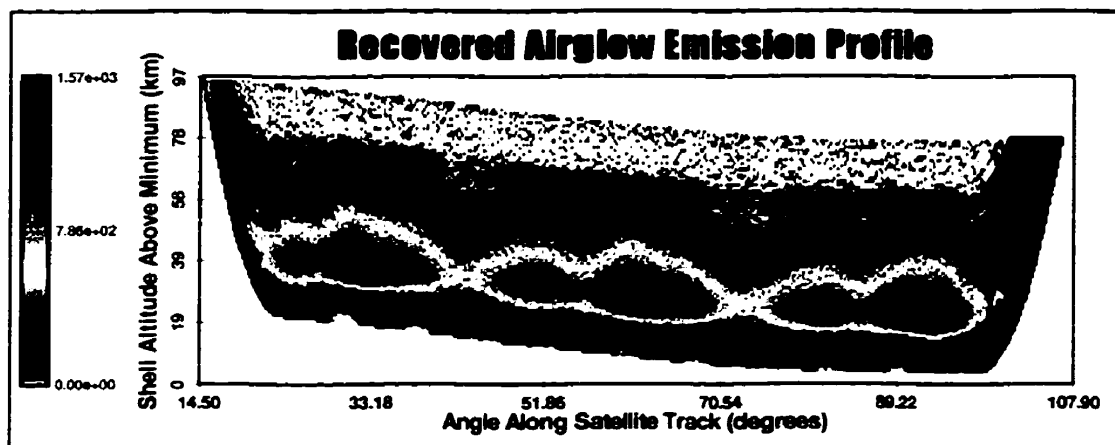
The error histograms for the best and worst retrievals are shown in Figure 8.9. For the 1 Hz imaging rate with 500 kR noise the error distribution is quite narrow. The quadratic fit to this distribution (Appendix C) has a halfwidth of 4.9%. In contrast the quadratic fit to the error distribution corresponding to the retrieval in the presence of 10 MR noise, at a 0.33 Hz imaging rate, has a halfwidth of 31.9%. The quadratic fit is not shown in Figure 8.9b as its shape is not relevant to the width of the distribution.



(a)



(b)



(c)

Figure 8.8: The input and the best and worst case retrievals for the different noise values and imaging rates.

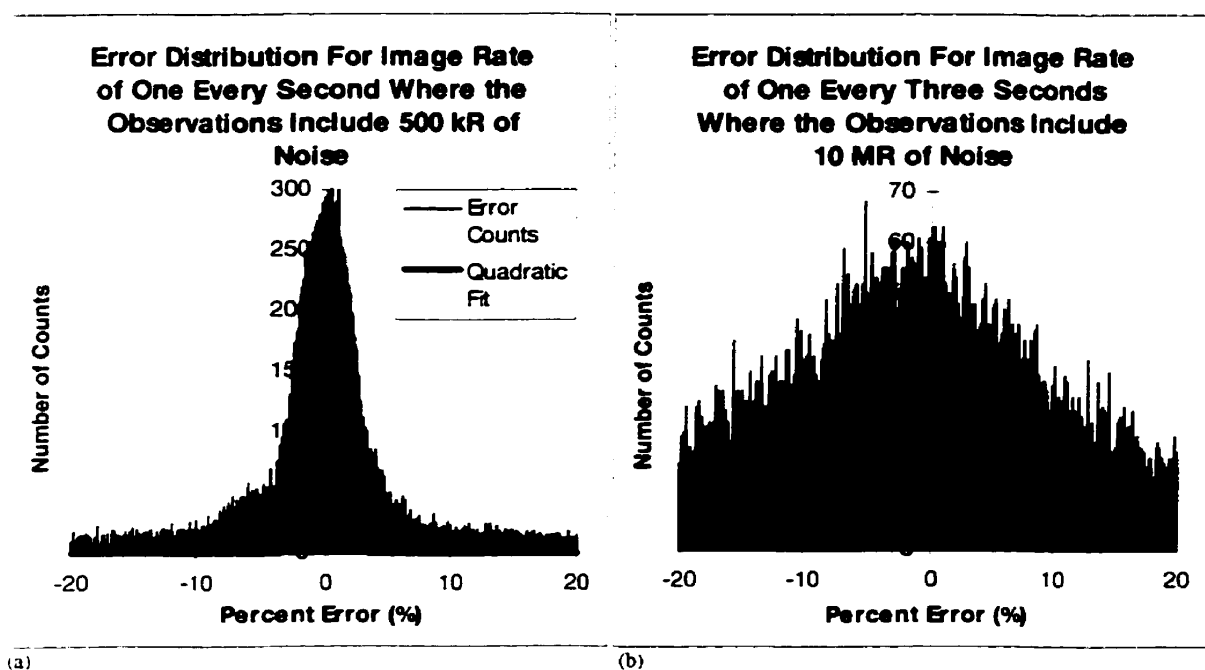


Figure 8.9: The error histograms for the best (a) and worst (b) case retrievals for the fifteen test conditions.

8.5 Concluding Remarks

The results of the imaging rate with noise experiment are summarized in Figure 8.10 and it is apparent that in the presence of noise the imaging rate is an important parameter for the recovery. For each of the five different noise levels the best recovery, the one that corresponds to the narrowest error histogram, resulted from the fastest imaging rate. This is due to the operation of the algorithm as it takes a weighted average, over the observations that sample each cell, to determine the next estimate of the volume emission that is contained within that cell. Thus, higher imaging rates imply that more measurements sample each cell and so the inversion algorithm, which acts as a measurement filter, is more effective.

While the results presented in Figure 8.10 are quite clear they do not identify the optimum imaging rate for measurements in the presence of noise. For low noise levels the computational speed gain associated with a lower imaging rate may be preferred as the inversion accuracy is only slightly compromised. The final choice for the imaging

rate depends on the details of the measurement. These include the signal to noise ratio that can be achieved with the available detector.

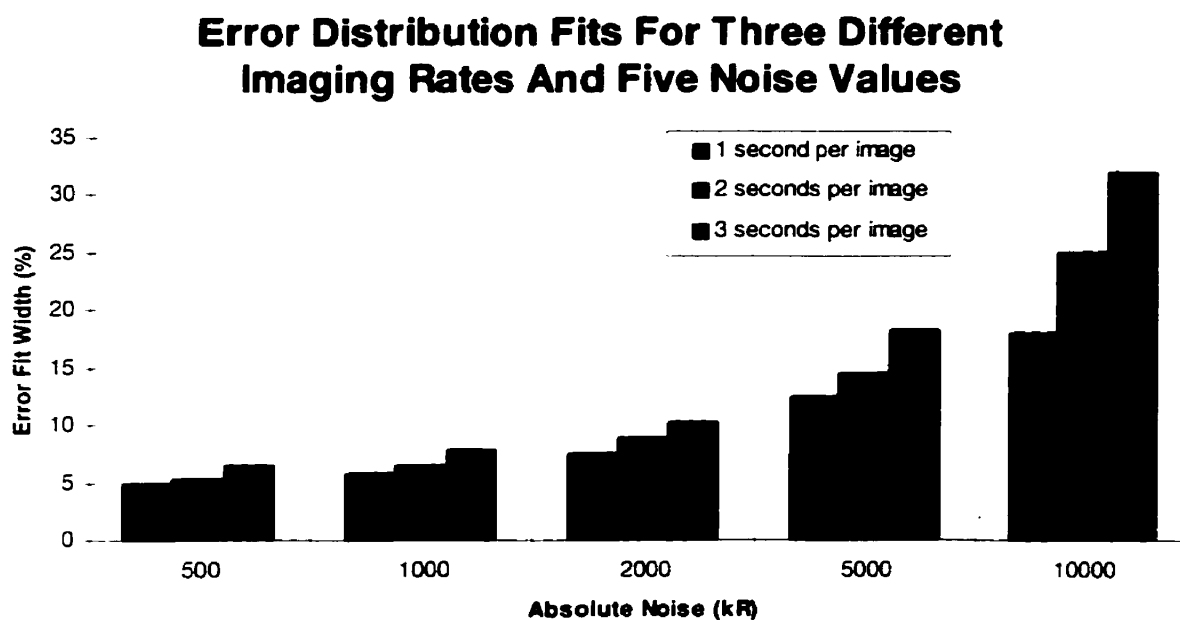


Figure 8.10: Error histogram widths for three imaging rates and five noise levels.

The effects of nodding the imager optical axis through a range of tangent altitudes has also been investigated in this Chapter. It was shown that if the optical axis is fixed at a given tangent altitude or if the nod range is sufficiently small (10 km to 60 km) the retrieved solutions are acceptable. It was also shown that if the nod range is too large (10 km to 110 km) the tomographic retrieval technique performed poorly as many of the grid cells are undersampled. This indicates that it is necessary to ensure that there are sufficient measurements to properly cover the atmospheric region.

CHAPTER IX

SCALE SIZE EXPERIMENT

9.1 Introduction

In order to test the capability of the developed tomographic recovery routine to recover wave-like structure under different operating conditions a scale-size experiment was designed. In this experiment a series of operational modes and input volume emission profiles were tested. The results of the experiment, which are presented in this chapter, indicate that a three degree wave structure (300 km wavelength in the horizontal direction) is fully resolvable for most observational conditions, even in the presence of extreme noise.

9.2 Preliminary Comments on the Test Conditions

The adopted operational modes for the scale size experiment are consistent with, but not specific to, the modes of the Odin/OSIRIS instrument and include both different imaging rates and different nod modes (Chapter 8). The actual experiment considered the stare and nod pointing modes and the 1.0, 0.5 and 0.33 Hz imaging rates. In the stare mode the tangent altitude of the optical axis was fixed at 40.5 km above the surface of the earth and the effects of all three imaging rates evaluated. In the nod mode the tangent altitude of the optical axis was varied from 10 km to 60 km, at 1 km/s, in a saw-toothed fashion. For this mode only the 0.5 Hz imaging rate was tested.

9.2.1 Noise and Error Types

For each of the operational modes different types and magnitudes of noise were imposed on the observations. Four types of noise were examined: Gaussian random noise with an absolute standard deviation; Gaussian random noise with a standard deviation that was determined by the signal to noise level; observation sets in which there was a random loss of images; and observation sets produced with a random

number of bad pixels. Tomographic inversions were made with data sets that contained various combinations of these different noise types.

9.2.2 Structure Types

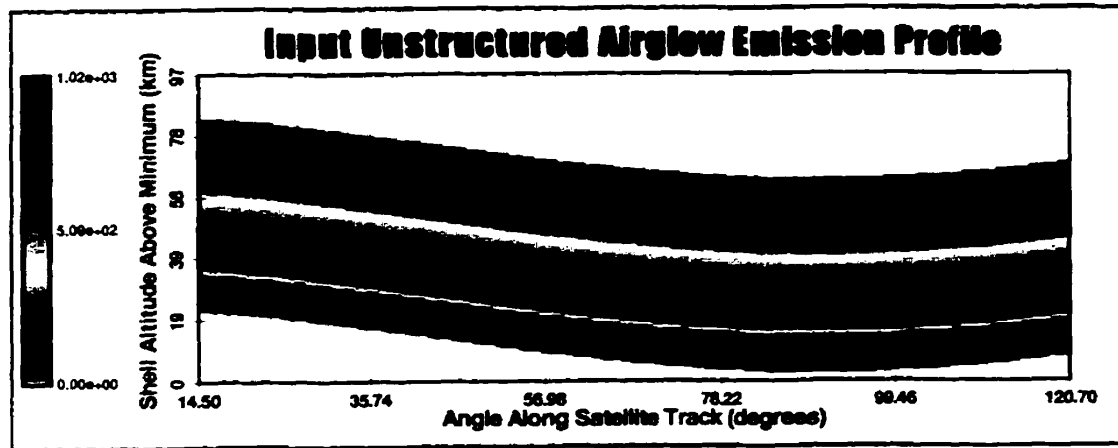
The purpose of the experiment was to determine the scale size of resolvable features that might be present in atmospheric wave structures. The type of simulated structure that was imposed on the volume emission profile is given by equations 4.6 and 4.7, for convenience these equations are repeated here.

$$M = 1 - \left(A_{\min} + \frac{e^{\beta(r-r_{\text{mr.}})}}{H} \right) e^{-\frac{(\gamma-\gamma_0)^2}{2\sigma^2}} \cos(k_{\text{alt}} r) \cos(k_r \gamma) \quad [9.1]$$

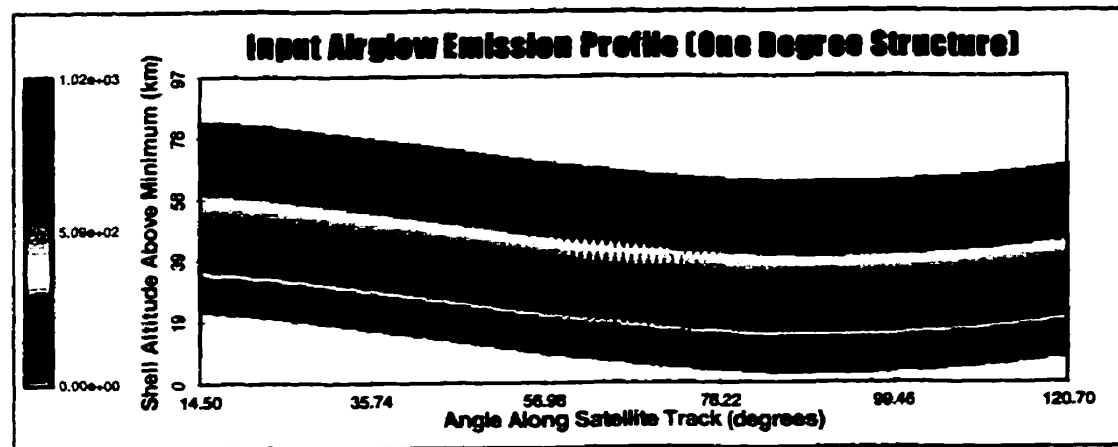
$$A_{\min} + \frac{e^{\beta H}}{H} = A_{\max} \quad [9.2]$$

The vertical wavelength was set to 10 kilometers and the horizontal wavelength was varied from 1° to 5° in 1° steps.

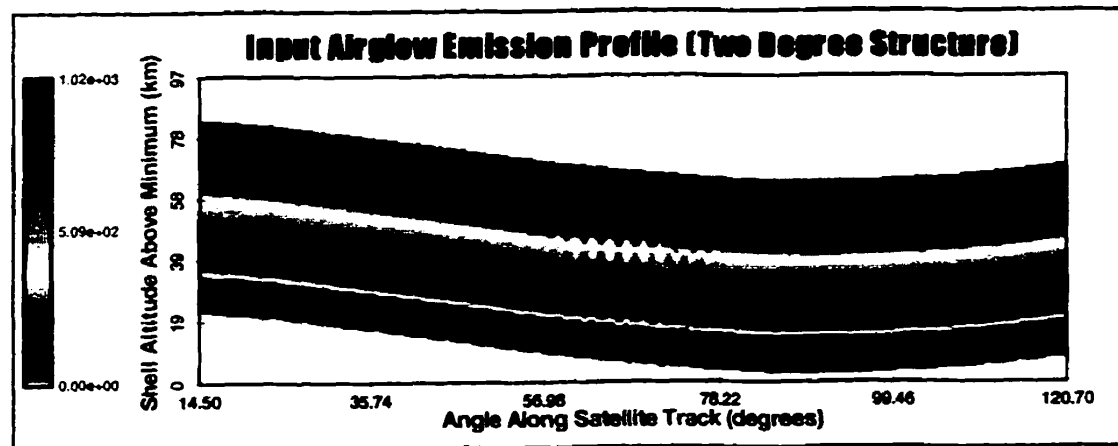
The input volume emission grid shown in Figure 9.1a illustrates the basic unstructured emission profile where the slow angular modulation is due to the Earth oblateness. It is this simple profile that has been modified to produce the structured input emission profiles shown in the other grids in Figure 9.1, (b) through (f). These grids represent the input signals for structure scale sizes of 1 to 5 degrees (in one degree increments) and have an angular range that is appropriate to 700 images at a 0.5 Hz imaging rate. The colour scale in each of these grids corresponds to a volume emission rate in kR/km.



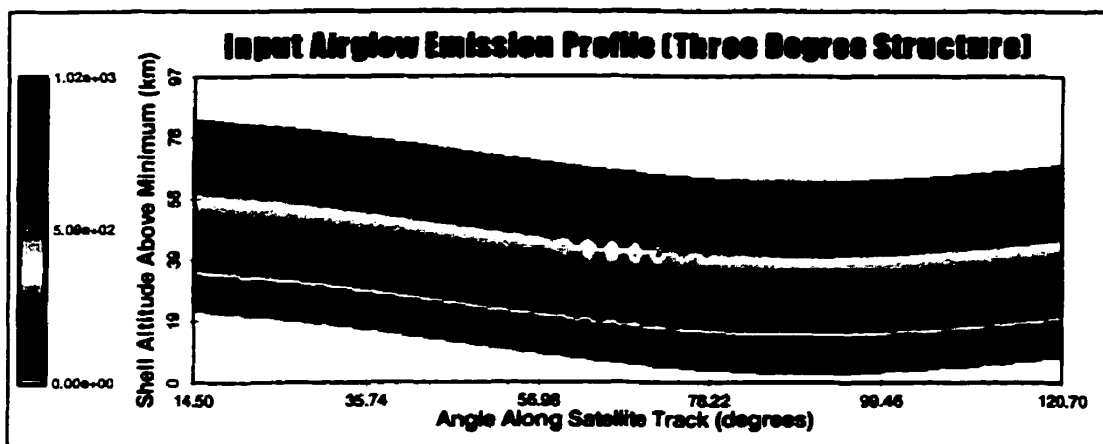
(a)



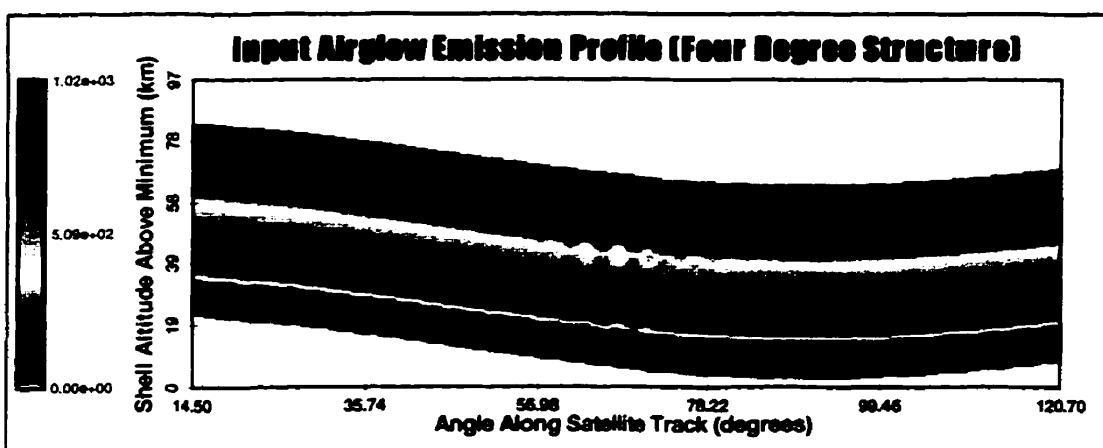
(b)



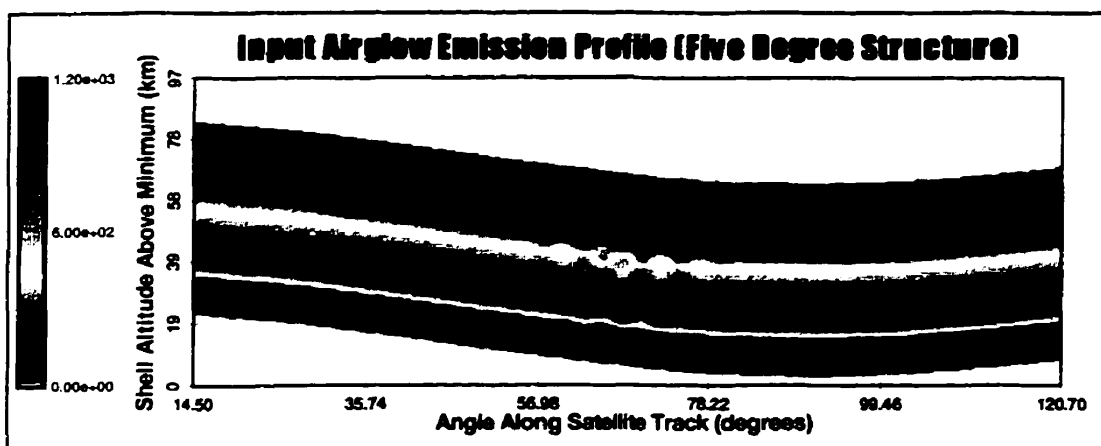
(c)



(d)



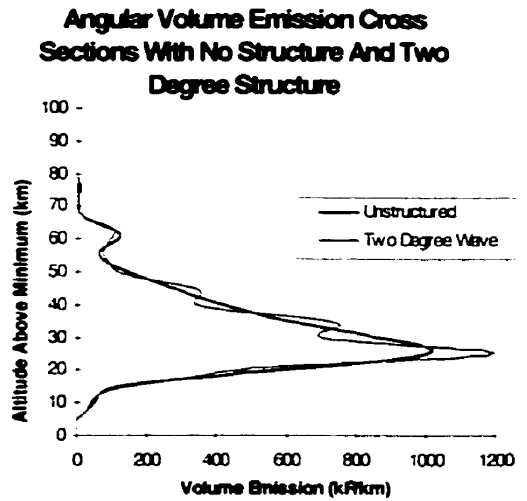
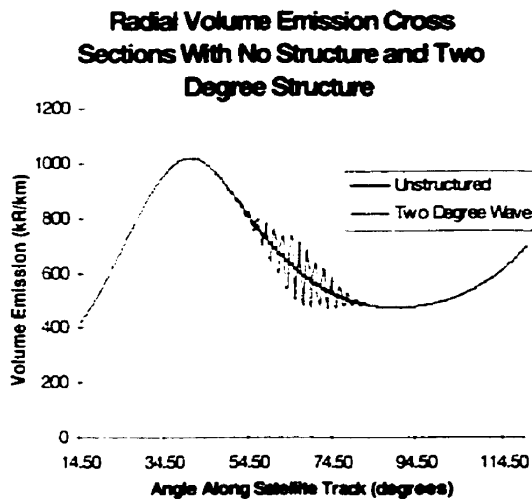
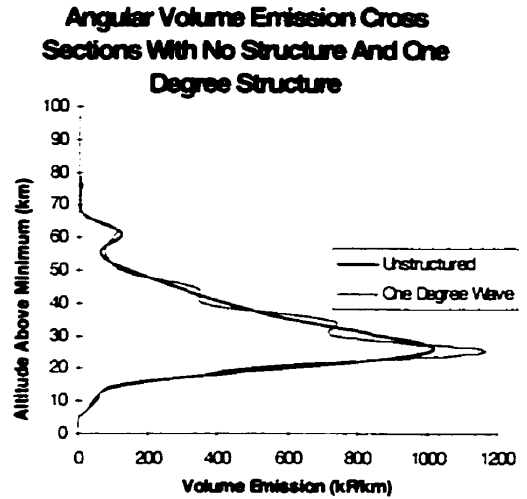
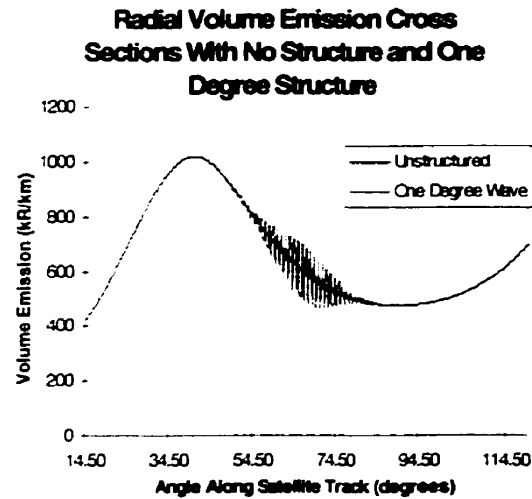
(e)



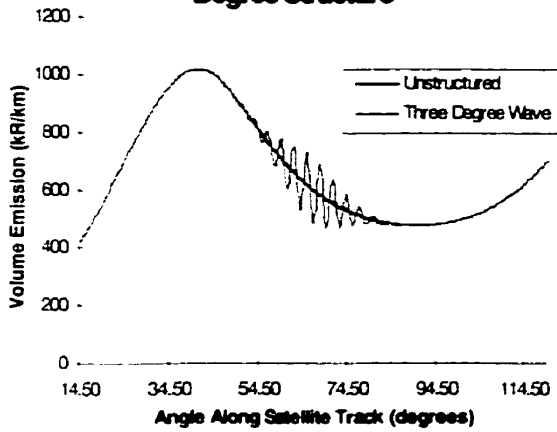
(f)

Figure 9.1: Input two dimensional volume emission profiles for various scale size structures. The low frequency modulation is due to the Earth's oblateness.

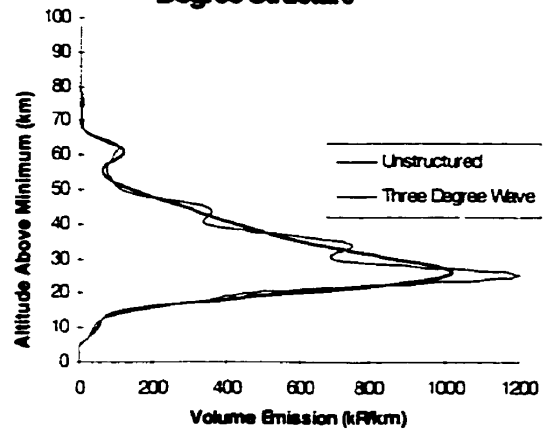
Cross sections for the structured and unstructured input grids are shown in Figure 9.2. In each case these cross sections are taken from near the centre of the grids. As the total angular extent of the perturbation was the same for all input grids there are considerably more wavelengths (peaks and troughs) evident in the radial cross sections for the shorter scale structure than for the five degree horizontal structure waves. This is not the case for the angular cross sections as the vertical wavelength was fixed at 10 km. The apparent lack of vertical structure seen in the five degree horizontal structure case is simply due to the location of the shown cross section. The selected angle location was identical for each of the shown structures, and for the five degree structure this happened to correspond to a position where the modulation was almost a minimum.



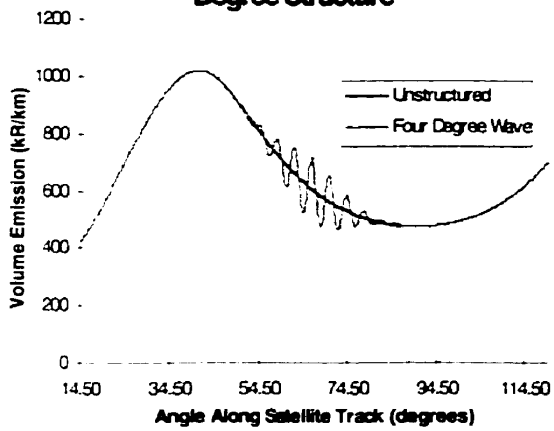
Radial Volume Emission Cross Sections With No Structure and Three Degree Structure



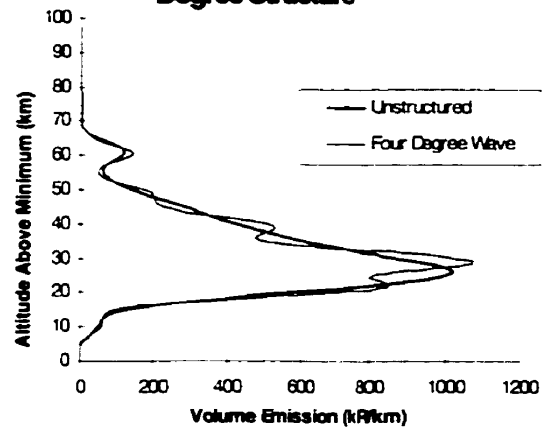
Angular Volume Emission Cross Sections With No Structure And Three Degree Structure



Radial Volume Emission Cross Sections With No Structure and Four Degree Structure



Angular Volume Emission Cross Sections With No Structure And Four Degree Structure



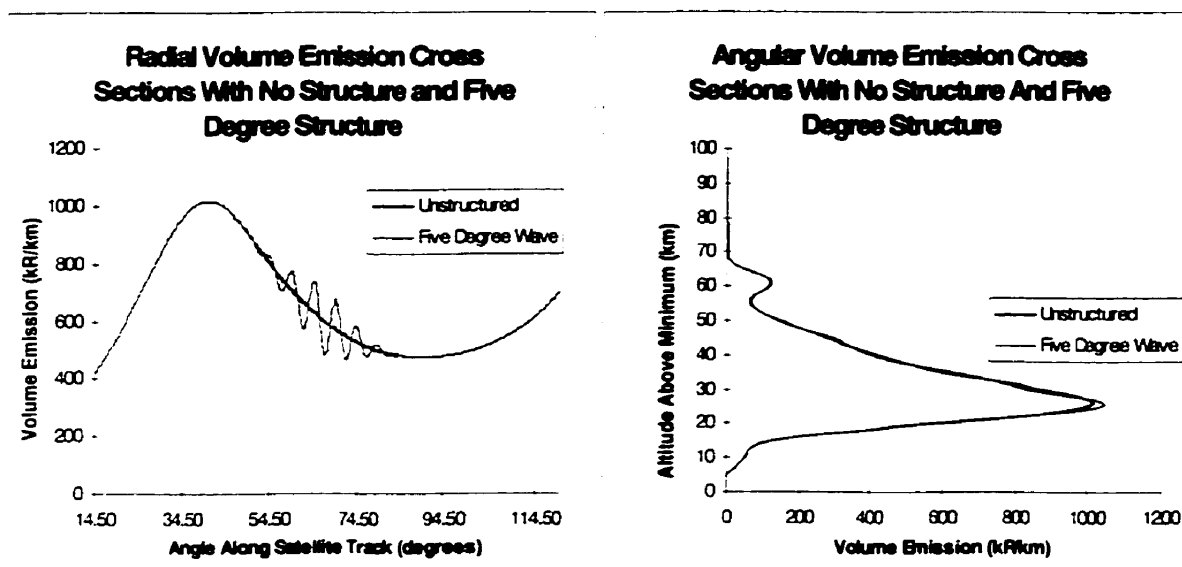
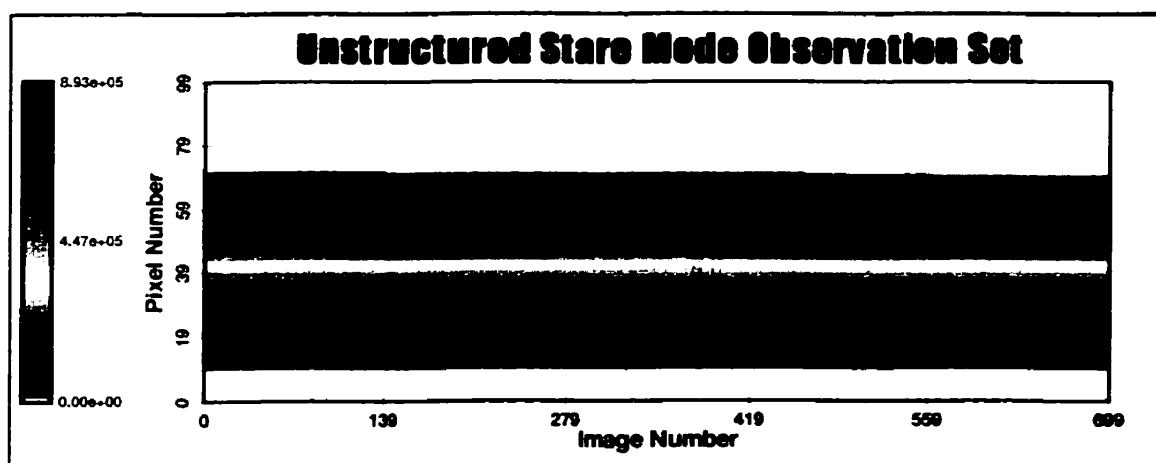


Figure 9.2: Radial and angular cross sections for the two dimensional input volume emission grids shown in Figure 9.1. These plots illustrate the structure imposed on the basic airglow profile.

9.3 The Simulated Observations Used in the Experiment

Examples of the simulated observations (kR) used in the scale size experiment are shown in Figure 9.3. These observations correspond to a 0.5 Hz imaging rate with the input volume emission profiles taken from the grids given in Figure 9.1. In the absence of noise the imposed structure is only just observed for the small scale modulations although it is readily apparent in the observations for the five degree structures.



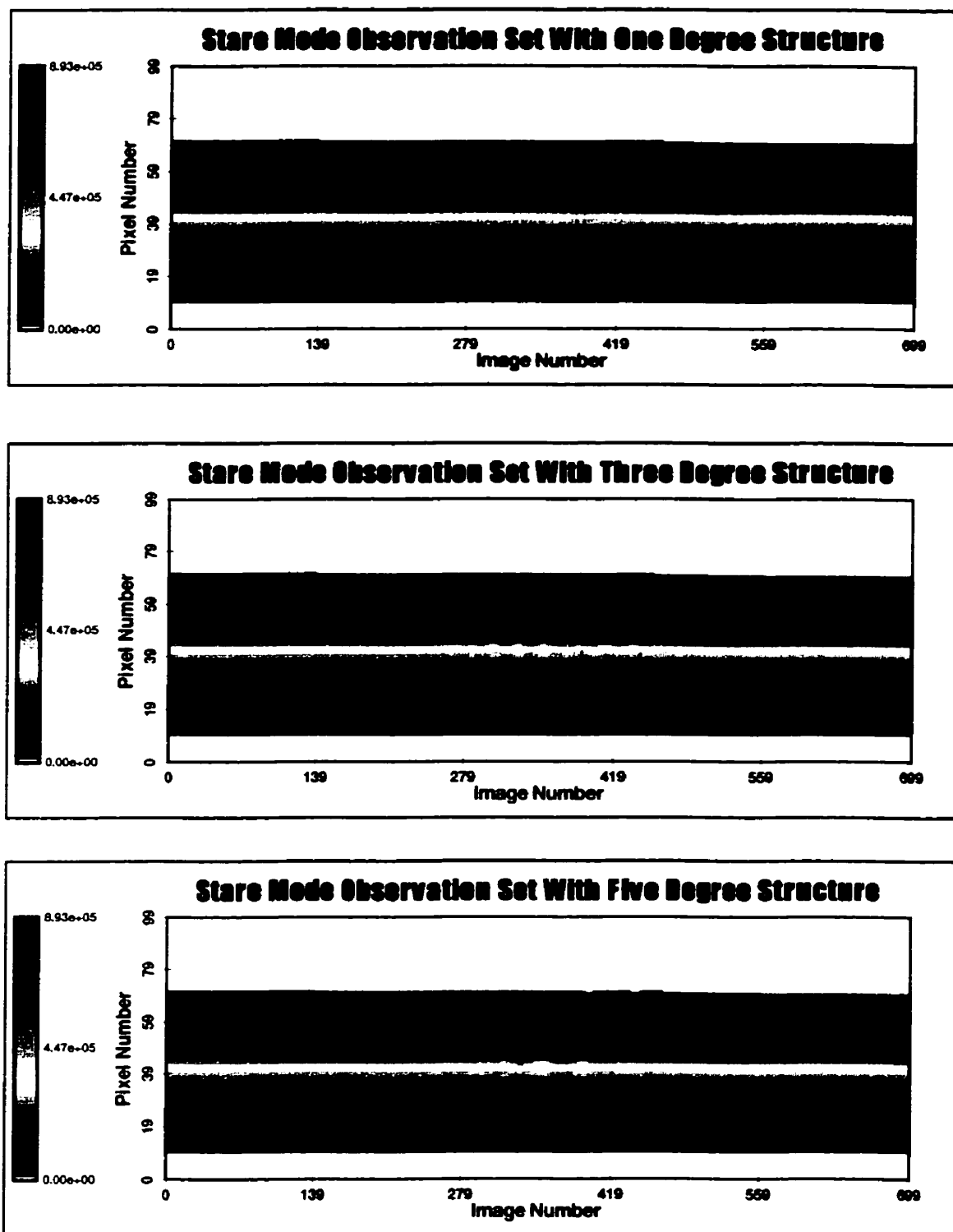


Figure 9.3: Simulated observation sets (with no noise) generated from selected structured input volume emission grids shown in Figure 9.1.

The possible detection of the modulation associated with small scale structures is well demonstrated by the cross sections presented in Figure 9.4. For the shown pixel (number 50) the observations for the 1° structure indicate an obviously periodic signal, although the modulation amplitude is less than 1%. By comparison the observations for the 3 and 5 degree structures indicate a well defined pattern with a modulation amplitude greater than 5%. The low contrast in the observations for the small scale structures is due to the smoothing effect of the line of sight integration through the high frequency structures.

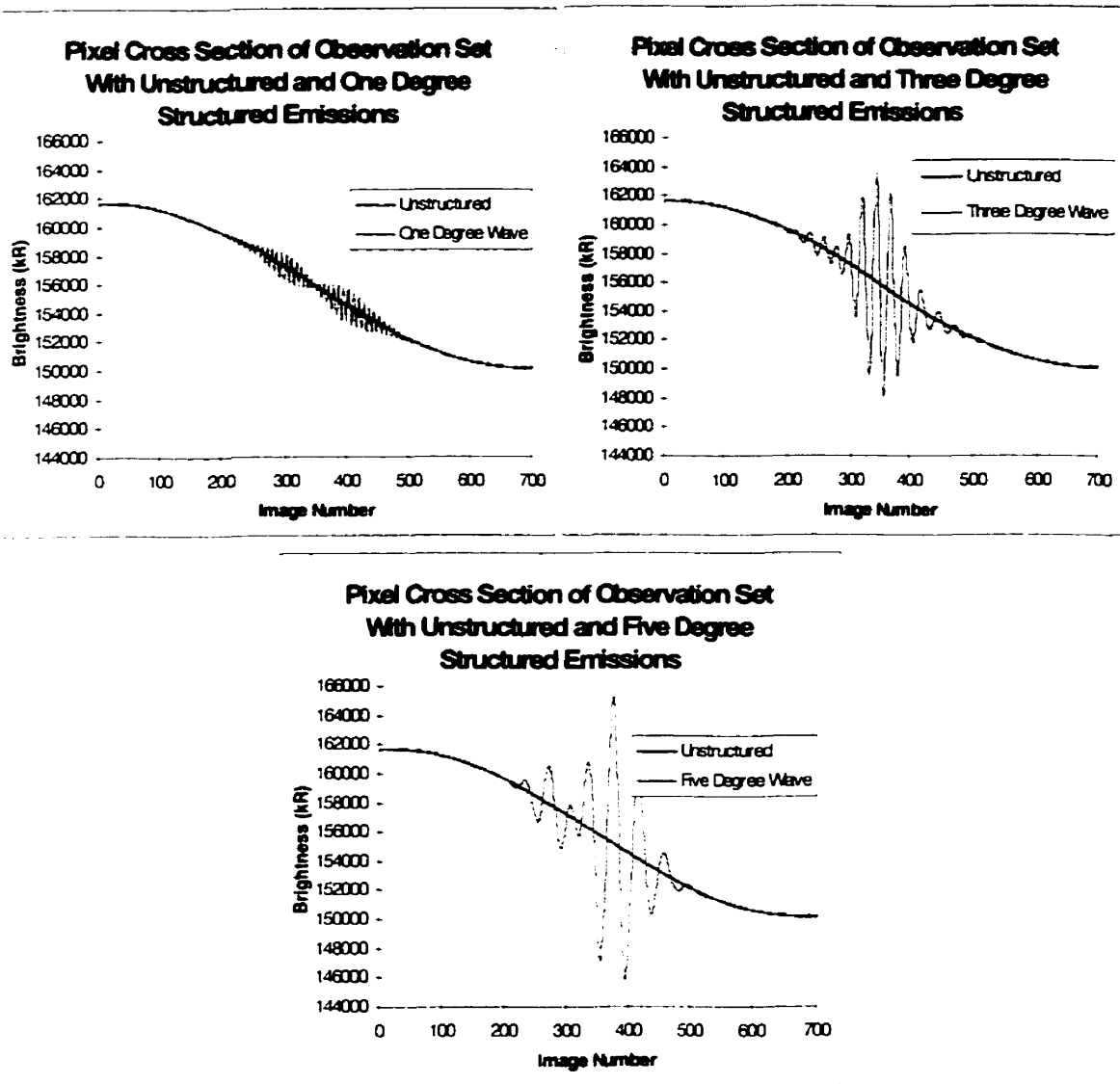


Figure 9.4: Cross sections for a single pixel (number 50) taken from the selected observation sets shown in Figure 9.3.

In the presence of noise it is extremely difficult to identify (visually) the signal modulations due to the small scale structures. The cross sections shown in Figure 9.4 are repeated in Figure 9.5 for the case where Gaussian random noise (standard deviation 2 MR) has been included. For the one degree structured input profile (Figure 9.5a) the modulation that was apparent in the noiseless case is completely absent. For the three degree structure (Figure 9.5b) the modulation is just apparent and for the five degree structure (Figure 9.5c) it is obviously present.

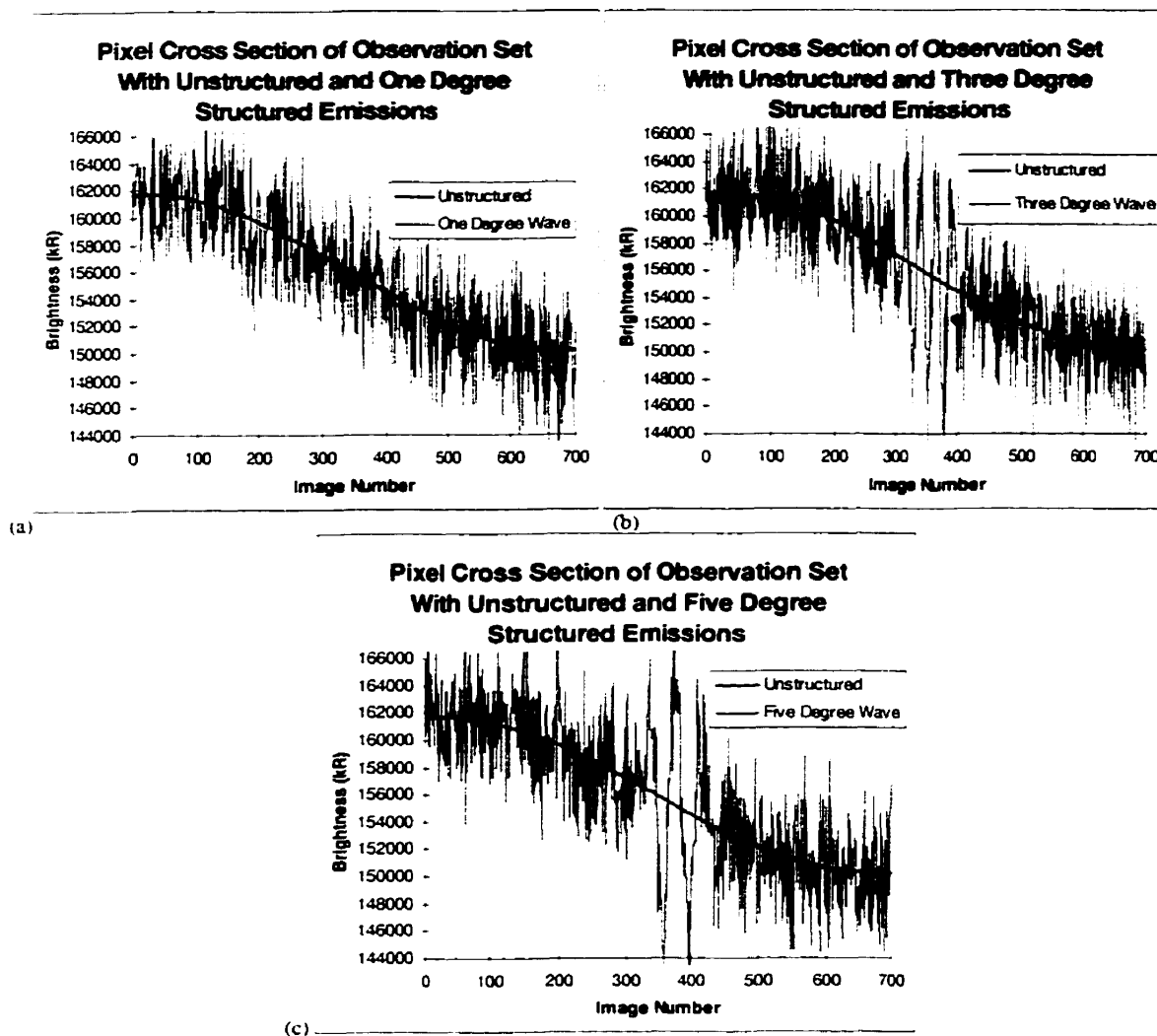


Figure 9.5: *The same pixel cross sections as those shown in Figure 9.4 but with an absolute random Gaussian noise (standard deviation 2 MR) imposed on the observations.*

The visibility of the structure is even more apparent in the Fourier decomposition of the observations for pixel number fifty. The relevant Fourier coefficients (magnitude only)

for the three different structures are shown in Figure 9.6. In each case the first 10 coefficients have been omitted in order to maintain a scale appropriate to the coefficients of interest. For the one degree structure, Figure 9.6a, the Fourier coefficients for the noiseless observations exhibit a monotonic decrease except for coefficient numbers near 80, these correspond to the one degree structure in the input grid. For the observations that include the 2 MR noise level this region is indistinguishable from the background noise.

For the three and five degree structure the Fourier coefficients that represent the wave structure, Figures 9.6b and 9.6c, are easily visible in both data sets. It appears that the noise in the coefficient sets becomes less important, with respect to the structure, as the scale size increases.

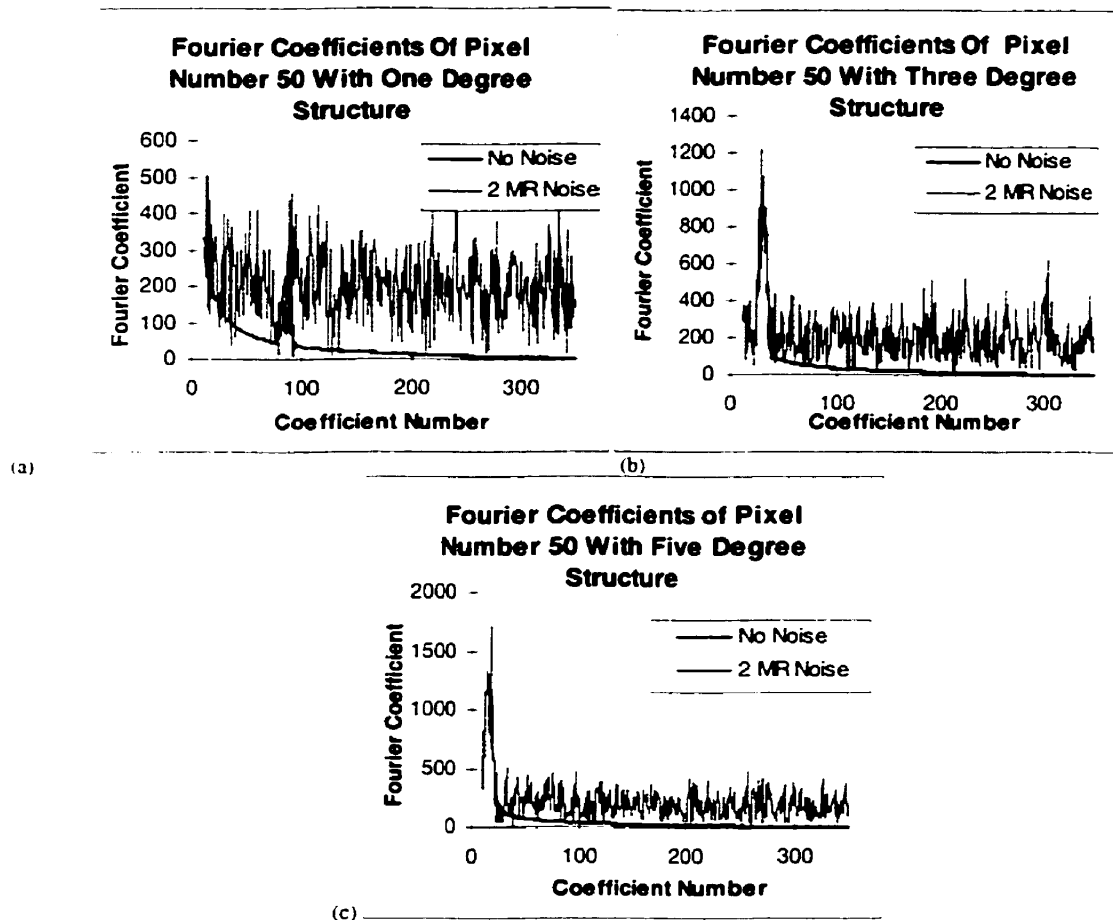
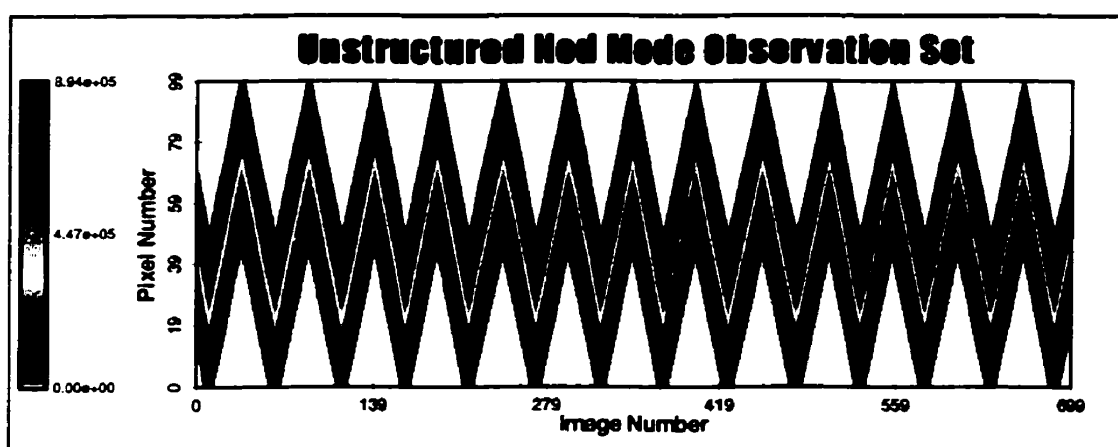
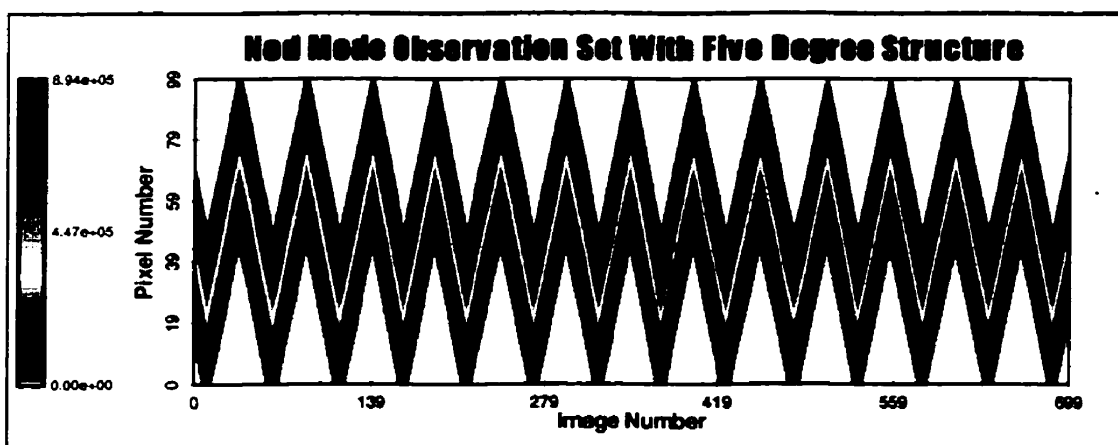


Figure 9.6: Fourier coefficients for the observations at pixel number 50 for different structures and a 2 MR Gaussian (absolute) random noise level.

Figures 9.7 and 9.8 are examples of noise free observations generated for less than ideal conditions. The observation sets illustrated in Figure 9.7 are for the case where the satellite platform nods so that the tangent altitude of the imager optical axis varies between 10 and 60 km in a regular sawtooth manner at 1 km/second. In the upper panel (Figure 9.7a) the observations correspond to the unstructured volume emission profile shown in Figure 9.1a. The lower panel (Figure 9.7b) is for observations generated with the volume emission profile that contains the five degree wave structure (Figure 9.1f). An examination of the two observation sets (Figure 9.7) indicates only minor visible differences.



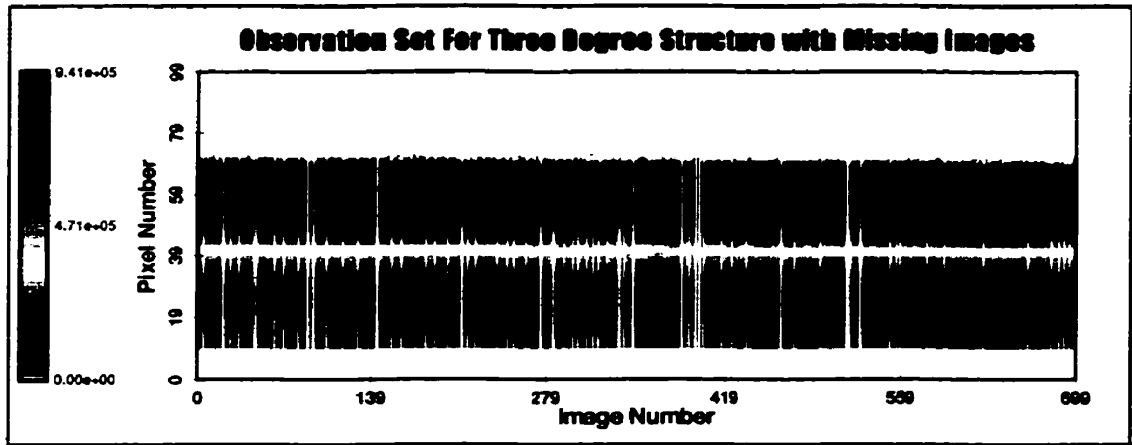
(a)



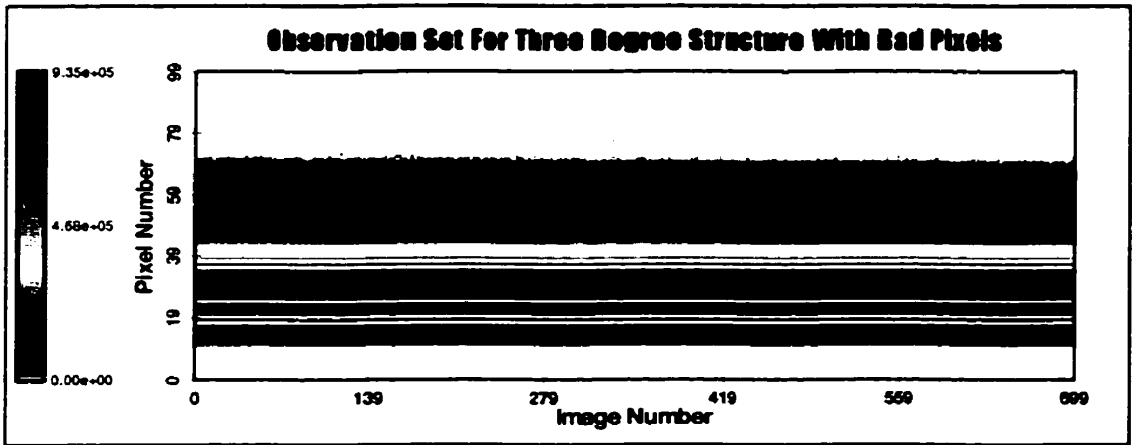
(b)

Figure 9.7: Noise free observation sets generated for the 10 to 60 km nod mode.

The observation sets shown in Figure 9.8 correspond to measurements that are made under faulty operating conditions. These can be due to telemetry dropouts that result in missing data; for these observation sets it has been assumed that the probability of data loss is 0.1. The upper panel (Figure 9.8a) shows an image set generated from the volume emission grid with three degree angular structure (Figure 9.1d) and a random loss of entire images. A Gaussian random noise (2 MR standard deviation) has also been imposed on these measurements in order to simulate realistic conditions.



(a)



(b)

Figure 9.8: Observation sets that include 2 MR absolute Gaussian random noise and either missing images (a) or missing pixels (b). The probability of data loss is 0.1 in both cases.

The lower panel (Figure 9.8b) corresponds to an observation set made with a detector that has non-responsive, or dead, pixels. The dead pixels (common throughout the entire observation set) were randomly selected with a 10% probability. A Gaussian random noise (standard deviation 2 MR) has also been superimposed on the measurements.

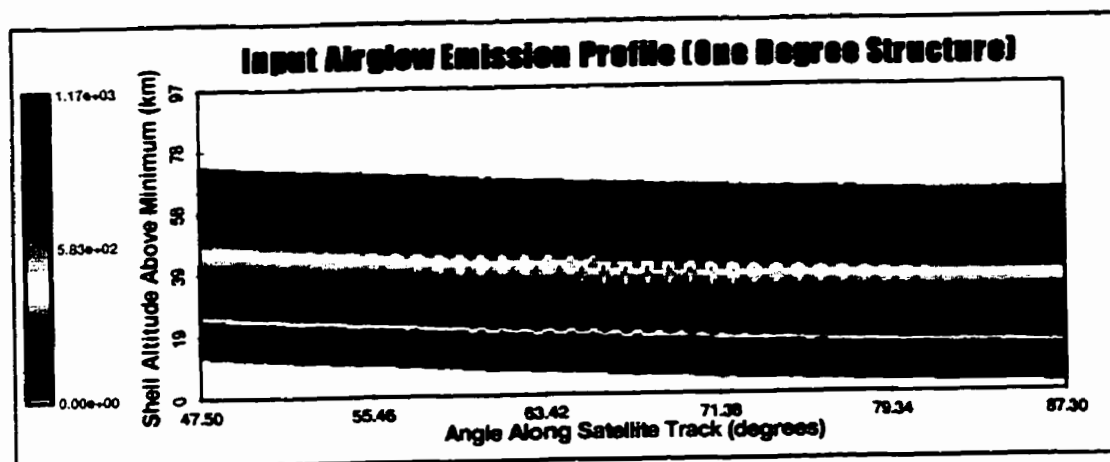
9.4 Inversion Results

The observations that are discussed in Section 9.3 have been used in the tomographic retrieval and the results for noiseless and noisy observations are presented in this section. It is shown that a wavelike structure with scale size of 300 km can be fully resolved under almost all observing conditions.

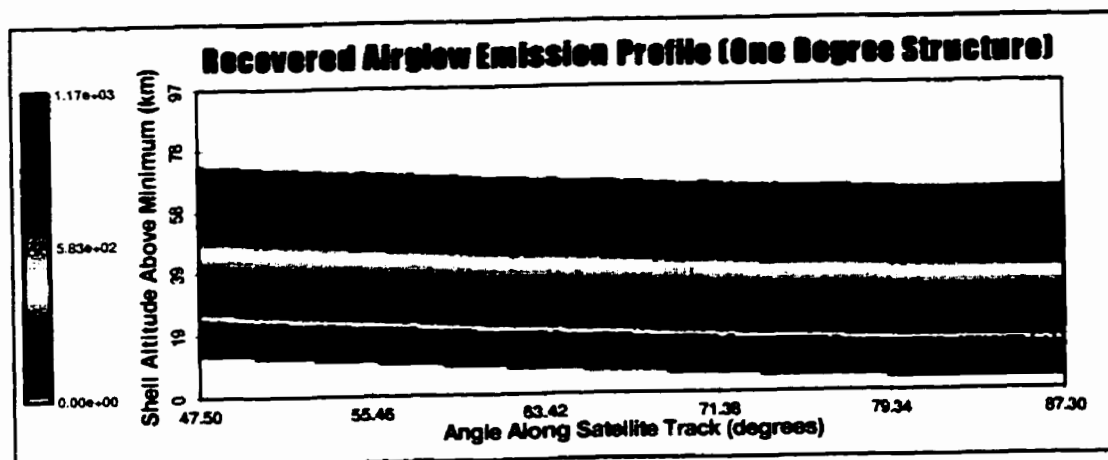
9.4.1 Results With Noise-Free Input Data

The simulated observation sets were first inverted for ideal conditions (no noise and no missing data). The inversions were made for both the 10 km to 60 km nod mode, imaging rate 0.5 Hz, and the stare mode for imaging rates of 1.0, 0.5 and 0.33 Hz. A subset of the results from these inversions, and the actual input grids, are presented in Figure 9.9. For this figure the shown retrievals correspond to a 0.5 Hz imaging rate and the angular extent of the grids has been decreased in order to emphasize the retrieval in the region of the structured emissions. The colour scale in these figures corresponds to the volume emission rate in kR/km.

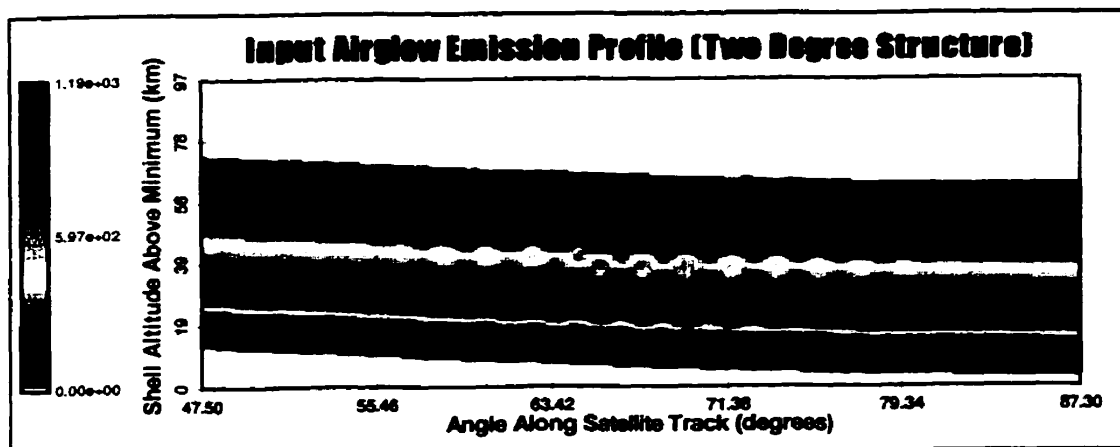
A comparison of the input and retrieved one degree structure (Figures 9.9a and 9.9b) indicates that in this case the scale sizes are too small for accurate retrieval. However, as the scale size increases (Figures 9.9c through 9.9j) so the retrieved grid appears to become identical with the input grid. Direct support for this conclusion is provided by the profile cross sections shown in Figures 9.10 and 9.11.



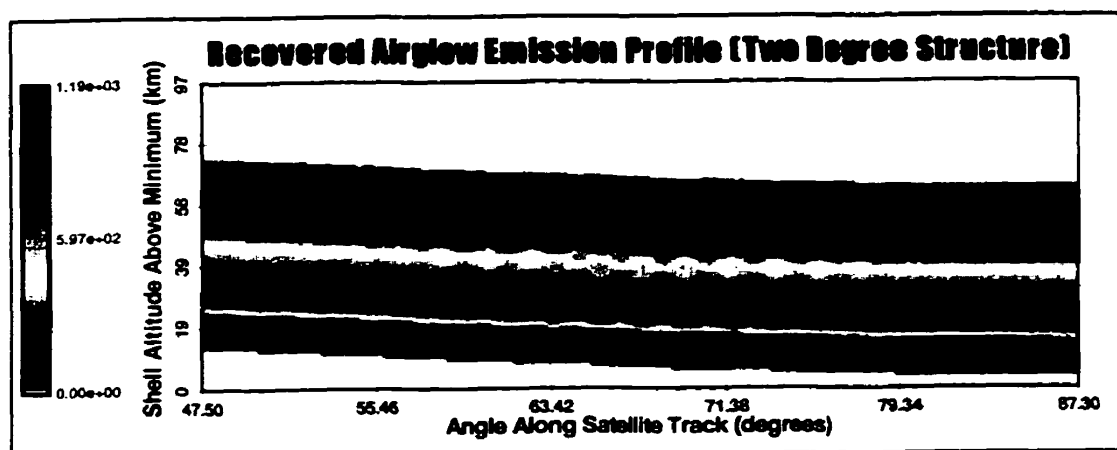
(a)



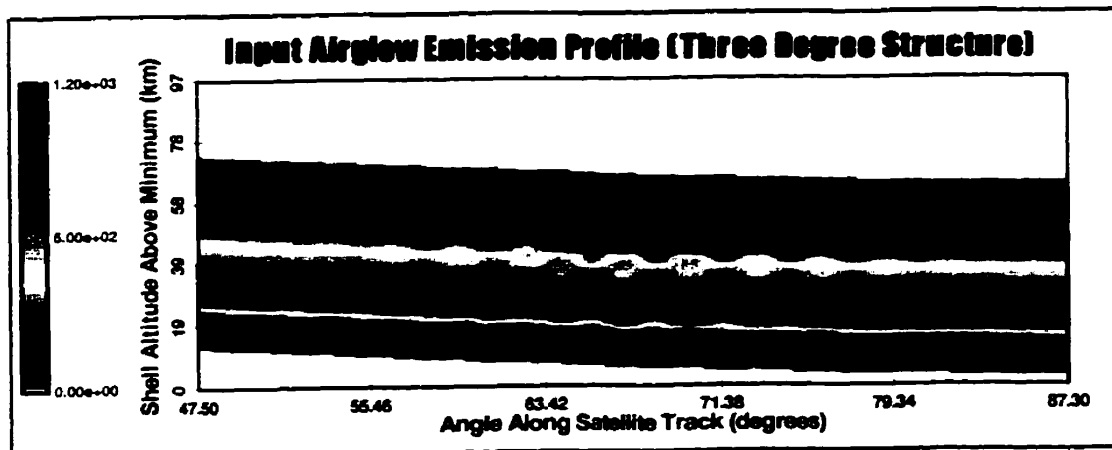
(b)



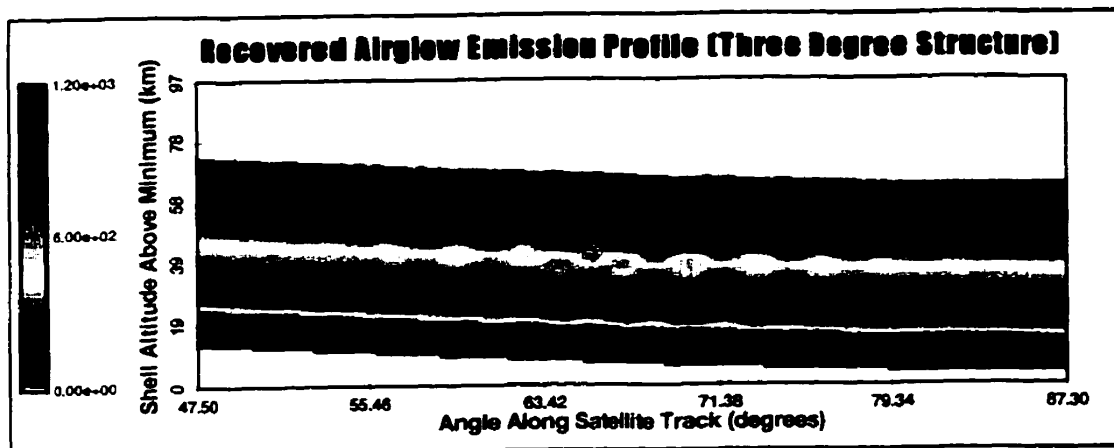
(c)



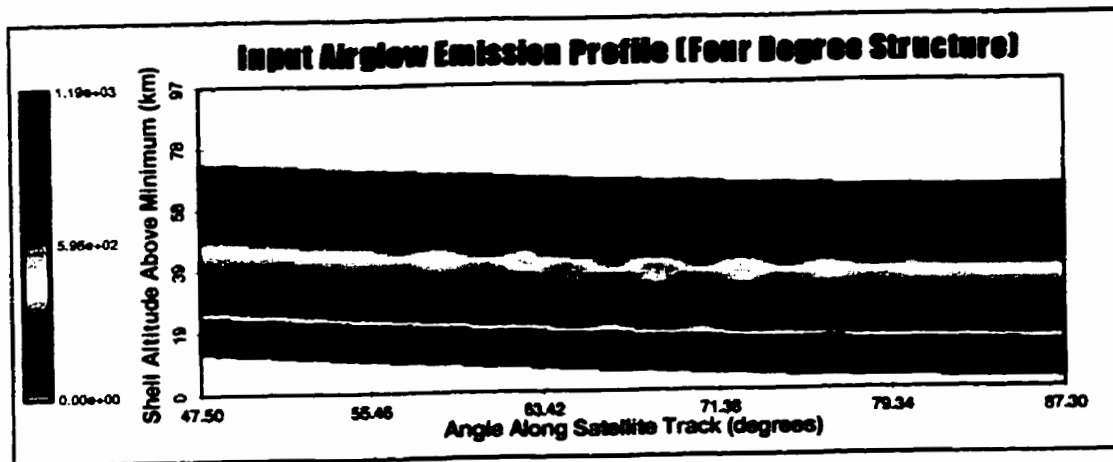
(d)



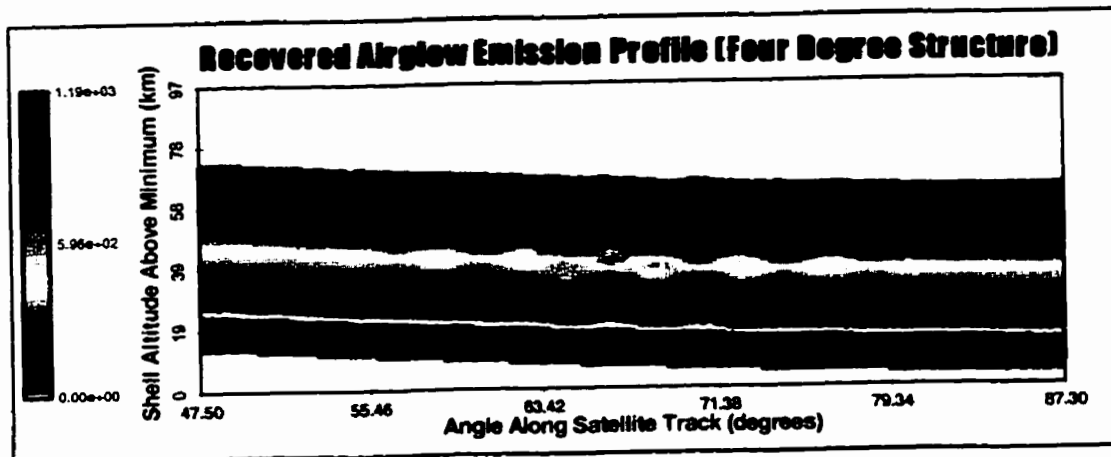
(c)



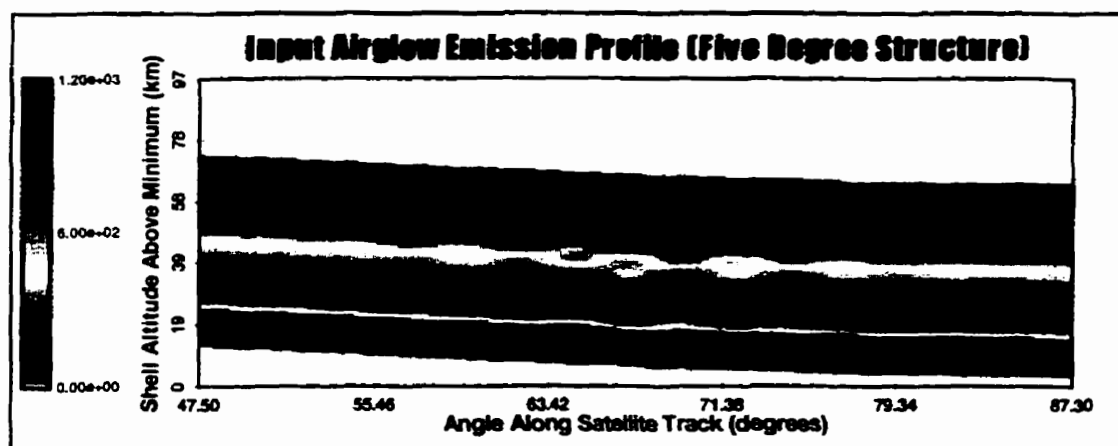
(f)



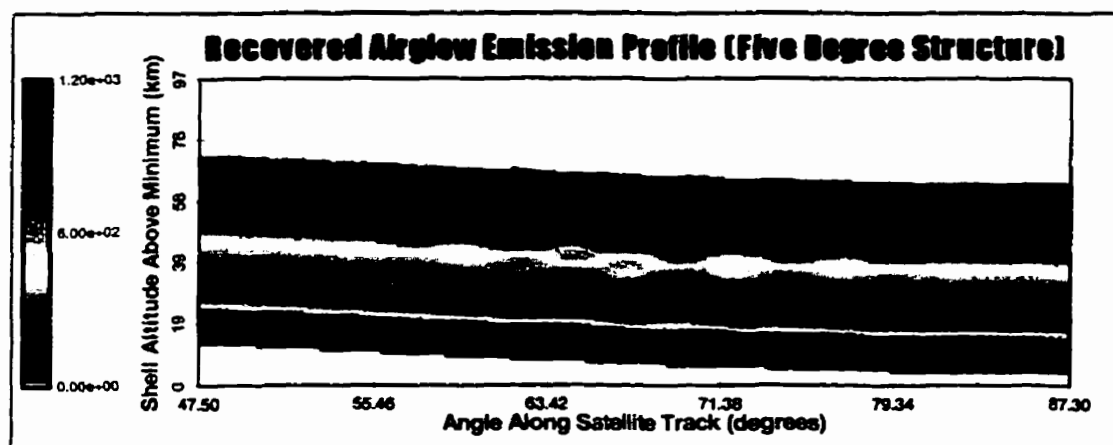
(g)



(h)



(i)



(j)

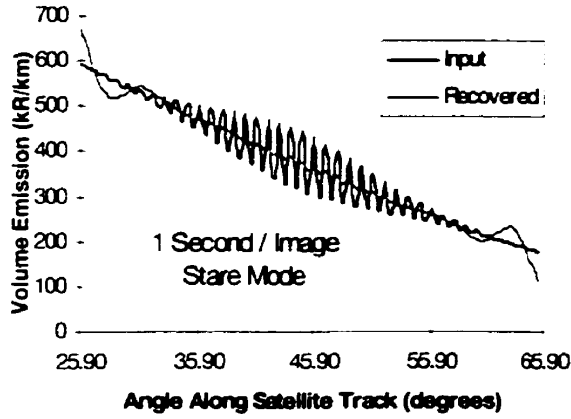
Figure 9.9: Recovered volume emission grids for the different structures that were tested. These two dimensional plots include only forty degrees of the grid in order to emphasize the structure retrieval.

The radial and angular cross sections, shown in Figures 9.10 and 9.11, are for both the different structure scale sizes and the different operational modes. The first set of four plots (Figure 9.10a) illustrate that for an input structure of 1° none of the operational modes is able to resolve the structure along the satellite track. It is apparent that the recovery procedure is ineffective when the structure scale size approaches this lower limit.

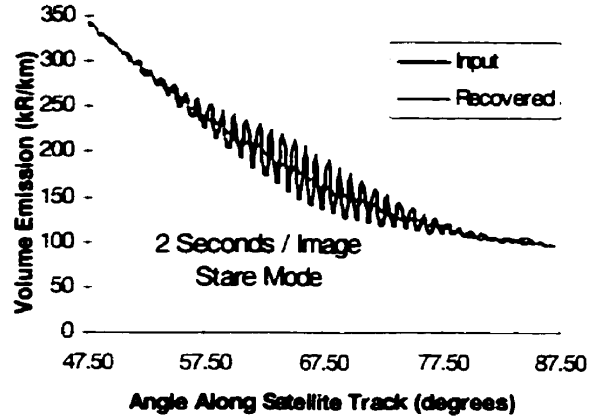
The cross sections shown in Figure 9.10b indicate that while the recovery is not ideal it is possible to resolve structures with scale sizes of two degrees, *i.e.* 200 km, along track. Although the waves are not exactly retrieved the structure in the recovered emission grid does correspond to the two degree input structure. These plots also indicate there are no large apparent differences in the retrievals for the different operational modes.

The plots shown in Figure 9.10c illustrate the retrieval within a single radial shell for a three degree angular structure. For the stare mode and 1.0 Hz and 0.5 Hz imaging rates the retrieval is very good but for the 0.33 Hz imaging rate there is a small loss of detail in the retrieval. This is due to undersampling of the wave structure. The same high quality retrieval is also obtained for the nod mode observations. Hence it is concluded from these retrievals, and from those for the 4 and 5 degree structures (Figure 9.10d and 9.10e), that for noise-free observations angular structures of three degrees along the satellite track can be fully resolved, even with the satellite nod mode.

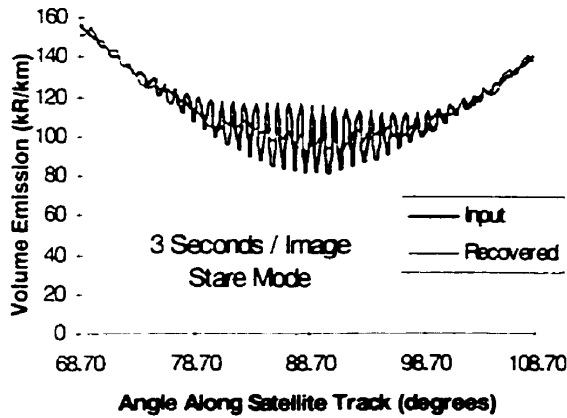
Comparison of Input and Recovered Emission Profile Radial Shell Cross Sections For One Degree Structure



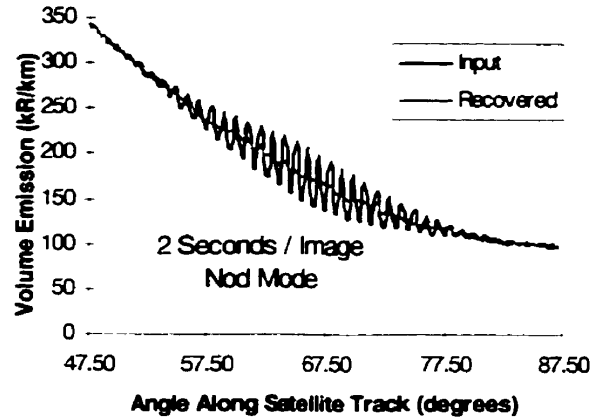
Comparison of Input and Recovered Emission Profile Radial Shell Cross Sections For One Degree Structure



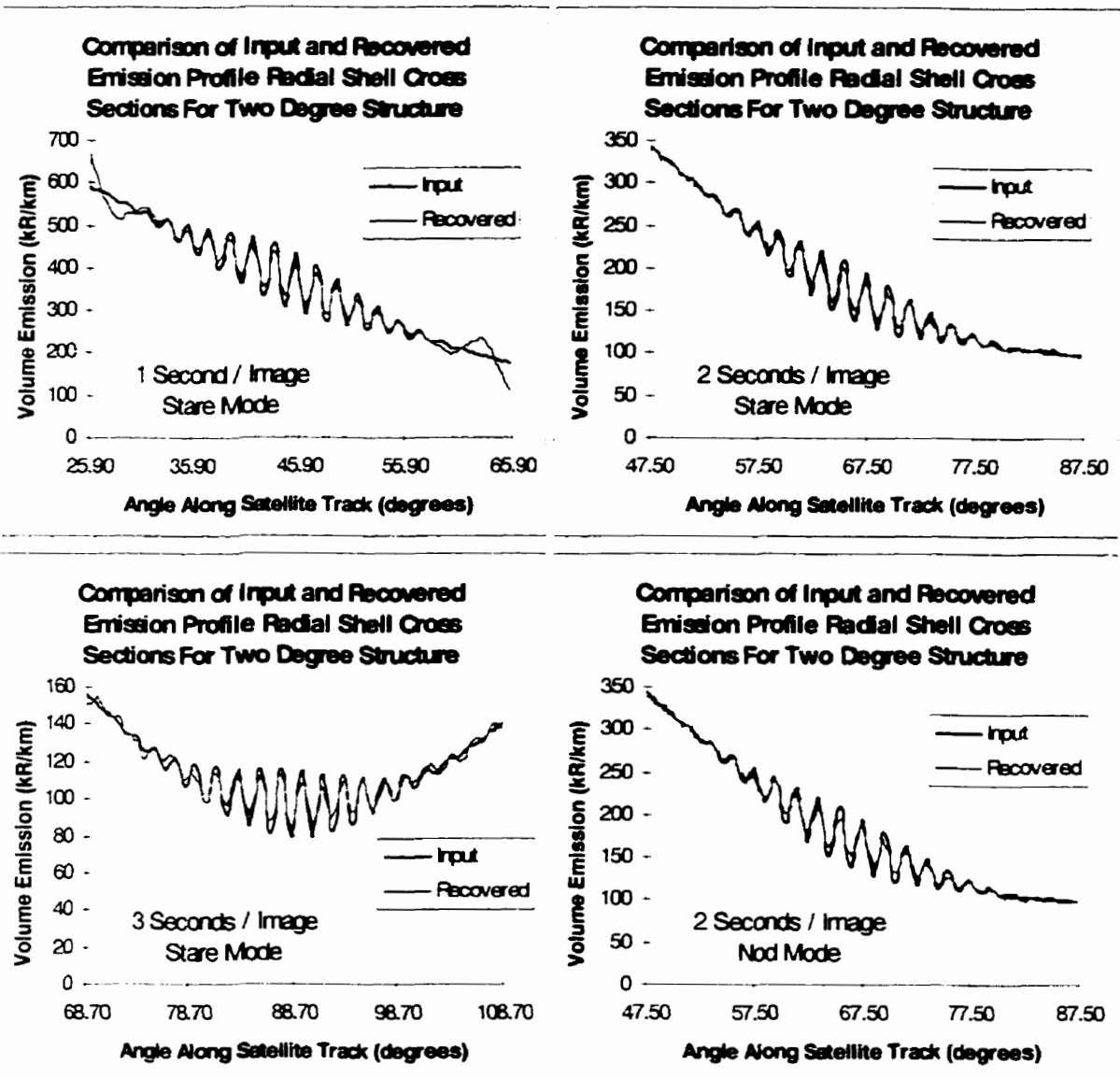
Comparison of Input and Recovered Emission Profile Radial Shell Cross Sections For One Degree Structure



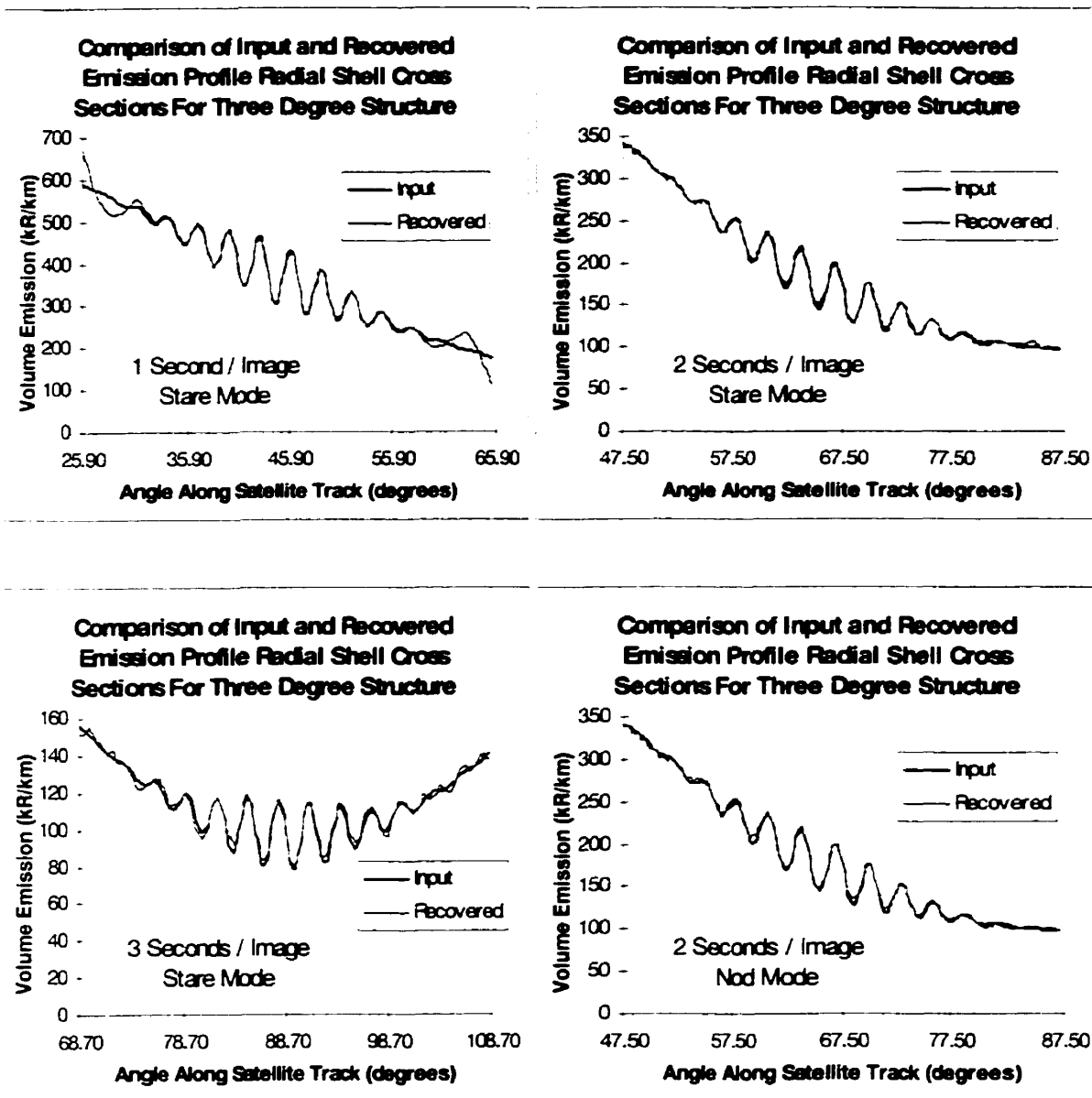
Comparison of Input and Recovered Emission Profile Radial Shell Cross Sections For One Degree Structure



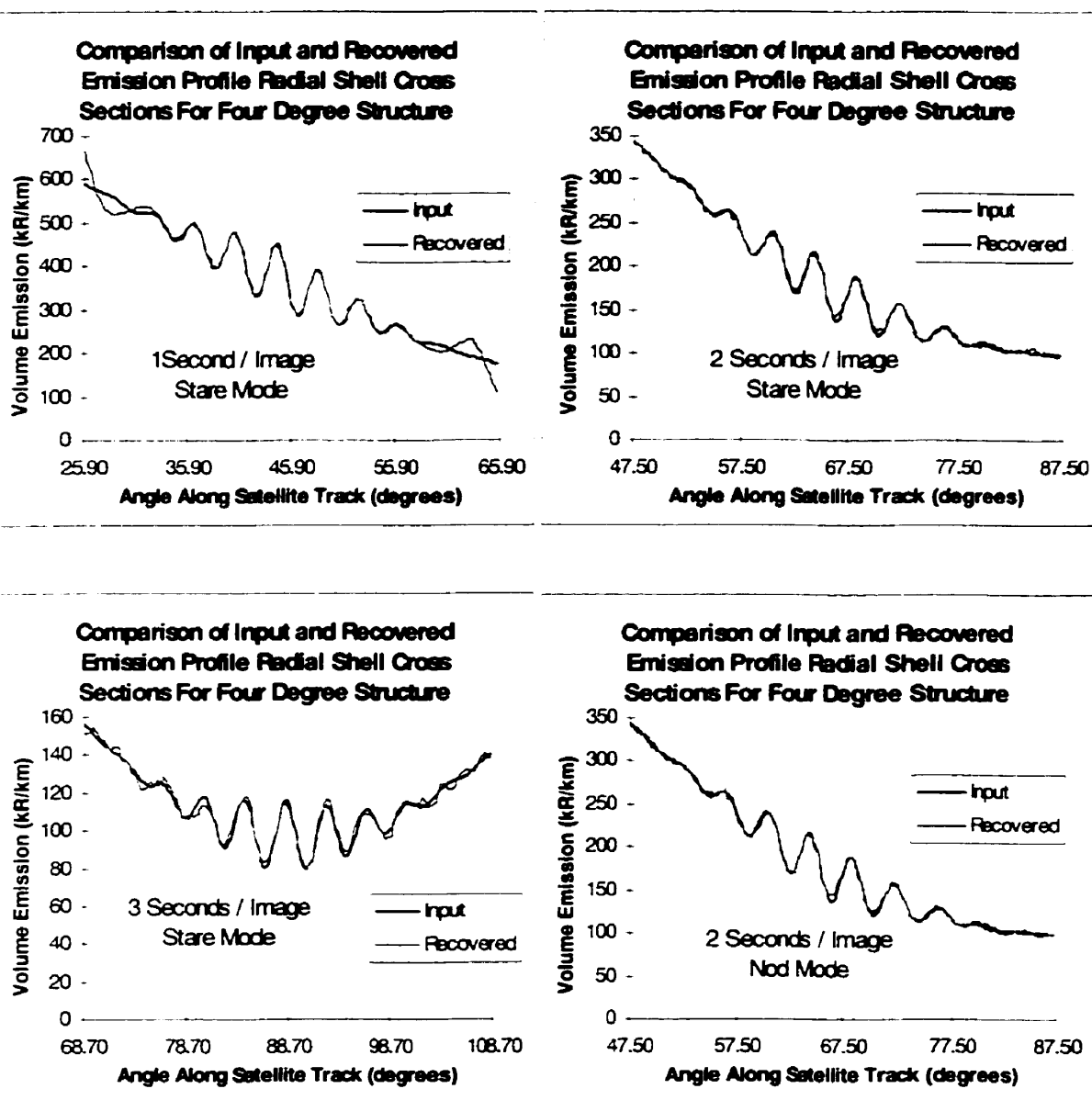
(a)



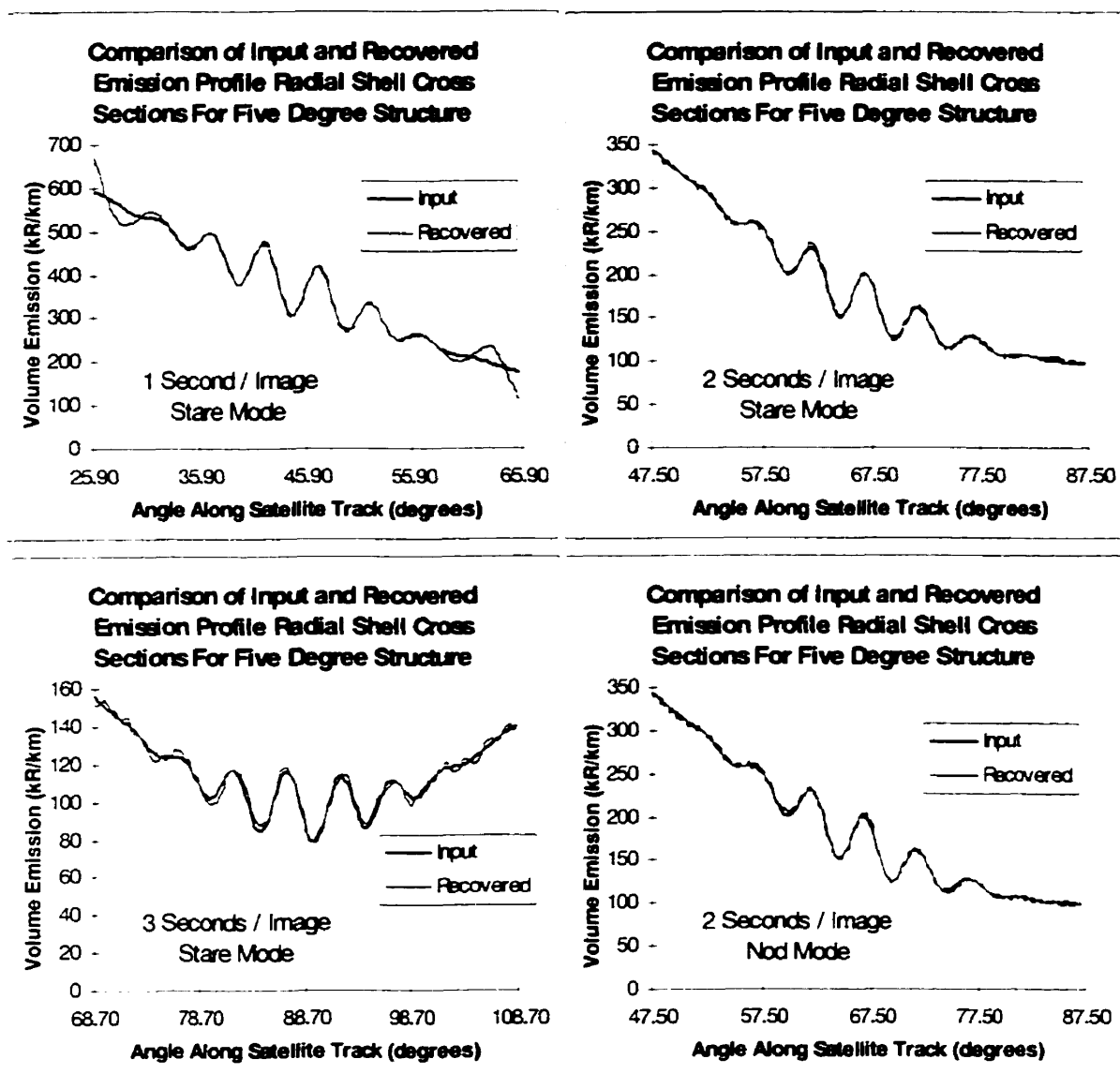
(b)



(c)



(d)

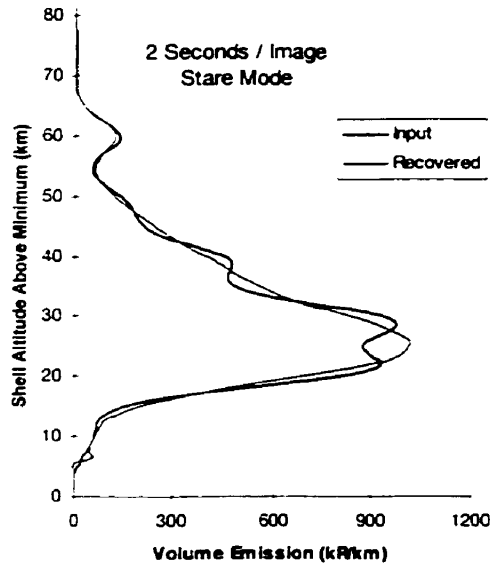


(e)

Figure 9.10: A series of radial shell cross sections for different imaging rates, nod modes and structures.

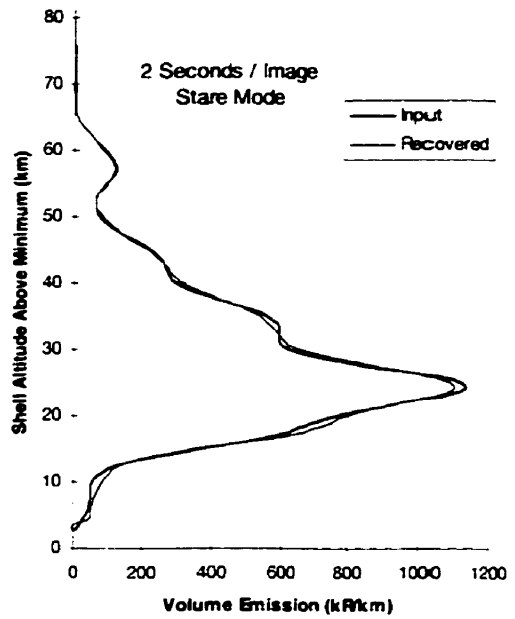
The angular cross sections shown in Figure 9.11 also indicate good altitude recoveries for horizontal structure scale sizes of three degrees and larger. For smaller scale size structures the tomographic retrieval smooths the volume emission profile to give some average value. The presented results are only for the 2 seconds per image stare mode and are representative of the entire set of operational modes.

Comparison of Input and Recovered Emission Profile Angular Cross Sections For One Degree Structure



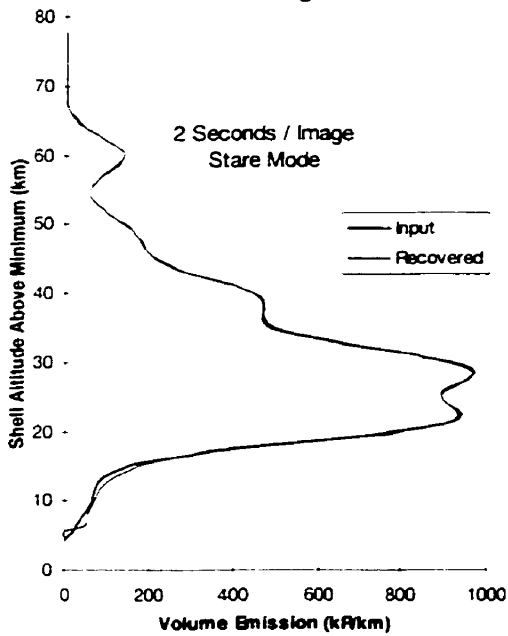
(a)

Comparison of Input and Recovered Emission Profile Angular Cross Sections For Two Degree Structure



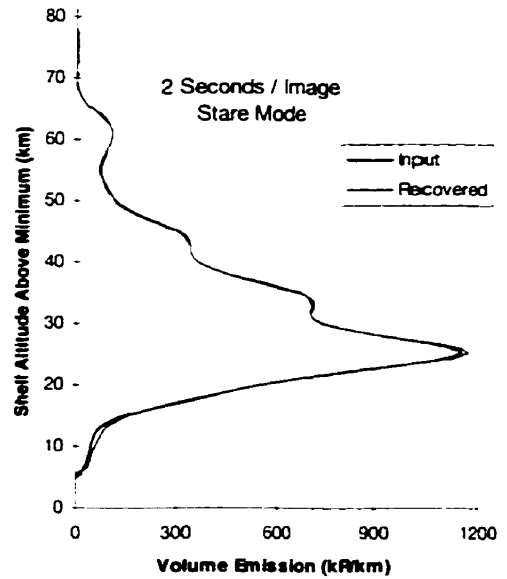
(b)

Comparison of Input and Recovered Emission Profile Angular Cross Sections For Three Degree Structure



(c)

Comparison of Input and Recovered Emission Profile Angular Cross Sections For Four Degree Structure



(d)

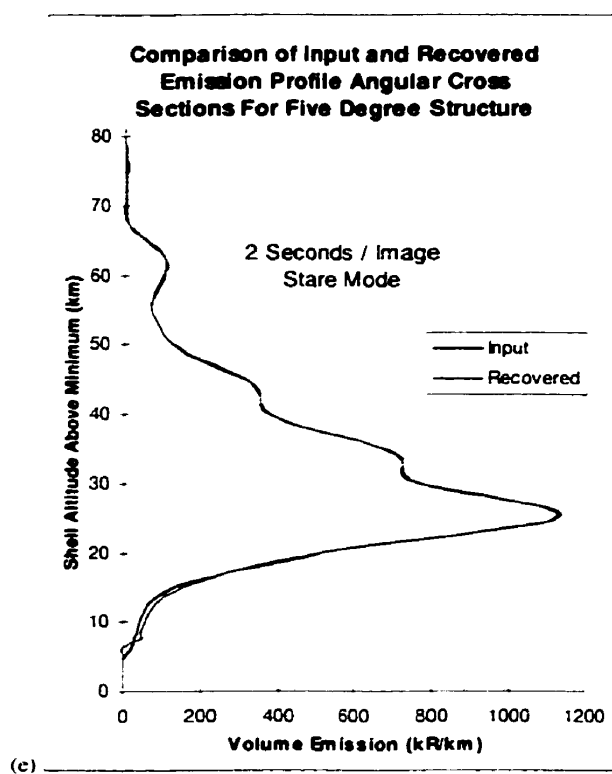


Figure 9.11: A series of angular cross sections for the different scale size structures. The stare mode and a fixed 0.5 Hz imaging rate was used for each of these retrievals.

9.4.2 Results With Absolute and Relative Noise Levels

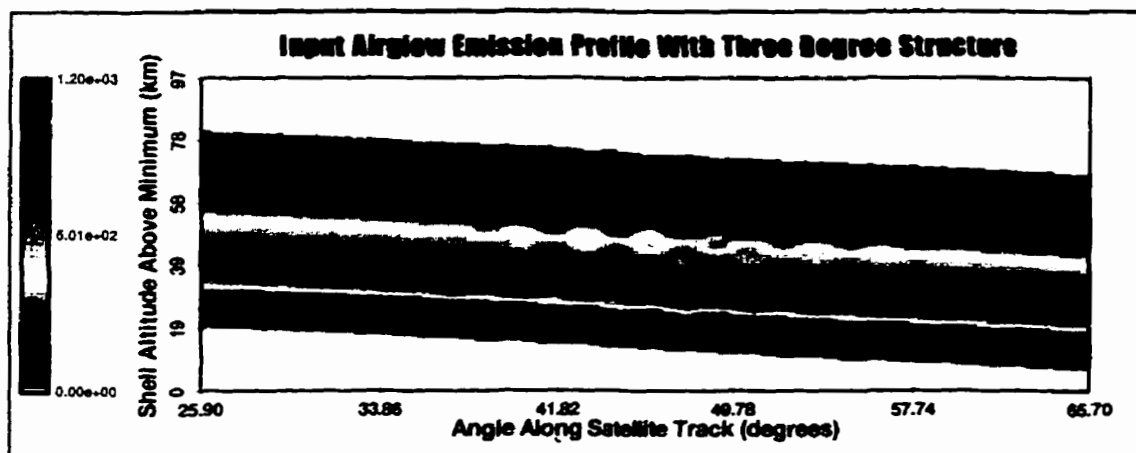
In Section 9.4.1 only inversions of noiseless observations were considered and any errors were due to computational rounding and the resolution of the measurement estimates. However, for a real instrument there is observational noise and it is important to recognize the limitations of the tomographic technique with real observations. In this case two types of noise, absolute and relative, have been considered. The former is commonly associated with infrared detectors while the latter is typical of photon counting systems. The detailed results presented here are for the three degree structure (Figure 9.1d) The results for larger scale size structures are at least as good and are only considered briefly through the error histogram halfwidths (Appendix C).

9.4.2.1 Absolute Noise

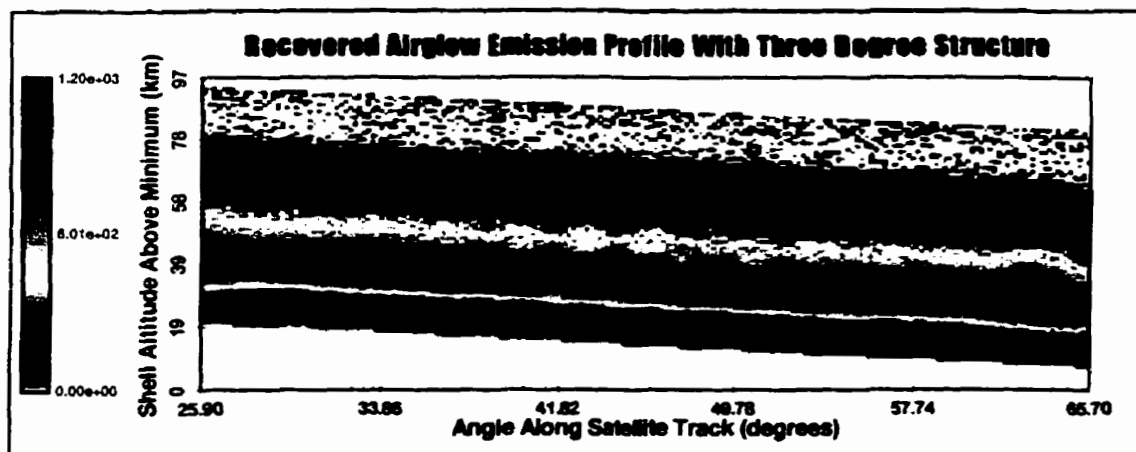
Absolute Gaussian random noise with five different levels, that ranged from 500 kR to 10 MR, was applied to each of three sets of simulated measurements. The simulated observations were generated from the input grids that contained three, four and five degree angular structure (equations 9.1 and 9.2).

The input and recovered two dimensional volume emission grids (kR/km) for the three degree angular structure with 10 MR noise are shown in Figure 9.12. The different plots represent the different stare modes at 1, 2 and 3 seconds per image and the 0.5 Hz imaging rate nod mode. It is apparent from these plots that the input structure has been recovered, although it is partially obscured by high frequency random noise.

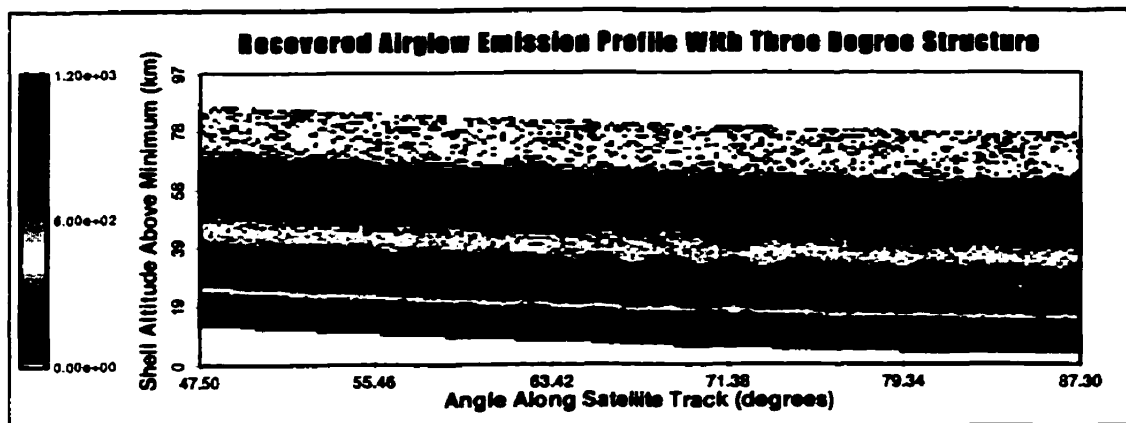
(a) Input Grid



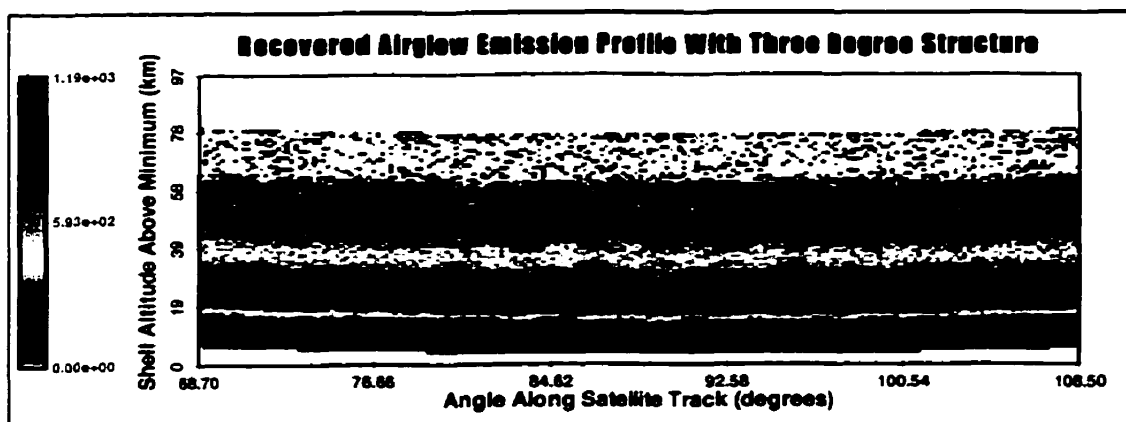
(b) Stare mode, 1 Hz imaging rate



(c) Stare mode, 0.5 Hz imaging rate



(d) Stare mode, 0.33 Hz imaging rate



(e) Nod mode, 0.5 Hz imaging rate

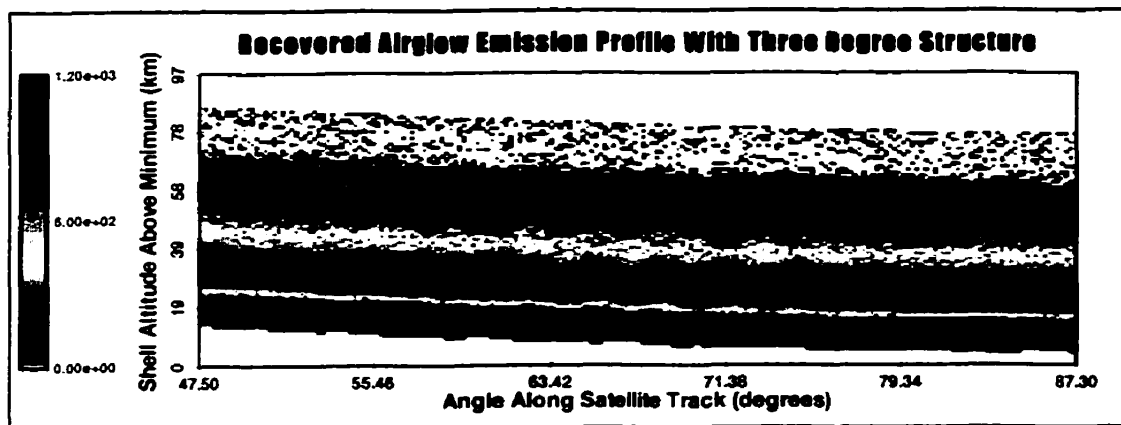


Figure 9.12: The input and retrieved volume emission grids for the three degree structure with different operational modes. The observations contain random Gaussian noise with a standard deviation of 10 MR.

The effectiveness of the recovery is even more apparent in the cross section plots shown in Figure 9.13. These plots are made at various different shell altitudes in order to maintain similar signal magnitudes. The retrieval for the 1 Hz imaging rate stare mode is good, all of the salient features contained in the input structure are evident although there are some obvious random errors. It is also quite clear from Figure 9.12 and Figure 9.13 that the quality of the retrieval decreases as the imaging rate decreases from 1 Hz to 0.33 Hz, although the real angular structure is still apparent for all recoveries.

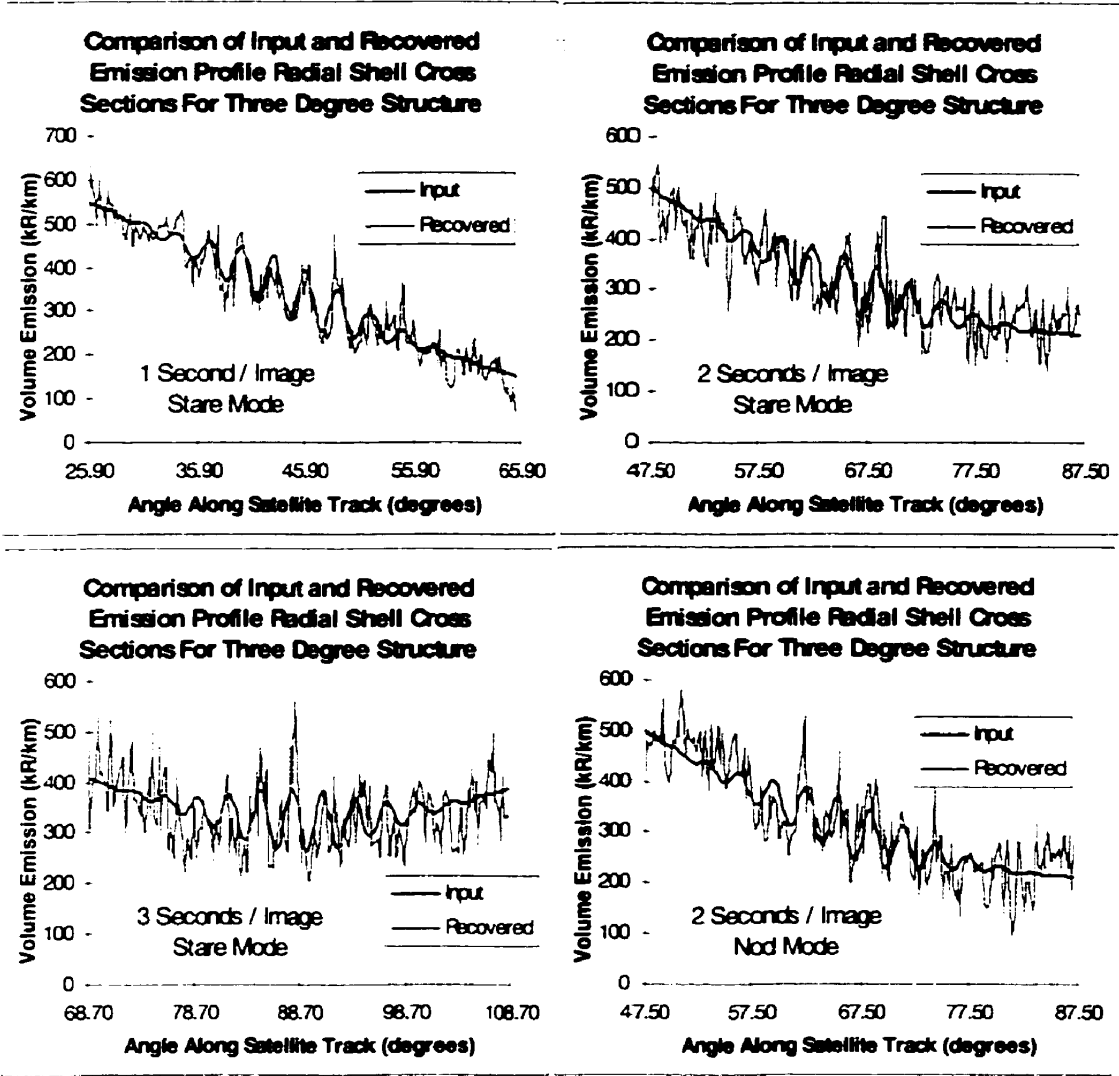


Figure 9.13: Selected radial shell cross sections from the recovery grids shown in Figure 9.12.

In an attempt to reduce the noise in the retrieval grids a simple boxcar filter was applied to the recovered data. The boxcar filter was one element wide on all sides of the element of interest and weighted each element uniformly. The results of this filtering process are shown in Figure 9.14 and it is apparent that the angular structure, which could be seen in the original unfiltered results (Figure 9.13), has been enhanced. For the worst case recovery (0.33 Hz imaging rate) there are clearly identifiable peaks and troughs that correspond to the three degree structure. The post-filtering of the retrievals obtained from noisy observations obviously enhances the retrieval. It also indicates that the tomographic algorithm is effective in localizing the effects of random noise and does not disperse undesirable results throughout the solution.

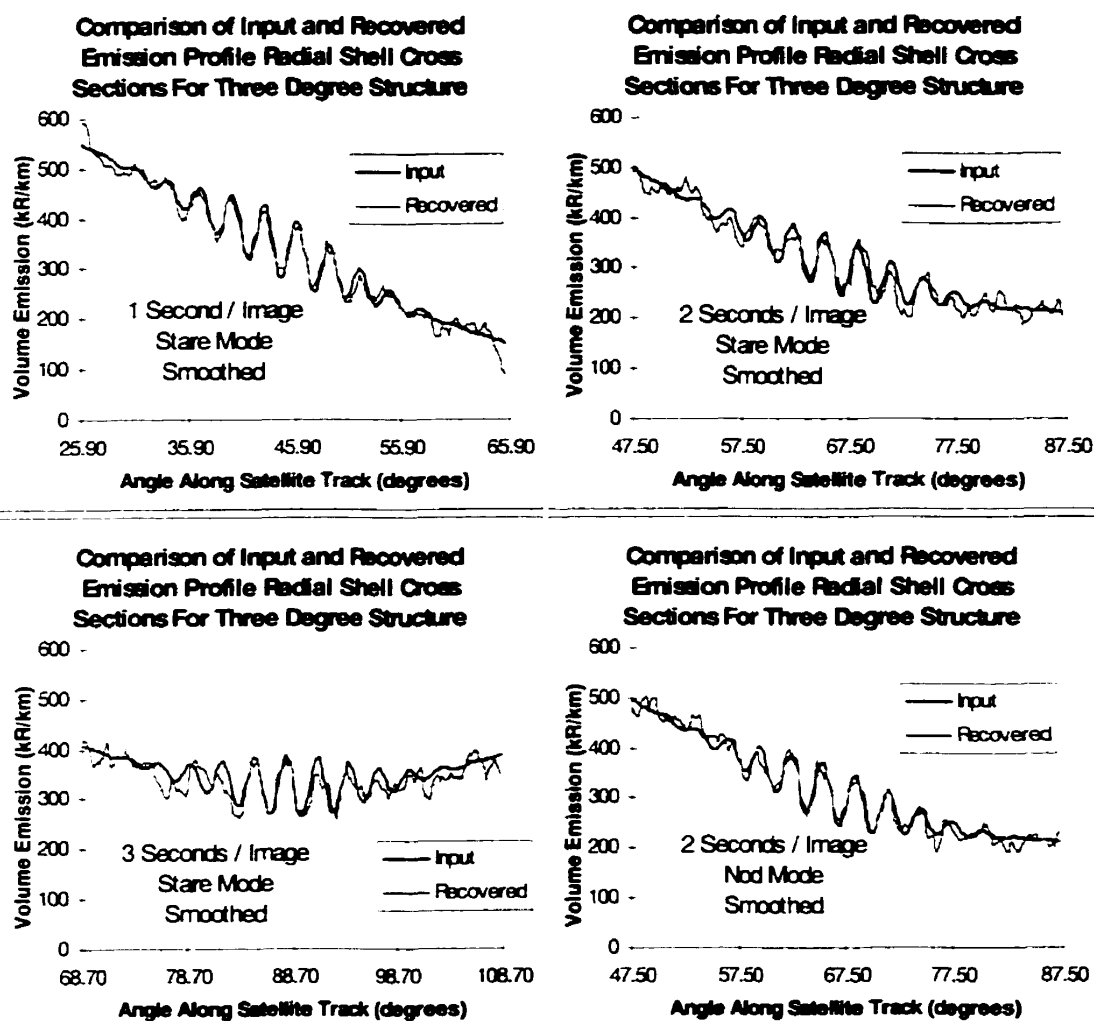
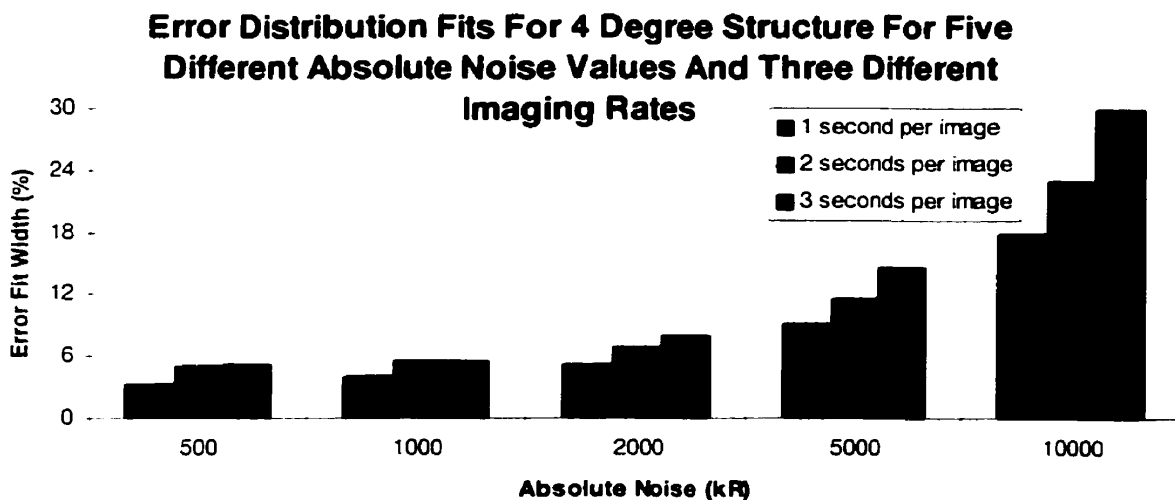
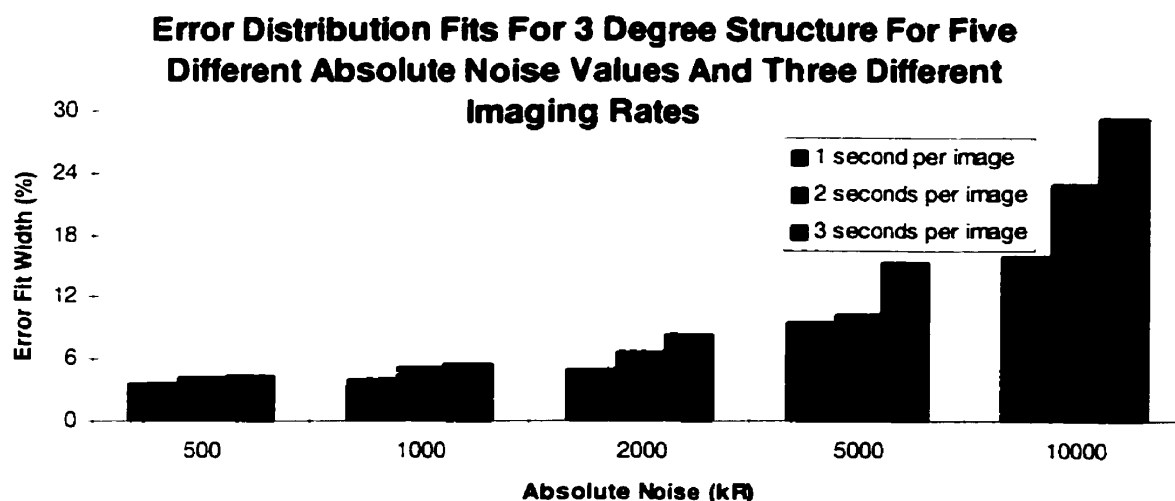


Figure 9.14: Selected radial shell cross sections from the recovery grids shown in Figure 9.12 that illustrate the effects of a simple box car filter.

The error distribution widths (for the unfiltered data), for each of the three different structures and the three operational states modes, are shown in Figure 9.15. These distributions indicate that faster imaging rates are preferred (with respect to inversion quality) when there is noise in the data. The smaller the error histogram width the more accurate the fit. As the inversion algorithm includes an internal averaging, which acts as an observation filter, the faster imaging rates average more observations and thus are more effective at eliminating artifacts due to noise.



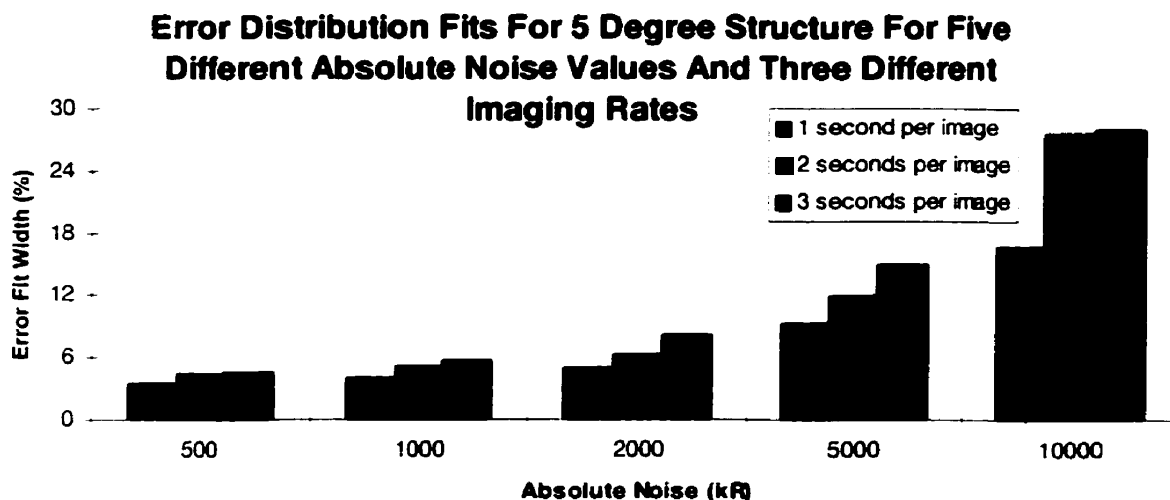
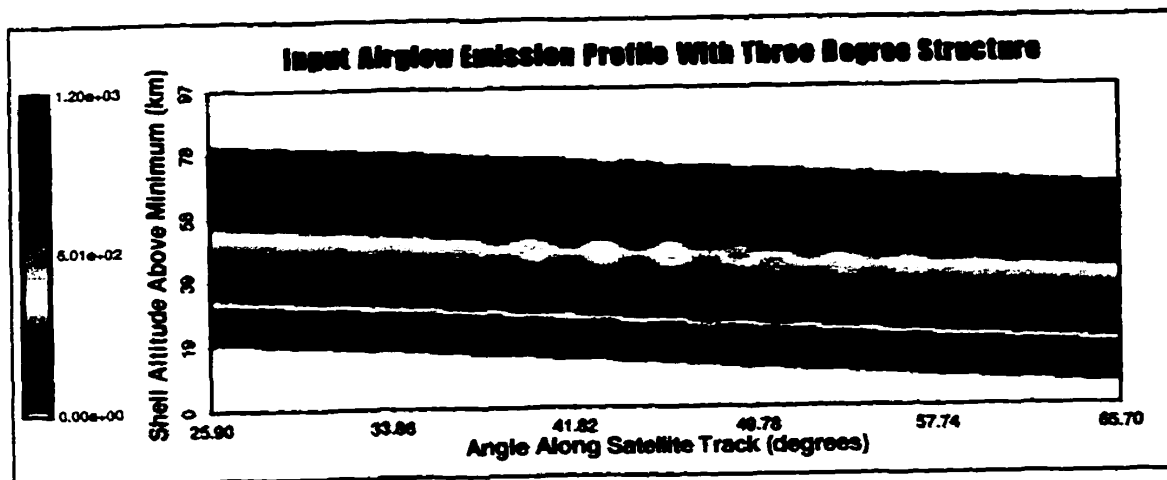


Figure 9.15: Error histogram widths for results obtained with different wave structures and different observational modes for different absolute noise levels.

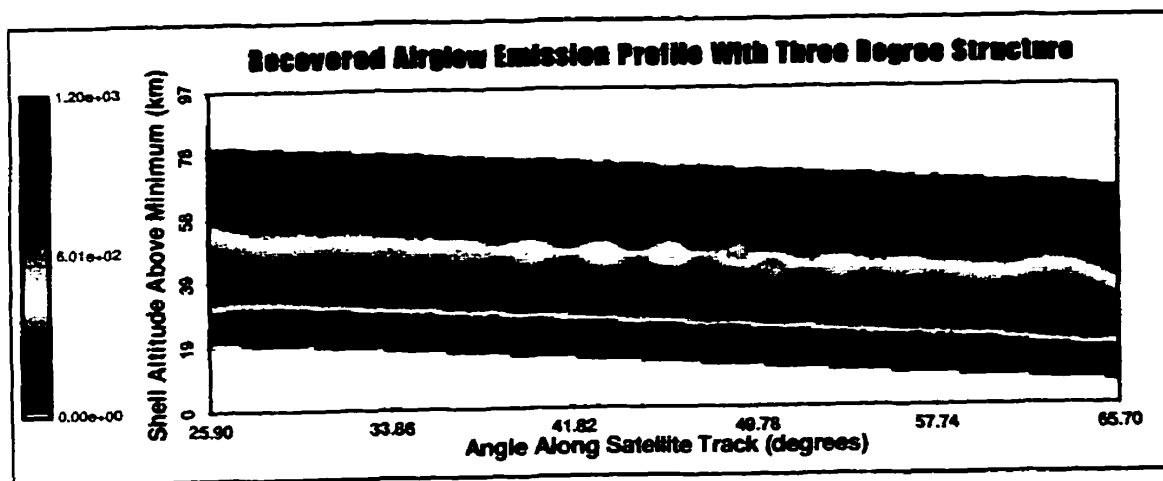
9.4.2.2 Relative Noise

Simulated observations that included five different relative noise levels were also analyzed for the different structures and observational modes discussed in Section 9.2. The signal to noise levels that were investigated ranged from 200:1 to 10:1. The two dimensional volume emission plots (kR/km) shown in Figure 9.16 illustrate the recovery for the five different signal to noise levels at a 1 Hz imaging rate. In each case, with the possible exception of the final one (Figure 9.16f), the expected three degree structure is obviously apparent. For the higher radial shells these recoveries do not contain the same large deviations as for those that contain absolute noise (Figure 9.12). This is expected as the noise levels are much smaller at the higher tangent altitudes where the measured signal is small.

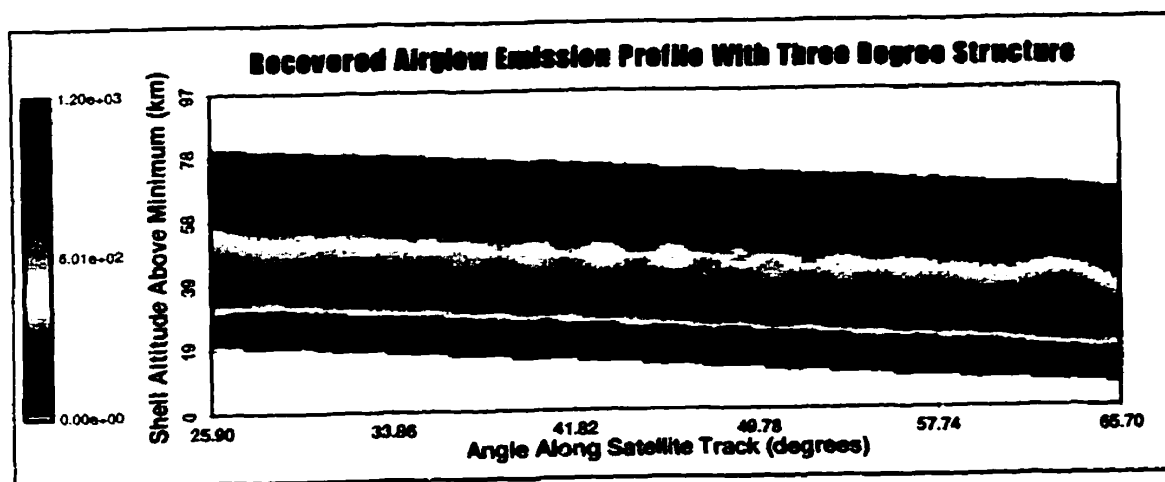
(a) Input Grid



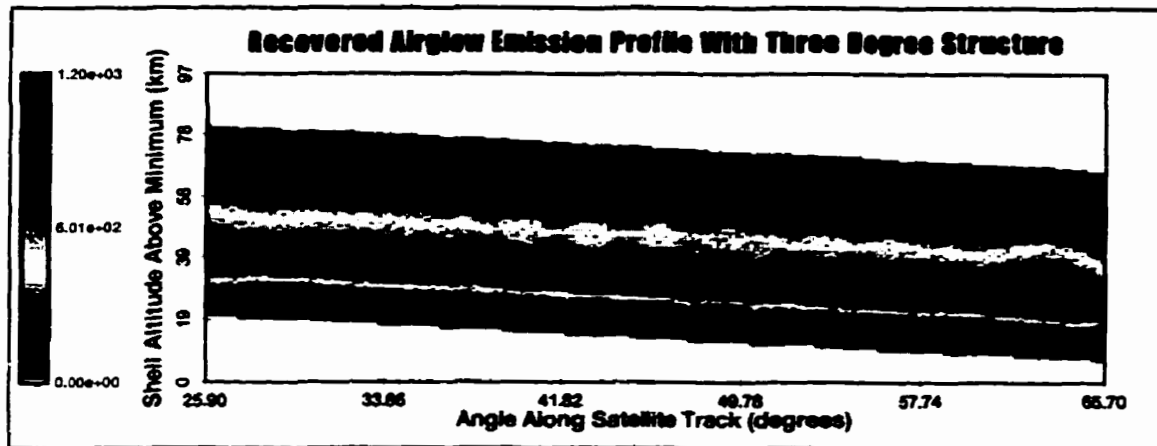
(b) S/N ratio 200:1



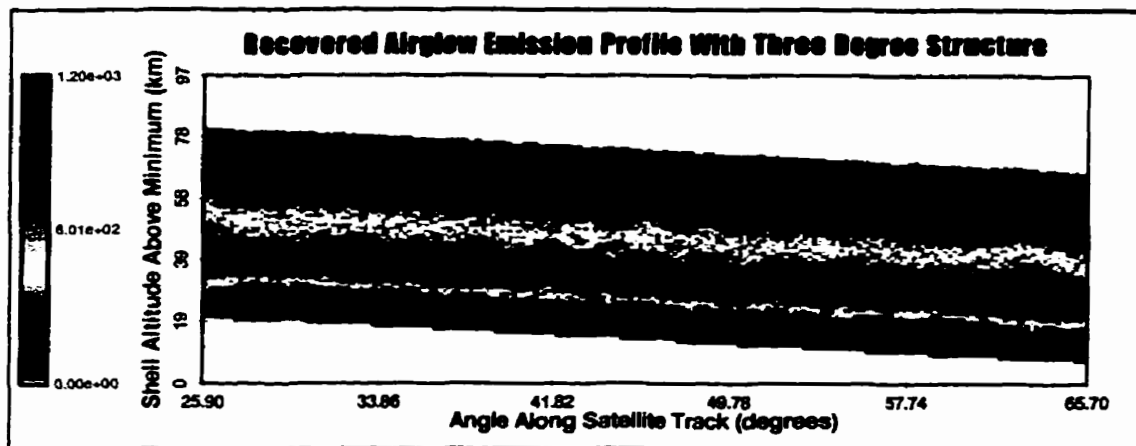
(c) S/N ratio 100:1



(d) S/N ratio 50:1



(e) S/N ratio 20:1



(f) S/N ratio 10:1

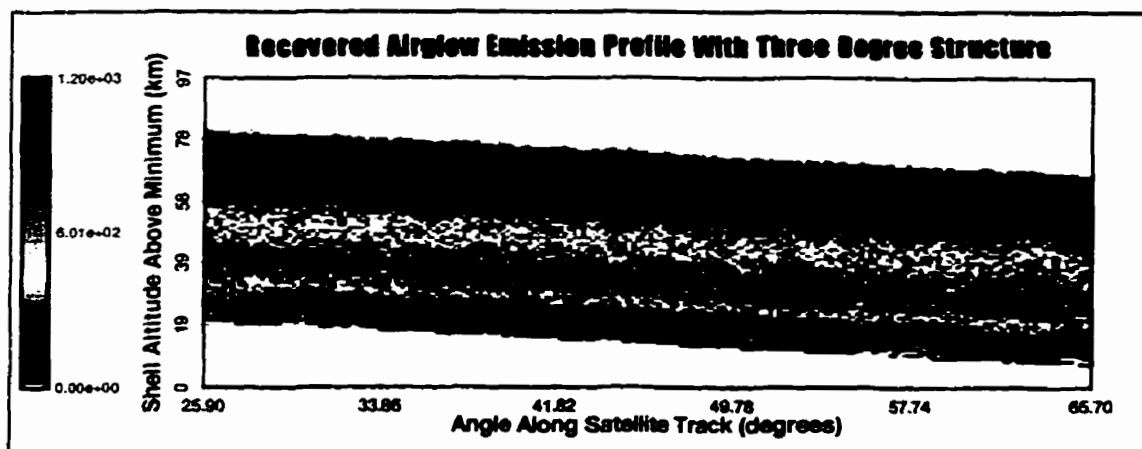
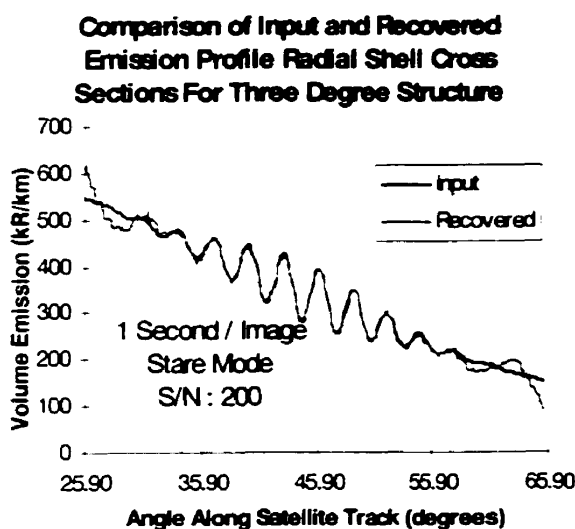
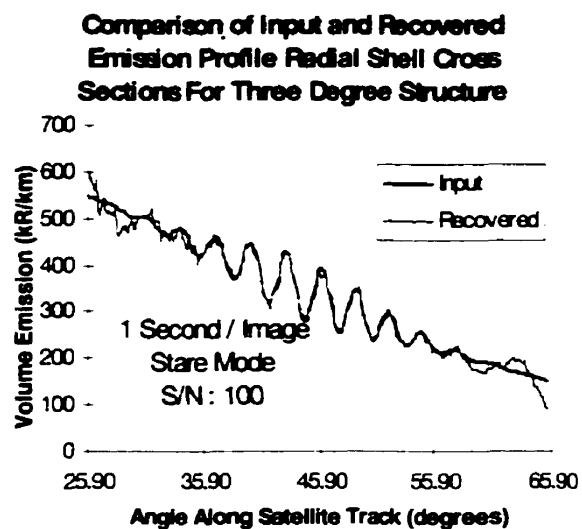


Figure 9.16: Retrieval of the three degree structure for different signal to noise levels.

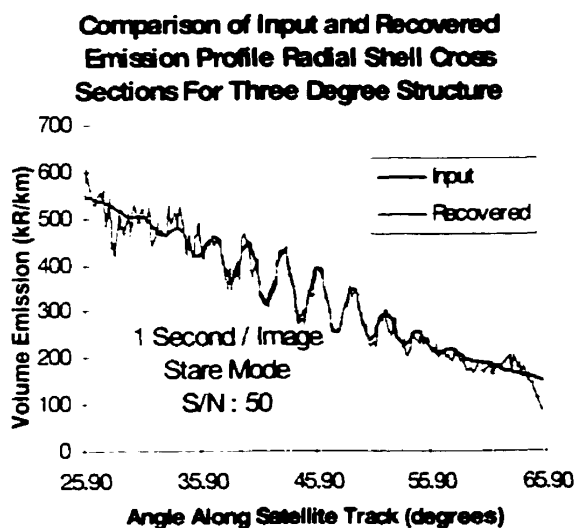
Radial shell cross sections from the two dimensional grids shown in Figure 9.16 are presented in Figure 9.17. The high signal to noise ratio plots (a and b) show very little difference between the recovered and input values. For the 50:1 signal to noise level (c) there are some differences as the high frequency random noise becomes more apparent. For the 20:1 S/N observations (d) the expected structure is still apparent, although it is partially obscured by the random noise. For the 10:1 signal to noise measurements (e) only the high frequency random fluctuations are clearly evident.



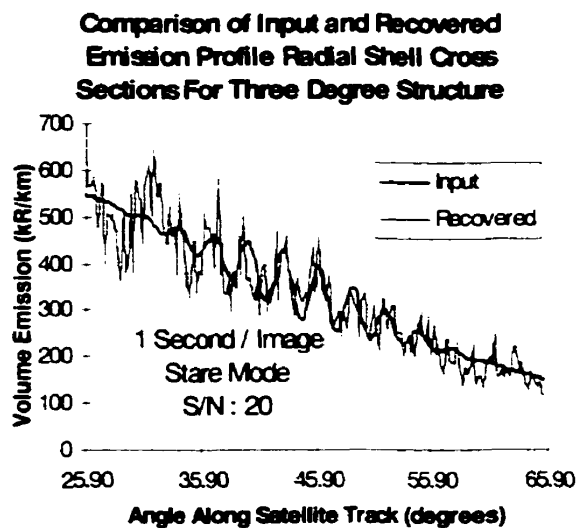
(a)



(b)



(c)



(d)

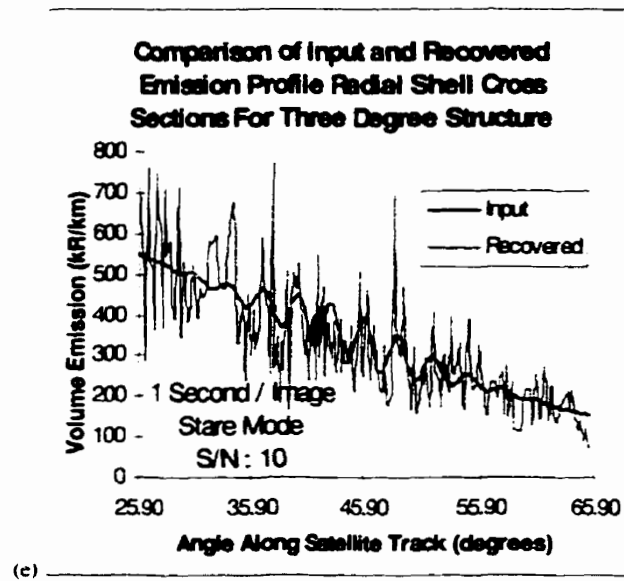
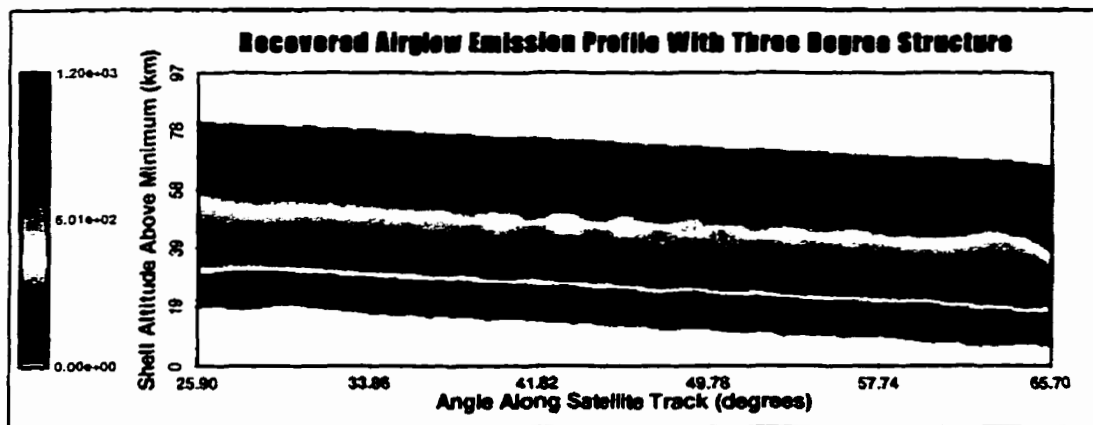


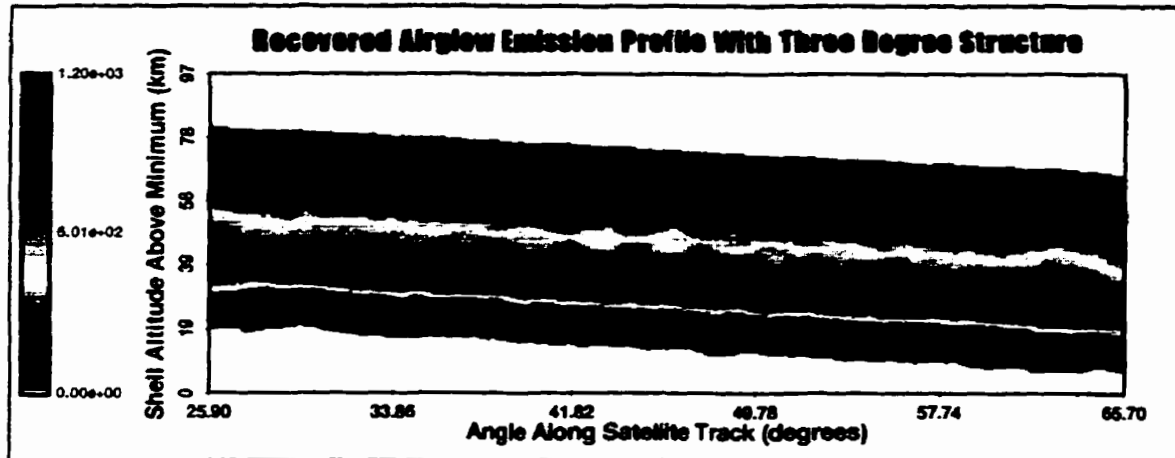
Figure 9.17: Selected radial shell cross sections for the recovery grids shown in Figure 9.16.

As for the absolute noise level retrievals a simple one element wide boxcar filter was applied to the relative noise inversions. The effect of this filter is illustrated in Figure 9.18 which shows the same but filtered recovered two dimensional plots as those shown in Figure 9.16 for S/N of 50:1, 20:1 and 10:1. In these cases the three degree structure is apparent, and even more so in the radial shell cross sections shown in Figure 9.19. Again the simple post inversion smoothing has improved the identification of the structure in the presence of a large observational noise component.

(a) S. N ratio 50:1



(b) S:N ratio 20:1



(c) S:N ratio 10:1

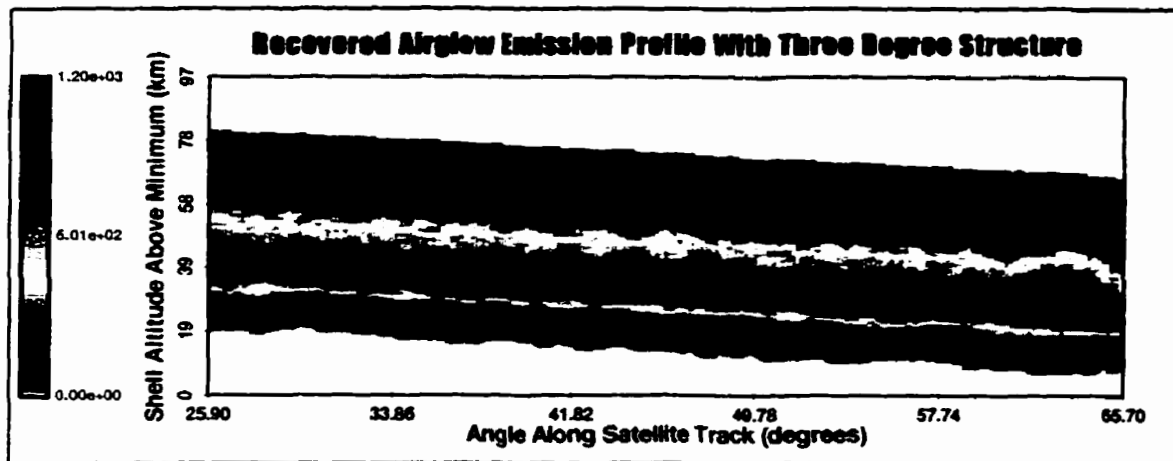


Figure 9.18: The filtered recoveries of the three degree structure for different signal to noise levels.

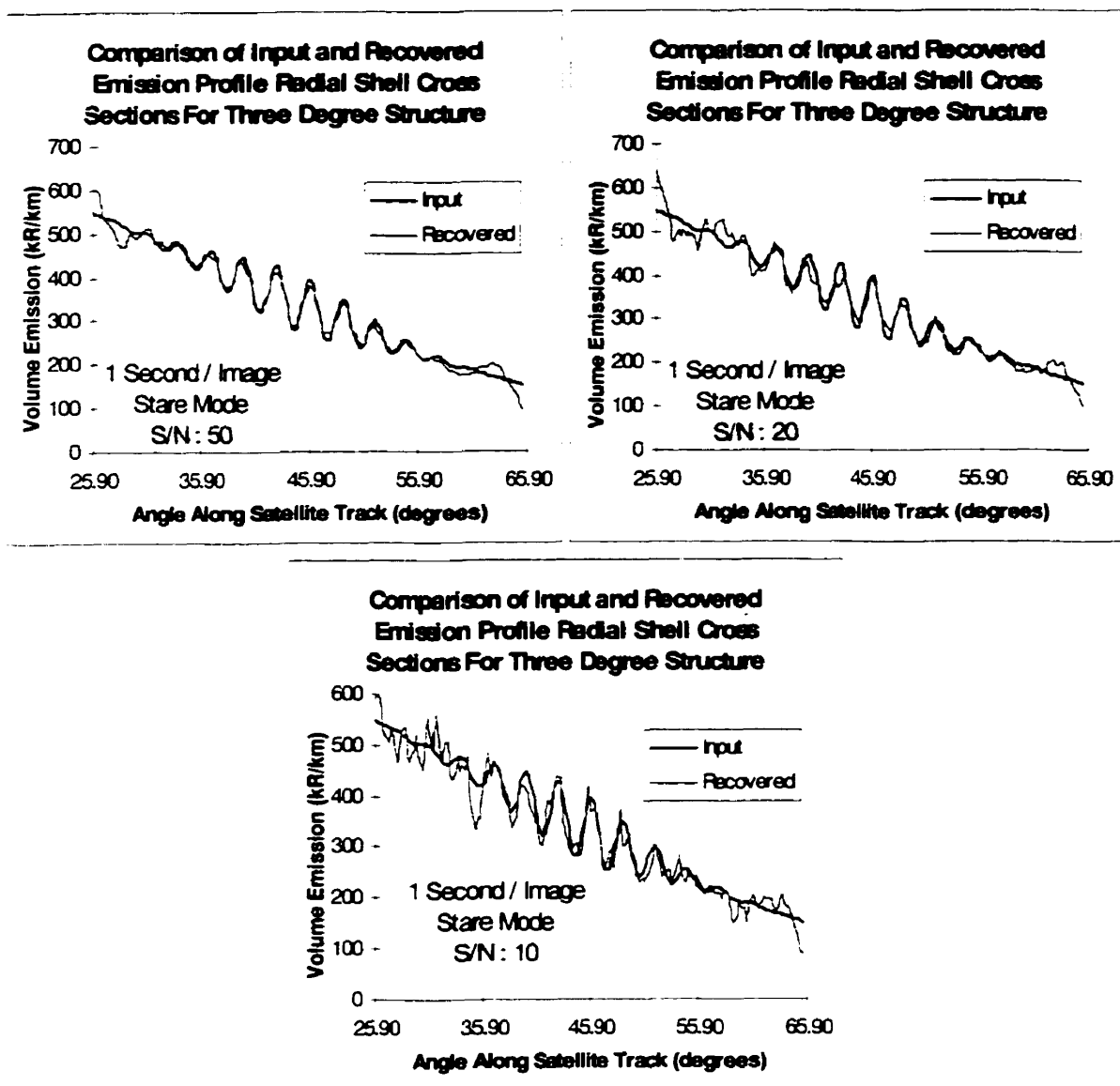
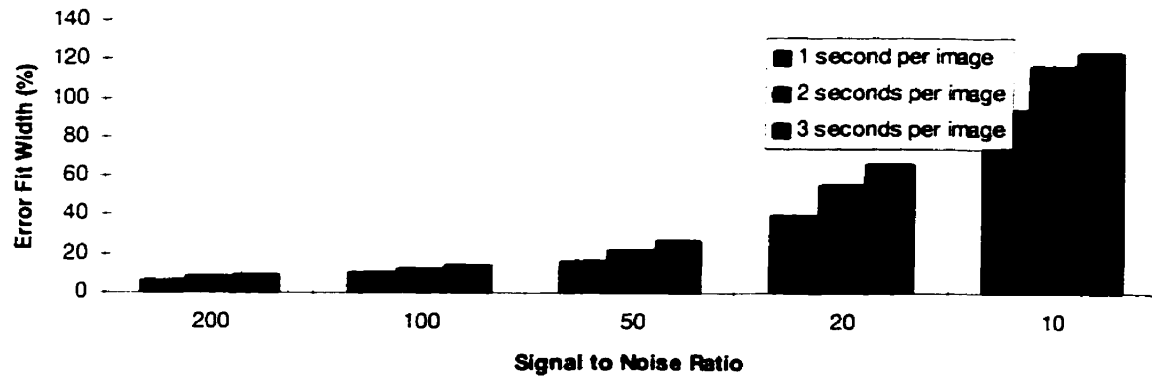


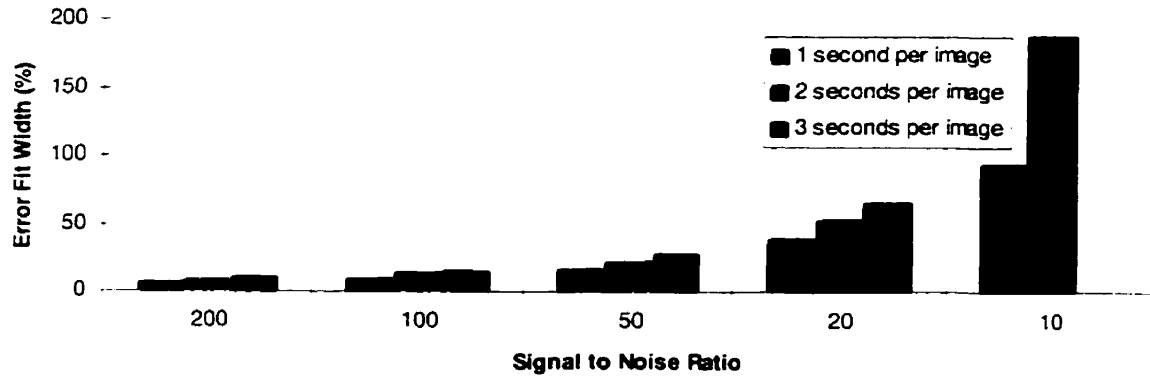
Figure 9.19: Selected radial shell cross sections from the recovery grids shown in Figure 9.18.

The error histogram widths for the set of stare mode unfiltered inversion results are given in Figure 9.20. There is the same general trend as for the absolute noise levels, shown in Figure 9.15, with faster imaging rates yielding better retrievals. The error fit width is omitted in some cases as the errors were so large that a quadratic fit to the error histogram was not appropriate (Appendix C).

Error Distribution Fits For 3 Degree Structure For Five Different S:N Levels And Three Different Imaging Rates



Error Distribution Fits For 4 Degree Structure For Five Different S:N Levels And Three Different Imaging Rates



Error Distribution Fits For 5 Degree Structure For Five Different S:N Levels And Three Different Imaging Rates

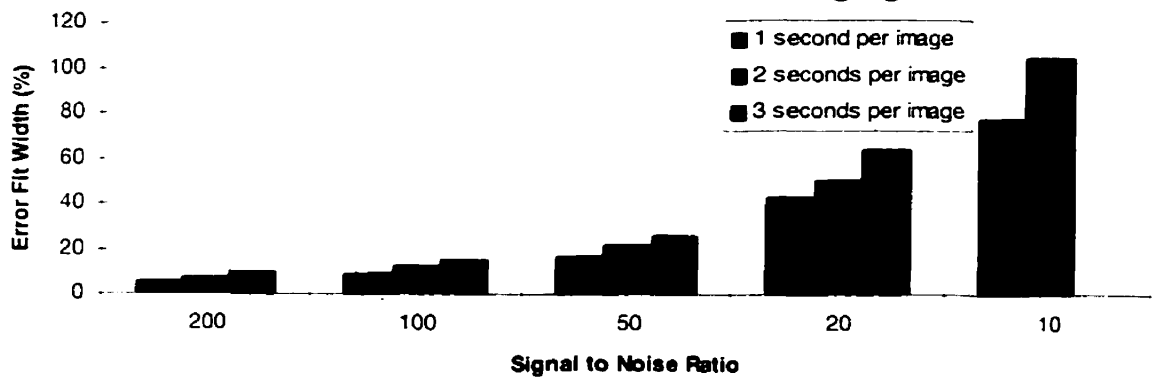


Figure 9.20: Error histogram widths for the results obtained with three different wave structures and three observational modes for five different signal to noise levels.

9.4.3 Results for Missing Images and Bad Pixels

Inversions were also made for both noisy and missing data. Six different missing image and bad pixel rates have been analyzed. These ranged from a 1% to 50% chance of bad data. For these tests each image or pixel was given the same probability of being bad. A bad pixel was considered to be dead for all images in the set.

The cross sections for retrievals made with the 2 seconds/image operational mode and with 20% missing images and 20% bad pixels are shown in Figure 9.21. Although there is no post inversion filtering it is clear that the three degree structure is resolved. The error histogram widths for the missing image and bad pixel analysis are presented in Tables 9.1 and 9.2. These results, as with those in Figures 9.15 and 9.20, clearly illustrate the effectiveness of the higher imaging rates.

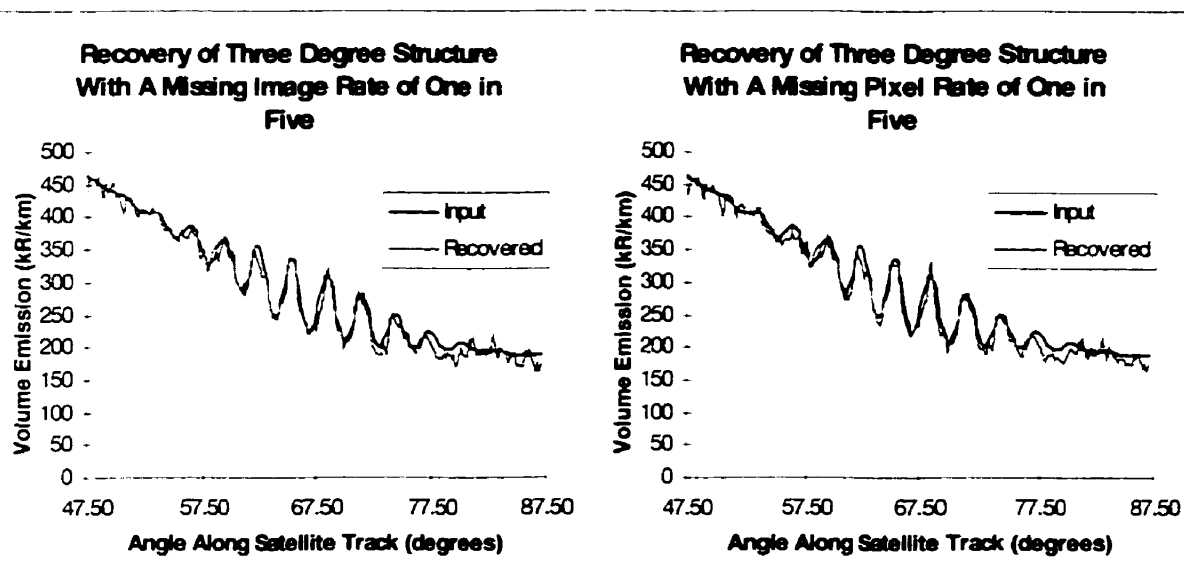


Figure 9.21: Selected radial shell cross sections from retrievals made with missing images and pixels.

**Error Histogram Halfwidths
(%)**

	3° Structure	4° Structure	5° Structure
1 image in every 100			
<i>1 Second / Image</i>	5.57	4.85	5.04
<i>2 Seconds / Image</i>	6.78	7.50	6.62
<i>3 Seconds / Image</i>	8.39	8.01	8.36
1 image in every 50			
<i>1 Second / Image</i>	5.12	4.91	4.62
<i>2 Seconds / Image</i>	6.83	6.79	6.47
<i>3 Seconds / Image</i>	8.38	7.74	8.15
1 image in every 20			
<i>1 Second / Image</i>	5.34	5.45	5.36
<i>2 Seconds / Image</i>	6.87	7.43	6.90
<i>3 Seconds / Image</i>	8.61	7.63	8.21
1 image in every 10			
<i>1 Second / Image</i>	5.46	5.85	5.26
<i>2 Seconds / Image</i>	6.93	7.81	7.15
<i>3 Seconds / Image</i>	9.36	9.01	8.99
1 image in every 5			
<i>1 Second / Image</i>	6.91	7.30	5.73
<i>2 Seconds / Image</i>	7.69	7.56	7.19
<i>3 Seconds / Image</i>	10.34	8.90	9.21
1 image in every 2			
<i>1 Second / Image</i>	9.37	10.15	8.15
<i>2 Seconds / Image</i>	12.02	10.89	10.80
<i>3 Seconds / Image</i>	12.56	12.36	17.40

Table 9.1: Error histogram halfwidths for the retrieval of different wave structures with different observational modes and six different missing image probabilities.

Error Histogram Halfwidths
(%)

	3° Structure	4° Structure	5° Structure
1 pixel in every 100			
<i>1 Second / Image</i>	6.28	5.09	4.87
<i>2 Seconds / Image</i>	6.56	6.77	6.22
<i>3 Seconds / Image</i>	8.27	7.86	9.23
1 pixel in every 50			
<i>1 Second / Image</i>	5.29	5.31	6.20
<i>2 Seconds / Image</i>	7.96	6.77	7.26
<i>3 Seconds / Image</i>	8.43	7.73	8.15
1 pixel in every 20			
<i>1 Second / Image</i>	5.06	4.76	5.70
<i>2 Seconds / Image</i>	8.18	6.73	6.42
<i>3 Seconds / Image</i>	9.29	8.22	9.03
1 pixel in every 10			
<i>1 Second / Image</i>	6.70	8.36	6.71
<i>2 Seconds / Image</i>	10.98	9.49	9.91
<i>3 Seconds / Image</i>	10.63	7.63	11.21
1 pixel in every 5			
<i>1 Second / Image</i>	8.97	7.45	5.82
<i>2 Seconds / Image</i>	9.96	8.16	15.54
<i>3 Seconds / Image</i>	16.88	11.82	13.94
1 pixel in every 2			
<i>1 Second / Image</i>	28.08	22.32	40.88
<i>2 Seconds / Image</i>	11.23	37.89	27.12
<i>3 Seconds / Image</i>	18.33	28.41	31.16
every second pixel			
<i>1 Second / Image</i>	23.36	18.99	20.08
<i>2 Seconds / Image</i>	22.00	19.91	20.63
<i>3 Seconds / Image</i>	24.74	24.34	25.56

Table 9.2: Error histogram halfwidths for the retrieval of different wave structures with different observational modes and seven different bad pixel probabilities.

9.5 Scale Size Experiment Conclusions

The results presented in this chapter have shown the scale sizes of wavelike structures that can be identified and fully resolved. The effects of observational noise and missing, or bad, data on the tomographic technique have also been investigated. It has been shown that a two degree wave structure along the satellite track can be identified, although not fully resolved, and that a three degree structure can be fully resolved under even extreme observational noise conditions. The three degree structure represents approximately 300 km (in the horizontal direction) along the satellite track.

In the presence of observational noise the results of the tomographic retrievals are not as good. The error histogram widths are larger when the observations contain noise. It was shown with a simple post inversion filtering that the effects of noise are localized, and that the inversion process is capable of handling even very large amounts of random noise with no systematic effects.

The analysis has also illustrated the need for an appropriate imaging rate. It was shown that for every noise and error condition tested that the higher imaging rates gave an improved inversion. This improvement is due to the internal averaging mechanism that is contained within the tomographic algorithm. It has also been shown that the algorithm is effective for the Odin/OSIRIS instrument operating in the standard operational mode, a 0.5 Hz imaging rate.

CHAPTER X

OSIRIS ON ODIN

10.1 Introduction

OSIRIS is part of the Canadian contribution to the Odin satellite program, a joint Sweden-Canada-France-Finland mission to investigate ozone depletion mechanisms at high latitude, particularly in the Northern Hemisphere, and to search for water and molecular oxygen in star-formation regions. The OSIRIS (Optical Spectrograph and Infrared Imaging System) instrument was developed in Canada by Routes Inc. in association with the University of Saskatchewan, York University, the University of Calgary and Trent University. The primary function of the OSIRIS instrument is to make measurements that relate to ozone depletion chemistry in the atmosphere. The Odin spacecraft also includes a sub-millimeter radiometer that will be used to make simultaneous atmospheric measurements that also relate to ozone depletion chemistry, as well as conduct an astronomical search for water and molecular oxygen.

Odin is scheduled for launch early in the year 2000 and will be inserted into a sun-synchronous dusk-dawn orbit, inclination 97° , at an altitude of approximately 600 km. A schematic representation of Odin in its orbit is given in Figure 10.1. It is expected that the Odin mission will have a two year lifetime, although this is dependent on solar activity. The work described in this chapter is related to one component of OSIRIS, the Infrared Imaging System, and shows how the tomographic technique described in previous chapters can be used to retrieve oxygen infrared atmospheric band ($a^1\Delta_g - X^3\Sigma_g^-$) volume emission profiles that are an important component of ozone chemistry in the mesosphere.

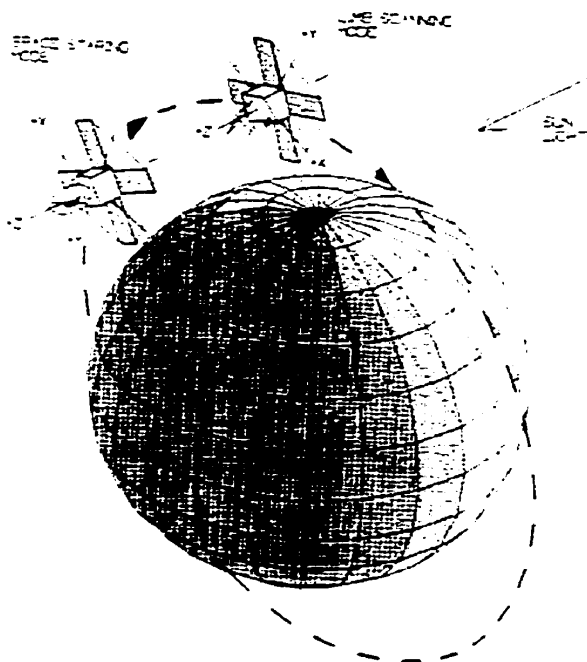


Figure 10.1: A representation of the Odin spacecraft in its sun-synchronous orbit.

10.2 Introduction to OSIRIS

As noted OSIRIS is actually two separate, but related, instruments. The Optical Spectrograph component uses a diffraction grating and a CCD to simultaneously measure over the wavelength range from 280 nm to 800 nm (1 nm resolution) along a single tangent altitude line of sight. The slit dimension mapped on to the limb is 1 km by 18 km (height by length). The other component is an InfraRed Imaging System that provides vertically extended images of the atmosphere that can be used with the tomographic technique.

The OSIRIS infrared imager (Figure 10.2) has two channels that make measurements of the airglow emission from the oxygen infrared atmospheric band, near 1.27 μm , and a third channel that measures near 1.53 μm . The two oxygen band channels have 10 nm Gaussian passbands and are centred at 1.266 μm and 1.273 μm . It is the measurements made with these three channels, and specifically those made with the oxygen infrared

atmospheric band channels, that will be used with the tomographic algorithm to retrieve the true two-dimensional volume emission profile.

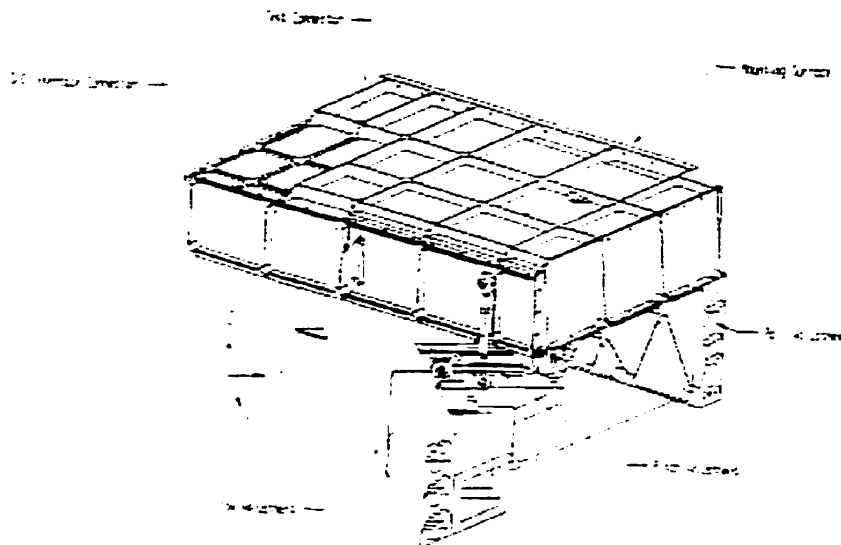


Figure 10.2: The OSIRIS instrument. The upper module is the electronics unit while the lower module is the optical unit. The three entrance apertures for the InfraRed Imaging System are in the bottom left corner.

The Infrared Imaging System consists of three separate telescopes, one for each passband with its own entrance aperture (23 mm diameter), a Zinc Selenide (ZnSe) plano-convex lens, a narrowband interference filter and a linear InGaAs detector array. The design of the three channels is such as to maximize the length of the front end baffles. The f-number for each channel is 6.2 and the boresights of the three channels are parallel. The interference filter is mounted directly on to the IR detector and acts as a window for the detector. In the region between the lenses and the filter/detector combinations there is a shutter mechanism that has the dual role of shutter and diffuse reflector for a calibration source.

Each InGaAs detector has 128 photo-diodes, or pixels, with 20 pixels masked off at one end that provides a dark reference for each image. The detector diodes act as current sources, with the integrated current being proportional to the total incident light plus the dark current, and are read out by a self scanning multiplexer. The nominal (-40°C) operating temperature for each detector is achieved with a Thermo-Electric Cooler

(TEC). At this temperature the dark current contribution to the measured signal is insignificant. The imager sensitivity in each channel is 50 kR/pixel/s.

Each infrared channel in OSIRIS is optimized for a 40 km vertical field of view, each pixel has a field of view, mapped on to the limb, of 1km vertical by 2 km horizontal. However, as each InGaAs detector has 128 pixels, with 20 masked off, the infrared channels collect light over a total field of view of nearly 110 km. Thus the infrared channels make 108 simultaneous measurements at different tangent altitudes.

The work presented in this chapter is concerned with the modifications that are needed to the tomographic algorithm for the retrieval of the oxygen infrared atmospheric band two dimensional profiles from the OSIRIS measurements.

10.3 Introduction to the Oxygen Infrared Atmospheric Band

The oxygen infrared atmospheric band emission spectrum results from the spin forbidden magnetic dipole transition between the excited $O_2(a^1\Delta_g)$ state and the $O_2(X^3\Sigma_g^-)$ ground state. An extended discussion of the emission spectrum is presented in Appendix E and a sample synthetic emission spectrum is shown in Figure 10.3a. This spectrum includes the 135 most intense lines of the emission band and represents the emission from an altitude of 40 km, where the rotational temperature is close to the assumed value of 240 K.

However, as the infrared atmospheric band emission involves a transition to the ground state absorption by the atmospheric column between the source and the detector can cause significant differences between the observed and emitted spectra. These differences are readily apparent in Figure 10.3b which shows the observed spectrum for a satellite borne instrument viewing the 40 km emission along a line of sight that is tangent to it. The integrated emission band signal has been normalized to unity and only 0.41, or 41%, of the total emission reaches the detector.

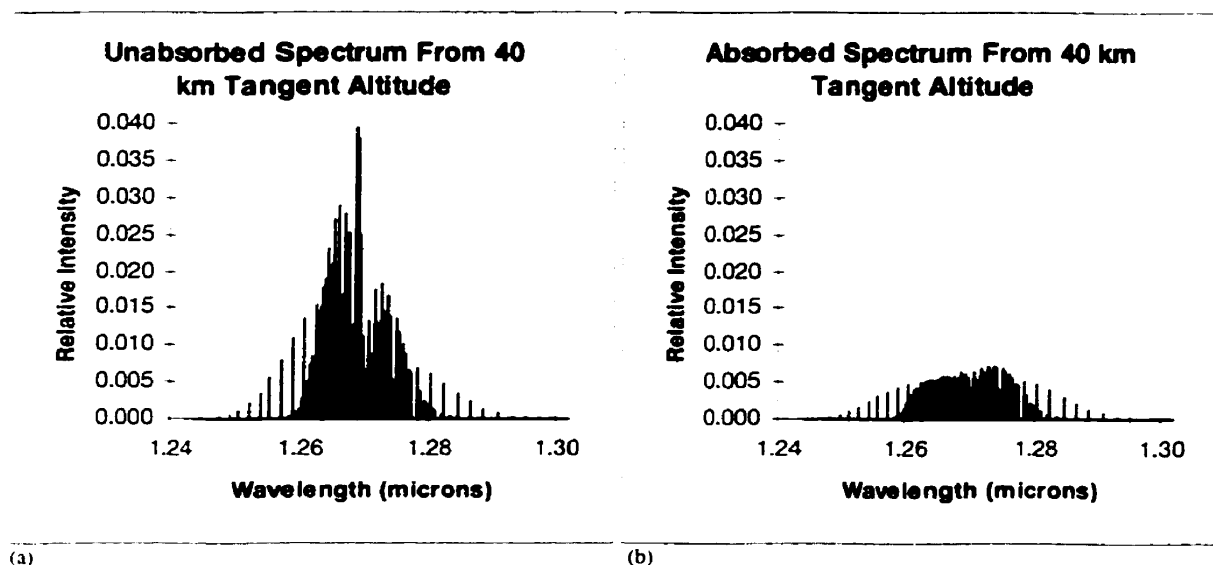


Figure 10.3: *The oxygen infrared atmospheric band emission spectrum as emitted at 40 km (a) and the same spectrum as seen by a satellite borne instrument looking along a 40 km tangent altitude line of sight (b).*

The determination of the attenuation of the spectrum through self absorption requires a line by line calculation that includes the effects of the individual line shapes. This is discussed in Appendices E and F. The attenuation of a single line from the QQ branch, with $J' = J'' = 3$, is shown in Figure 10.4. Typically the central region of the line is strongly absorbed and exhibits self-reversal.

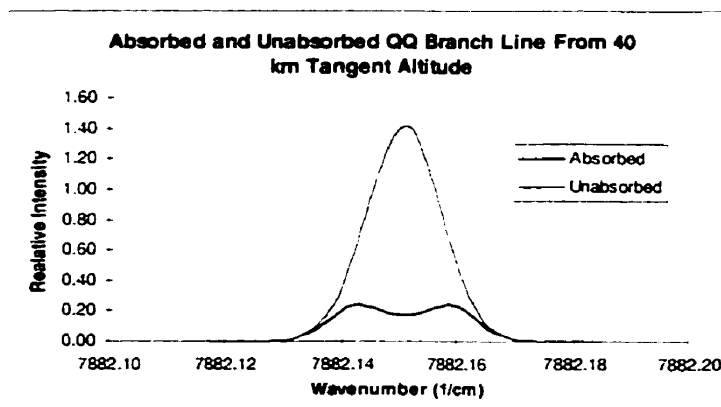


Figure 10.4: *The QQ branch line, with $J' = J'' = 3$, for the two oxygen infrared atmospheric band spectra shown in Figure 10.3.*

10.4 Changes to the Tomographic Technique that are Required for Odin/OSIRIS

The effects of absorption and the Odin/OSIRIS instrument require modification of the tomographic retrieval technique to recover the oxygen infrared atmospheric band volume emission rate profiles. The major change to the technique is in the forward model that estimates the observations based on the current volume emission rate solution. There are some other minor changes to the observation weighting filter due to these absorption and instrument effects but these have been shown to be insignificant.

10.4.1 Effects of the Optical Filters and Absorption of the Oxygen Infrared Atmospheric Band

The emitted $O_2(a^1\Delta_g - X^3\Sigma_g^-)$ spectrum is not the one that is measured by the infrared imager. The spectrum is absorbed along the line of sight between the emitting region and the detector and is also limited by the optical filter in front of the detector. The result is that the measured intensity is significantly less than that emitted. The effect of absorption was introduced in Section 10.3 and the effect of the optical filter is illustrated in Figure 10.5. The two spectra shown in this figure are the same as those in Figure 10.3 but now include the Odin/OSIRIS 1.266 μm filter (Section 10.2). In each case the filter passband has been normalized to the scale of the shown spectrum with unity transmission corresponding to the intensity of the strongest line in the spectrum. The actual peak transmission of the OSIRIS filter is 76%.

The oxygen infrared atmospheric band capture fraction (*i.e.* the fraction of the emitted spectrum that is transmitted by the filter) for the unabsorbed emission, at a rotational temperature of 240 K, is 0.56 (56%) for the 1.266 μm filter in OSIRIS. The band capture fraction is reduced when there is absorption, for a 40 km tangent point emission the capture fraction is 0.19 (19%).

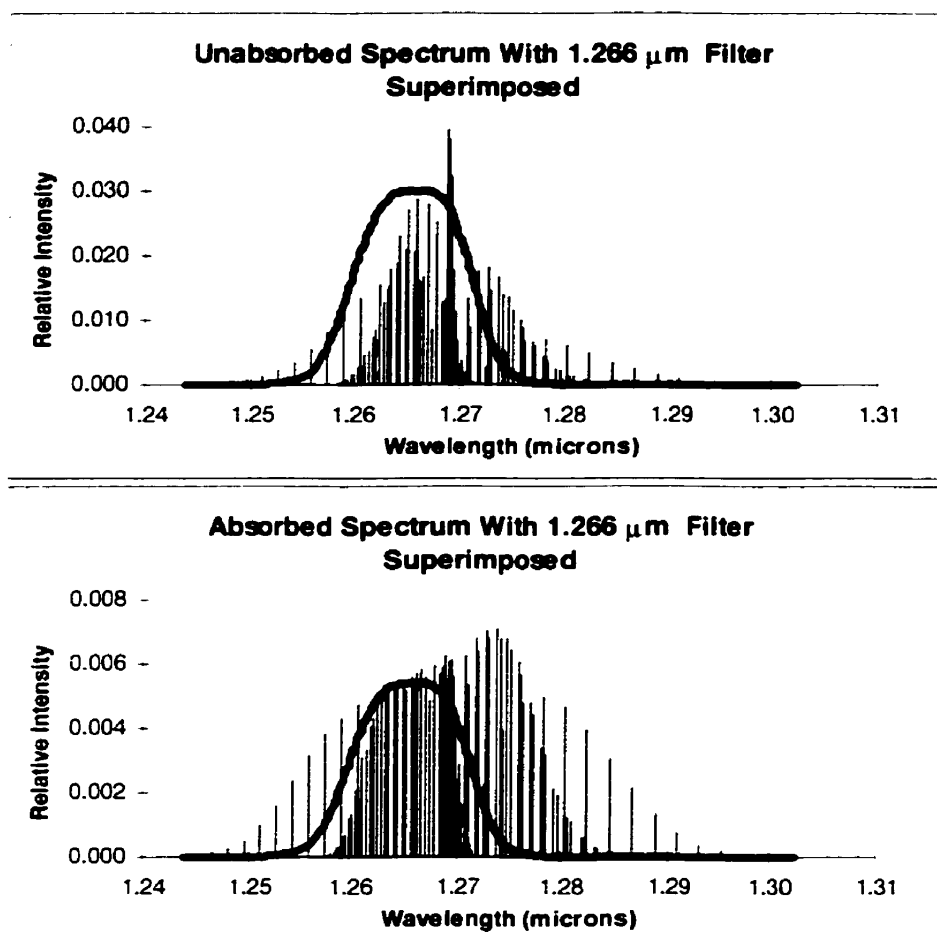
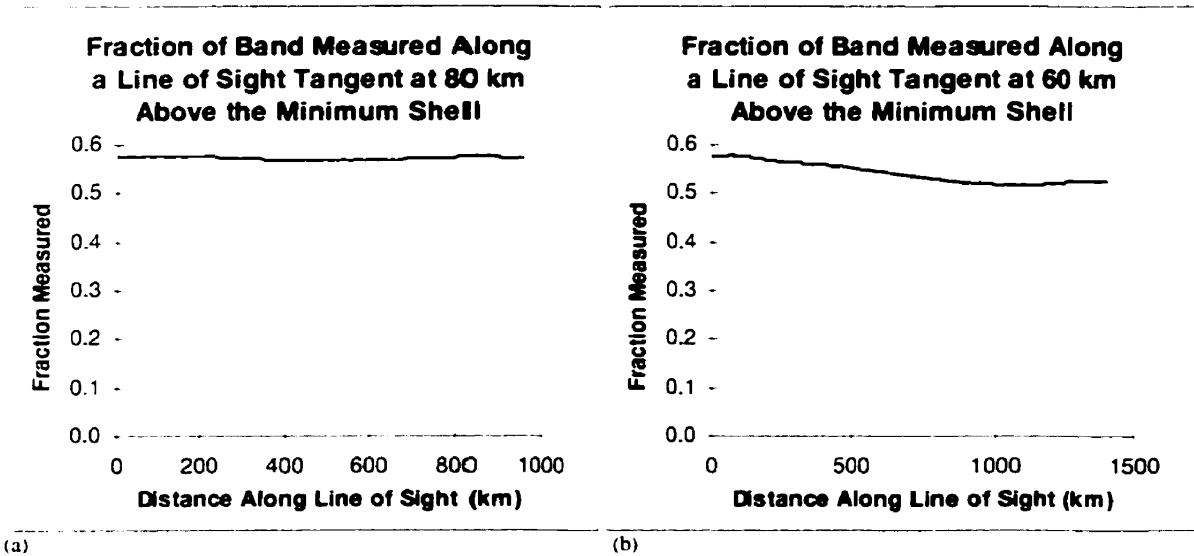


Figure 10.5: The unattenuated and the absorbed spectra (Figure 10.3) with the 1.266 μm filter superimposed.

As the absorption of the oxygen infrared atmospheric band depends on the overlying atmospheric column the band capture fraction, for emission from a particular point in the atmosphere, depends on the viewing geometry. Thus, the different absorptions associated with different lines of sight must be properly accommodated in the tomographic algorithm used with OSIRIS. The effects of these different absorptions are shown in the various plots in Figure 10.6. These plots indicate the infrared atmospheric band capture fraction as a function of distance along the line of sight for four different tangent altitudes. A complete description of the calculations for the band capture fractions is given in Appendix F. The zero on the x -axis in each of these plots corresponds to the point where the line of sight enters the highest radial shell. For a line of sight that is tangent at 80 km above the minimum shell altitude (Figure 10.6a) the

band capture fraction is nearly constant at 58%. The deviations from a uniform flat response are due to the different rotational temperatures along the line of sight. For a tangent altitude 60 km above the minimum shell (Figure 10.6b) there is some absorption, again the deviations from a monotonically decreasing curve are due to temperature differences along the line of sight.

The plots shown in Figure 10.6c and 10.6d are for tangent altitudes where there is significant absorption even on the near side of the tangent point. The difference between the measured signal at the tangent point and that associated with the spectra shown in Figures 10.3 and 10.5 (for the 40 km emission viewed along the 40 km tangent altitude line of sight) is because the tangent altitudes in Figure 10.6 are for the spherical grid. In this case 40 km above the minimum shell altitude does not correspond to an altitude of 40 km above the surface of the earth. The band capture fraction associated with the 20 km line of sight minimum altitude (Figure 10.6d) indicates that all emission that originates on the far side of the tangent point is completely absorbed. This implies that only scattered sunlight is transmitted from these lower altitudes and so allows the complete separation of the scattered sunlight signal and the oxygen emission. Hence, the retrieval of scattered sunlight from the OSIRIS measurements can verify the atmospheric temperature climatology that is used in the calculation of the atmospheric transmission (Appendix F).



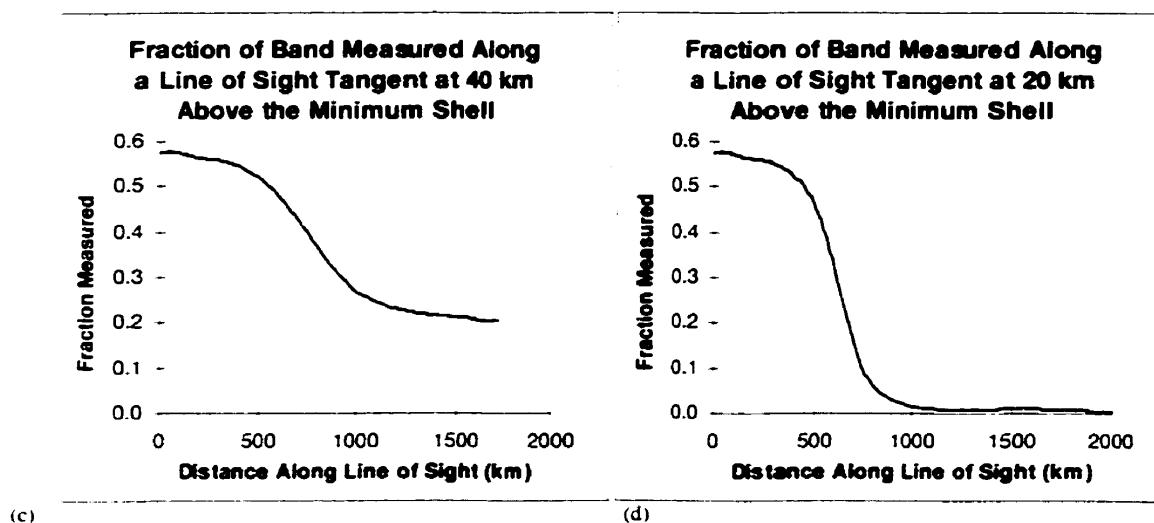


Figure 10.6: The band capture fractions for different lines of sight tangent at various radial distances in the two dimensional recovery grid.

10.4.2 Changes Required to the Tomographic Equations

It has been indicated above that a knowledge of the absorption of the oxygen infrared atmospheric band emission is essential if the tomographic technique is to recover the true oxygen emission at each point in the grid. The band capture curves, like those shown in Figure 10.6, give the detected fraction of the signal from any point along the line of sight. For an observation i , the band capture fraction of the signal, from volume emission element j , can be determined if the distance along the line of sight to element j is known; these band capture fractions are denoted as α_{ij} .

The tomographic technique presented in Chapter 5 must therefore be modified to account for the self-absorption of the signal. This requires that equation 5.14 be rewritten to include the variation in the band capture fraction along each line of sight. For the oxygen infrared atmospheric band the equation becomes

$$\sum_j \alpha_{ij} L_{ij} V_j^{(n-1)} = O_{i_{ov}}^{(n-1)}. \quad [10.1]$$

This equation represents the estimate of the observation based on the volume emission grid, the atmospheric transmission and the effect of the optical filter. The term α_{ij} is the band capture for the volume emission cell j along the i^{th} line of sight.

The actual iterative equation used in the modified tomographic technique (equation 10.2) is unchanged from the case where there is no attenuation (equation 5.15).

$$V_j^{(n)} = V_j^{(n-1)} \sum_i \left(\frac{O_i}{O_{i_{cr}}^{(n-1)}} \beta_{ij} \right) \quad [10.2]$$

Thus the inversion technique does not change, only the model for the $(n-1)^{th}$ estimate and the observation weighting filter are modified. The final calculated volume emission values, V_j , are the true band emission and not the apparent volume emission.

10.4.3 Effect on the Observation Weighting Filters

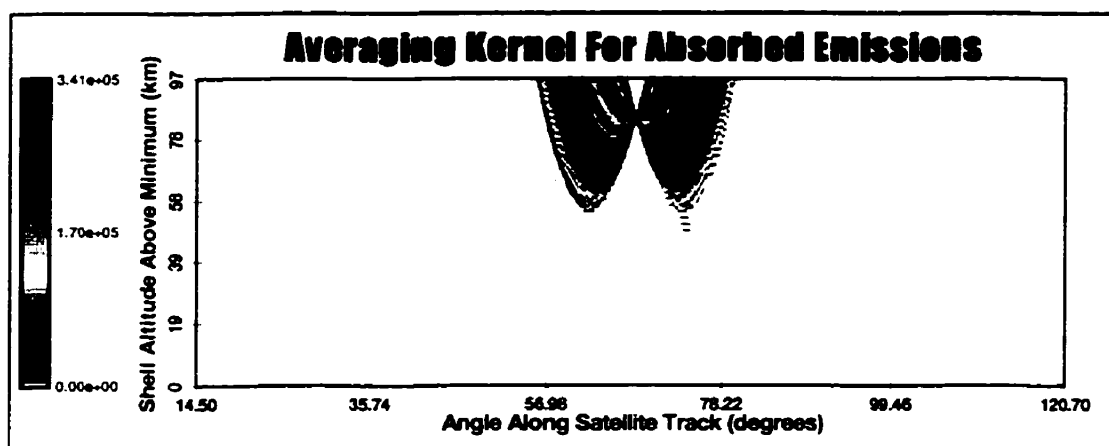
While the analytic form of equation 10.2 is identical to that of equation 5.15 the weighting factor β_{ij} (Chapter 7) is modified. The corrected weighting factor, which includes the absorption factor α_{ij} , is given by equation 10.3,

$$\beta_{ij} = \frac{(\alpha_{ij} L_{ij})^m}{\sum_i (\alpha_{ij} L_{ij})^m}. \quad [10.3]$$

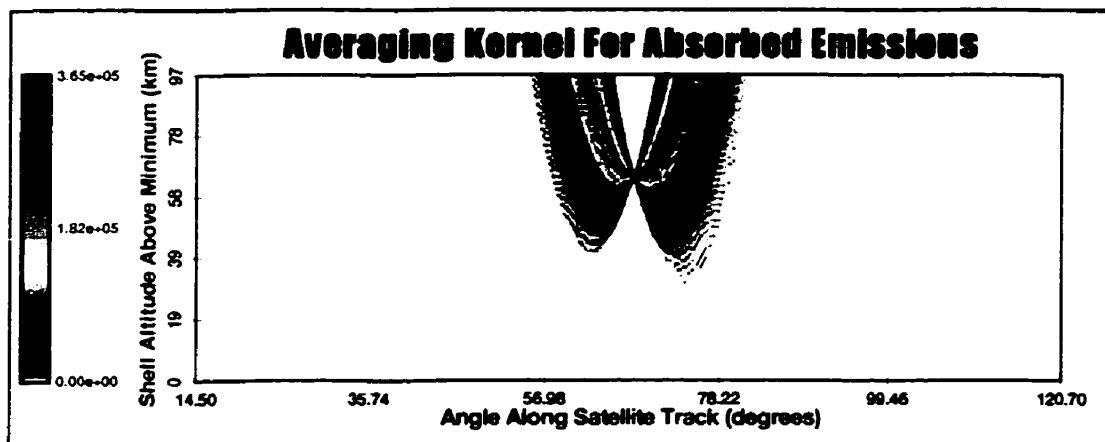
The result of this absorption correction is to change the observation weighting filters and, therefore, the averaging kernels. However, the effect is limited and has little impact on the tomographic inversion as the observation weighting filters are only significantly modified for those cells at the lowest altitudes.

The averaging kernels defined through equation 10.3 with the power $m = 5$ (Section 7.4.2) for central cells, at four different radial shell distances, are shown in Figure 10.7. The image rate for this data is 0.5 Hz. For the cell at 85 km above the minimum shell the averaging kernel (Figure 10.7a) is almost symmetric. This is expected as there is no significant absorption at these altitudes. Even at 65 km above the minimum shell altitude the averaging kernel (Figure 10.7b) is nearly symmetric, although there is a slight decrease in weight on the left hand side of the cell. Note that for the angle of the cells of interest in Figure 10.7 the minimum shell altitude corresponds to approximately 24 km above the surface of the Earth.

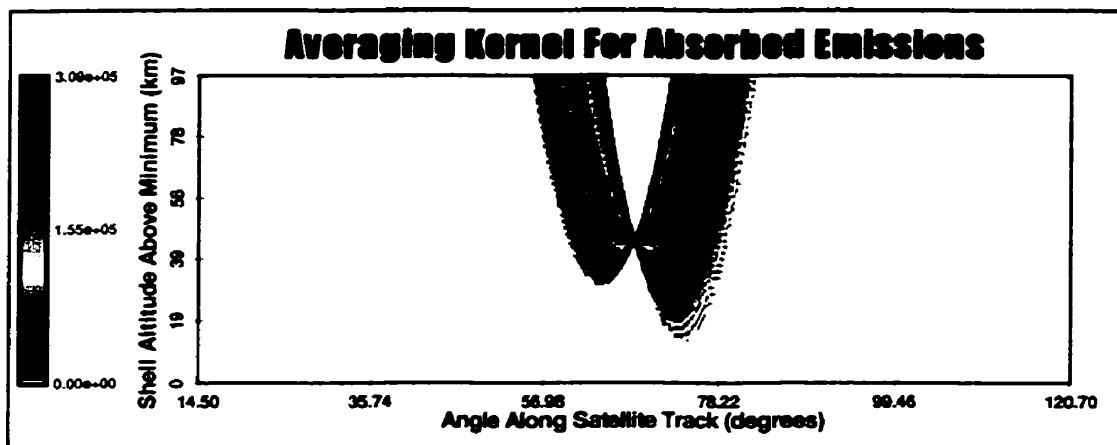
For the plots shown in Figure 10.7 the lines of sight (from the left of the cell of interest) that are ascending through the cell of interest are tangent at a lower altitude before the cell of interest. Therefore, for these observations there is significant absorption of the emission from the cell and so the $\alpha_{ij} L_{ij}$ values are smaller. These lower values imply that the cells intersected by the observations have less significance in the weighted average term. Hence, the averaging kernel is asymmetric. This asymmetry is particularly apparent in Figure 10.7 (c) and (d) where the cell of interest is quite low in the atmosphere. In these cases there is significant absorption and the averaging kernel neglects those observations (and the cells they sample) that are tangent well before the cell of interest.



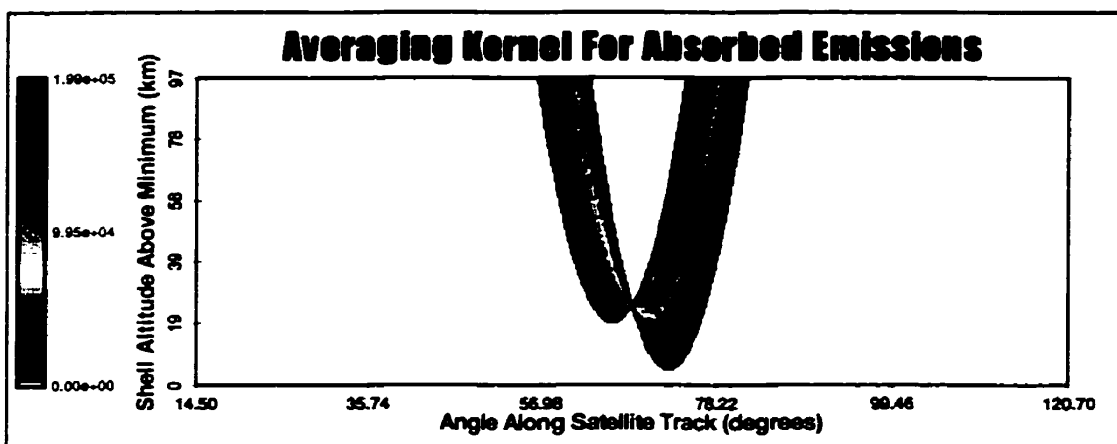
(a)



(b)



(c)



(d)

Figure 10.7: The averaging kernels for absorbed emissions at shell altitudes of 85 km (a), 65 km (b), 45 km (c) and 25 km (d) above the minimum. The weighting factor exponent m is equal to 5.

The effect of absorption of $O_2(a^1\Delta_g - X^3\Sigma_g^-)$ on the observation weighting filters is shown in Figure 10.8. Again the weighting factor exponent is 5 and the data are from the same inversion set as used for Figure 10.7. The observation weighting filter shown in Figure 10.8a has the same nearly flat uniform region, that corresponds to *Angle-Angle* intercepts, that is seen when the emissions are not absorbed (Figure 7.6c). The deviation from the flat uniform region in the envelope is due to the variations in the emission temperature along the line of sight. It should be noted that this temperature effect impacts the weighting filter in the opposite sense to that due to absorption.

The plot that corresponds to a tangent altitude of 65 km above the minimum shell (Figure 10.6b) begins to show the effects of absorption on the weighting filter. Those observations that are tangent before the cell of interest, *i.e.* lines of sight that are ascending through the cell of interest, have a smaller weight than those lines of sight that are tangent after the cell of interest. This absorption effect on the weighting filter envelope is clearly apparent in the plots for the tangent altitudes 45 and 25 km above the minimum shell altitude (Figures 10.8c and 10.8d). Although these weighting filter envelopes are different from their unabsorbed counterparts (Section 7.5) their shapes, except for the lowest altitudes where there is significant absorption, are relatively unchanged. It should be noted that the shell altitudes are 24 km lower than the altitude above the surface of the Earth at the angle of interest.

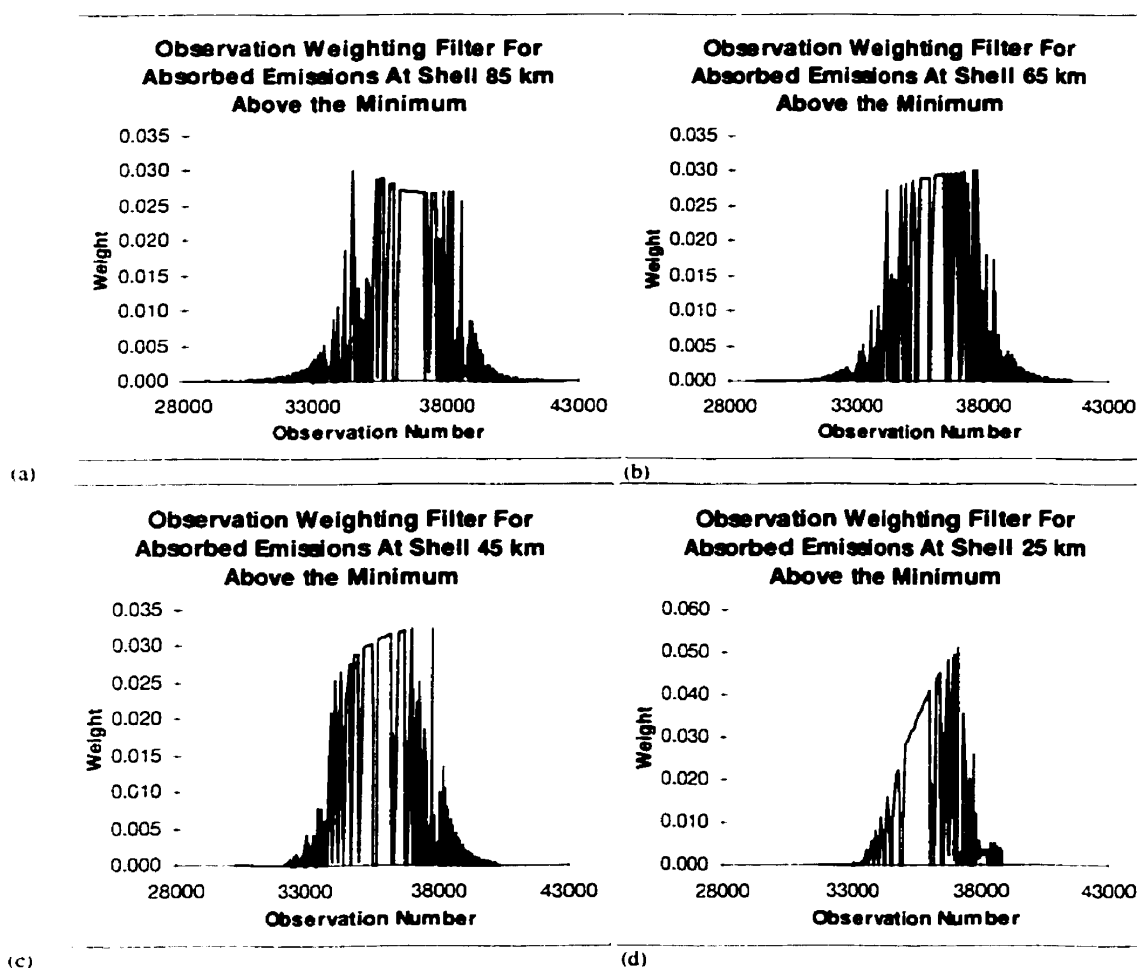


Figure 10.8: The observation weighting filters (for the absorbed emissions) at shell altitudes 85 km (a), 65 km (b), 45 km (c) and 25 km (d) above the minimum shell altitude.

10.5 The Need for the Absorption Correction

As noted in Section 10.4 there is significant absorption of the oxygen infrared atmospheric emission due to the overlying atmospheric column. The effect of the absorption is illustrated in Figure 10.9 which shows a limb profile in the presence and absence of absorption. The unabsorbed observations were simulated with the simple discrete summation for each line of sight according to equation 10.4,

$$O_i = \sum L_{ij} V_j . \quad [10.4]$$

The limb intensities in the presence of absorption were calculated using equation 10.5,

$$O_i = \sum \alpha_{ij} L_{ij} V_j \quad [10.5]$$

where α_{ij} is the transmission along the line of sight (Section 10.4.1). The α_{ij} term is necessarily positive and less than, or equal to, one. In both of these equations (10.4 and 10.5) the summations are over the non-stationary time dependent total field of view (Chapter 2). As the line of sight looks to lower tangent altitudes so the overlying atmospheric column and the absorption increase. Thus, for the OSIRIS imager there is a large absorption effect for the low altitude pixels and almost insignificant absorption for the upper pixels. This fact is readily apparent from the limb profiles shown in Figure 10.9 and further indicates that the tomographic technique for OSIRIS images must properly accommodate the absorption correction.

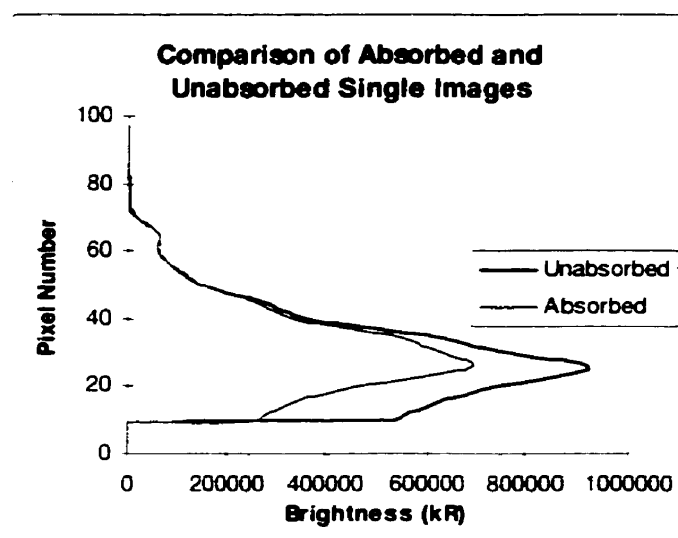


Figure 10.9: The effect of absorption on limb images generated with identical volume emission profiles.

A tomographic recovery without the absorption correction was made from an observation data set that had been generated with the proper absorption correction. The angular cross section for this retrieval is shown in Figure 10.10 and indicates that the retrieved volume emission rates, in the absence of the absorption correction, are much lower than the input rates. The percent difference plot, also included in this figure, illustrates that the lower altitudes are more significantly affected. The reason for this difference, between input and recovered volume emission rates, is that without α_{ij} included in the estimate of the observation the estimate is always high, and thus forces the volume emission rate low. A similar effect occurs if the atmospheric profile used for the absorption correction factors is more, or less, dense than the actual profile. This results in volume emission profiles that are either too large, or too small, respectively.

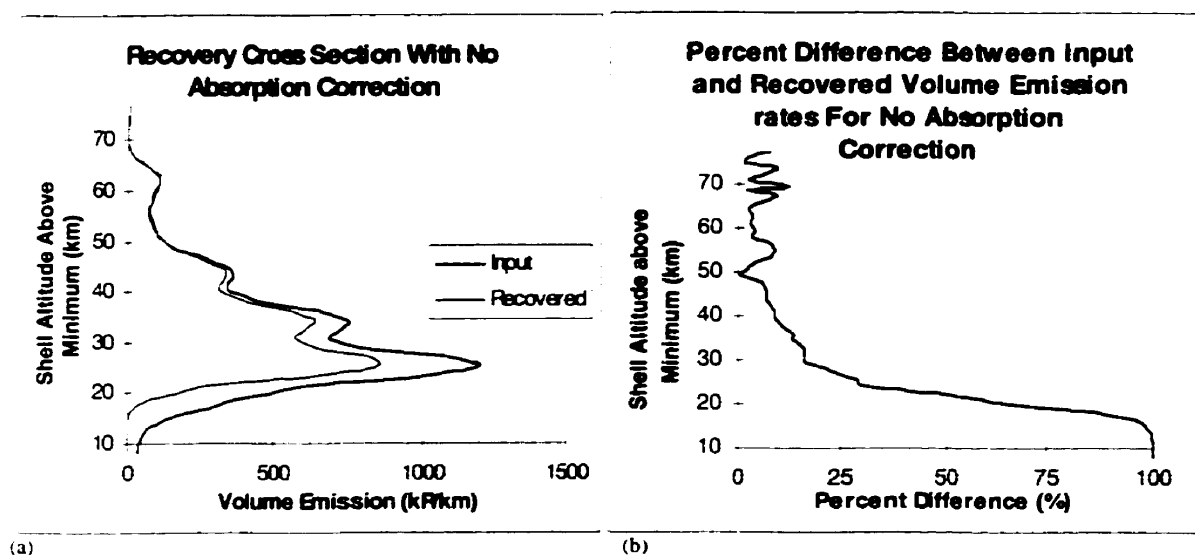


Figure 10.10: The tomographic retrieval with no absorption correction.

10.6 Tests for Emission Structure in the Presence of Absorption

In order to investigate the effect of absorption on the tomographic retrieval a series of model runs, similar to those for the generic unabsorbed emissions, have been made. In all cases the observation data sets have been generated with absorption corrections that are appropriate for the assumed two dimensional atmospheric temperature and density profiles. Only the best, stare mode with no observational noise, and worst, nod mode from 10 to 60 km with 2 MR absolute Gaussian random noise, case scenarios have been investigated in any detail. The structure scale size has also been limited to the three degree wave structure, this is the smallest scale size that is fully resolvable in the absence of absorption. The effects of both an accurate and inaccurate knowledge of the model atmosphere (temperature and density) have also been investigated.

10.6.1 Stare Mode Without Noise

For the stare mode study a set of observations that correspond to a volume emission profile with three degree horizontal structure and the tangent altitude of the OSIRIS imager optical axis fixed at 40.5 km (above the surface of the Earth) have been simulated. The images were recorded at 0.5 Hz with no noise.

10.6.1.1 Correct Atmospheric Weighting Parameters

In this sub-section tomographic retrievals are presented for the case where the atmospheric temperature and density profiles are exactly known and the observations are noise-free. The input and recovered two dimensional volume emission grids for this case are shown in Figure 10.11 and clearly indicate that the retrieval is good. This conclusion is supported by the cross section plots shown in Figure 10.12. It is quite evident in the angular cross section (Figure 10.12b) that the retrieval is better at high altitudes where the absorption effects are weaker. At lower altitudes absorption effects impact the recovery and the structure is not completely resolved. This is due to the skewing of the averaging kernel.

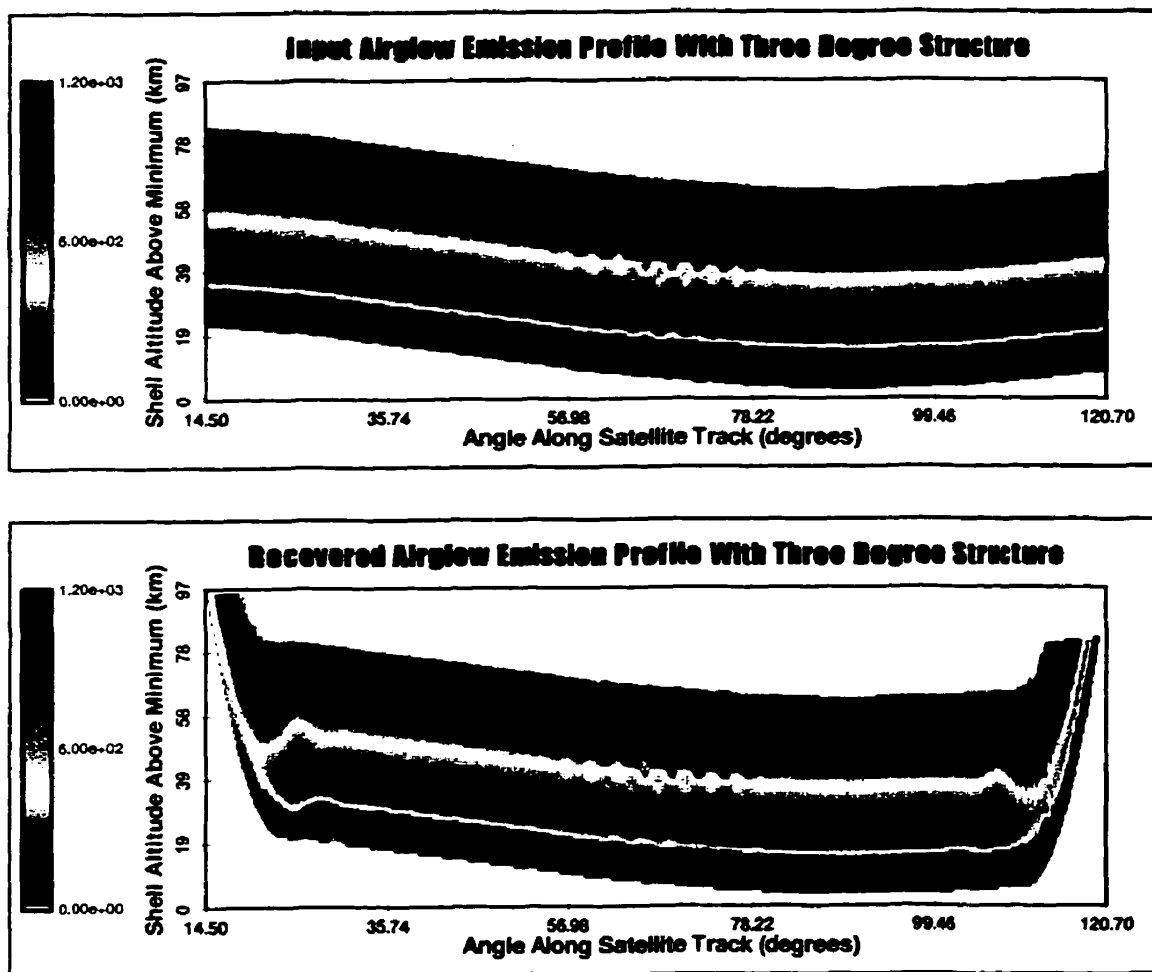
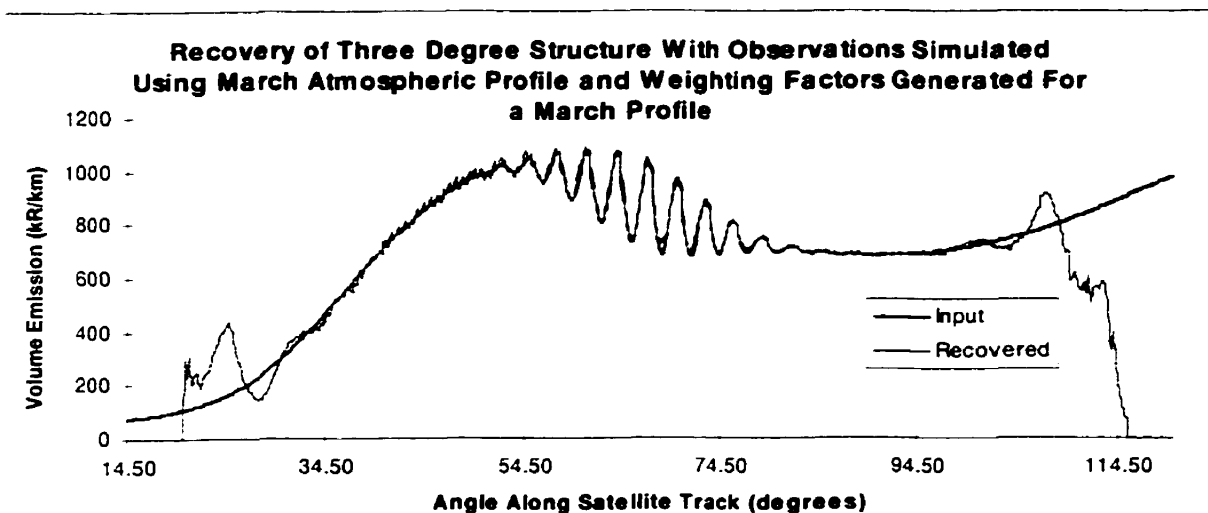
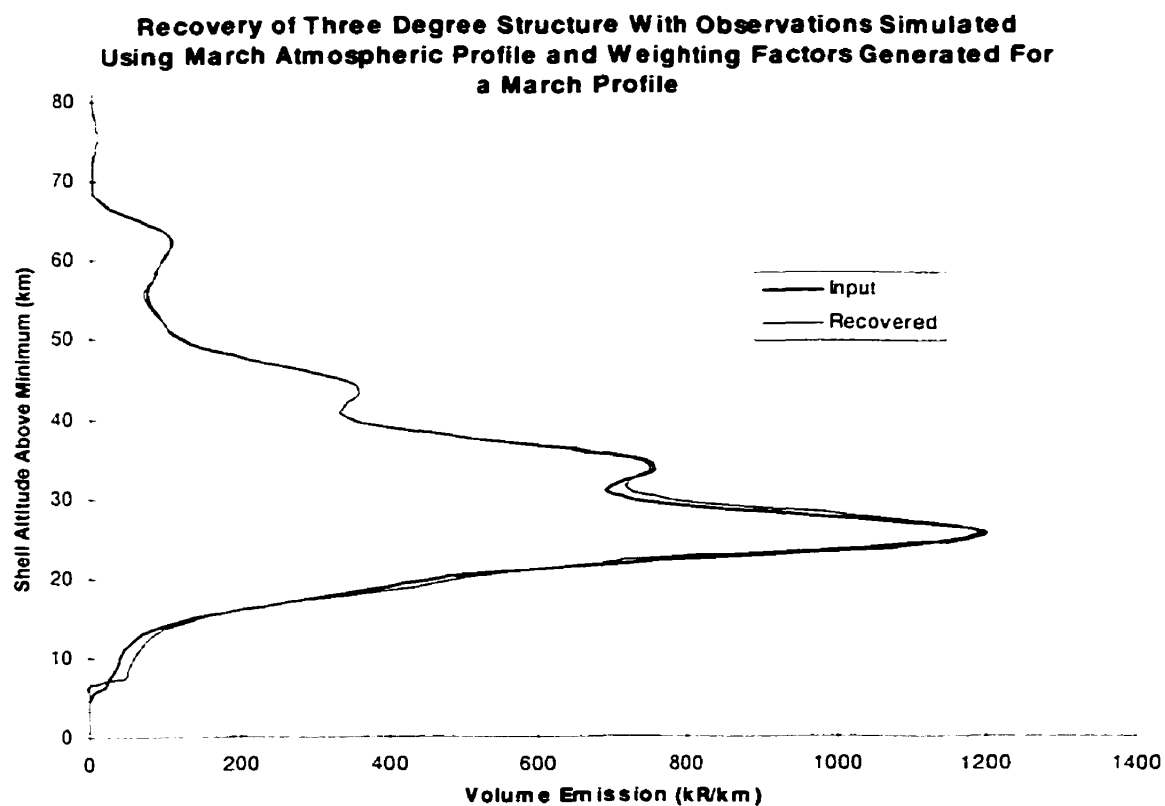


Figure 10.11: Input and recovered volume emission grids for the correct absorption weighting factors.



(a)



(b)

Figure 10.12: Cross sections of the input and recovered oxygen infrared atmospheric band grids for the correct absorption weighting factors.

The high quality of the retrieval is also indicated by the error histogram shown in Figure 10.13. The width is narrow, 2.97%, and the quadratic fit to the histogram is centred near zero, the offset of the peak is -0.07%.

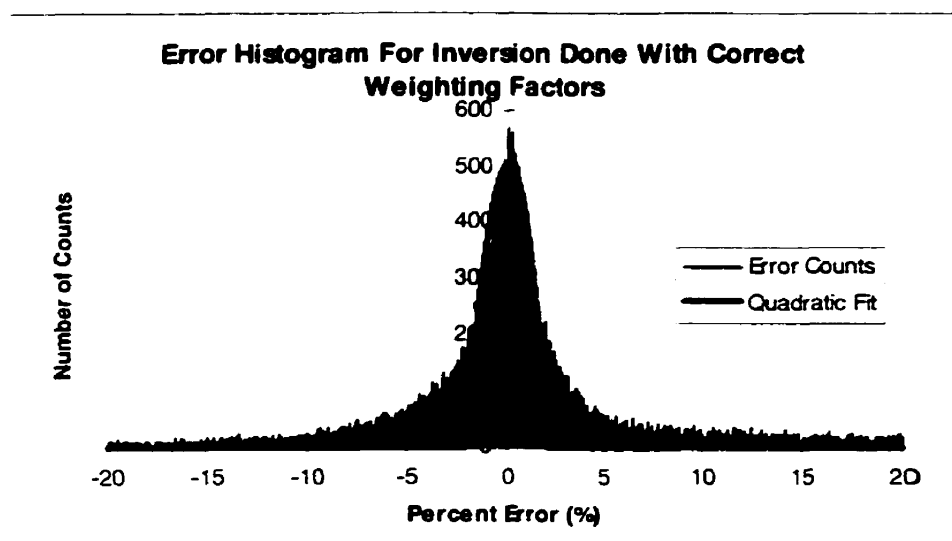


Figure 10.13: Error histogram for the recovery with the correct absorption weighting factors.

10.6.1.2 Incorrect Atmospheric Weighting Parameters

It is quite clear from the results already presented that the tomographic recovery of two dimensional structure in the oxygen infrared atmospheric band is good if the atmospheric transmission is known, *i.e.* the temperature and density profiles are known. However, if the procedure is to be of value for the OSIRIS instrument the sensitivity of the retrieval to the knowledge of the atmospheric profiles must be known.

To test this sensitivity simulated observations were generated with one atmospheric temperature and density profile, and retrieved with absorption correction factors that were calculated for a different model atmosphere. As before the input observations are assumed to be noise-free. The different vertical temperature profiles are shown in Figure 10.14a and the percentage differences between the two vertical density profiles are shown in Figure 10.14b. The percentage difference is defined as

$$\%diff = (NovemberDensity - MarchDensity) / NovemberDensity \times 100\%. \quad [10.6]$$

These profiles were used at all points along the satellite track and adjusted, with respect to shell altitude, by including the Earth oblateness.

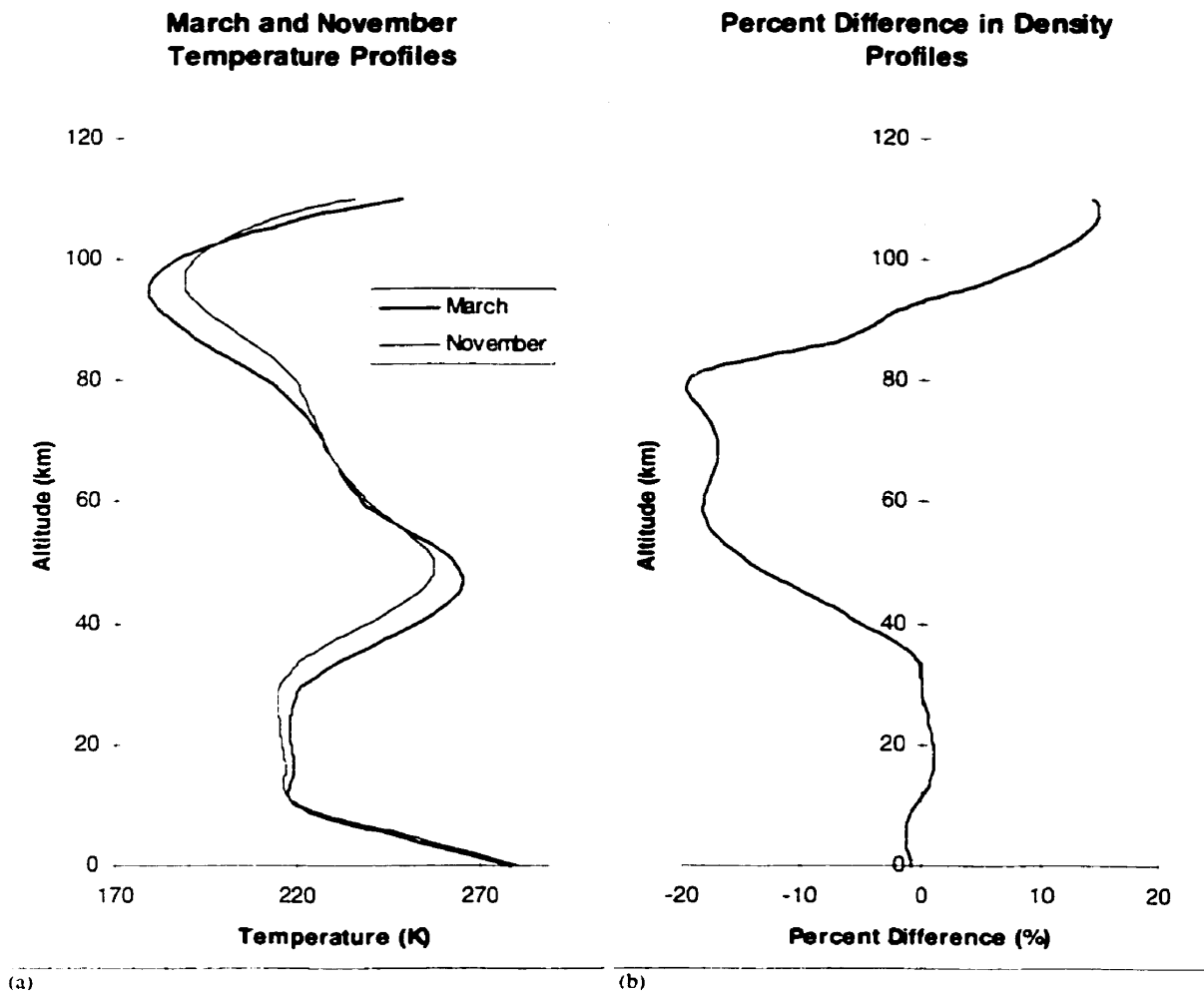


Figure 10.14: The temperature profiles and the percentage differences between the density profiles used to study the effect of profile knowledge on the tomographic retrieval.

The volume emission rates retrieved from observations simulated with a March atmospheric temperature and density profile, with absorption correction factors derived from a November atmospheric profile, are shown in Figures 10.15 and 10.16. It is readily apparent that the angular and vertical structure is completely resolved.

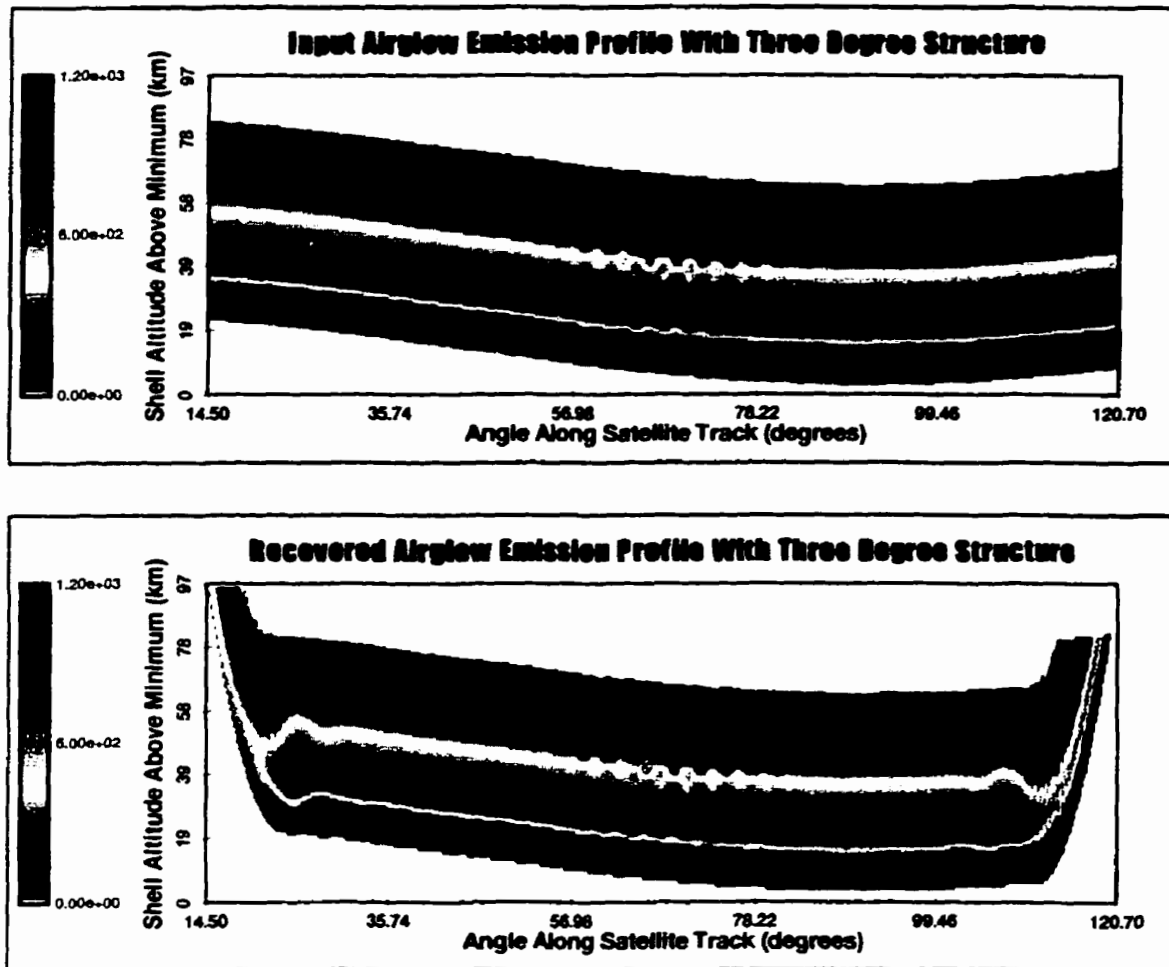


Figure 10.15: Input and recovered volume emission grids for incorrect absorption weighting factors.

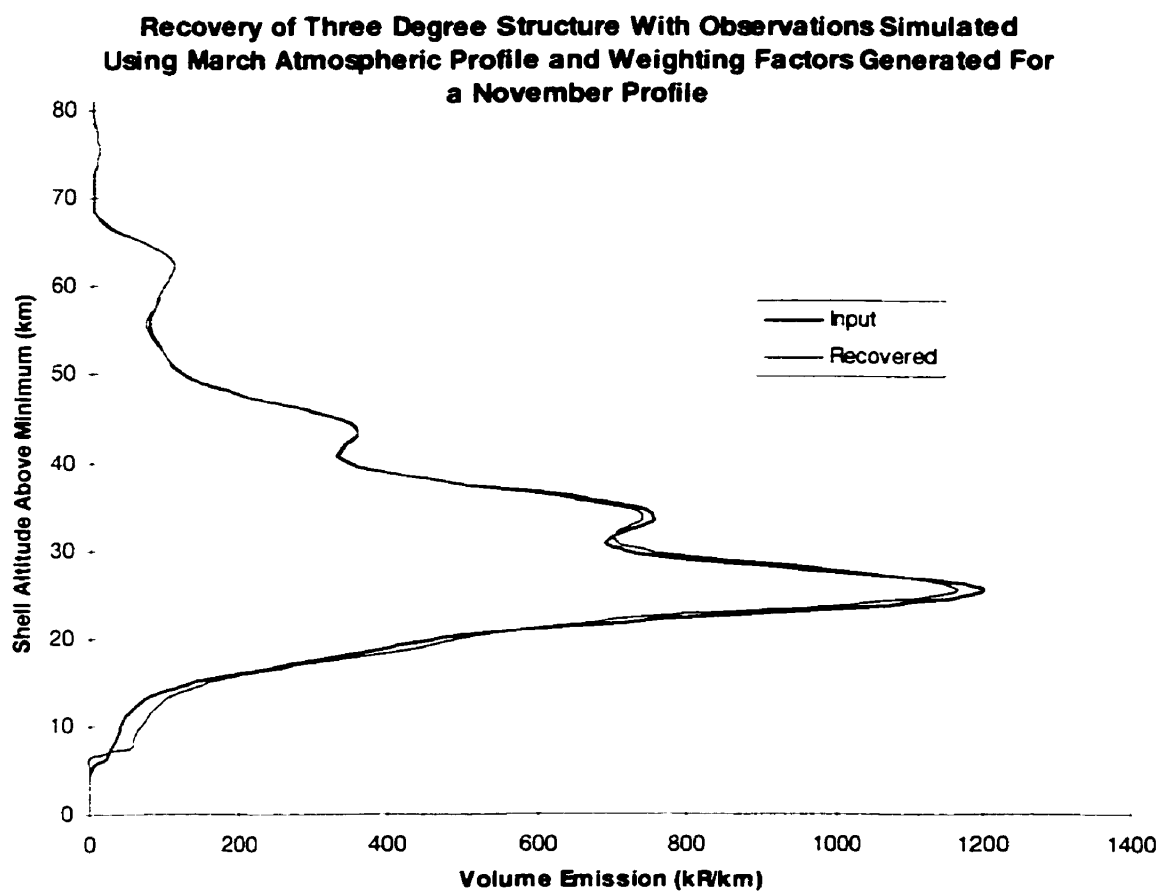
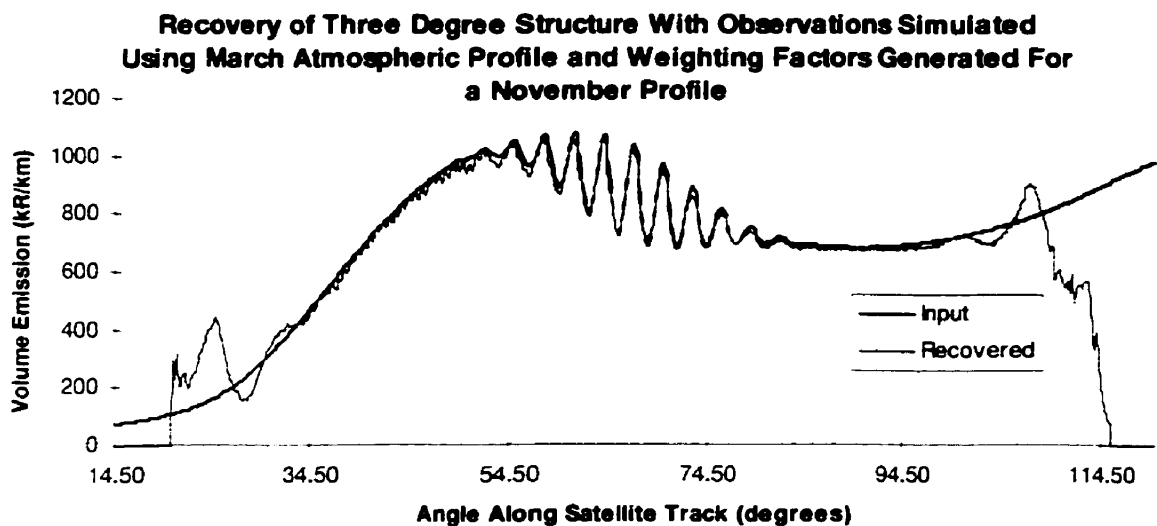


Figure 10.16: Cross sections of the input and recovered volume emission grids for the incorrect absorption weighting factors.

The error histogram for this retrieval is shown in Figure 10.17. It is wider, width 4.15%, than for the retrieval done with the true absorption correction factors (Figure 10.13) and is offset, -0.72%, from the centre position. This latter implies that the recovery is systematically low.

The systematic offset in the error histogram is due to the differences in the assumed atmospheric density profiles. The November atmospheric profile, used for the absorption correction factors, has a consistently lower density, at the altitudes of significant absorption, than the March profile that was used to generate the observations. A consistently lower density implies that the α_{ij} values are systematically high which, as for the unabsorbed case (Figure 10.10), yields a retrieval that is consistently low.

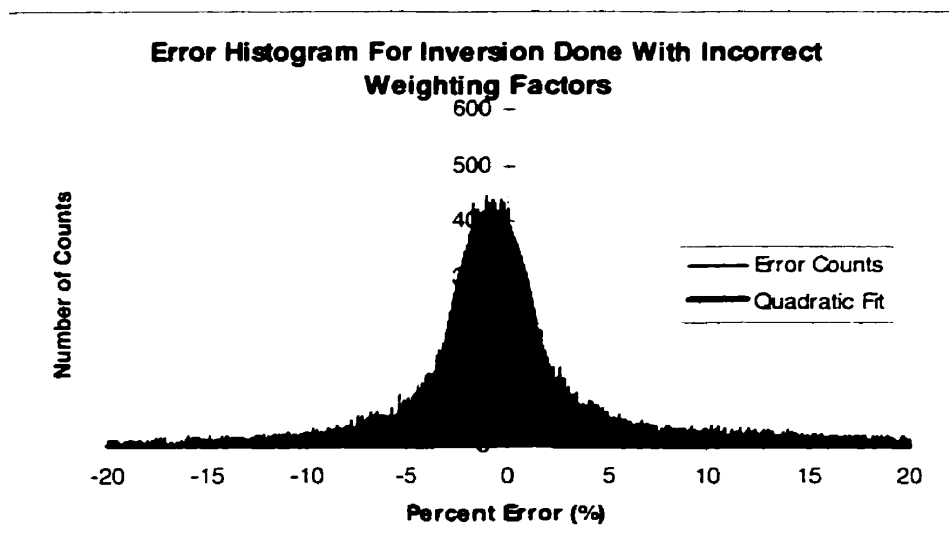


Figure 10.17: Error histogram for the recovery with incorrect absorption weighting factors.

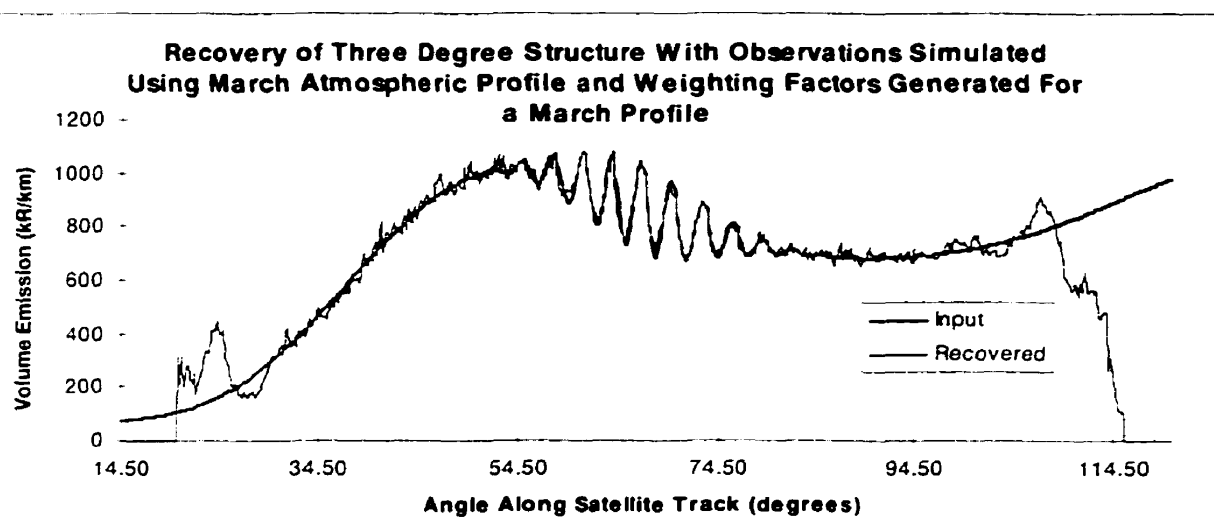
10.6.2 10 to 60 km Nod Mode With Noise

It is expected that the standard operating mode for OSIRIS will involve a spacecraft nod so that the tangent altitude of the optical axis of the detector array scans the limb between 10 km and 60 km. In addition the OSIRIS imager has noise. Therefore simulated observations for a nod mode that include an absolute Gaussian random noise

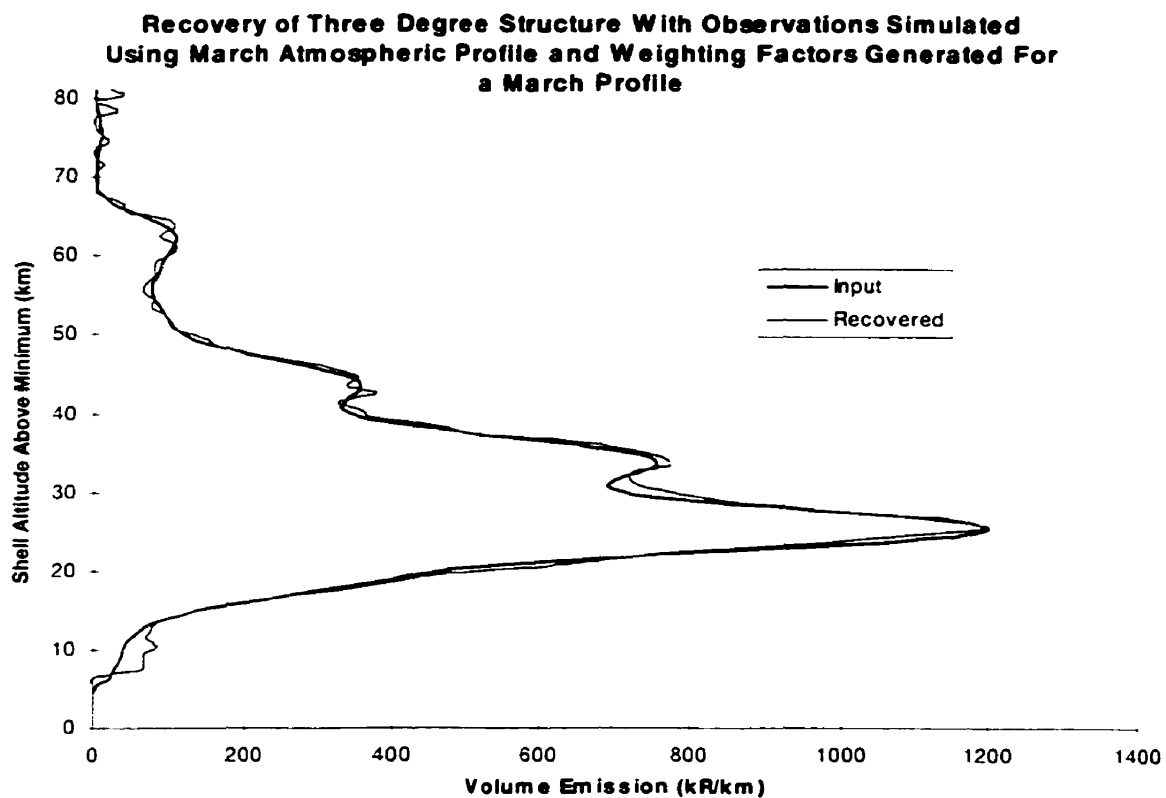
of 2 MR have been used as test data. The assumed noise level is much higher than that measured for the flight version of OSIRIS. Retrievals have been made for this test with the weighting factors (α_{ij}) calculated both correctly, for a known temperature and density profile, and incorrectly where the weighting factors contain systematic errors due to an inaccurate knowledge of the model atmosphere.

10.6.2.1 Correct Atmospheric Weighting Parameters

The cross sections for the retrieval with the correct weighting factors are shown in Figure 10.18. It is apparent from the radial shell cross section (Figure 10.18a) that noise does impact the inversion, but the overall quality of the retrieval is good. The angular cross section (Figure 10.18b) indicates that the retrieval contains some error at high altitudes due to the random noise and does not completely resolve the vertical structure at lower altitudes. However, the overall quality of the retrieval is very good.



(a)



(b)

Figure 10.18: Cross sections of the input and recovered volume emission grids with the correct absorption weighting factors.

The error histogram for this retrieval is shown in Figure 10.19. The width of the histogram is 8.93%; this is larger than for the no noise stare equivalent inversion but the offset of the quadratic fit is still close to zero, 0.03%. These values imply that the fit between the input and recovered volume emission grids is still good, in agreement with the cross sections shown in Figure 10.18.

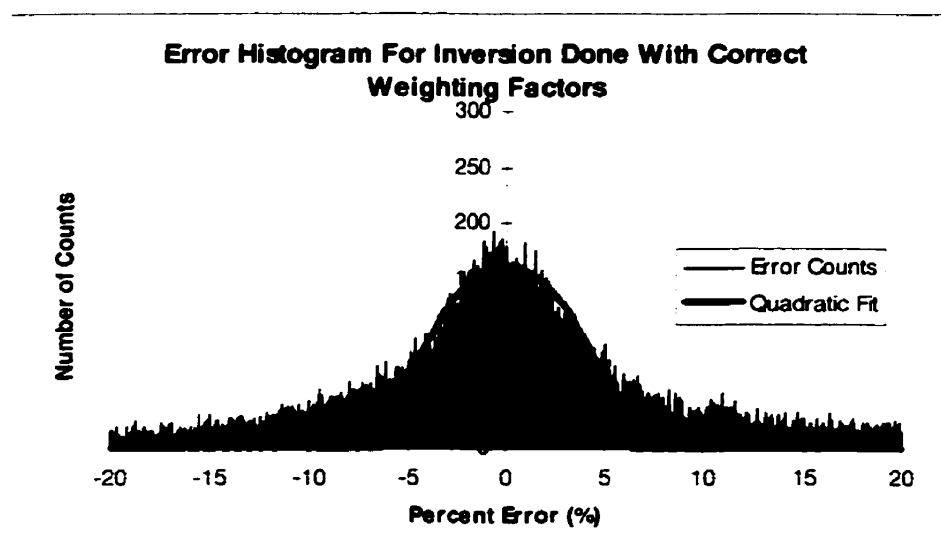
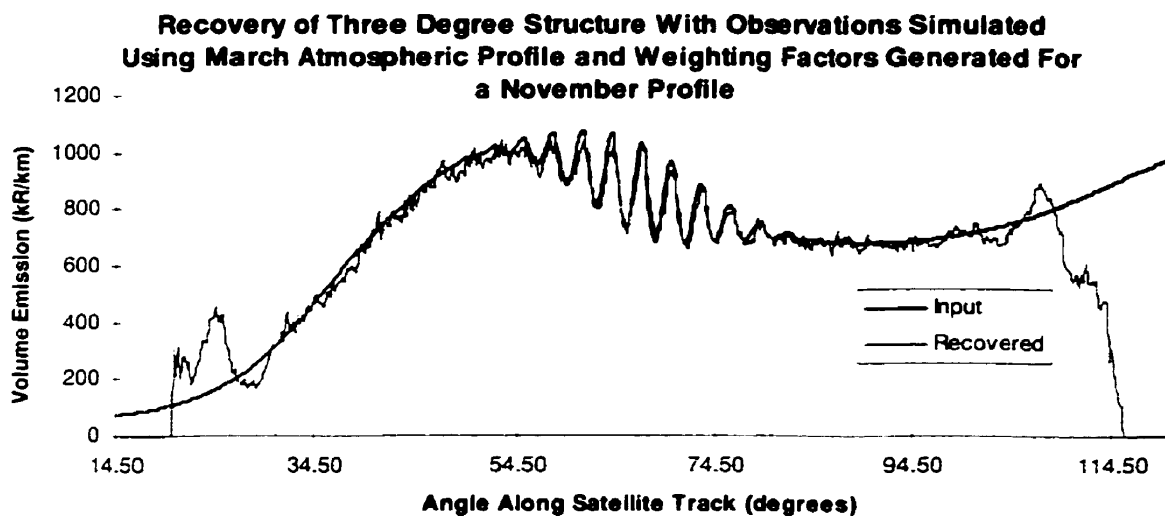


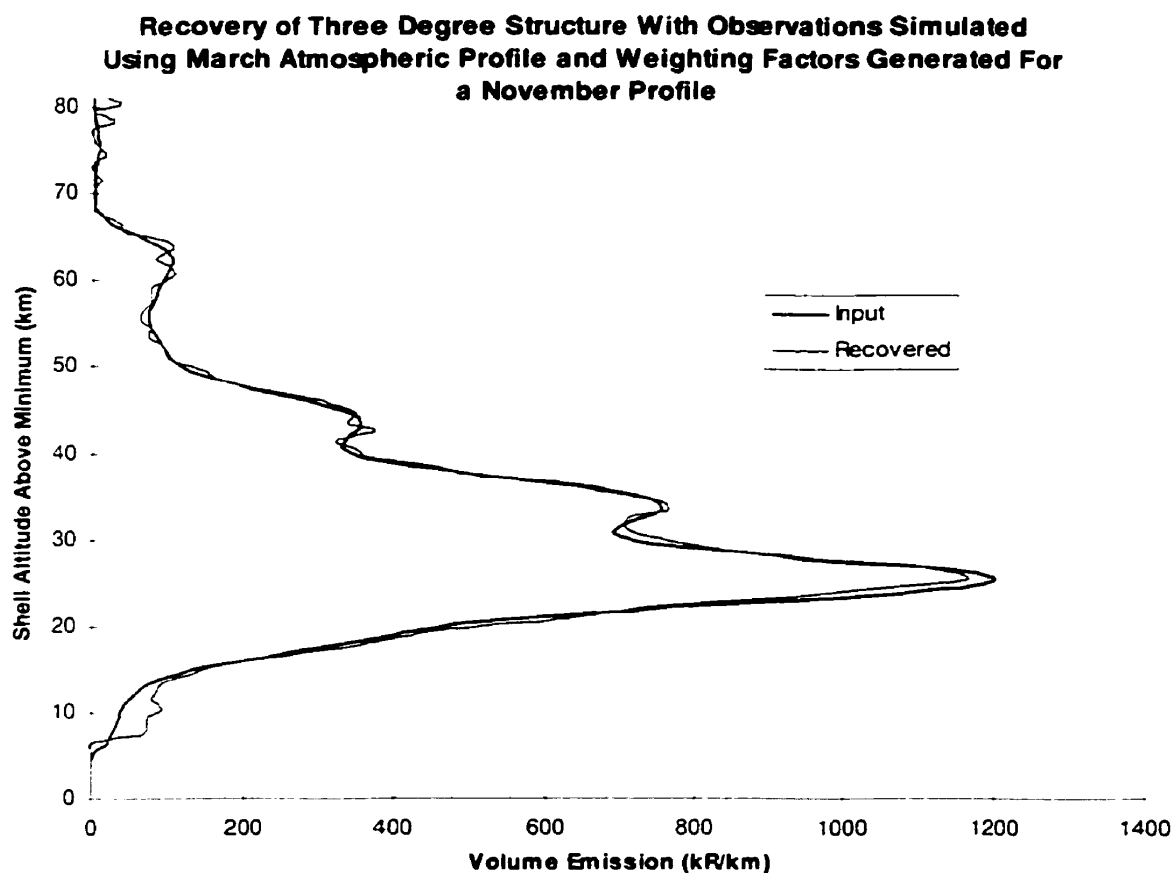
Figure 10.19: Error histogram for the recovery with the correct absorption weighting factors.

10.6.2.2 Incorrect Atmospheric Weighting Parameters

As for the noise-free stare mode the effect of an inaccurate model atmosphere has been tested. The volume emission rates were recovered from observations simulated with the March atmosphere with absorption factors appropriate to the November atmosphere. Cross sections for this retrieval are shown in Figure 10.20. The radial shell cross section (Figure 10.20a) indicates that the horizontal structure has been resolved, although the noise does affect the recovery. It also appears from Figure 10.20a that the retrieval is systematically low. The vertical profile shown in Figure 10.20b is consistent with the vertical profile shown in Figure 10.18b and, while the vertical structure is not completely resolved, the overall recovery is very good.



(a)



(b)

Figure 10.20: Cross sections of the input and recovered volume emission grids with the incorrect absorption weighting factors for the 10 to 60 km nod mode.

The error histogram (Figure 10.21) for this retrieval with incorrect weighting factors indicates a peak offset to the quadratic fit. The offset is -1.60% and the width of the histogram is 9.15%. The observational noise and the inaccurate knowledge of the atmospheric temperature and density profiles have resulted in a recovery with both an increased uncertainty and a larger systematic error. This latter corresponds to the offset of the peak of the quadratic fit from zero and is consistent with the retrieval for the similar stare mode (Figure 10.17).

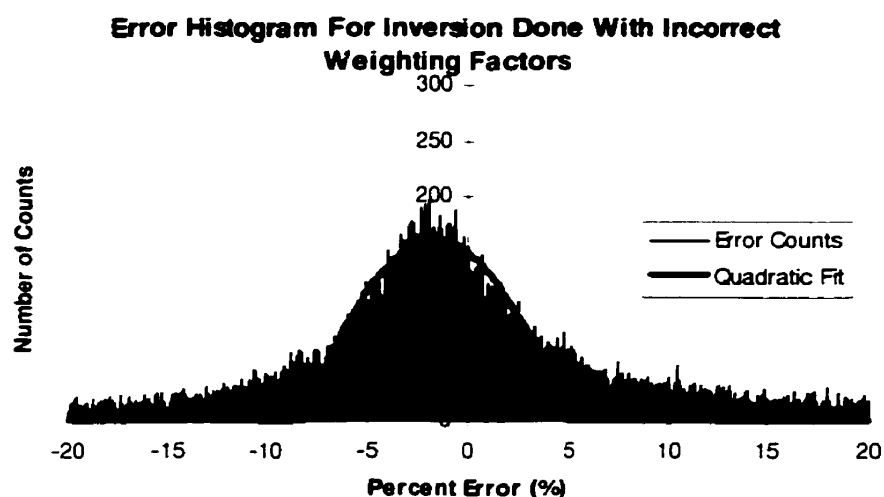


Figure 10.21: Error histogram for the recovery with the incorrect absorption weighting factors.

10.7 Conclusions for OSIRIS on Odin

The tests presented in this chapter have shown that the absorption of the oxygen infrared atmospheric band emission along the line of sight must be considered in the tomographic inversion. It was shown that if absorption is neglected the recovered volume emission rates are low because the band capture factors (α_{ij}) are inappropriately high.

If the effect of absorption is included, through the use of weighting factors that modify the brightness along a line of sight (equation 10.5), the inversion quality is not impacted

although there is a slight loss of resolution due to skewing of the observation weighting filters.

The primary results presented here show that for operational conditions similar to those for OSIRIS the inversion technique yields good retrievals. It has also been shown that accurate temperature and density profiles are not required, and that the inaccuracies result in only a small systematic offset between the recovered and input volume emission rates.

Thus, it is concluded that the adapted tomographic technique is appropriate for the Odin/OSIRIS mission.

CHAPTER XI

SUMMARY AND CONCLUSIONS

11.1 Summary of the Present Work

In the present work an algorithm, or technique, that can be used to recover two dimensional structure in airglow emission profiles has been described in some detail. The actual algorithm is based on the Maximum Probability technique developed by Lloyd and Llewellyn [1989] and expanded by McDade and coworkers in an initial study of atmospheric tomography [1991a, 1991b, 1993]. The Maximum Probability technique is similar to the Maximum Likelihood Expectation Maximization technique that has been used by Shepp and Vardi [1982] to recover two dimensional positron emission fields in medical imaging of the human brain.

Unfortunately due to on-going delays with the launch of the Odin satellite the results presented in this thesis were only for a model of a satellite borne vertical imager that made multiple simultaneous measurements at different tangent altitudes. These measurements provided the set of line integrals that are required for the current tomographic technique. It was shown that the set of available line integrals, or measurements, is heavily dependent on the specific observation geometry and that this latter is dictated by both the satellite orbit and instrument properties. It was also shown that the current tomographic technique is influenced by this set of geometry dependent line integrals and that the satellite geometry is fundamental to the actual retrieval technique.

The parameters required for the algorithm, specifically the grid cell size and the weighting factor exponent, must be carefully selected with a full consideration of the satellite geometry. In fact it was shown that for the algorithm to provide an accurate and computationally efficient solution these parameters must be optimized with respect to the satellite geometry. The adopted values for the grid cell size and the weighting factor exponent were 0.2° by 1 km and $m = 5$ respectively. This choice of inversion parameters

gives an optimal set of weighting filter functions and, therefore, averaging kernels, for each cell. These kernels are important as they eliminate the effect of cells that are physically far from the cell of interest when the solution for this cell is calculated. This results in a more accurate initial estimate and, consequently, a more accurate final solution if small scale structures are to be identified.

This thesis also showed that there is an edge effect, or regions of poorly recovered data at the angular extremes of the grid, for all inversions. This edge effect was shown to be geometry dependent with a definite angular extent of 22° for the adopted inversion grid parameters. For angular distances more than 22° from either edge of the grid the retrieval is not compromised from the edge effect.

The current algorithm is particularly useful, and necessary, if the measured volume emission profile contains two dimensional structure. In the absence of these structures simple inversion methods, such as the Abel transform or the onion peel technique, can be used. The results presented in this thesis indicated that for a range of reasonable noise levels and realistic satellite viewing conditions wave structure in the emission profile, with a wavelength of 3° (approximately 300 km), could be completely resolved. It was also shown that shorter wavelength structures (2°) could be identified, although the structures were not completely resolved. The retrieval technique failed for structures with shorter (1°) scale size as it was unable to identify these perturbations.

One of the fundamental conclusions of the present work is that faster imaging rates are more effective in reducing the impact of observational noise on the retrieved profiles. For all satellite nod modes, input emission profiles and noise values it was found that the retrieved and input values were in better agreement for the higher imaging rates.

The other operational mode that was tested was the nod mode. It was shown that if the satellite is forced to nod (as is the case for Odin) the inversion technique is still effective provided that the nod range is not too large. A tangent altitude nod from 10 km to 60 km at a rate of 1 km/s did not impact the retrievals. However, a nod from 10 km to 110, km at the same rate, is unacceptable as there is too much missing data.

The ultimate objective of this work is to determine a method that is suitable for the retrieval of two dimensional structure in the oxygen infrared atmospheric band emissions that will be measured with the OSIRIS instrument on the Odin satellite. This satellite is now scheduled for launch early in the year 2000. These airglow emissions, which are related to the local ozone concentrations through atmospheric photochemistry, are self absorbed by ground state molecular oxygen. The necessary modifications to the more general tomographic technique to accommodate the OSIRIS specific measurements have been developed and tested. It was shown that for realistic operating conditions the modified tomographic technique will yield the same high quality retrievals as the generic technique with the same horizontal resolution. Indeed the tomographic approach is capable of determining, with high spatial resolution in both the horizontal and vertical dimensions, accurate and computationally efficient volume emission profiles from the Odin/OSIRIS infrared channel measurements.

11.2 Recommendations for Future Work

As with all tomographic problems the technique presented here has evolved as a solution to a specific problem. The motivation for this work is the forthcoming launch of the Odin/OSIRIS instrument and, for this reason, many of the simulations presented here are specific to the characteristics of the Odin platform and the OSIRIS imager. It is important that future work eliminate these constraints, although the presently available computational power severely limits the modifications that can be made to the simulated imager, or satellite platform.

An obvious modification to the measurements would be to increase the vertical resolution of the observations. This could be done with an imager that has twice the number of pixels but with the same vertical field of view. Essentially this would double the number of measurements and allow the number of retrieved cells to increase, but still maintain an over-determined set of linear equations. This work would determine if this simple modification is alone sufficient to decrease the fully resolvable scale size of the current technique.

The tests results presented here were for low imaging rates and it was shown that the faster imaging rates afforded better noise reduction. It would be useful to determine the extent of this noise reduction for arbitrarily fast imaging rates. It would also be useful to determine if the imaging rate has an effect on the scale size that can be fully resolved.

The current simulations were all limited to a single vertical imager that made measurements within the orbit plane of a single satellite platform. The idea of satellite clusters and multiple imagers all looking in different directions to produce true three-dimensional retrievals is intriguing and potentially promising. In addition the concept of satellite rollover maneuvers, that allow direct nadir looks with the shortest possible path length through the atmospheric grid cells, might improve the inversion results if the albedo effects can be properly accommodated. Many different viewing geometries from a satellite platform can be imagined and should be examined. In the present work only a very limited set has been studied.

Even for the limited viewing geometry that is present with Odin/OSIRIS many more tests can be made of the technique itself. The observational weighting filter was arbitrarily chosen to include the path length of an observation through a cell raised to an integral power. Other observation weighting filter shapes should be evaluated in order to determine the optimal weighting filter function.

The final future work is perhaps the most obvious. The presented tomographic technique has been developed for the Odin/OSIRIS instrument and now needs to be tested on real data!

APPENDIX A

THE REQUIREMENT FOR TWO DIMENSIONAL TOMOGRAPHY

For optical atmospheric remote sensing all measurements are an integration of the volume emission rate along a path or ray. This implies that the measurements do not correspond to a single point in the atmosphere but rather are a function of the optical path. For satellite borne observations this path is constrained to a plane, that can be the orbit plane, where both dimensions of the plane are required to describe its trajectory.

A straight line path through a simulated atmospheric volume emission profile is shown in Figure A.1. This line of sight appears curved due to the rectangular representation of the radial grid that is delimited by radial distance and angle along the satellite track. If the vertical extent of the volume emission profile ranges from the ground to 100 km the integration path can cover an extent of 20° . It is quite likely that the vertical volume emission profile will change over this angular range. In this case techniques such as the onion peel, that require the volume emission rate to be identical at the same altitude on both sides of the tangent point, are not appropriate. This is clearly not the case for the line of sight drawn in Figure A.1 where the asymmetric nature of the volume emission rate along the ray is as shown in Figure A.2.

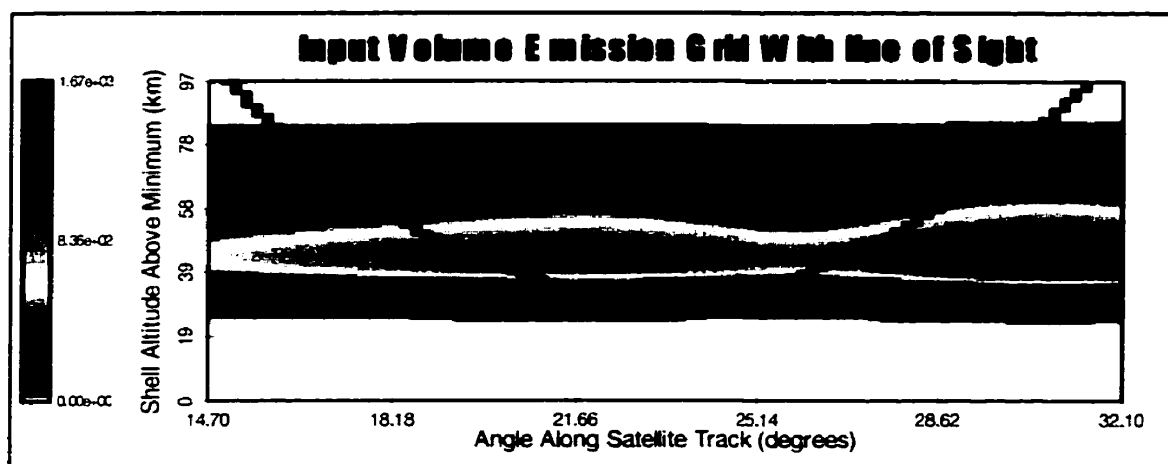


Figure A.1: A line of sight (ray) drawn on a volume emission grid that contains structure in the horizontal, or angular, dimension. The line of sight appears curved due to the rectangular representation of the radial volume emission grid.

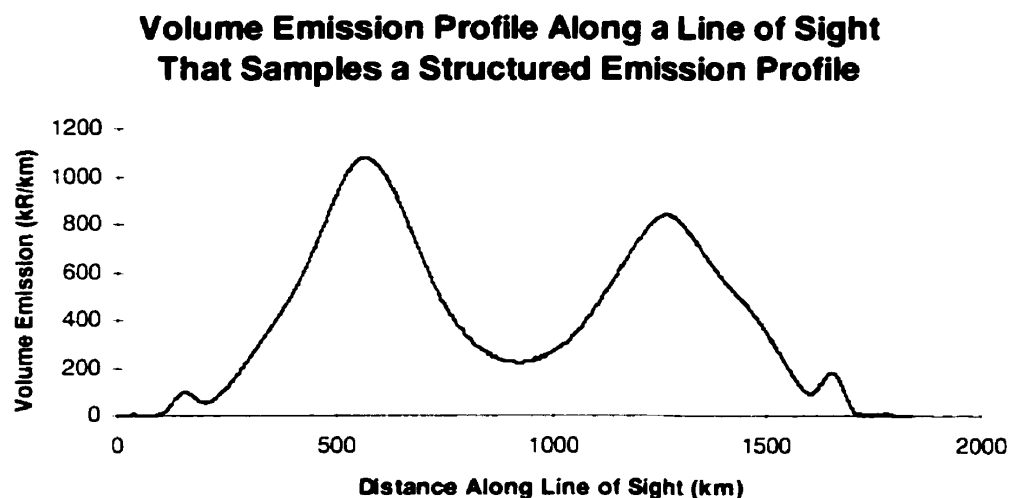


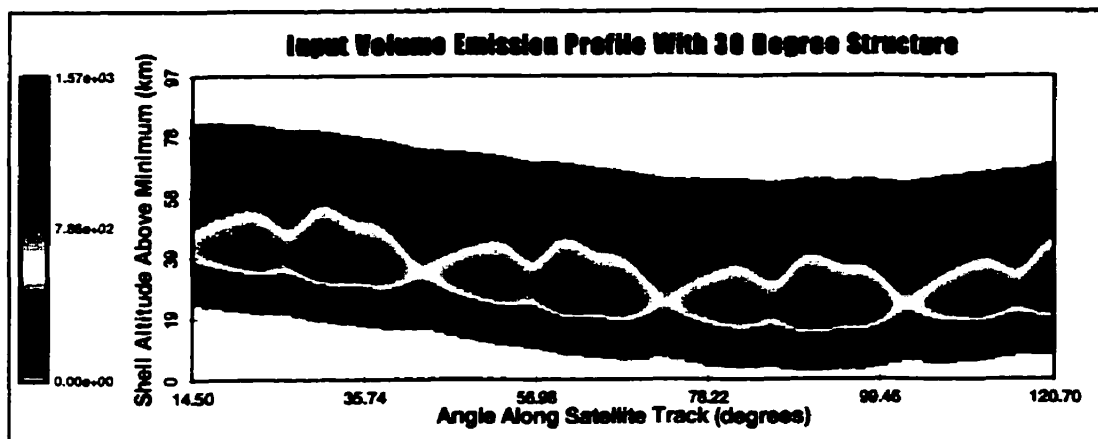
Figure A.2: The volume emission rate along the line of sight shown in Figure A.1. The volume emission is not symmetric as there is no horizontal homogeneity.

Any one dimensional technique that uses optical measurements made from a satellite platform with the atmospheric source function shown in Figure A.1 will not retrieve a true vertical profile. However, some one dimensional techniques can retrieve a single

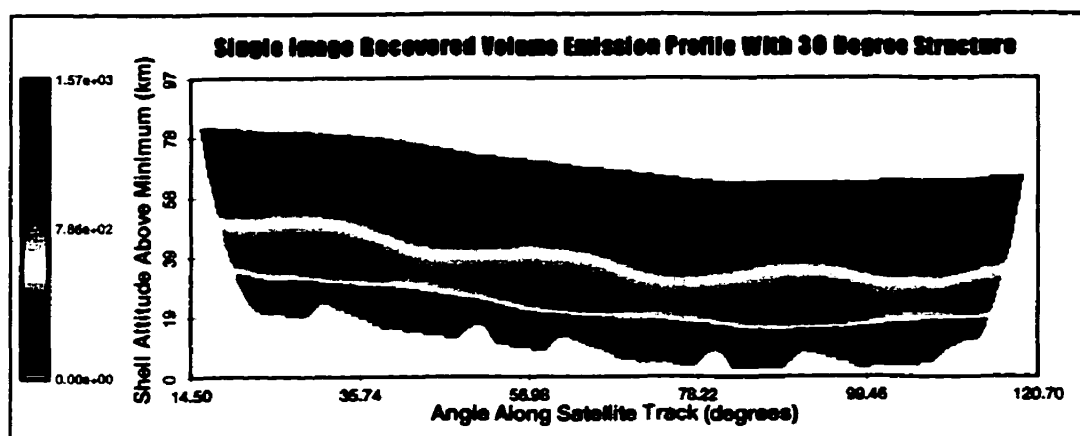
vertical profile that is a blurred average of the multiple vertical profiles seen in Figure A.1.

To further demonstrate the need for a routine that retrieves the two dimensional structure a simulated volume emission profile with structure along the satellite track (Figure A.3a) was sampled at 100 different tangent altitudes simultaneously at 700 points, each separated by 0.125° , along a satellite orbit. This results in 700 limb profiles, each with 100 measurements, that cover an angular range of over 100° . A separate vertical retrieval was performed for each of the limb profiles to determine a vertical volume emission profile that could be considered valid for the angular range covered by the rays associated with that limb profile. The resulting 700 vertical profiles were then merged to produce the retrieved two dimensional profile shown in Figure A.3b. Clearly much of the structure that is apparent in the input profile is absent in the retrieved profile, although the large scale structure is identified.

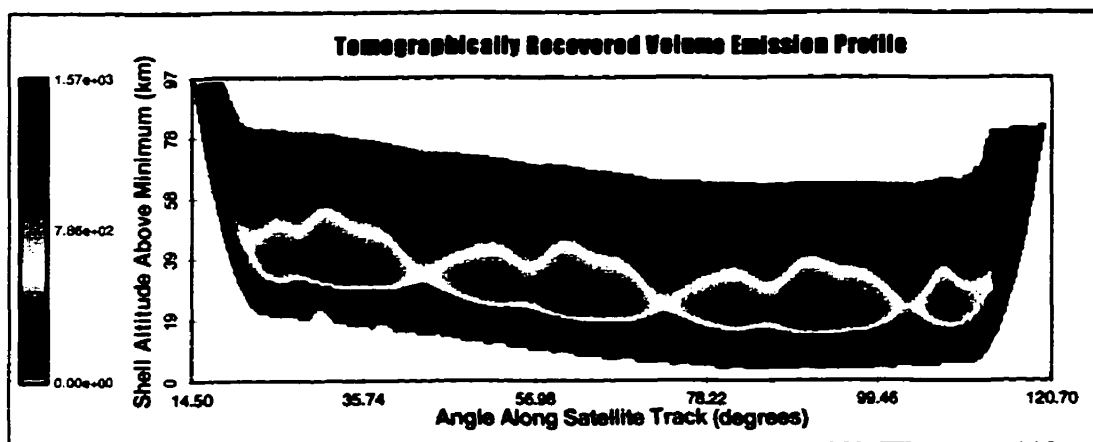
A true two dimensional recovery that used the technique described in this thesis was also performed for the same set of measurements. The result of this retrieval is the two dimensional profile shown in Figure A.3c. It is apparent that, except for the edges of the recovery grid, the two dimensional tomographic retrieval is far superior and recovers the structured volume emission profile. This is even more apparent in the radial shell cross sections shown in Figure A.4 where the two dimensional solution almost exactly matches the input profile while the one dimensional technique appears to act as a low pass filter and so fails to recover the high frequency structure.



(a)



(b)



(c)

Figure A.3: An input two dimensional volume emission profile and two retrieved profiles. The first retrieval (b) used a series of one dimensional retrievals to form the two dimensional profile while the other retrieval (c) used the tomographic technique.

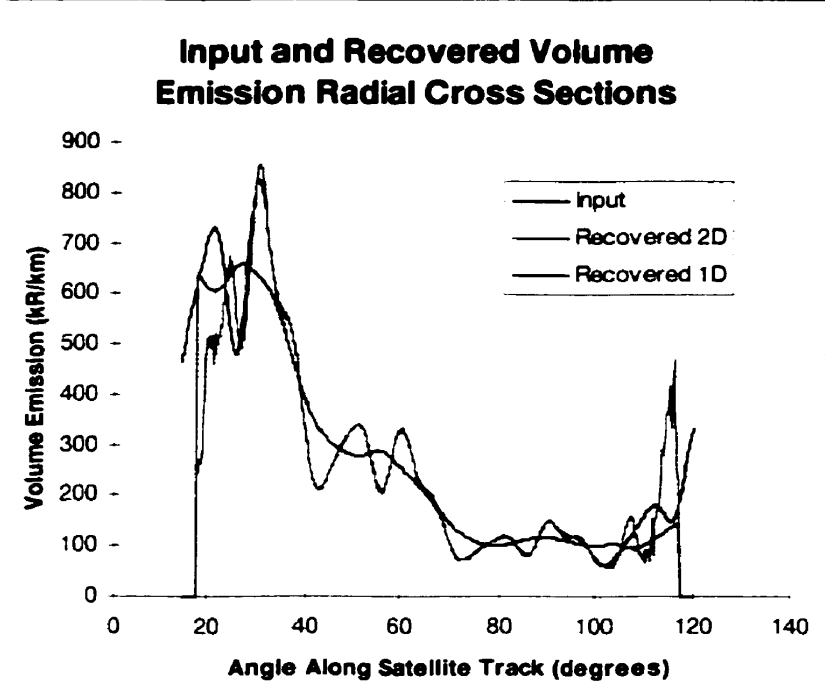


Figure A.4: Radial cross sections for the two dimensional plots shown in Figure A.3.

APPENDIX B

CALCULATION OF MODEL OBSERVATION PARAMETERS

In Chapter 3 a method was developed to simulate model observations. The method, summarized by equation 3.13b, requires a knowledge of the sampled grid cells and the path lengths through these grid cells for each of the lines of sight that make up a complete observation. In this appendix the method used to determine this information is presented in some detail.

B.1 Location of Angle and Radial Distance at Points Along a Line of Sight

The total field of view (Section 3.3.2) samples an atmospheric volume emission source function along a set of lines of sight. The discrete atmospheric source function is contained within grid cells defined in the ascending node coordinate system (Section 3.2). The cell boundaries of this grid are defined by the angle along the satellite track and the radial distance from the centre of the Earth (Section 3.3.3). The method used to determine (in the ascending node coordinate system) the radial distance and the ascending node angle for any distance along a look direction vector $\underline{P}_{sat}(\beta_k)_l$ (Section 3.3.2) with origin at the satellite is as follows.

The x , y , and z coordinates (in the satellite system) of any point at a distance s from the satellite, along the unit vector $\underline{P}_{sat}(\beta_k)_l$, are given by equations B.1, B.2 and B.3,

$$x_{sat} = R_{sat} + P_x s, \tag{B.1}$$

$$y_{sat} = P_y s, \tag{B.2}$$

$$z_{sat} = P_z s, \tag{B.3}$$

where P_x , P_y and P_z are the x , y and z components of $\underline{P}_{sat}(\beta_k)_l$ respectively, and R_{sat} is the satellite distance from the centre of the Earth. The radial distance r_{sat} and the angle

γ_{sat} along the orbit track (in the satellite coordinate system) at any point $(x_{sat}, y_{sat}, z_{sat})$ are given by equations B.4 and B.5 respectively.

$$r_{sat} = \sqrt{x_{sat}^2 + y_{sat}^2 + z_{sat}^2}. \quad [\text{B.4}]$$

$$\gamma_{sat} = \tan^{-1}\left(\frac{z_{sat}}{x_{sat}}\right). \quad [\text{B.5}]$$

It is a simple procedure to determine the corresponding values in the ascending node coordinate system. The radial distance from the centre of the earth remains constant while the angular distance along the satellite track is simply incremented by α_l (Section 3.3.2). Thus the final value of γ_{asc} in the ascending node system is given by equation B.6,

$$\gamma_{asc} = \tan^{-1}\left(\frac{z_{sat}}{x_{sat}}\right) + \alpha_l. \quad [\text{B.6}]$$

In practice the angle γ is first calculated in the satellite system and then translated to the ascending node system as this avoids any problems that occur when γ_{asc} exceeds 360° .

Once the angle γ_{asc} (equation B.6) and the radial distance $r_{asc} = r_{sat}$ (equation B.4) are known it is a simple matter to determine which cell contains the point $(x_{sat}, y_{sat}, z_{sat})$ at distance s . The actual angle and shell numbers are given by equations B.7 and B.8,

$$AngleNumber = \text{floor}\left(\frac{\gamma_{asc}}{DeltaAngle}\right), \quad [\text{B.7}]$$

$$ShellNumber = \text{floor}\left(\frac{r_{asc} - ShellMin}{DeltaShell}\right), \quad [\text{B.8}]$$

where the floor function truncates the argument to the next lowest integer. The actual cell number j is defined by equation 3.7. In this way it is possible to determine the cell number, in the ascending node coordinate system, from the distance along the look direction vector $\underline{P}_{sat}(\beta_k)$, in the satellite system, and the spacecraft position values

$$(R_{sat}, \alpha)_l.$$

B.2 Intersection With Grid Cell Elements

Each relevant line of sight, or look direction unit vector, intersects at least two grid cell boundaries. If all of the intersections with grid cell boundaries are known in increasing order, with respect to distance along the line of sight, then the distance between two consecutive intersections defines the geometric path length through a cell. The exact cell for this geometric path length is defined by the radial distance and angle of any point, along the line of sight, between the consecutive intersections (equations B.7 and B.8).

A line of sight can intersect the radial shell defined by equation B.9,

$$r = \sqrt{x^2 + y^2 + z^2}. \quad [\text{B.9}]$$

Substitution from equations B.10, B.11 and B.12,

$$x_{asc} = S_x + P_x s, \quad [\text{B.10}]$$

$$y_{asc} = P_y s, \quad [\text{B.11}]$$

$$z_{asc} = S_z + P_z s, \quad [\text{B.12}]$$

that represent the ascending node position of a point at a distance s along a look direction \underline{P}_{asc} , into equation B.9 yields equation B.13. This gives the distances, along the line of sight, to the intersections. It should be noted that S_x and S_z are the ascending node satellite coordinates.

$$s = -(\underline{S}_{asc} \bullet \underline{P}_{asc}) \pm \left[(\underline{S}_{asc} \bullet \underline{P}_{asc})^2 - R_{sat}^2 + r^2 \right]^{\frac{1}{2}}. \quad [\text{B.13}]$$

Any line of sight intersects a radial shell either twice or not at all according to the sign of the term under the square root in equation B.13. No radial shells below the tangent radius of the line of sight (equation B.14)

$$r_{\tan} = \left[-(\underline{S}_{asc} \bullet \underline{P}_{asc})^2 + R_{sat}^2 \right]^{\frac{1}{2}} \quad [\text{B.14}]$$

will be intersected while shells above *ShellMax* need not be considered. Thus the distances to all relevant shells within the grid can be easily calculated and saved.

A line of sight will intersect the plane defined by equation B.15,

$$z = x \tan \gamma_{asc} \quad [\text{B.15}]$$

where γ_{asc} , defined in the ascending node coordinate system, is the angle of the plane along the orbit track. The distance to the only intersection is given by equation B.16,

$$s = \frac{S_x \tan \gamma_{asc} - S_z}{P_z - P_x \tan \gamma_{asc}} \quad [\text{B.16}]$$

where S_x and S_z are the satellite x and z coordinates respectively (in the ascending node coordinate system) and P_x and P_z are the look direction unit vector direction cosines in the ascending node coordinate system.

The determination of the angular boundaries associated with intersections within the grid is a more complicated process than for the intersections with radial shells. The angles at which the line of sight intersects the maximum radius shell of the grid defines the relevant total angular extent covered by that look direction. The distances to these intersections are determined from equation B.13. The maximum distance determines the last angular cell that is intersected. Similarly the minimum distance determines the first angular cell that is intersected. All angular divisions between these cell bounds must be evaluated using equation B.16 for intercept distance. This is illustrated in Figure 3.8 where the line of sight enters the grid at *AngleNumber* = 2 and leaves the grid at *AngleNumber* = 4. Only the angular boundaries 3 and 4 are intersected by this particular $\underline{P}_{asc}(\beta_k)_i$ look direction.

The two sets of intercept distances, those for radial shells and angular planes, can be

separately determined and merged into a single set that increases with distance s .

B.3 Determination of the Parameters

Once the intercept distances to the grid surfaces have been calculated and stored in increasing order it is a very simple process to determine the path length through each cell and the corresponding cell index. The distance between successive intercepts, in the set of intercepts (Section B.2), determines the path length $L_{p_{ax},j}$ [km] through any intersected cell. The index j is found according to the method outlined in Section B.1 for any point between the intercepts. Hence, all of the required parameters for the calculation of the observed brightness (equation 3.13b) can be readily determined.

APPENDIX C

ESTIMATE OF ACCURACY

It is important to be able to determine the quality of the volume emission profile, recovered with the tomographic analysis technique. It can be determined from simple visual inspection that some data sets are either good or poor recoveries. Where this technique is applicable it is implemented. However, when visual analysis fails, it is important to have a mathematical representation of the quality of the recovery as the effectiveness of certain inversion parameters can be determined from such a mathematical representation.

The chosen method, for this thesis, involves a histogram that represents the percentage error distribution of the recovered profile from the known input profile. The quality of the inversions have been determined through both the Full Width at Half Maximum (FWHM) of a quadratic that is fit to this distribution and the offset of the maximum of the quadratic fit from 0% error. This appendix contains a complete description of the error histogram method and a discussion of these two parameters.

The upper plot of Figure C.1 shows an input volume emission grid with a relatively high degree of structure. It was generated with equation 4.5 where λ , the angular period, was equal to 30° . The final two plots of Figure C.1 are the recovered volume emission grids for observations generated without noise and with a moderate signal to noise ratio (S/N) of 50:1. There are some visible differences in the two solutions. The first solution, with no noise, is very smooth and almost exactly represents the input grid in the interior angles. The recovery, where noisy data was used as input, does not show the same smoothness and there is some visible fuzziness in the recovered solution. This solution does, however, closely resemble the input grid. The error histogram method is used to determine a figure of merit for the superiority of the first solution.

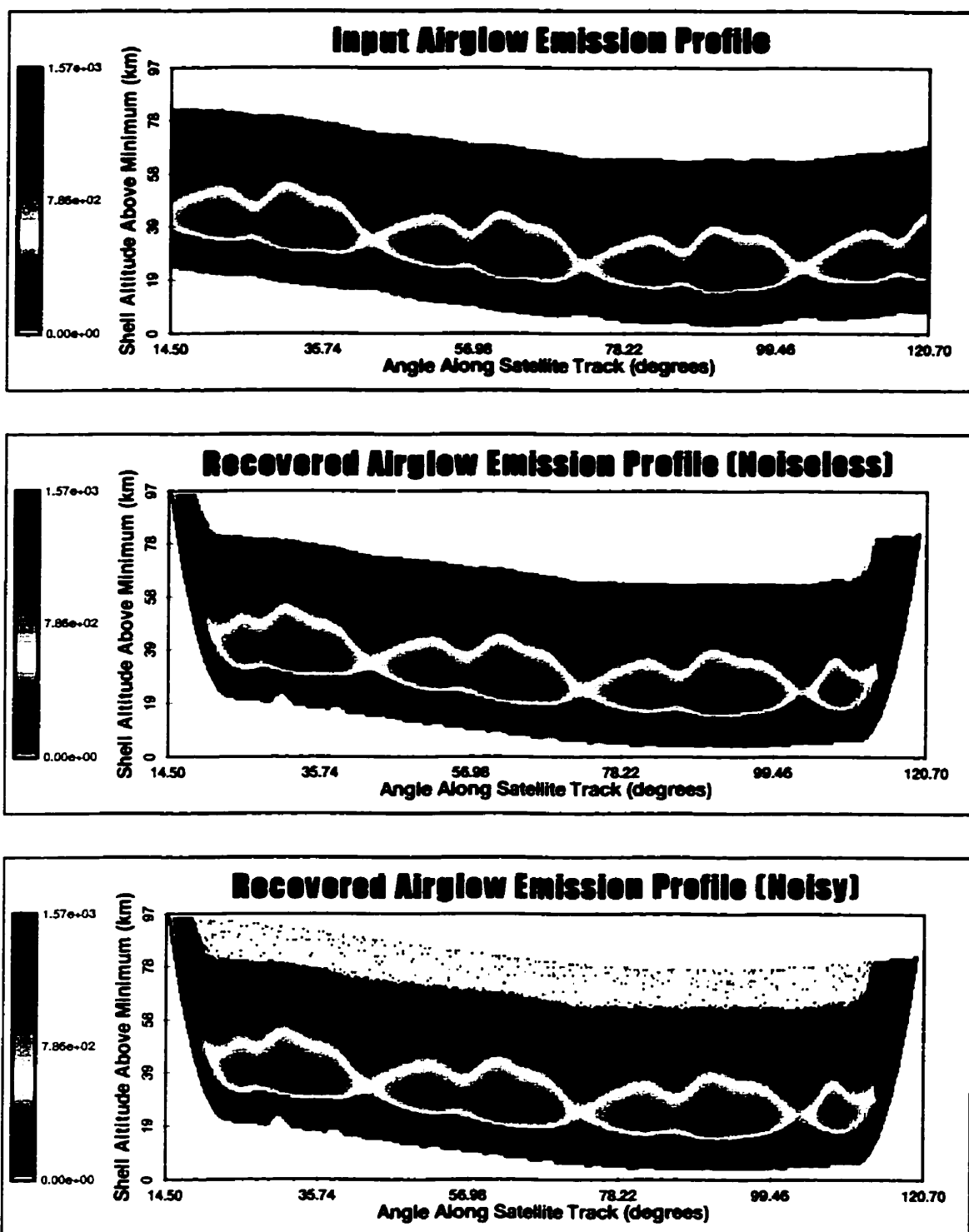


Figure C.1: A moderately structured input volume emission profile and two tomographic recoveries for simulated observations that were generated without and with measurement noise.

This method involves calculating the percentage error, between the input and the solution, at each point in the two dimensional grid. A percentage error histogram is then formed for all errors falling within $\pm 20\%$ of zero. The range of the histogram is limited to 40% in order to eliminate the effect of outlying points, especially those near the edges of the recovery grid. The histogram is made by counting those percentage errors that fall within a 0.1% bin interval with a given central percentage error. Therefore, the histogram from -20% to $+20\%$ contains 401 of these 0.1% bins.

The quadratic fitting procedure involves determining the bin with the maximum number of counts and fitting every bin that contains a count that is more than 40% of the maximum count. The limitation to bins that are greater than 40% of the maximum count is to eliminate the effects of outlying points and make the quadratic fit approach a Gaussian fit.

Both the FWHM and the offset of the maximum point of the parabola are used as the measure of the quality of the inversion. Examples of both the error distribution histograms and the quadratic fits are shown in Figure C.2. The FWHM of the fit for the inversion on noiseless data is 3.61% and the offset of the peak from zero is -0.07% . The error histogram appears to be quite narrow and sharply peaked around 0% .

The second plot in Figure C.2 corresponds to the error distribution and the quadratic fit for the data recovered from the same set of observations in the presence of $50:1$ S/N. This distribution is visibly wider, the FWHM for the quadratic fit is 12.05% . There is also a slight (-1.02%) offset from 0% . These two distributions indicate, as expected, that recoveries for the noiseless data are superior to those when the observations contain noise.

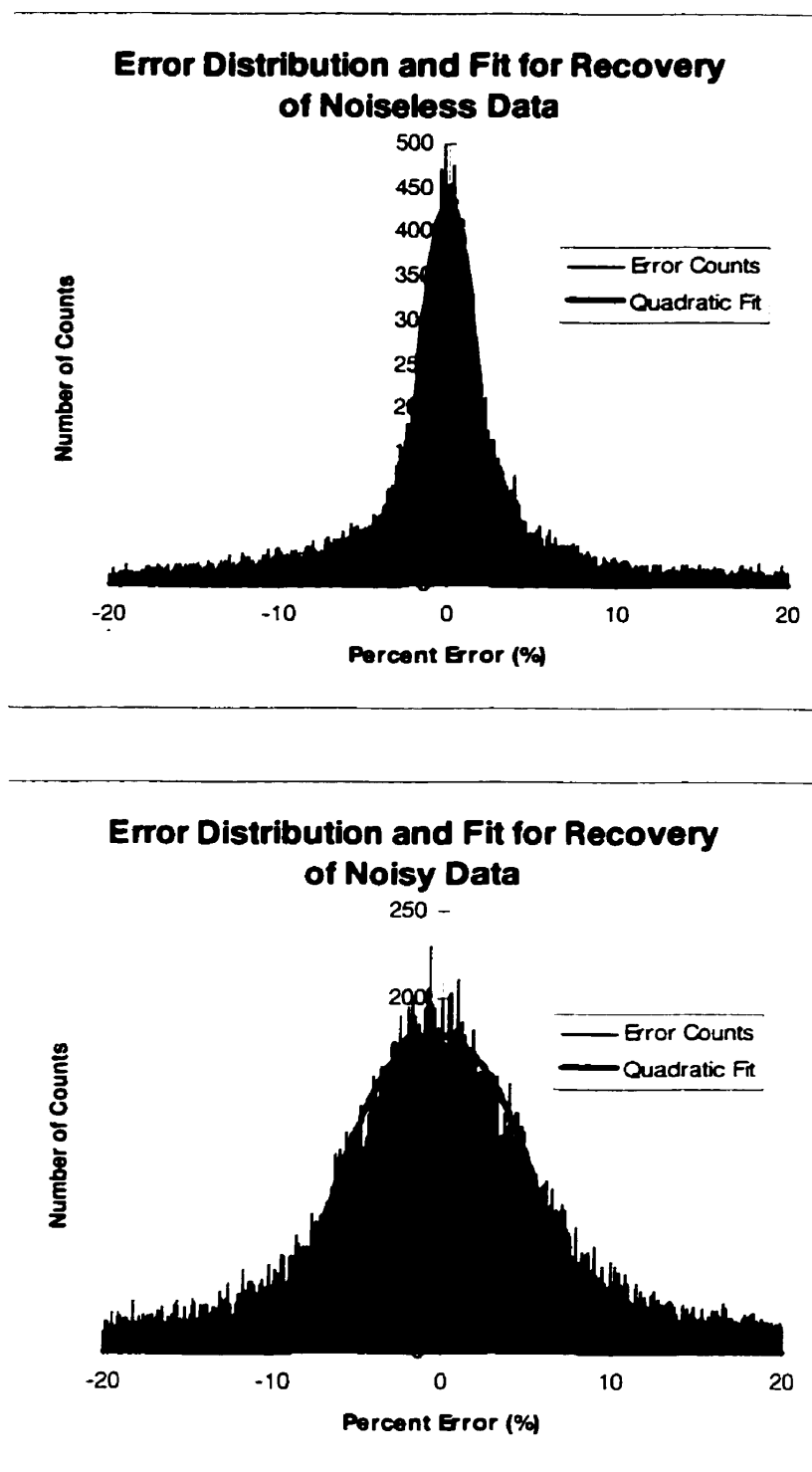


Figure C.2: Error distribution histograms and quadratic fits for the two recoveries shown in Figure C.1. The distribution for the recovery with noisy data is wider than that for the noiseless data.

However, the error distribution histogram and quadratic fit method is not always applicable as illustrated in Figure C.3. The input volume emission profile shown in the upper plot is highly structured. The recovery, shown in the bottom plot, is unable to resolve all of the structure that is present. This is even more apparent in the cross sections shown in Figure C.4.

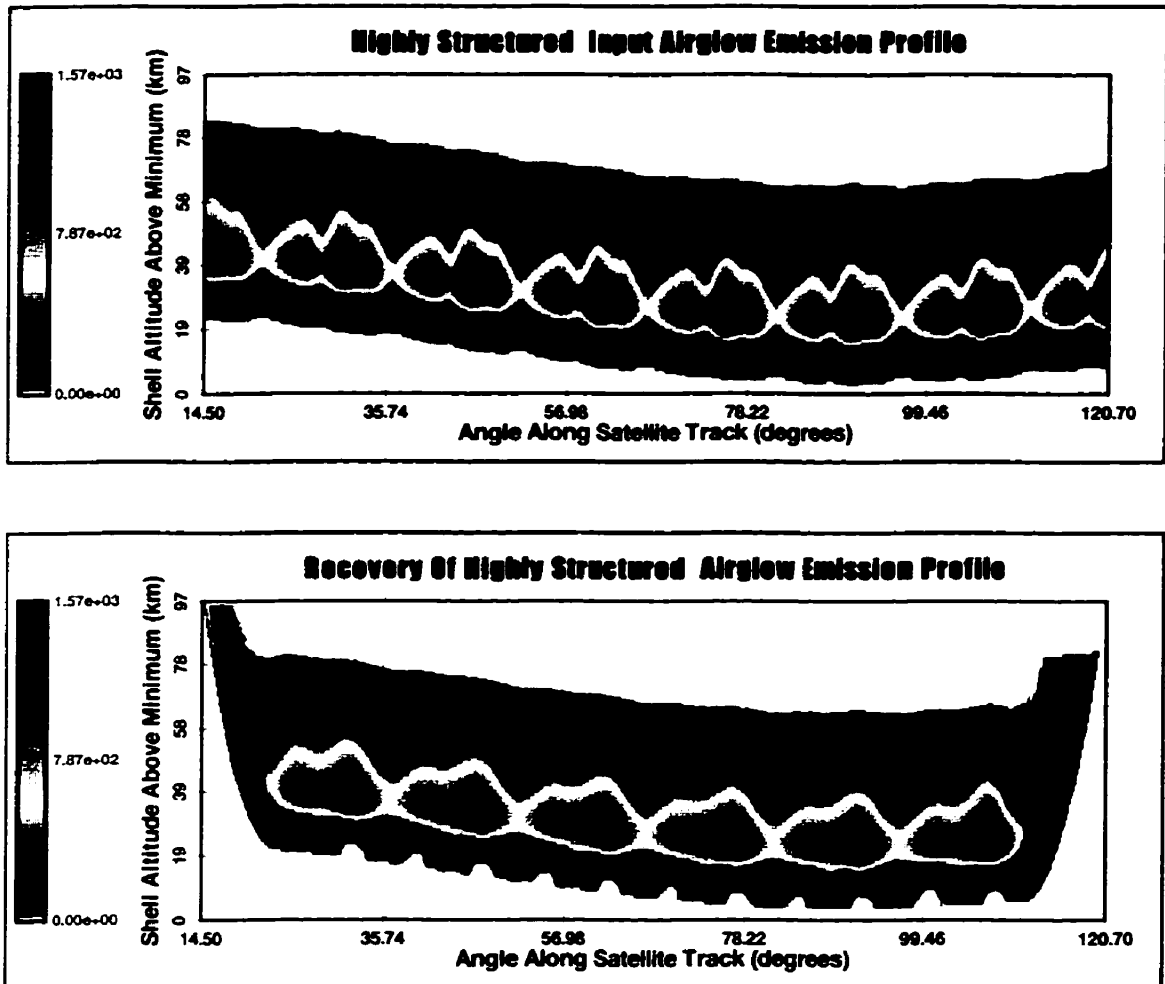


Figure C.3: A highly structured input volume emission profile and the tomographic recovery in the absence of observational noise.

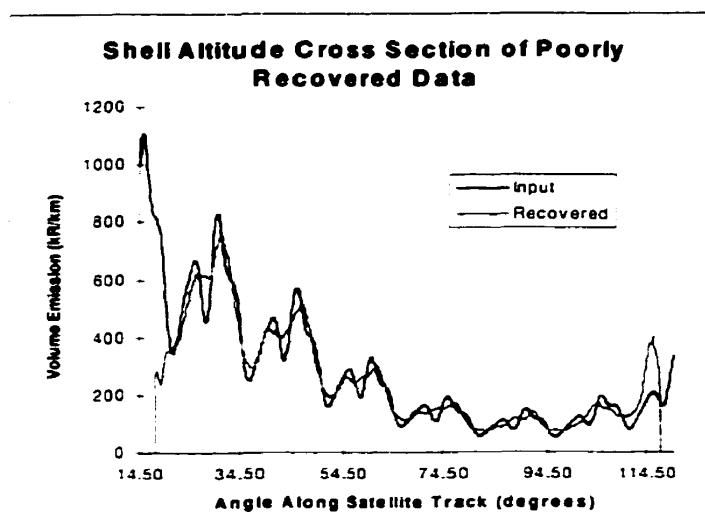


Figure C.4: Radial shell cross sections of the two volume emission grids shown in Figure C.3. This plot illustrates the inability of the tomographic recovery to fully resolve the small scale structures.

The error distribution associated with the recovery in this case is not random. It results in a failure of the tomographic technique to resolve fully the input emission structure. The percentage error distribution histogram and quadratic fit cannot be used reliably in these cases. Figure C.5 shows the histogram for the recovery. The quadratic fit is quite meaningless because the errors do not approach Gaussian. For recoveries of this nature a visual inspection of the solution is sufficient.

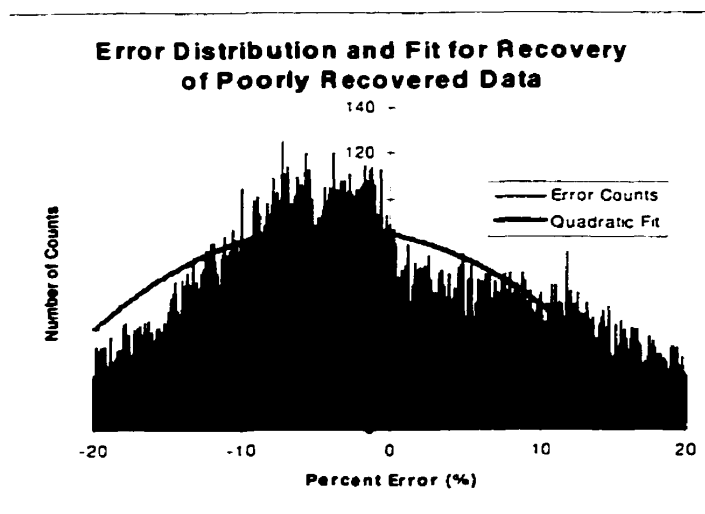


Figure C.5: Error distribution histogram and quadratic fit for the recovery shown in Figure C.3. The errors are not random and suggest a failure of the technique.

APPENDIX D

COMPUTATIONAL OPTIMIZATION TECHNIQUES

The computer used for the present thesis work is a dual processor 200 MHz Pentium Pro machine with 128 MB of RAM. The operating system is Windows NT and the code was written in C using WIN32 API function calls. Although this computing power is not minimal many optimizations had to be made. The L_{ij} path lengths, together with the β_{ij} weighting factors, that are used in each iteration require significant calculation time. Therefore, to save calculation time the storage requirements of these parameters must be optimized to facilitate the maximum number of images that can be processed simultaneously. Also, because only a limited set of images can be processed at any one time, there is a need for a technique to join successive inversions to form a larger data set. The computational techniques that are required for accurate and efficient inversions are discussed in this appendix.

D.1 The Path Length Precision Required to Model Observations

Storage requirements and computational speed are critical for the tomographic technique. For a 700 image set of observations, where each image has one hundred pixels, 9.5 million cells, each 1.0 km by 0.20°, are sampled. This implies that almost 10 million intersection path lengths and the cell to which they correspond are required in equation 5.15. The calculation of these values requires significant time and as these values are required multiple times throughout the iterative inversion it is prudent to make only a single calculation of these parameters and store them (in RAM) for timely access as required.

It is not possible to store the value of the cell index, for each path length, as anything other than a 32 bit integer. A 16 bit integer provides only 65536 unique cell identification numbers. As an entire orbit of a grid with a resolution of 1.0 km by 0.20°

consists of 1800 angles and 100 radial shells, or 180000 cells, there is no method to limit the data size requirements for the storage of the cell index.

However, the intersection path length is different. The maximum length path in the absence of angular divisions is less than 255 km. In the presence of angular divisions this maximum length becomes even less. Therefore, it is possible to store the path length, in km, in only one byte if the fractional or decimal part is ignored. This implies rounding but the storage requirements are minimal. It is also possible, for more precise path lengths, to store them in 32 bit, or 4 byte, floating point representation. The storage requirements increase by a factor of 8/5 (4 bytes are always required for the cell index) but the precision is greater. A third method in which the integer part of the path length is stored in a single byte and the fractional part, multiplied by 255, is stored in another byte may also be used. This is called the modified floating point method and uses only 6 bytes for each path length rather than 8 as in the floating point method.

The three plots shown in Figure D.1 illustrate the error distribution histograms and their respective quadratic fits for recoveries from observations generated using unstructured input volume emission data. The first plot, with FWHM equal to 1.47%, suggests that the floating point precision accurately recovers the volume emission profile. Conversely the second plot suggests that the byte precision does not recover the data as well. The width of the quadratic fit in this plot is 3.10% and there is a suggestion, because the peak is offset 0.50%, of a nonrandom error that most likely originates from the round off associated with the single byte precision. The third plot shows results that are equally as accurate as the first. The modified floating point technique produces an error distribution histogram that has an identical width (1.47%) to that for the floating point precision histogram. This suggests that in the presence of slowly varying angular structure the accuracy of the modified floating point method is equal to that of the floating point method.

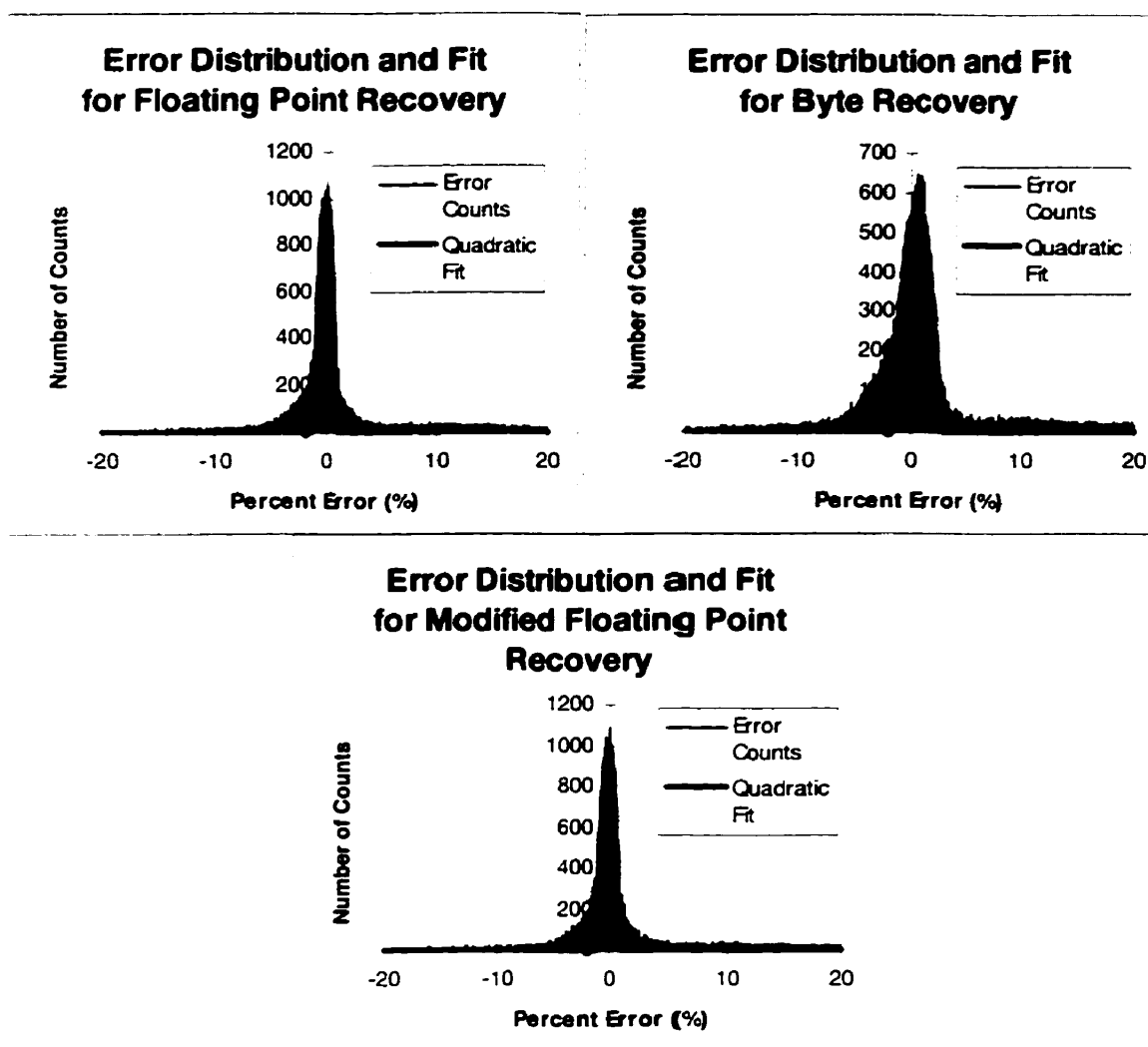


Figure D.1: Three error distribution and fit plots that illustrate the percentage errors associated with the recovery of an unstructured volume emission profile. Each plot is for a different path length precision.

The values in Table D.1 suggest that the modified floating point technique does not suffer in comparison with the floating point technique even in the presence of a high degree of angular structure. Additional structure was imposed on the input volume emission grid and measurements were simulated. Each observation set consisted of 700 images and the recoveries were made at the same 1.0 km by 0.20° resolution with identical inversion parameters. A comparison of the results contained in the table indicates that the byte precision method suffers with respect to accuracy and that there is no significant difference between the results produced by either the floating point or the modified floating point techniques.

The storage and time requirements for these inversions are included in Table D.1. It is interesting to note that the time required to complete the inversion is minimum for the modified floating point method. This is probably due to the way that the Windows NT operating system stores the data internally. It is quicker to access the two bytes used by the modified floating point scheme than either the single byte used in the byte method or the four bytes used in the floating point scheme. Because of the speed, the storage requirements and no apparent loss of accuracy the modified floating point method is used throughout this thesis.

Path Length Type	Structure Scale Size (°)	Error Fit Width (%)	Error Fit Peak Offset (%)	Time Required (s)	Memory Required (bytes)
float	NONE	1.47	-0.07	176	76525896
float	30	6.14	-0.35	178	76525896
float	60	1.56	-0.06	180	76525896
float	180	1.51	-0.08	180	76525896
byte	NONE	3.10	0.55	192	47828685
byte	30	6.68	-0.12	193	47828685
byte	60	3.20	0.52	192	47828685
byte	180	3.07	0.55	192	47828685
modified	NONE	1.47	-0.03	167	57394422
modified	30	6.19	-0.32	166	57394422
modified	60	1.57	-0.04	166	57394422
modified	180	1.50	-0.03	167	57394422

Table D.1: Error fit widths and offsets together with the calculation times and storage requirements for different path length precisions and different structure scale size.

D.2 Joining Inversions to Produce Arbitrarily Large Recovered Profiles

In Section D.1 the limitations imposed by the available computational power was discussed. To invert more data than can be handled at a single time it is necessary to break the input data into sets and to invert these separately and then merge the results. This process is complicated by the poorly recovered data due to the edge effect (Section 6.5). It is, however, a simple matter to accommodate this problem as the exact angular extent of the edge effect is well known from the geometry. A technique for joining inversion sets is outlined in this section.

The input and recovery grids shown in Figure D.2 each have an angular extent that covers almost an entire orbit. Except for the extreme edges the recovery appears to be quite good. The recovery grid was produced by inverting data sets that included only 700 images, taken once every two seconds, and overlapping these sets to eliminate the intermediate edge effects.

The third plot in Figure 6.22 shows good recovery out to nearly 100° , excluding the far left of the cross section. This recovery is identical to the first inversion in the recovery shown in Figure D.2. A second recovery grid can be appended to the first only if it contains data that is good for angles greater than 100° . The exact right hand extent of a 700 image inversion, for images taken at 2 second intervals, is 120.1° . If 22° on the right hand side of the grid is excluded, due to the edge effect, the data is considered good out to 98.1° . The next or successive inversion will have a 22° edge effect on the left hand side of the grid so it will not contain good data at 98.1° unless the recovery starts at 76.1° . This implies that 44° of images must overlap to eliminate the right hand edge effect from the first inversion and the left hand edge effect from the second recovery, in order to join the inversions at 98.1° .

The 44° data range corresponds to approximately 350 images at an image rate of one every two seconds. Even though 350 images must be reused in the next inversion each inversion produces about 60° of good data if the images are taken at a rate of one every

two seconds. This means that seven separate inversions were needed, each on a 700 image observation set, to produce the results shown in Figure D.2.

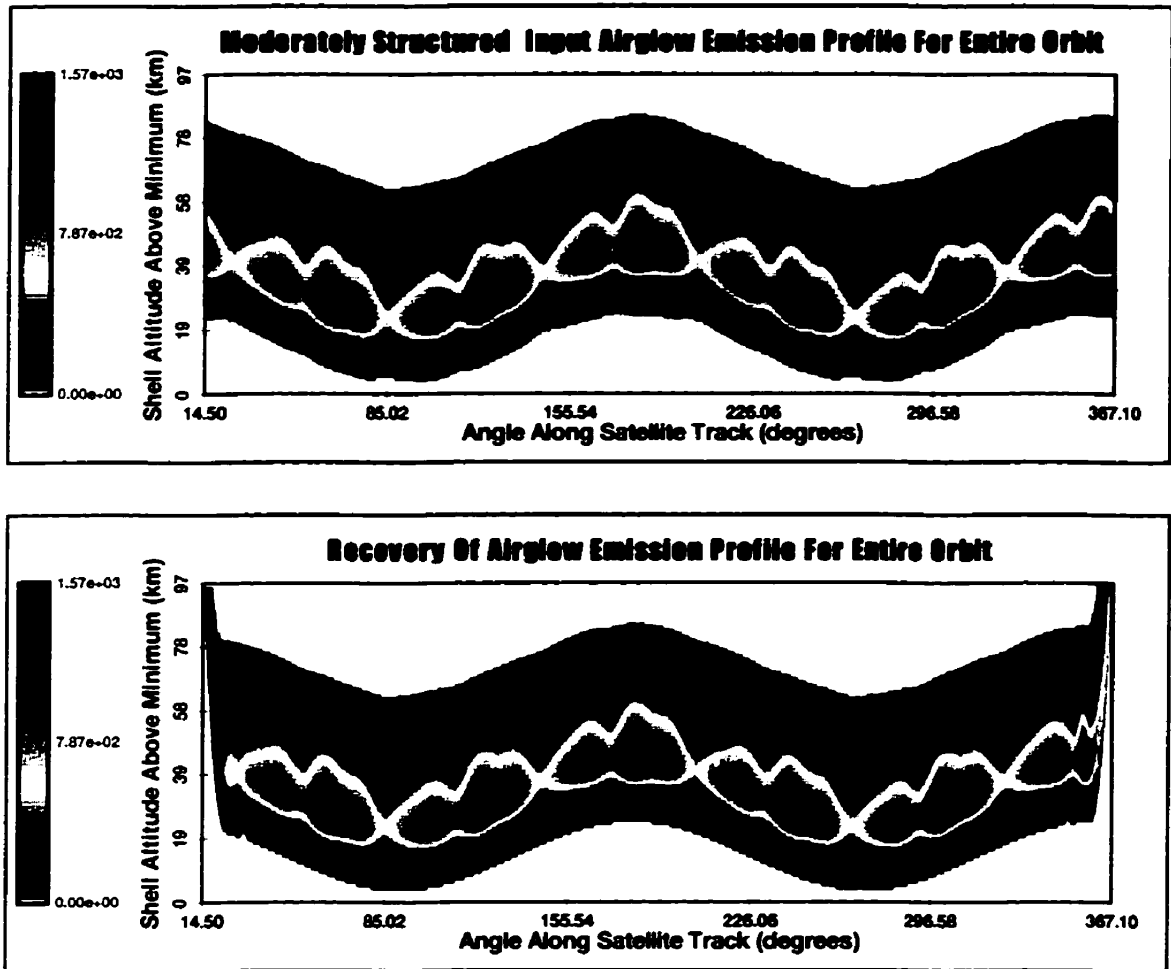
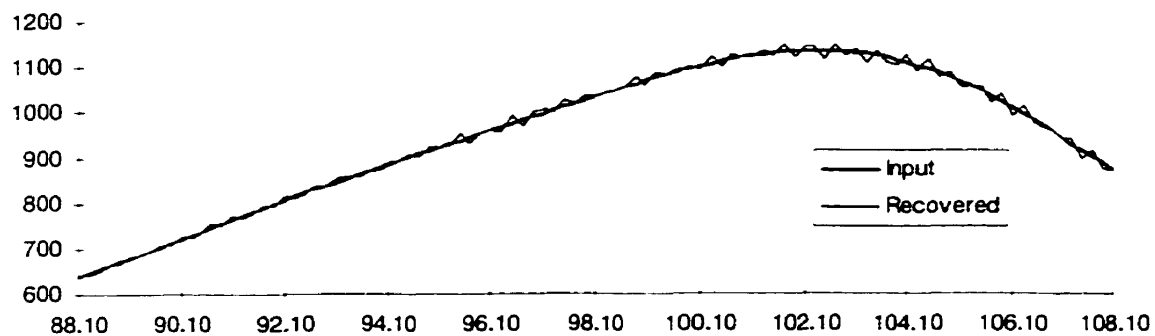


Figure D.2: Recovery for an entire orbit using 700 images per inversion and joining the individual recoveries.

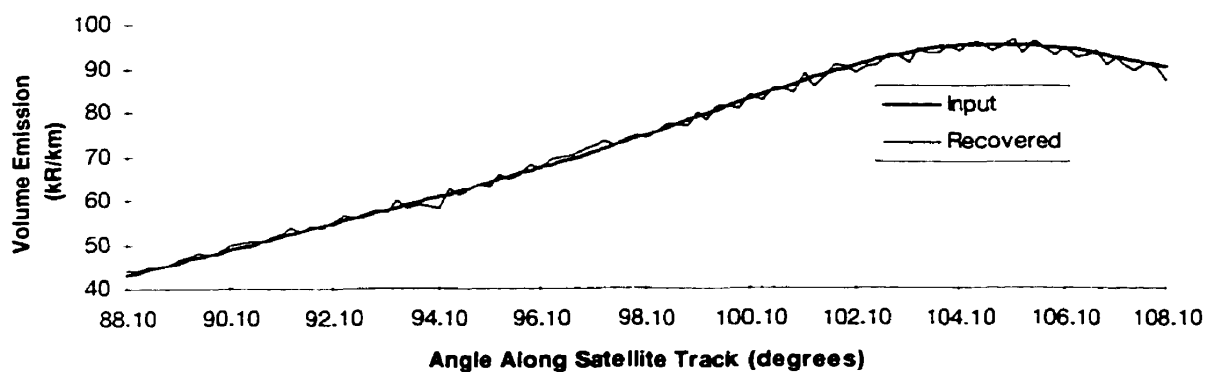
The first join in Figure D.2 occurs at 98.1° . There are no visible discontinuities in the data in this figure. Cross sections, that are magnified around the 98.1° data point, of the grids shown in Figure D.2 are given in Figure D.3. These plots also indicate that there are no obvious discontinuities. Three different radial shell cross sections are shown and each indicates that even for the different magnitudes of volume emission there are no obvious discontinuities in the merged solutions. This method of joining inversions is

clearly acceptable for appending the results of successive inversions to produce a continuous data set that can cover as large an angular extent as required.

Cross Sections at Radial Shell 23 Illustrating No Discontinuity at Inversion Join



Cross Sections at Radial Shell 51 Illustrating No Discontinuity at Inversion Join



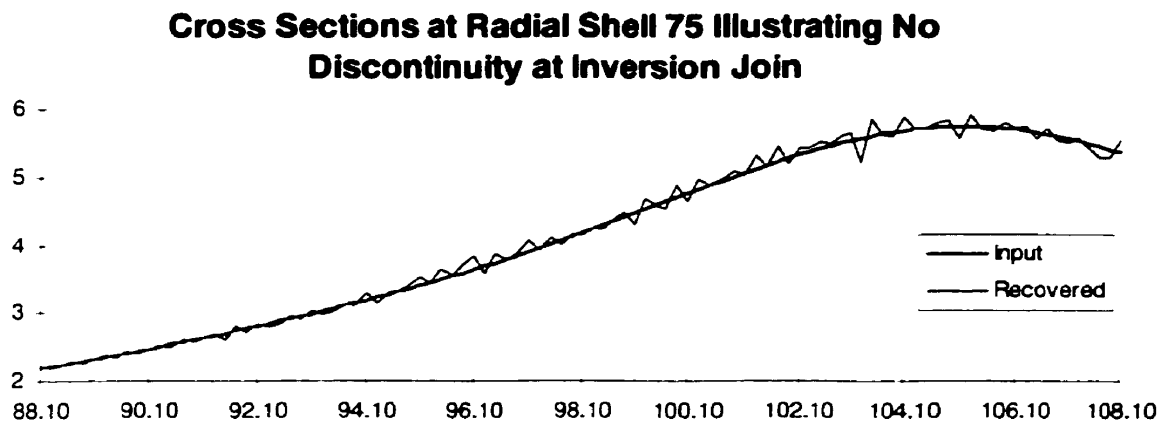


Figure D.3: Three cross sections for different magnitudes of the volume emission that illustrate no discontinuity at 98.1 ° where the join occurred

Computational speed is an underlying factor for the work in this thesis. Table D.2 shows the various calculation times and the determined error values associated with the recovery of an entire orbit of data. The table is subdivided into two sections. The first section corresponds to an image rate of one every two seconds while the other section is for a one image per second rate. As the angular overlap of the images is constant, independent of the image rate and the number of images used, it is the largest image set and lowest imaging rate that produces the fastest inversion. Conversely the smallest image set and the highest sampling rate results in the slowest inversion. This table also indicates that the error widths associated with the inversions is independent of the number of images in the observation set and depends only on the imaging rate. For these reasons, and the lack of computational power to easily handle observation sets with more than 700 images, the standard image set size is 700 for all imaging rates.

Imaging Rate (secs/Image)	Images per Inversion	Inversion Time (min:sec)	Error Fit Width (%)	Error Fit Peak Offset (%)
2	1100	11:24	1.86	-0.03
2	900	11:57	1.86	-0.03
2	700	13:11	1.86	-0.03

1	1100	30:45	0.59	0.00
1	900	32:08	0.59	0.00
1	700	41:08	0.59	0.00

Table D.2: Inversion times and accuracies for different numbers of images and imaging rates.

APPENDIX E

CALCULATION OF THE OXYGEN INFRARED ATMOSPHERIC BAND SPECTRUM

A band spectrum is identified by the position of its lines and their relative magnitudes and shapes. The calculation of these parameters (for both emission and absorption spectra) requires a knowledge of the energy levels of both the upper and lower states, the selection rules and the line broadening coefficients. The details of the calculations used to determine the synthetic emission and absorption spectra of the oxygen infrared atmospheric band are presented in this appendix. These synthetic spectra have been used to adapt the tomographic algorithm for use with the Odin/OISRIS measurements (Chapter 10).

E.1 Energy Levels for the States of the $O_2(a^1\Delta_g - X^3\Sigma_g^-)$ Spectra

In order to calculate the synthetic spectrum for the oxygen infrared atmospheric band ($a^1\Delta_g - X^3\Sigma_g^-$) the rotational energy levels of both the ($a^1\Delta_g$) upper state and the ($X^3\Sigma_g^-$) lower state must be known. The rotational energy of each level in the upper state is given by equation E.1 [Herzberg, 1950],

$$F(K) = \nu_{00} + B_0 K(K+1) - D_0 K^2 (K+1)^2 \quad [E.1]$$

where $\nu_{00} = 7882.39 \text{ cm}^{-1}$ is the energy difference between the two electronic states in the absence of both rotational and vibrational contributions. The coefficients $B_0 = 1.41783 \text{ cm}^{-1}$ and $D_0 = 4.86 \times 10^{-6} \text{ cm}^{-1}$ [Herzberg and Herzberg, 1947] are respectively the rotational constant for a rigid rotator and the correction term for centrifugal stretching in a non-rigid rotator.

The energy levels for the ($X^3\Sigma_g^-$) ground state of O_2 are represented by a more complicated model. The triplet nature of the state means that the total angular

momentum quantum number J'' has values, $J'' = K'' + 1$, K'' and $K'' - 1$ for every value of K'' . The interaction between the spin vector and the magnetic field produced by the rotation of the nuclei, as well as a spin-spin interaction, causes a small energy separation between levels with the same K'' and different values of J'' . The equations for the three energy levels are [Herzberg, 1950],

for $J'' = K'' + 1$

$$F_1(K) = B_0 K(K+1) - D_0 K^2 (K+1)^2 + B_0 (2K+3) - \lambda + \gamma(K+1) - \sqrt{B_0^2 (2K+3)^2 + \lambda^2 - 2\lambda B_0} \quad [\text{E.2}]$$

for $J'' = K''$

$$F_2(K) = B_0 K(K+1) - D_0 K^2 (K+1)^2 \quad [\text{E.3}]$$

for $J'' = K'' - 1$

$$F_3(K) = B_0 K(K+1) - D_0 K^2 (K+1)^2 - B_0 (2K-1) - \lambda - \gamma K + \sqrt{B_0^2 (2K-1)^2 + \lambda^2 - 2\lambda B_0} \quad [\text{E.4}]$$

with $B_0 = 1.43777 \text{ cm}^{-1}$, $D_0 = 4.913 \times 10^{-6} \text{ cm}^{-1}$, $\lambda = 1.984 \text{ cm}^{-1}$ and $\gamma = -0.00837 \text{ cm}^{-1}$ [Babcock and Herzberg, 1948]. The constants B_0 and D_0 have the same rigid rotator and correction for centrifugal stretching relationship as those for the $a^1\Delta_g$ upper state. The constants λ and γ are spin coupling constants that compensate for the spin-spin interaction.

E.2 Selection Rules for the $O_2(a^1\Delta_g - X^3\Sigma_g^-)$ Spectra

The selection rules for the $O_2(a^1\Delta_g - X^3\Sigma_g^-)$ transition are required to generate the synthetic spectra. The $O_2(a^1\Delta_g - X^3\Sigma_g^-)$ spectrum results from a spin forbidden magnetic dipole transition and the exact selection rules are $\Delta K = 0, \pm 1, \pm 2$, $\Delta J = 0, \pm 1$, and symmetric states go to symmetric states [Herzberg, 1950]. The anti-symmetric to anti-symmetric transitions are allowed, for $O_2(a^1\Delta_g - X^3\Sigma_g^-)$ transitions, but none are present as O_2 has zero nuclear spin. The nine branches allowed by the selection rules are shown in Figure E.1 [Herzberg, 1950].

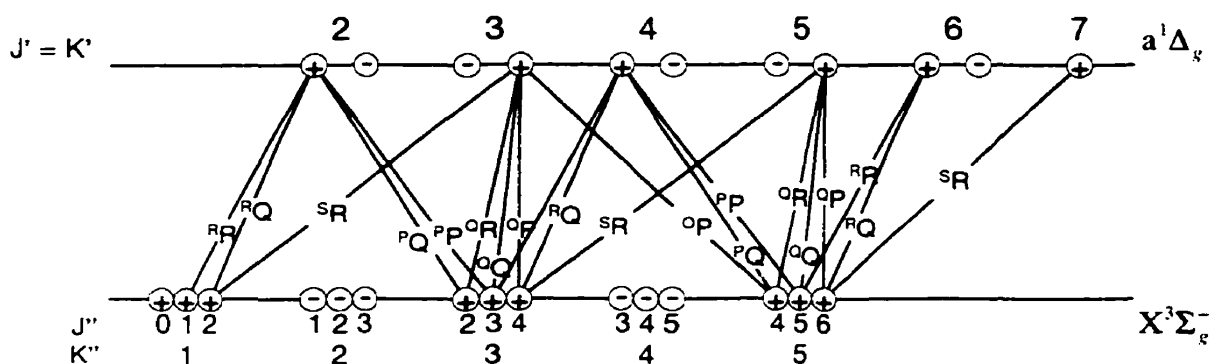


Figure E.1: The nine branches allowed in the $O_2(a^1\Delta_g - X^3\Sigma_g^-)$ spectrum.

E.3 Intensities of the $O_2(a^1\Delta_g - X^3\Sigma_g^-)$ Emission and Absorption Spectra

For the synthetic spectra the normalized intensity of each line is required. The Einstein A and B coefficients are only required to determine the effects of self absorption in the oxygen infrared atmospheric band.

For a particular $O_2(a^1\Delta_g \rightarrow X^3\Sigma_g^-)$ emission line (defined by E' and E'' , the energy of the upper and lower states respectively, J'' and K'' , the rotational quantum numbers of the lower state, the branch, and rotational temperature T) the intensity is given by [Herzberg, 1950],

$$I_{em}(E', E'', J'', \text{Branch}, T) = C_{em} S_{\text{Branch}}(J'') \nu_0 (E', E'')^3 e^{-E''/kT} \quad [\text{E.5}]$$

where ν_0 is the central wavenumber of the line, C_{em} is the emission constant, and $S_{\text{Branch}}(J'')$ is the line strength for the transition. The population of the excited upper state is considered to be in Local Thermodynamic Equilibrium (LTE) because the lifetime of the upper state, on the order of one hour, is long enough to thermally distribute the molecules.

Similarly for an absorption line the intensity is defined as [Herzberg, 1950],

$$I_{abs}(E'', J'', \text{Branch}, T) = C_{abs} S_{\text{Branch}}(J'') e^{-E''/kT} \quad [\text{E.6}]$$

where C_{abs} is the absorption constant. The ground state population is also in thermal equilibrium. It should be noted that the equations for emission and absorption intensities are both in photon units and not energies.

The line strength factors $S_{\text{Branch}}(J'')$ are given in Table E.1 [Van Vleck, 1934]. All J values in Table E.1 refer to J'' , the rotational quantum number in the lower ($X^3\Sigma_g^-$) state. The superscript in the branch designation refers to the change in K .

Branch	S_J	Branch	S_J	Branch	S_J
0P	$\frac{(J-2)(J-1)}{4(2J+1)}$	1P	$\frac{(J-2)(J-1)}{4J}$	2P	$\frac{(J-2)(J-1)(J+1)}{4J(2J+1)}$
1Q	$\frac{(J-1)(J+2)}{4(J-1)}$	2Q	$\frac{(J-1)(J+2)(2J+1)}{4J(J+1)}$	3Q	$\frac{(J-1)(J+2)}{4J}$
2R	$\frac{J(J+2)(J+3)}{4(J+1)(2J+1)}$	3R	$\frac{(J+2)(J+3)}{4(J+1)}$	4R	$\frac{(J+2)(J+3)}{4(2J+1)}$

Table E.1: Line strengths for $a^1\Delta_g - X^3\Sigma_g^-$ transitions.

The synthetic spectra included 135 separate lines; 15 lines from each of the 9 branches shown in Figure E.1. Additional lines made a negligible contribution to the intensity of the normalized spectra.

E.4 Line Shapes of the $O_2(a^1 \Delta_g - X^3 \Sigma_g^-)$ Spectra

Each of the individual lines in the oxygen infrared atmospheric band emission and absorption spectra are both Doppler and pressure broadened. In modeling the synthetic spectral lines, broadening must be done in a manner that properly considers the requirements of both precision and computational speed.

A Doppler broadened line has a profile given by

$$\phi(\nu) = \frac{2}{\omega_D} \sqrt{\frac{\ln 2}{\pi}} e^{-\frac{(\nu - \nu_0)^2}{\omega_D^2}} \quad [E.7]$$

where the width of Doppler broadened lines is

$$\omega_D = \nu_0 \left(\frac{8 \ln(2) k_B T}{m c^2} \right)^{\frac{1}{2}}. \quad [E.8]$$

In equation E.8 ν_0 is the central wavenumber of the line, m is the mass of the O_2 molecule and T is the rotational temperature. The true Voigt line shape, which is the convolution of the Lorentz (pressure) and Doppler (temperature) broadened line shapes, is precisely represented by

$$\phi(\nu) = \frac{2}{\omega_D} \sqrt{\frac{\ln 2}{\pi}} K(x, y) \quad [E.9]$$

where

$$K(x, y) = \text{Re}[w(z)] = \text{Re}[e^{-z^2} (1 - \text{erf}(-iz))] \quad [E.10]$$

with $z = x + iy$, $x = \frac{\nu - \nu_0}{\omega_D} 2\sqrt{\ln 2}$, $y = \frac{\omega_L}{\omega_D} \sqrt{\ln 2}$ and ω_L is the pressure broadened halfwidth of the line.

This true Voigt profile is computationally intensive as it requires the evaluation of $w(z)$. It has been shown [Abramowitz and Stegun, 1972] that this evaluation can be approximated by different forms, for x and y contained in three separate regions, with an

error less than 10^{-6} . These regions are : **Region III** where $x > 6$ or $y > 6$; **Region II** where $x > 3.9$ or $y > 3.0$; and **Region I** which contains all other points in the x, y plane.

The functional form of $w(z)$ in **Region I** is

$$w(z) = e^{-(x^2-y^2)} [\cos(2xy) + i \sin(2xy)] \left(1 - \frac{2}{\sqrt{\pi}} \sum_n^{n_{\max}} \frac{(-1)^n (-iz)^{2n+1}}{n!(2n+1)} \right). \quad [\text{E.11}]$$

This is extremely computationally intensive due to the series expansion and the number of terms required for convergence. From a comparison of calculated values with those tabulated in Abramowitz and Stegun it was found that $n_{\max} = 150$ provided the necessary accuracy in **Region I**.

Approximations are also given by Abramowitz and Stegun that are accurate for **Regions II and III**. These are of the form,

$$w(z) = iz \left(\frac{0.4613135}{z^2 - 0.1901635} + \frac{0.09999216}{z^2 - 1.7844927} + \frac{0.002883894}{z^2 - 5.5253437} \right) \quad [\text{E.12}]$$

for **Region II** and

$$w(z) = iz \left(\frac{0.5124242}{z^2 - 0.2752551} + \frac{0.05176536}{z^2 - 2.724745} \right) \quad [\text{E.13}]$$

for **Region III**.

An improvement in computational speed over that for the method of Abramowitz and Stegun is possible if the two widths, the Doppler and Lorentz, are combined into a representative line width given by the Voigt width, ω_V , where

$$\omega_V = \frac{\omega_L}{2} + \left(\omega_D^2 + \frac{\omega_L^2}{4} \right)^{\frac{1}{2}}. \quad [\text{E.14}]$$

The entire Voigt profile can then be approximated by

$$\phi(\nu) = \frac{\left(1 - \frac{\omega_L}{\omega_V}\right) e^{-\left(\frac{\ln 2}{\omega_V}\right)^2 \left(\frac{\Delta\nu}{\omega_V}\right)^2} + \frac{\omega_L}{\omega_V} \frac{1}{1 + 4 \left(\frac{\Delta\nu}{\omega_V}\right)^2} + 0.0016 \left(1 - \frac{\omega_L}{\omega_V}\right) \frac{\omega_L}{\omega_V} \left[e^{-0.4 \left(\frac{\Delta\nu}{\omega_V}\right)^{2.25}} - \frac{10}{10 + \left(\frac{\Delta\nu}{\omega_V}\right)^{2.25}} \right]}{\omega_V \left(1.076 + 0.447 \frac{\omega_L}{\omega_V} + 0.057 \left(\frac{\omega_L}{\omega_V}\right)^2\right)}. \quad [\text{E.15}]$$

This formulation was first used by Whiting [1968] and then by Evans *et al.* [1970].

Both equations E.10 and E.15 have been included here for completeness, although for the purpose of this thesis the less computationally intensive Voigt profile (equation E.15) has been used for absorption lines. The computationally efficient Doppler profile has been used for emission lines as they originate where the pressure is low (Evans *et al.*, 1970).

E.5 Algorithm for the $O_2(a^1\Delta_g - X^3\Sigma_g^-)$ Synthetic Spectra

The algorithms for generating the normalized synthetic emission and absorption spectra are identical except for the relative line intensities and the line profiles. The procedure for any given temperature is:

- i) Calculate the central wavenumber for the first fifteen lines in each branch (135 lines in total); the selection rules are indicated in Figure E.1. This requires subtraction of the lower state energy (given by equations E.2, E.3 or E.4) from the upper state energy (given by equation E.1).
- ii) Calculate the normalized intensity of each line using either equation E.5 (emission) or equation E.6 (absorption) and the line strengths in Table E.1.
- iii) Calculate the line shape for each line using equation E.7 or E.15. Each line is broken into 51 positions, 25 on either side of the central wavenumber. The wavenumber range covered by these 51 divisions is made sufficiently large to completely contain the line (*i.e.* numerical integration of the broadened line gives the line intensity to within 0.001%).

The final result is a synthetic spectrum that has intensities associated with 6885 (135 lines x 51 divisions/line) wavenumber positions. The numerical precision is such that if each spectral line is integrated and the results from each line summed the corresponding total band intensity is accurate to within 0.01%. Two sample spectra, both emission and absorption, for a rotational emission temperature of 300 K are shown in Figure E.2. The individual lines appear as delta functions as the resolution is not sufficient to indicate their shapes (Figure 10.4).

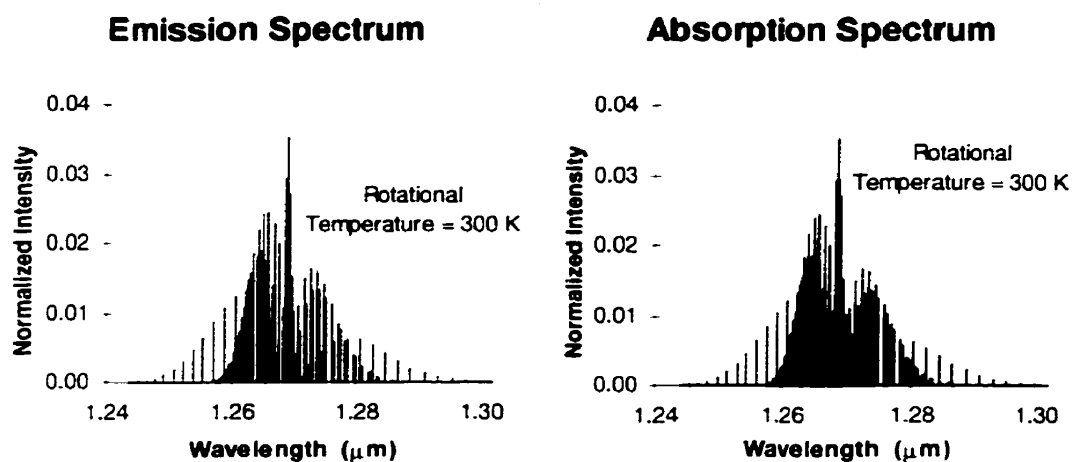


Figure E.2: Emission and absorption spectra for a 300 K rotational temperature. These two spectra are visually identical.

APPENDIX F

ATTENUATION OF $O_2(a'\Delta_g \rightarrow X^3\Sigma_g^-)$ THROUGH SELF ABSORPTION

The $O_2(a'\Delta_g \rightarrow X^3\Sigma_g^-)$ emission spectrum is attenuated by absorption of ground state O_2 . As oxygen comprises approximately 20% of the total atmospheric number density self absorption can be significant in the lowest altitudes along a line of sight from the source region to the detector.

The major source of the attenuation of the total band signal comes from self absorption by the line with the same transition as the emission line. However, it is possible at lower altitudes, where there is significant pressure broadening, to have absorption by neighbouring lines.

Thus to calculate the extinction of a line at any point in its Voigt profile the Einstein B value, the density of the absorbers and the normalized absorption spectrum (Appendix E), at the absorbing temperature and pressure must be known. This information and the knowledge of the path length in the homogeneous absorbing region determines the optical depth at each point in the emission line profile (Appendix E). In this appendix the details of the calculation of the optical depths are presented.

F.1 Calculation of Extinction Coefficients Due to the $O_2(a'\Delta_g \leftarrow X^3\Sigma_g^-)$ Absorption Spectrum

The attenuation of an incident beam due to a transition from molecular state n to state m can be expressed by [Herzberg, 1950]

$$I_{abs}^{nm} = I_0^{nm} N_m B_{nm} h\nu_{nm} dx \left[\frac{erg}{cm^2 s} \right] \quad [F.1]$$

where I_{abs}^{nm} is the total absorbed intensity, I_0^{nm} is the incident intensity/cm⁻¹, N_m is the number density of the molecular absorber, B_{nm} is the Einstein coefficient for absorption

for the particular transition, h is the Planck constant, ν_{nm} is the wavenumber of the incident radiation, and dx is the differential thickness of the absorbing layer.

This equation is well suited to the calculation of the self-absorption of an oxygen infrared atmospheric band emission line divided into small wavenumber intervals, where the intensity may be assumed constant over each division. Figure F.1 is a representation of an emission line partitioned in this manner. The emitted intensity is assumed constant across each rectangular division.

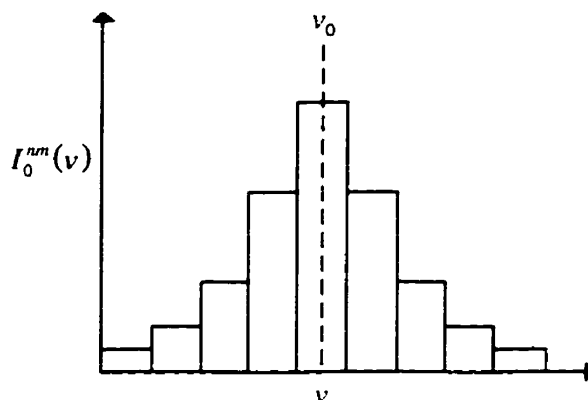


Figure F.1: Histogram representation of a line shape. Each bar represents a region of constant emission or absorption.

The intensity per unit wavenumber within any interval is given by

$$I_0^{nm}(\nu) = I_{tot}^{nm} \phi_c(\nu) \left[\frac{\left(\frac{\text{erg}}{\text{cm}^{-1}} \right)}{\text{cm}^2 \text{s}} \right] \quad [\text{F.2}]$$

where I_{tot}^{nm} is the total integrated intensity of the line and $\phi_c(\nu) = \left[\frac{1}{\text{cm}^{-1}} \right]$ is the line profile such that

$$\int_{-\infty}^{\infty} \phi_c(\nu) d\nu = 1. \quad [\text{F.3}]$$

For the $O_2(a^1\Delta_g \rightarrow X^3\Sigma_g^-)$ emission lines this distribution can be assumed Gaussian with no significant loss of precision [Evans *et al.*, 1970]. Thus, for a wavenumber interval, with central wavenumber ν , shown in Figure F.1 the incident intensity per unit wavenumber at all points in the rectangle can be expressed as

$$I_0^{nm}(\nu) = \frac{I_{tot}^{nm}}{\sqrt{2\pi}\sigma} e^{-\left(\frac{\Delta\nu^2}{2\sigma^2}\right)} \quad [F.4]$$

where

$$\sigma = \frac{\nu_0}{c} \left(\frac{kT}{m} \right)^{\frac{1}{2}} \quad [F.5]$$

and $\Delta\nu$ is the wavenumber difference from the line centre. Equation F.4 is the incident intensity used in Equation F.1 for self absorption.

The total number of absorbers is the number of O_2 molecules in the state m that can absorb photons in the wavenumber interval. The total number of molecules with $\Lambda'' = 0$, $\nu'' = 0$ and J'' is [Herzberg, 1950]

$$N_{J''} = \frac{(2J'' + 1)e^{-\frac{F(J'')hc}{kT}}}{Q_{J''}} [O_2] \quad [F.6]$$

where

$$Q_{J''} = \sum_{J''} (2J'' + 1)e^{-\frac{F(J'')hc}{kT}} \quad [F.7]$$

is the partition function for the J'' state, $F(J'')$ is the energy of the state and $[O_2]$ is the atmospheric number density. This assumes that all oxygen molecules in the atmosphere are in the electronic and vibrational ground states.

The probability that molecules in the state J'' can absorb photons of wavenumber ν is distributed, about the central wavenumber ν_0 , with a Voigt profile. The total number of molecules distributed in the wavenumber range is

$$N_m = N_{J''} \phi_a(v) dv \quad [\text{F.8}]$$

where $\phi_a(v)$ is the normalized Voigt profile such that

$$\int_{-\infty}^{\infty} \phi_a(v) dv = 1 \quad [\text{F.9}]$$

and dv is the wavenumber range. Substitution of equation F.8 into F.6 and the result into F.1 gives

$$I_{abs}^{nm} = I_0^{nm}(v) \frac{[O_2] (2J'' + 1) e^{-\alpha(J'')} \phi_a(v) dv}{Q_{r''}} B_{nm} h \nu_{nm} dx \quad [\text{F.10}]$$

where

$$\alpha(J'') = \frac{F(J'') hc}{kT} \quad [\text{F.11}]$$

The Einstein coefficient B_{mn} for a transition J'' to J' can be written as

$$B_{J''J'} = \frac{Q_{r''} \nu_{00} A(0,0) S_{J'}}{\left[\sum_{lines} \nu_{J''J'}^4 S_{J'} e^{-\alpha(J')} \right] (2J'' + 1) 8hc\pi} \quad [\text{F.12}]$$

where $A(0,0)$ is the Einstein A value for the vibrational 0-0 transition and ν_{00} is the wavenumber of the band origin.

Substitution of equation F.12 into F.10 and rearranging the terms gives

$$I_{abs}^{nm} = I_0^{nm}(v) dv \frac{[O_2] e^{-\alpha(J'')} \phi_a(v) \nu_{00} \nu_{J''J'} A(0,0) S_{J'}}{8c\pi \left[\sum_{lines} \nu_{J''J'}^4 S_{J'} e^{-\alpha(J')} \right]} \frac{Q_{r''}}{Q_{r''}} dx \quad [\text{F.13}]$$

which is used to give a differential equation with respect to $\frac{dl}{dx}$ and obtain the extinction value

$$\beta(\nu) = \frac{[O_2] e^{-\alpha(J')} \phi_a(\nu) \nu_{00} \nu_{JJ'} A(0,0) S_J Q_r}{8c\pi \left[\sum_{lines} \nu_{JJ'}^4 S_J e^{-\alpha(J')} \right] Q_r} \quad [F.14]$$

If this value is multiplied by the absorption path through a homogeneous layer then the optical depth for that layer, for the fraction of the emission line, is obtained and

$$I_f(\nu) = I_0(\nu) e^{-\beta(\nu)\Delta x} \quad [F.15]$$

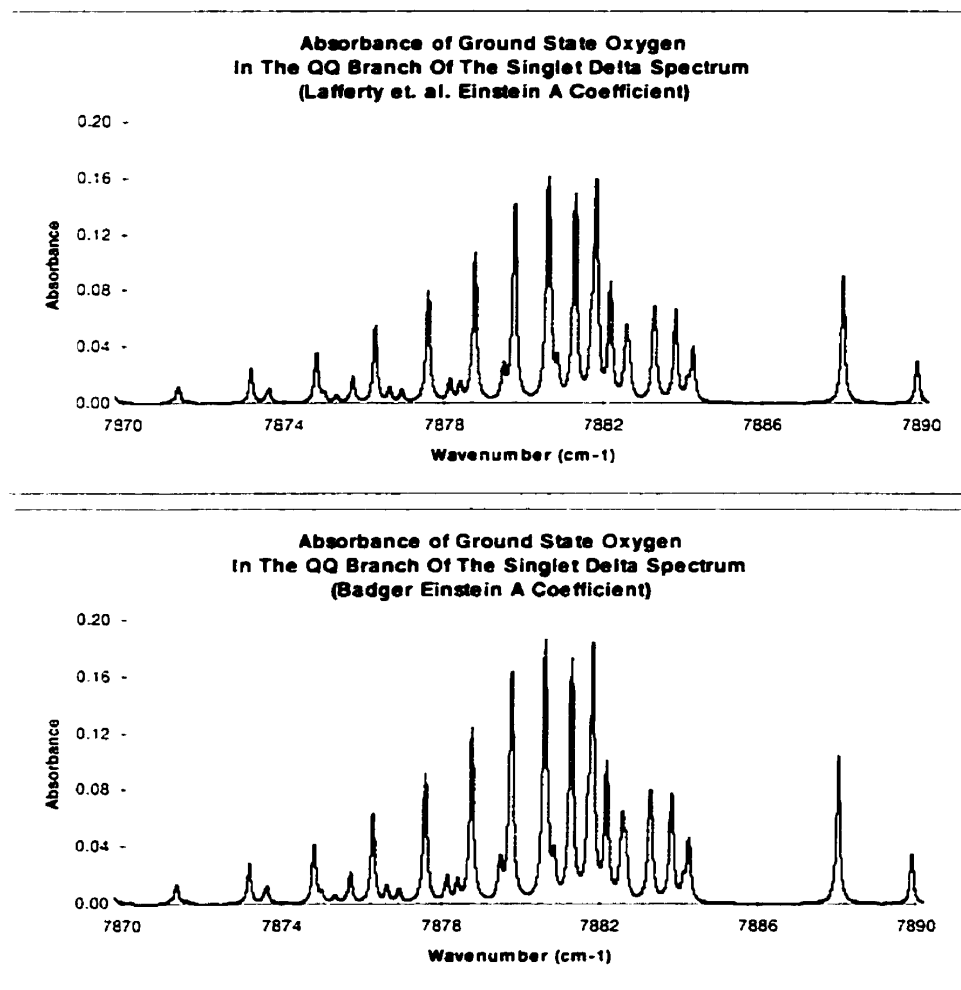
is the intensity that remains, where $I_0(\nu)$ is the total intensity within the wavenumber interval.

F.2 The Selection of Coefficients and Comparison With Measured Values

The Einstein A value for the $O_2(a^1\Delta_g \rightarrow X^3\Sigma_g^-)$ transition is a matter of considerable contention. In this work the widely accepted value of $2.58 \times 10^{-4} \text{ s}^{-1}$ (Badger *et al.*, 1965) has been used. This value is slightly larger than a recently reported value, $2.237 \times 10^{-4} \text{ s}^{-1}$ (Lafferty *et al.*, 1998). The pressure broadening coefficient also has some uncertainty. The work of Lafferty *et al.* suggested the pressure broadening coefficient was dependent upon the quantum number N with an average value of $0.1024 \text{ cm}^{-1} \text{ atm}^{-1}$. This is in disagreement with the previously accepted value, $0.08 \text{ cm}^{-1} \text{ atm}^{-1}$ (Badger *et al.*, 1965), that has been used in this thesis. In this section the effects on the model of the values used in this thesis and those determined by Lafferty *et al.* are compared and are shown to give good general agreement.

Figure F.2 contains three plots that relate the absorbance, on a \ln scale, to wavenumber for lines contained within the $^Q Q$ branch of the absorption spectrum. The first two plots are calculated values while the third plot is the actual measurements made by Lafferty *et al.* for an O_2 pressure of 104.3 kPa and an optical path length of 84.05 m. The measurements were made at 0.01 cm^{-1} resolution, although the calculations are for a higher resolution.

The first plot in Figure F.2 illustrates the calculated absorbance values for conditions identical to the measurements made by Lafferty *et al.* In this plot the Lafferty *et al.* Einstein A value and their average pressure broadening coefficients were used with the current model. There is excellent agreement between the calculated absorbance values and those measured by Lafferty *et al.* and shown in the final plot of Figure F.2. The second plot contains the calculated absorbance values for the same experiment but the Einstein A value and pressure broadening coefficients are those that are used in this thesis. This plot, which contains line shapes that peak at marginally higher values, is expected because the Einstein A value is higher and the pressure broadening coefficient is lower.



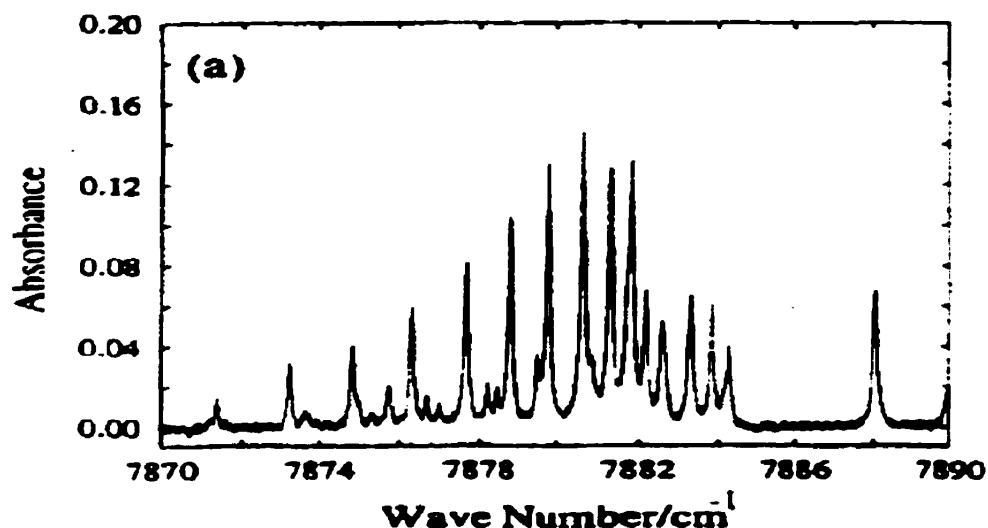


Figure F.2: Comparison between the absorbance values used throughout this thesis with those measured by Lafferty *et al.* [1998]. The first two plots are models while the third is an actual measurement.

The differences between the absorbance values used in this thesis and those measured by Lafferty *et al.* are small. For the purposes of the present work they may be considered insignificant. Small changes in the absorbance do not affect the total fraction of the band that is attenuated through self absorption at altitudes where the pressure is significantly lower than that used in the Lafferty experiment. Thus, the line-by-line calculation of the self absorption of the oxygen infrared atmospheric band emissions used in this thesis is appropriate.

F.3 Method Used to Calculate Absorption Correction Coefficients

The absorption correction coefficients α_{ij} that refer to the fraction of the band from cell j , that is seen by the detector along line of sight i , require a line-by-line absorption calculation that follows equations F.14 and F.15. As mentioned previously the oxygen infrared atmospheric band spectrum is divided into 135 lines and each of these lines is further subdivided into 51 partitions that totally cover the emission. The line-by-line calculation of the α_{ij} coefficients has been made at this resolution. It was found that for any increase in either the number of spectral lines or the number of divisions for each

line there is no significant gain in precision. Thus, this resolution was chosen for both computational speed and precision.

The geometry used to calculate the line by line absorption, along a given line of sight, is shown in Figure F.3. A two dimensional grid, similar to the emission grids discussed in this thesis (Section 3.3.3), is used. At each grid cell, that has both angular and radial boundaries, both the atmospheric temperature and density are required. It is not sufficient to use a one dimensional model as the Earth's oblateness would result in altitude errors. Using the geometry outlined in Figure F.3 it is a simple, although computationally extensive process, to determine α_{ij} at any point along the line of sight.

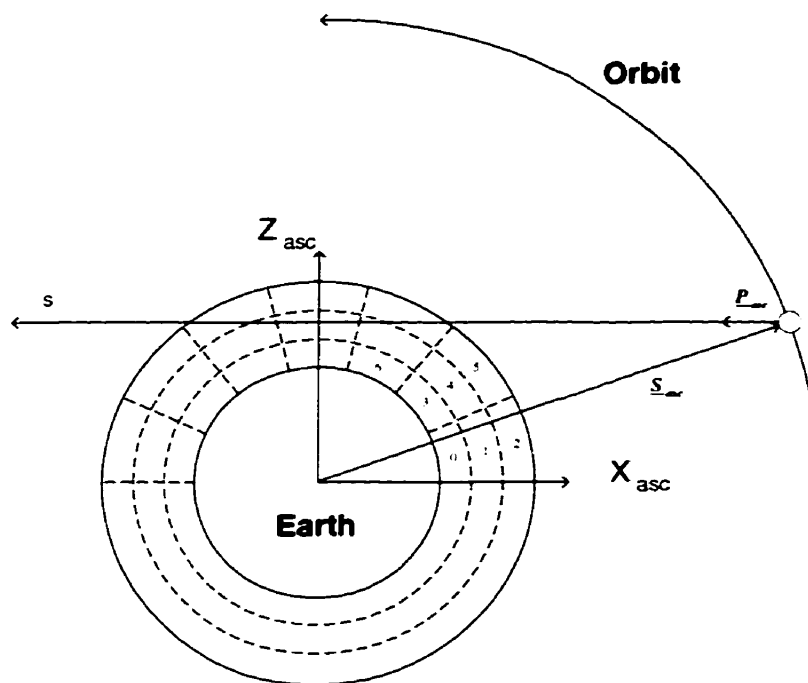


Figure F.3: The geometry used to calculate the remaining band signal from any position along any given line of sight.

At each point, along any given line of sight, the cell that contains this point can be determined with the method outlined in Appendix B. The atmospheric temperature can be determined for this point and a synthetic emission spectrum generated following the

method outlined in Appendix E. Synthetic absorption spectra, and therefore optical depths, can be generated for all the points along the line of sight from the point of interest through to the satellite. The extinction values are calculated at each of the 51 points within each spectral lines according to equation F.14 where neighbouring lines are allowed to overlap. The optical depths are then calculated by multiplication of the extinction by the path length through the grid cell. The spatial resolution of the step size between points is dependent on the grid cell resolution. After the total optical depth, the sum of the depths for each grid cell between the point of interest and the satellite, has been calculated equation F.15 can be applied to each point in the emission spectrum to give the attenuated spectrum, or the spectrum from the point of interest as seen by the detector. Examples of both the emitted and absorbed spectra for a cell at 40 km above the surface of the Earth, viewed along a 40 km tangent altitude line of sight, are given in Figure F.4.

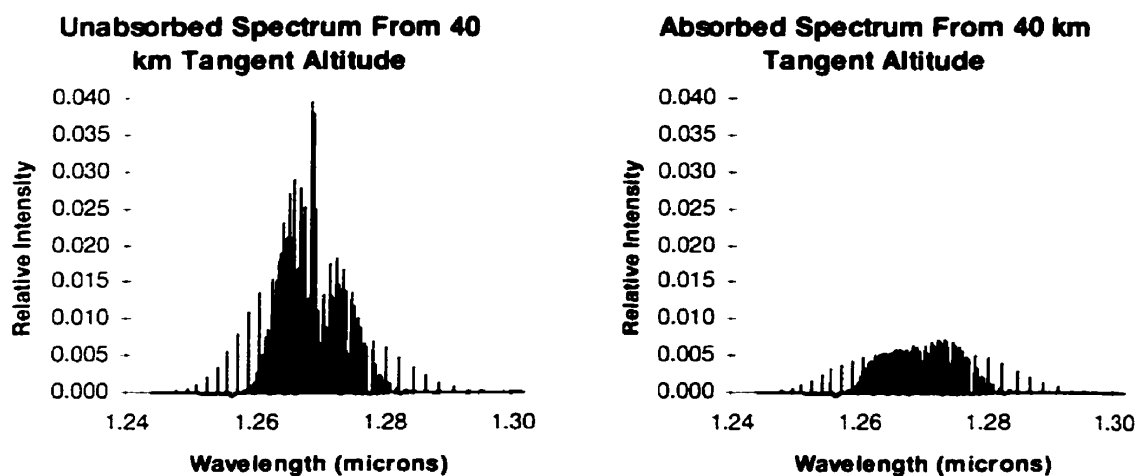


Figure F.4: $O_2(a^1\Delta_g \rightarrow X^3\Sigma_g^-)$ emission spectrum emitted at 40 km and the same spectrum as seen by a satellite borne instrument looking along a 40 km tangent altitude line of sight.

Integration of the attenuated line intensities in the second plot of Figure F.4 gives the fraction of the band that reaches the detector. As the Odin/OSIRIS instrument has an optical filter before the detector the total band is not measured by the detector. Figure

F.5 illustrates the effect for the 1.266 μm filter, one of the OSIRIS channels, superimposed on the remaining band signal. It is clear from Figure F.5 that the entire band is not visible to the OSIRIS detector. The α_{ij} value for this particular example is calculated by first multiplying each of the attenuated line intensities with the filter transmission at the appropriate wavelength and summing over the lines. For this example the α_{ij} value was found to be 0.19.

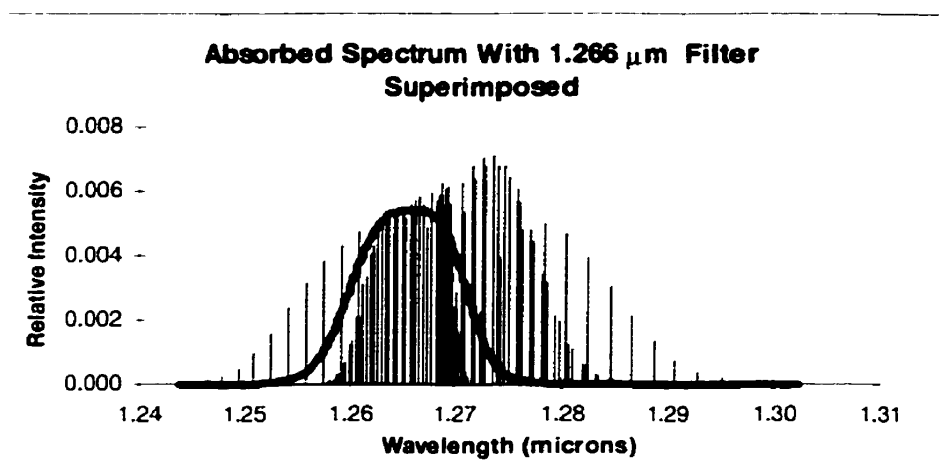


Figure F.5: Remaining band signal from the second plot of Figure F.4 with the Odin/OSIRIS 1.266 μm filter superimposed upon it.

Using the method outlined above the attenuation coefficient, that includes the attenuation of the signal due to the filter, can be calculated for any point along any line of sight. This was done, at high spatial resolution, for all lines of sight required by the tomographic recovery. Examples of the absorption correction factors are given in Figure 10.6 and a cubic spline was used to interpolate the absorption correction coefficients at the required points along the lines of sight.

REFERENCES

- Abramowitz, M. and I.A. Stegun, *Handbook of Mathematical Functions*, (Dover Publications, Inc., New York, 1972).
- Anderson, J.M.M., B.A. Mair, M. Rao and C. Wu, Weighted least-squares reconstruction methods for positron emission tomography, *IEEE Trans. On Med. Imag.*, **16**, 159 (1997).
- Austen, J.R., S.J. Franke and C.H. Liu, Ionospheric imaging using computerized tomography, *Radio Science*, **23**, 299 (1988).
- Babcock, H.D. and L. Herzberg, Fine structure of the red system of atmospheric oxygen bands, *Astrophys. J.*, 108, 167 (1948).
- Badger, R.M., A.C. Wright and R.F. Whitlock, Absolute intensities of the discrete and continuous absorption bands of oxygen gas at 1.26 and 1.065 μ and the radiative lifetime of the $a^1\Delta_g$ state of oxygen, *J. Chem. Phys.*, **43**, 4345 (1965).
- Bertero, M. and P. Boccacci, *Introduction to Inverse Problem in Imaging* (Institute of Physics Publishing, London, 1998).
- Blankespoor, S.C., X. Wu, K. Kalki, J.K. Brown, H.R. Tang, C.E. Cann and B.H. Hasewaga, Attenuation correction of SPECT using x-ray CT on an emission-transmission CT system: Myocardial perfusion assessment, *IEEE Trans. On Nucl. Sci.*, **43**, 2263 (1996).
- Chinn, G. and S. Huang, A general class of preconditioners for statistical iterative reconstruction of emission computed tomography, *IEEE Trans. On Med. Imag.*, **16**, 1 (1997).
- Cormack, A.M., Representation of a function by its line integrals, with some radiological applications, *J. Appl. Phys.*, **34**, 2722 (1963).
- Cormack, A.M., Representation of a function by its line integrals, with some radiological applications. II, *J. Appl. Phys.*, **35**, 2908 (1964).
- Csiszar, I. and G. Tusnady, Information geometry and alternating minimization procedures, *Statistics & Decisions*, **Suppl. No. 1**, 205 (1984).
- Daube-Witherspoon, M.E. and G. Muehllehner, An iterative image space reconstruction algorithm suitable for volume ECT, *IEEE Trans. On Med. Imag.*, **MI-5**, 61 (1986).

Dempster, A.P., N.M. Laird and D.B. Rubin, Maximum likelihood from incomplete data via the EM Algorithm, *Journal of the Royal Statistical Society*, **39**, 1 (1977).

De Pierro, A.R., Multiplicative Iterative Methods in Computed Tomography, in *Mathematical Methods in Tomography* (eds G.T. Herman, A.K. Louis and F. Natterer) Springer-Verlag., Berlin-Heidelberg, 167-186, 1991.

Evans, W.F.J., H.C. Wood and E.J. Llewellyn, Transmission of the infrared oxygen emission at 1.27 μ in the atmosphere, *Can. J. Phys.*, **48**, 747 (1970).

Fesen, C.G., and P.B. Hays, Two-dimensional inversion technique for satellite airglow data, *Appl. Opt.*, **21**, 3784 (1982).

Fessler, J.A., E.P. Ficaro, N.H. Clinthorne and K. Lange, Grouped-coordinate ascent algorithms for penalized-likelihood transmission image reconstruction, *IEEE Trans. On Med. Imag.*, **16**, 166 (1997).

Fuchs, C., Maximum likelihood estimation and model selection in contingency tables with missing data, *Journal of the American Statistical Association*, **77**, 270 (1982).

Gilbert, P., Iterative methods for the reconstruction of three-dimensional objects from their projections, *J. Theoret. Biol.*, **36**, 105 (1972).

Gordon, R. and G.T. Herman, Three-dimensional reconstruction from projections, a review of algorithms, *Int. rev. Cytol*, **38**, 111 (1974).

Gordon, R., R. Bender and G.T. Herman, Algebraic reconstruction techniques (ART) and three-dimensional electron microscopy and x-ray photography, *J. Theoret. Biol.*, **29**, 471 (1970).

Green, P.J., Bayesian reconstructions from emission tomography data using a modified EM algorithm, *IEEE Trans. On Med. Imag.*, **9**, 84 (1990).

Heaton, J.A.T., S.E. Pryse and L. Kersley, Improved background representation, ionosonde input and independent verification in experimental tomography, *Ann. Geophysicae*, **13**, 1297 (1995).

Herman, G.T., *Image Reconstruction From Projections* (Academic Press 1980).

Herzberg, G. *Spectra of Diatomic Molecules* (Van Nostrand, New York, 1950).

Herzberg L. and G. Herzberg, Fine structure of the infrared atmospheric oxygen bands, *Astrophys. J.*, **105**, 353 (1947).

Kersley, L., J.A.T. Heaton, S.E. Pryse and T.D. Raymond, Experimental ionospheric tomography with ionosonde input and EISCAT verification, *Ann. Geophysicae*, **11**, 1064 (1993).

Lafferty, W.J., A.M. Solodov, C.L. Lugez and G.T. Fraser, Rotational line strengths and self-pressure-broadening coefficients for the 1.27- μm $a^1\Delta_g - X^3\Sigma_g^-$, $v = 0-0$ band of O_2 , *Applied Optics*, **37**, 2264 (1998).

Levitan, E., G.T. Herman, A Maximum *a posteriori* probability expectation maximization algorithm for image reconstruction in emission tomography, *IEEE Trans. On Med. Imag.*, **MI-6**, 185 (1987).

Lipinski, B., H. Herzog, E. Rota Kops, W. Oberschelp and H.W. Muller-Gartner, Expectation maximization reconstruction of positron emission tomography images using anatomical magnetic resonance, *IEEE Trans. On Med. Imag.*, **16**, 129 (1997).

Lloyd, N.D. and E.J. Llewellyn, Deconvolution of blurred images using photon counting statistics and maximum probability, *Can. J. Phys.*, **67**, 89 (1989).

Matej, S. and R.M. Lewitt, Practical considerations for 3-D image reconstruction using spherically symmetric volume elements, *IEEE Trans. On Med. Imag.*, **15**, 68 (1996).

McDade I.C., N.D. Lloyd and E.J. Llewellyn, A rocket tomography measurement of the N_2^+ 3914 Å emission rates within an auroral arc, *Planet. Space. Sci.*, **39**, 895 (1991a).

McDade, I.C. and E.J. Llewellyn, Inversion techniques for recovering two-dimensional distributions of auroral emission rates from rocket photometer measurements, *Can. J. Phys.*, **69**, 1059 (1991b).

McDade, I.C. and E.J. Llewellyn, Satellite airglow limb tomography: methods for recovering structured emission rates in the mesospheric airglow layer, *Can. J. Phys.*, **71**, 552 (1993).

Mitchell, L.N., L. Kersley, J.A.T. Heaton and S.E. Pryse, Determination of the vertical electron density profile in ionospheric tomography : experimental results, *Ann. Geophysicae*, **15**, 747 (1997).

Nygren, T., M. Markkanen, M. Lehtinen, E.D. Tereshchenko and B.Z. Khudukon, Stochastic inversion in ionospheric tomography, *Radio Science*, **32**, 2359 (1997).

Pan, T., B.M.W. Tsui and C.L. Byrne, Choice of initial conditions in ML reconstruction of fan-beam transmission with truncated projection data, *IEEE Trans. On Med. Imag.*, **16**, 426 (1997).

Pryse, S.E., L. Kersley, D.L. Rice, C.D. Russell and I.K. Walker, Tomographic imaging of the ionospheric mid-latitude trough, *Ann. Geophysicae*, **11**, 144 (1993).

Raymund T.D., S.E. Pryse, L. Kersley and J.A.T. Heaton, Tomographic reconstruction of ionospheric electron density with european incoherent scatter radar verification, *Radio Science*, **28**, 8111 (1993).

Raymund, T.D., J.R. Austen, S.J. Franke, C.H. Liu, J.A. Klobuchar and J. Stalker, Application of computerized tomography to the investigation of ionospheric structures, *Radio Science*, **25**, 771 (1990).

Roble, R.G. and P.B. Hays, A technique for recovering the vertical number density profile of atmospheric gases from planetary occultation data, *Planet. Space. Sci.*, **20**, 1727 (1972).

Shepp, L.A., Y. Vardi, Maximum likelihood reconstruction for positron emission tomography, *IEEE Trans. Med. Imag.*, **MI-1**, 113 (1982).

Snyder, D.L., M.I. Miller, L.J. Thomas Jr. And D.G. Politte, Noise and edge artifacts in maximum-likelihood reconstructions for emission tomography, *IEEE Trans. On Med. Imag.*, **MI-6**, 228 (1987).

Solomon, S.C., P.B. Hays and V.J. Abreu, Tomographic inversion of satellite photometry, *Appl. Opt.*, **23**, 3409 (1984).

Solomon, S.C., P.B. Hays and V.J. Abreu, Tomographic inversion of satellite photometry. Part 2, *Appl. Opt.*, **24**, 4134 (1985).

Van Vleck. J.H., Magnetic dipole radiation and the atmospheric absorption bands of oxygen, *The Astrophysical Journal*, **80**, 161 (1934).

Vardi, Y., L.A. Shepp and L. Kaufman, A statistical model for positron emission tomography, *Journal of the American Statistical Association*, **89**, 8 (1985).

Warshaw, G.D., D.-L. Desaulniers and D.A. Degenstein, Optical design and performance of the odin uv/visible spectrograph and infrared imager instrument, *Proceedings of the Microsatellite Conference, Logan , UT* (1996).

Welch, A. and G.T. Gullberg, Implementation of a model-based non-uniform scatter correction scheme for SPECT, *IEEE Trans. On Med. Imag.*, **16**, 717 (1997).

Whiting, E.E., An empirical approximation to the voigt profile, *J. Quant. Spectry. Radiative Transfer*, **8**, 1379.

Yee, E., K.V. Paulson and G.G. Shepherd, Minimum cross-entropy inversion of satellite photometer data, *Appl. Opt.*, **26**, 2106 (1987).

BIOGRAPHICAL

- 1964 Born in Wynyard, Saskatchewan.
- 1965 B.Sc. (Computer Science), University of Saskatchewan.
- 1993 B.E. (Engineering Physics), University of Saskatchewan.
- 1994-96 CSA - U. of Sask - ROUTES Inc., Junior Scientist representing OSIRIS Science Team.
- 1998 CSA- U of Sask, Research Engineer for the Odin/OSIRIS instrument.

HONOURS

Undergraduate Scholarships (College of Engineering), 1992-93.

NSERC PGS A/B, 1993-97.

Currie Scholar, ISAS, University of Saskatchewan, 1996.

PetroCan Young Innovators Award, University of Saskatchewan, 1996.

PUBLICATIONS

I.K. Khabibrakhmanov, **D.A. Degenstein** and E.J. Llewellyn. (1999) Mesospheric Ozone: Determination from orbit with the OSIRIS instrument on Odin, *Can. J. Phys.*, accepted for publication.

E.J. Llewellyn, **D.A. Degenstein**, I.C. McDade, R.L. Gattinger, R. King, R. Buckingham, E.H. Richardson, D.P. Murtagh, W.F.J. Evans, B.H. Solheim, K. Strong, and J.C. McConnell. (1997) OSIRIS - an application of tomography for absorbed emissions in remote sensing, *Applications of Photonic Technology 2*, (Edited by G.A. Lampropoulos and R.A. Lessard), Plenum Press, New York, 627-632.

G. Warshaw, D.-L. Desaulniers and **D.A. Degenstein**. (1996) Optical design and Performance of the Odin uv/visible Spectrograph and Infrared Imager Instrument, Proceedings of the Microsatellite Conference, Logan, UT.

E.J. Llewellyn, W.S.C. Brooks, **D.A. Degenstein**, W.F.J. Evans, I.C. McDade, J.C. McConnell, B.H. Solheim, R. King, R.L. Gattinger, A. Hauchecorne, G. Leppelmeier, D. Murtagh, J. Stegman and G. Witt. (1995) The Measurement of Vertical Structure in the Airglow Using the OSIRIS Instrument on the Odin Satellite. *IAGA/IUGG Congress*, Boulder, Colorado.

E.J. Llewellyn, W.S.C. Brooks, **D.A. Degenstein** and I.C. McDade, Atomic Oxygen Concentrations Determined From Observations of the Oxygen Atmospheric Band, *EOS Trans. Amer. Geophys. Un.*, **74**, 113, 1993.